Faculty of Science, Palacký University

Olomouc

Department of Experimental Physics

2D Materials for Energy Storage and Photocatalysis: View into Intriguing Properties

PhD THESIS

Mgr. Jana Dzíbelová

supervisor:

Mgr. Jan Filip, Ph.D.

Olomouc November 2023

Bibliographic Details

Title	2D Materials for Energy Storage and Photocatalysis: View into Intriguing Properties
Czech Title	2D Materiály pro Ukládání Energie a Fotokatalýzu: Vhled do Zajímavých Vlastností
Type	Ph.D. thesis
Author	Mgr. Jana Dzíbelová
Supervisor	Mgr. Jan Filip, Ph.D.
University	Palacký University Olomouc
Study program	P1703 Physics
Department	Department of Experimental Physics
Language	English
Year	2023
Pages	175

Declaration

I hereby declare that this thesis is my own work and that I have completed it to the best of my knowledge and belief under the guidance of my former supervisor doc. Mgr. Jiří Tuček, Ph.D. and my current supervisor Mgr. Jan Filip, Ph.D. It does not contain any material previously published or written by any other person, or material that has been substantially accepted for the award of any other degree or diploma of a university or other institution of higher education, unless duly acknowledged in the text.

In Olomouc, date ....

Signature

Acknowledgment

I would like to express my gratitude first of all to the mentors who guided me through my PhD studies, namely my supervisor Jan Filip for all the consultations and valuable advice, Juri Ugolotti for introducing me to the world of thermal analysis, my former supervisor Jiří Tuček for guiding me through the early stages of my scientific life and last but not least Jani Kotakoski for his guidance during my internship in Vienna, subsequent advice and patience during data processing.

My profound thanks go to all colleagues and friends from both CATRIN-RCPTM at Palacký University and the PNM group at the University of Vienna for their cooperation, stimulating conversations and willingness to help. Special thanks to all the colleagues from office 2.25 for their support, friendship and motivation.

Finally, this work would never have been completed without the support of my husband, whom I thank from the bottom of my heart.

List of Publications to which the Author of This Dissertation Has Contributed as Main Author or Co-Author During Her Doctoral Studies (2017 - 2023)

i. **Havláková, J.**, Tuček, J., Zbořil, R.: *Stoichiometry issue of Iron(III) oxide nanomaterials by mossbauer spectroscopy*, NANOCON 2018 - Conference Proceedings, 10th Anniversary International Conference on Nanomaterials - Research and Application, 2019, pp. 93-99

ii. Tantis, I., Bakandritsos, A., Zaoralová, D., Medveď, M., Jakubec, P., **Havláková, J.**, Zbořil, R., Otyepka, M.: *Covalently Interlinked Graphene Sheets with Sulfur-Chains Enable Superior LithiumSulfur Battery Cathodes at Full-Mass Level*, **Advanced Functinoal Materials**, 2021

iii. Šedajová, V., Bakandritsos, A., Blonski, P., Medveď, M., Langer, R., Zaoralová, D., Ugolotti, J., **Dzíbelová, J.**, Jakubec, P., Kupka, V., Otyepka, M.: *Nitrogen doped graphene with diamond-like bonds achieves unprecedented energy density at high power in a symmetric sustainable supercapacitor*, **Energy Environmental Science**, 2022

iv. Karagiannaki, A., Konidakis, I., Kourmoulakis, G., Demeridou, I., **Dzíbelová, J.**, Bakandritsos, A., Stratakis, E.: *Probing the effect of a glass network on the synthesis and luminescence properties of composite perovskite glasses*, **Optical Material Express**, 2022

v. Hrubý, V., Zdražil, L., **Dzíbelová, J.**, Šedajová, V., Bakandritsos, A., Lazar. P., Otyepka, M.: *Unveiling the true band gap of fluorographene*

and its origins by teaming theory and experiment, **Applied Surface Science**, 2022

vi. **Dzíbelová, J.**, Hejazi, H.S.M., Šedajová, V., Panáček, D., Jakubec, P., Baďura, Z., Malina, O., Kašlík, J., Filip, J., Kment, Š., Otyepka, M., Zbořil, R.: *Hematene: A Sustainable 2D Conductive Platform for Visible-Light-Driven Photocatalytic Ammonia Decomposition*, **Applied Materials Today**, 2023

Please note that this thesis is compiled partially from the results and observations that were obtained during the work on publications ii. and vi. listed above and work on projects at the Regional Center of Advanced Technologies and Materials.

Participation at Conferences

i. **Mössbauer Spectroscopy in Material Science MSMS 2018**, Prague, Czech Republic, $25^{th} - 28^{th}$ June 2018
   Oral presentation: *Thermally induced transformations of iron(III) oxide polymorphs in various atmospheres*

ii. **NANOCON 2018**, Brno, Czech Republic, $17^{th} - 20^{th}$ October 2018
   Poster: *Stoichiometry issue of iron(III) oxide nanomaterials by Mossbauer spectroscopy*

iii. **Journal of Thermal Analysis and Calorimetry Conference JTACC 2019**, Budapest, Hungary, $18^{st} - 21^{th}$ June 2019
   Poster: *STA/MS investigation of functionalized graphene-based 2D materials*

iv. **International Conference on Applications of Mössbauer Effect ICAME 2019**, Dalian, China, $1^{st} - 6^{th}$ September 2019
   Poster: *Thermally induced transformations of iron(III) oxide polymorphs in various atmospheres* – poster award

v. **European Conference on Mineralogy and Spectroscopy ECMS 2019**, Prague, Czech Republic, $10^{st} - 13^{th}$ September 2019
   Poster: *Thermally induced solid-state transformations of* Fe_2O_3 *polymorphs in various atmospheres*

vi. **Workshop on low dimensional materials LDM 2022**, Liblice, Czech Republic, $19^{st} - 22^{th}$ September 2022
   Poster: *Non-van der Waals 2D materials from natural source*

List of Figures and Tables

List of Abbreviations

2D	two-dimensional
3D	three-dimensional
AFM	Atomic Force Microscopy
CPEM	Correlative Probe and Electron Microscopy
DSC	Differential Scanning Calorimetry
DTG	Derivative Thermogravimetric analysis
EEGS	Electrochemically Exfoliated Graphene Sulfide
EDX	Energy Dispersive X-ray Spectroscopy
EGA	Evolved Gas Analysis
EPR	Electron Paramagnetic Resonance
FC	Field Cooled
FG	Fluorographene
FFT	Fast Fourier Transformation
FIB-SEM	Focused Ion Beam Scanning Electron Microscopy
FOV	Field Of View
GA	Graphene Acid
GF	Graphite Fluoride
GN3	Nitrogen doped graphene
GS	Graphene Sulfide
GPS	Graphene Polysulfide derivative
LIBs	Lithium Ion Batteries
LSBs	Lithium Sulphur Batteries
n-vdW	non-van der Waals
RT	Room Temperature

SEM	Scanning Electron Microscopy
STA	Simultaneous Thermal Analysis
STEM	Scanning Transmission Electron Microscopy
STEM-HAADF	Scanning Transmission Electron Microscopy High Angle Annular Dark Field
STEM-MAADF	Scanning Transmission Electron Microscopy Medium Angle Annular Dark Field
TEM	Transmission Electron Microscopy
TGA	Thermogravimetric Analysis
VB	Valence Band
vdW	van der Waals
W-H plot	Williamson-Hall plot
XPS	X-ray Photoelectron Spectroscopy
XRD	X-ray Diffraction
ZFC	Zero Field Cooled

Abstract

The present dissertation thesis deals with the investigation of various 2D materials for energy storage and photocatalysis. These include materials based on graphene derivatives and MXenes as well as the so-called hematene, a member of a new class of 2D non-van der Waals materials. In the theoretical part, the reader is offered an introduction to the studied materials, as well as the basic principles of the experimental techniques employed in the thesis: thermogravimetric analysis (TGA), powder X-ray diffraction (XRD) and scanning transmission electron microscopy (STEM). The experimental part is then divided into two parts. Specifically, (i) XRD and TGA characterizations of graphene- or MXene-based materials for energy storage; (ii) synthesis optimization of hematene, study of its structural changes and variation of properties induced by dimensionality restriction and its application for photocatalytic ammonia decomposition.

Contents

Introduction

The material science community faces a major challenge considering growing society demand for sustainable energy sources and next generation energy storage devices. As a result, novel advanced materials are developed, explored and tested in the fields of energy storage and photocatalysis. The class of two-dimensional (2D) materials has gained significant attention in the past decade thanks to their attractive properties that are distinct compared to their bulk/three-dimensional (3D) material counterparts.

It is crucial to understand the structure and physico-chemical properties of the materials in order to tailor them to suitable application, as each usage requires different performance characteristics. In this sense, material research relies on the employment of a variety of techniques, combining the gained insight and putting them together as pieces of a puzzle to obtain the whole picture of the material characteristic and functionalization mechanisms.

The present thesis deals with the investigation of advanced 2D materials, in particular for energy storage and photocatalysis, using thermogravimetric analysis (TGA), powder X-ray diffraction (XRD) and scanning transmission electron microscopy (STEM) as key techniques, which provide detailed insight into the quantitative composition, structure and microstructure of nanomaterials, and, in the case of STEM, even into the structure at the atomic level.

There are three main aims in the present thesis:

- Investigation of different graphene derivatives and MXene heterostructure for energy storage by means of TGA and powder XRD to provide better understanding of the functionalization, structural properties and their effect on the material applicability.
- Preparation of novel 2D α-Fe_2O_3 material (hematene) with a focus on synthesis optimization in terms of sustainability.
- Subsequent detailed characterization of the prepared hematene with a focus on the structure, change of properties with reduced dimensionality and exploration of possible application.

1 Theoretical part

1.1 Two-dimensional van der Waals and non-van der Waals systems

2D materials have attracted the attention of scientists for decades because they have unique physicochemical properties compared to their bulk counterparts due to quantum confinement and enhanced surface states. The history of theoretical studies, predictions and experimental attempts on preparing ideally atomically thin graphite films, now known as graphene, goes back more than 70 years [1, 2]. Only the rediscovery of graphene by Geim and Novoselov in 2004, and in particular their work on describing the properties of graphene, marked a breakthrough was made and the so-called "gold rush" for 2D materials began [3]. Since then, a variety of 2D materials have been synthesized and studied, such as hexagonal boron nitride (h-BN), silicon carbide (SiC), transitional metal dichalcogenides (TMDs, e.g. MoS_2, WS_2, $MoTe_2$ ...), black phosphorus (or phosphorene), MXenes, as well as various graphene derivatives [4].

The family of 2D materials can be sorted into two groups based on the type of the parent material. The first group is called "van der Waals" (vdW) materials, because the bulk parents have strong chemical bonds oriented only in-plane and weak van der Waals bonding oriented out-of-plane, and includes well-known materials like graphene, black phosphorus, transitional metal dichalco-

genides (TMDs), metal-organic frameworks (MOFs), etc. The other group, so-called "non-van der Waals" (n-vdW) materials, have strong chemical bonds in all three directions, which makes them more challenging to cleave into individual sheets. The successfully prepared 2D n-vdW materials include MXenes, metals, metal nitrides, phosphides and of course oxides, such as hematene (from hematite, i.e. α-Fe_2O_3), magnetene (from magnetite, i.e. Fe_3O_4), chromiteen (from chromite, i.e. $FeCr_2O_4$), ilmenene (from ilmenite $FeTiO_3$), etc. [5, 6, 7, 8].

These n-vdW 2D nanostructures – few discovered and many others predicted [9, 10] – provide a playground for exploring the behaviour of physical phenomena in new constraints, and furthermore enable their application in a wide range of areas such as catalysis, energy production and storage, sensors, detectors and optoelectronic devices [11, 12, 13, 14, 15].

The stability of free-standing 2D materials had been a query of its own. It is known that a long-range ordering of 2D crystal lattice is not permitted and is destroyed by thermal fluctuations [16]. The existence of large sheets of monolayer graphene is accompanied by the formation of ripples, defects or wrinkles, that was proven by theory and experiment [17]. The 2D n-vdW materials rarely exist in monolayers and are often found to be at least several atomic layers thick. Therefore, they are sometimes referred to as quasi 2D materials [18, 19].

The following chapters are devoted to a brief description of graphene and its derivatives, MXenes and 2D iron oxides as examples of conventional and n-vdW 2D materials.

1.1.1 Graphene and its derivatives

Graphene is a typical representative of 2D vdW materials. It has many superlative features, such as superior mechanical strength, giant charge car-

rier intrinsic mobility and record thermal conductivity, as was proven in 2004 [3]. These qualities make graphene interesting from the point of view of both fundamental research on quantum phenomena and practical applications. However, there are some drawbacks limiting the applicability of pristine graphene, mainly relatively low reactivity, zero bandgap and hydrophobicity [20, 21].

Graphene consists of a single, freestanding layer of carbon atoms with sp^2 hybridization in honeycomb-like hexagonal structure, as depicted in Figure 1.1a. Adjacent carbon atoms are bonded both by an in-plane σ-bonding and by π-bonding of delocalized electrons in the plane perpendicular to graphene, see Figure 1.1b. The strong σ-bonds are the source of extraordinary mechanical strength – Young's modulus reaching up to 1 TPa (converted from 2D Young's modulus to conventional), while the exceptional electrical properties of graphene are controlled by an electron cloud of delocalized π-electrons [16, 22].

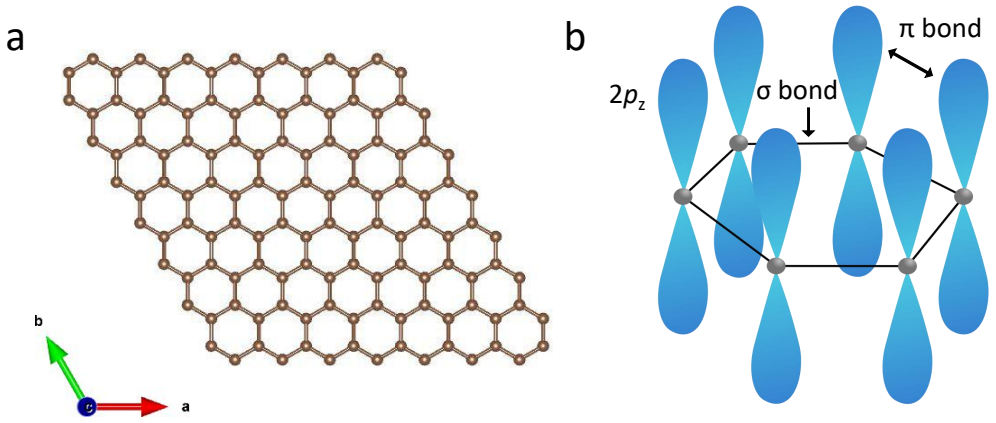

Figure 1.1: Scheme of the graphene structure, a: graphene structure from top-view; b: graphene p_z orbitals with σ and π bonds.

Graphene is known to be a zero bandgap semiconductor. Its electronic structure consists of two asymmetric sublattices of the conduction and valence

bands that touch at the so-called Dirac points. The electron waves lose their effective mass completely when propagating through the hexagonal lattice, and are therefore described as quasiparticles by the Dirac-like equation rather than by the Schrödinger equation, which is sufficient for electrons of other materials [20, 23]. Furthermore, the electrons in the atomically thin graphene are very little scattered during propagation, they are available to various scanning probes and sensitive to proximity of other materials with different electromagnetic properties. The above listed quantum effects can survive even at room temperature, which makes graphene a unique material compared to other condensed matter known to date and essentially a scientific playground for the investigation of the quantum phenomena [20].

However, there are characteristics that limit applications and full exploitation of graphene's exceptional properties. The zero bandgap prevents its use in semiconductor passive components in electronics, while its hydrophobic and inert nature restricts its use in bio-applications, catalysis, sensors and especially hinders large-scale industrial production [21].

Surface modification and tailored functionalization of graphene help to overcome these limitations.

Graphene derivatives

Graphene-like materials form a growing family of both morphological variants (nanotubes, bilayers, multilayers, nanosheets, nanoflakes) [24] and chemical relatives [25, 26]. These chemical derivatives with well defined structure and stoichiometry include graphane (hydrogenated graphene), fluorographene, graphene oxide, graphene acid, cyanographene, etc. All of these materials have been carefully developed and tuned to tackle some of graphene's limitations and to better suit the targeted application. These derivatives are thus used

in a broad range of fields, such as electronics, energy storage, optical applications, membranes, separation, biosensors and other biomedical applications [27, 28, 29, 30].

Among other graphene derivatives, fluorographene has a prominent place, as its extensive chemistry allows for new synthetic routes to various functionalities of excellent quality in terms of their yield and uniform distribution. The synthetic approaches utilize controlled partial/complete defluorination and/or substitution, enabling functionalization that cannot be achieved via plain graphene. [31]

Fluorographene is a monolayer of graphite fluoride, that can be prepared both by fluorination of graphene [32] or exfoliation of graphite fluoride [33]. Even a small amount of introduced fluorine atoms changes the structure and therefore the properties of graphene. It expands its band gap and changes the hybridization of the carbon atoms from sp^2 to sp^3, thus improving the applicability in electronics, significantly increasing reactivity and paving the way for the adoption of additional functionalities. [34].

Since even a small amount of dopant has a great influence on the properties of graphene derivatives, it is of course necessary not only to know how to prepare these derivatives, but also to characterize them correctly and to know the actual amount of the functional groups. Among other experimental methods, TGA has proved to be particularly useful for this purpose, as it can provide information not only on the thermal stability but also on the amount of functional groups or dopants. In terms of the atomic structure, powder XRD is one the key techniques.

1.1.2 MXenes

MXenes, first described in 2011, are a relatively new group of 2D materials based on cleaving the MAX phase – a ternary carbide or nitride with the general formula $M_{n+1}AX_n$, where M stands for an early transition metal (e.g. Ti, Nb, V, Cr, Mo, Ta), A is (mostly) 13 and 14 group element and X denotes carbon and/or nitrogen. MXenes are usually classified as n-vdW 2D materials, since the out-of plane bonding between the layers is stronger than vdW [14, 35]. However, they can be considered to be a link between vdW and n-vdW 2D materials, due to their layered structure.

Their classification in literature is not clear, MXenes are sometimes classified as vdW 2D materials (due to their layered structure) [**?**], on the other hand, they are sometimes classified as n-vdW 2D materials, since the bond between the layers is stronger than vdW [14, 35].

The so-called MAX phase forms a hexagonal laminated structure (with a space group of $P6_3/mmc$) with two formula units per unit cell. The M and X elements form planes of near close-packed M_6X octahedras, while interleaved by weaker (longer) bonds with pure A-group element layers, as can be seen in Figure 1.2 [36].

The relatively weak connection via A layers is used for selective etching that leads to multilayered MXene (without the A-group element), that is later delaminated into single flakes. Produced MXenes have a general formula $M_{n+1}X_nT_x$, where T_x represents the surface termination groups (e.g. $-$OH, =O, $-$F) [36, 37]. As their formula suggests, MXenes are among the most versatile 2D materials, of which more than 30 stoichiometric structures are known today [38]. The composition fundamentally influences the properties of these materials and thus their applicability. MXenes exhibit a rather unique combination of properties – they are highly conductive, possess the mechani-

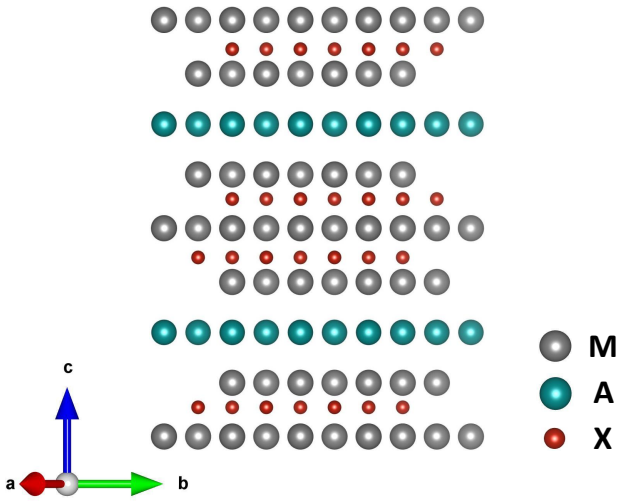

Figure 1.2: Schematic structure of a typical MAX phase, where M (metal) atoms are in grey, A (13 and 14 group element) atoms are in cyan and X atoms (C or N) are in red-brown.

cal properties of transition metal carbides/nitrides and their surface functional groups in turn provide hydrophilicity and binding capacity. As a result, they have application potential in many industries, ranging from energy storage, electronics, optics, bioapplications, catalysis, environmental applications, sensors, etc. [38, 39, 40].

The versatility of MXenes comes along with the need to properly characterize them in terms of composition, structure and properties. This is important in terms of possible applications and, moreover, in terms of replicability in materials science [41]. Approaches to the investigation of MXenes, in particular using powder XRD, will be discussed later in this thesis.

1.1.3 Iron oxides

Iron oxides display a complex variety of crystal structures with strong chemical bonding in all three directions and, therefore, can be referred to as non-van der Waals materials. They are Earth-abundant in both bulk and nanometric form and moreover, they can be easily prepared in the laboratory. Their accessibility, combined with their attractive properties, makes them an object of interest for a wide range of fields of mankind [42].

Crystal structure

There are three different non-hydrated iron oxide – FeO, Fe_3O_4 and Fe_2O_3, that consist of Fe^{2+} and/or Fe^{3+} cations and O^{2-} anions with radii of approximately 0.82 Å (Fe^{2+}), 0.65 Å (Fe^{3+}), and 1.4 Å (O^{2-}) As evident, the O^{2-} ions are larger and therefore their arrangement determines the crystal structure of the whole compound. As a result, there are also two basic ways of defining the crystal structure of iron oxides. One can describe either the arrangement of the anions (packing) or the link between the octa/tetrahedra formed by the cation centre and the nearest anions [43].

With respect to the anion arrangement, all of the iron oxides consist of stacked O^{2-} planes with interlayers of iron cations in different polyhedral coordination. In iron oxides containing trivalent iron cations, a need for charge compensation arises that leads to cation vacancies in the crystal structure of Fe_2O_3 or Fe_3O_4. This extra space, especially in Fe_2O_3, enables various arrangements of the vacancies and Fe^{III} cations and therefore allows stability of different crystal structures within the same chemical formula, known as polymorphs [43]. Four[1] different crystalline phases of Fe_2O_3 (α-Fe_2O_3, β-Fe_2O_3,γ-Fe_2O_3 and

[1]Tuek et al. [44] reported in 2015 a new fifth polymorph called ζ-Fe_2O_3 that is stable under ambient conditions (room temperature, atmospheric pressure). ζ-Fe_2O_3 was created

ε-Fe_2O_3) and one amorphous phase are well known [43]. The crystal structures of FeO, Fe_3O_4 and polymorphs of ferric oxide are shown in Figure 1.3.

The most thermodynamically stable ferric oxide polymorph is α-Fe_2O_3, commonly known as hematite (based on its blood red colour). The structure of hematite can be described in terms of a rhombohedral lattice with $a = 5.427\,\text{Å}$ and $\alpha = 55.3°$, see Figure 1.3a.

On the other hand, a better idea on the ion arrangement can be obtained from the oxygen anion point of view where hematite consists of O^{2-} arrays with hexagonal close-packed structure stacked along the [001] direction and the iron cations coordinated into face-sharing octahedra, where two cation positions are followed by a vacancy. The distance between O ions in face-sharing octahedra is smaller than between edge-sharing ones, which leads to a repulsion in the direction normal to the [001] distorting the cations towards edge-sharing positions [43]. The hexagonal unit cell has parameters of $a = 5.034\,\text{Å}$, $c = 13.75\,\text{Å}$ and six formula units per unit cell.

Since crystal structure governs the material magnetic, electric, optical and chemical properties, each iron oxide with different lattice arrangement has distinct features. Various iron oxides are utilized in medicine, (photo)catalysis, biosensors, energy storage, optoelectronics, environmental technologies and magnetic data storage [45, 46, 47, 48, 49, 50, 51].

via high pressure treatment of β-Fe_2O_3 and is the first ferric oxide with a monoclinic structure at room temperature.

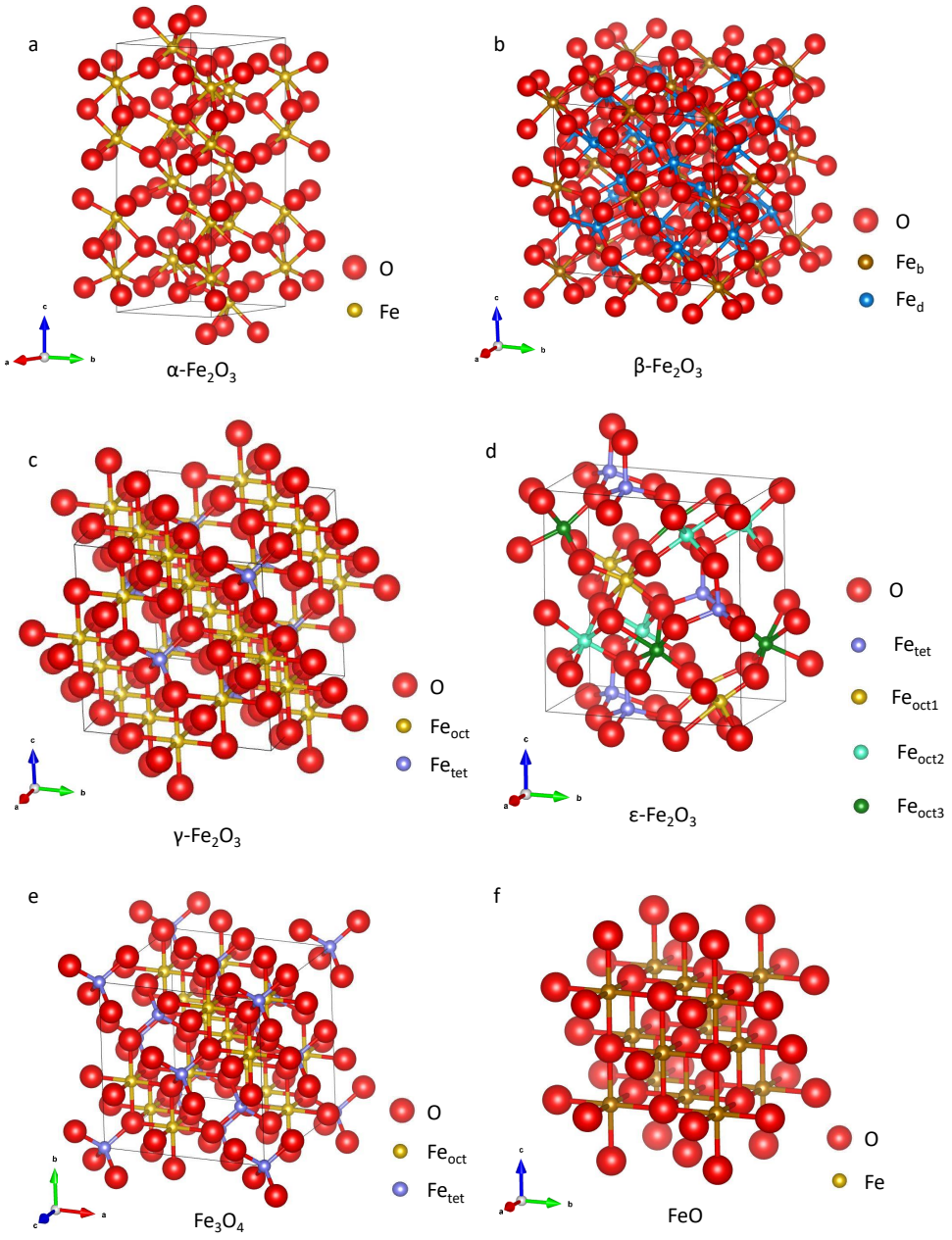

Figure 1.3: Schematic crystal structures of all iron oxide phases; a: α-Fe_2O_3; b: β-Fe_2O_3; c: γ-Fe_2O_3, d: ε-Fe_2O_3, e: Fe_3O_4 and f: FeO.

Properties of bulk and nanometric α-Fe_2O_3

Hematite[2] is a versatile ferric oxide polymorph since it can exist both in bulk and nanometric form in various sizes and morphologies, occurs naturally and can be synthesized as well in laboratory. α-Fe_2O_3 is the most thermodynamically stable phase that is formed when other polymorphs are heated in the presence of air or other oxidative atmosphere. Such a process is called thermal polymorphic transformation [52].

The magnetic behaviour of α-Fe_2O_3 is temperature dependent. At room temperature, hematite is known to be a weak ferromagnet. However, when cooled down, a magnetic transition connected to spin reorientation occurs. At the so-called Morin temperature $T_M \approx 260\,K$, we can observe the Morin transition to an antiferromagnetic state. This phenomenon is caused by the arrangement of spins in hematite. Above T_M, hematite has 2 alternating, partially intersecting antiferromagnetic sublattices. However, their spins are not exactly antiparallel (with a distortion of about 0.1°), causing a spin canting effect and weak ferromagnetism. At T_M, the spins rearrange to an angle of $\approx 7°$ to the c-axis and become perfectly antiparallel, making hematite antiferromagnetic below the Morin temperature [53]. Furthermore, the value of Morin transition is well known to depend on the nanoparticle size, vacancies, cation substitutions and crystal lattice defects. [54, 55, 56, 57].

In terms of electrical properties, α-Fe_2O_3 is known as an n type semiconductor with a band gap of ≈ 2.2 eV in visible-light region making it a good candidate for photochemistry and photocatalysis. However, hematite suffers from a low hole mobility at room temperature ($\approx 10^{-2}\,cm^2V^{-1}s^{-1}$) and fast electron-

[2]The mineralogical name is preferred only for the natural occurrence of iron oxide phases. If they are synthesized artificially, it is more appropriate to use the chemical formula, in this case α-Fe_2O_3.

hole recombination [53, 58], which is usually tackled by introducing various dopants [59, 60, 61], creating heterostructures or composites [62, 63, 64]. Furthermore, the electrical and optical properties also depend to some extent on morphology and particle size, which also applies to colour [53, 65].

2D iron oxides

Early indications of 2D iron oxides were based on thin films or layers grown by different vapor deposition methods (CVD, MBE, etc.) on various substrates and have been studied since the 1990s [66, 67, 68, 69]. However, the first freestanding 2D iron oxide – α-Fe_2O_3, so-called hematene – was introduced in 2018 by Puthirath et al. [5]. Soon after this pioneering work, Puthirath et al. [8] followed with report on ilmenene (2D $FeTiO_3$) in 2018 and Serles et al. [6] introducing magnetene (2D Fe_3O_4) in 2021.

The studies published so far suggest that 2D iron oxides open up a new class of interesting materials and the possibility of studying physical phenomena (especially magnetism) in 2D nanostructures. With respect to hematene, interesting features have been predicted [70, 71, 72, 73, 74, 75] and some so far observed - for example, a decrease in the Morin temperature (T_M) of the transition from the antiferromagnetic to the weakly ferromagnetic state [5, 76] and interesting optical properties - nonlinear optical behaviour suitable for protective devices [77, 78]. From a chemical point of view, the large surface to volume ratio combined with potential defect structure appears to have the prospect for various chemical reactions [79, 80].

Properties and characteristics of hematene

It has been shown by Puthirath et al. [5], that hematene forms sheets oriented along the [001] and [010] directions, where the (001) plane with hexag-

onal symmetry is presumed to be more stable. The predicted thickness of these monolayer sheets was estimated to 3.98 Å (in [001] direction) and 3.2 Å (in [010] direction) by molecular dynamic simulations. Bandyopadhyay et al. [72] explain the stability of [001] oriented hematene sheets by an absence of unpassivated Fe atoms on the surface. The lattice of monolayer hematene is theoretically predicted to consist of a hexagonal sublattice of octahedrally coordinated Fe_{in} ions directly stacked by two sublattices of trigonally coordinated Fe_{out} ions. Such monolayer hematene is presumed to have slightly higher lattice parameter $a = 5.16$ Å, compared to bulk hematite. However 2-layer ($a = 5.14$ Å), 3-layer ($a = 5.12$ Å), 4-layer ($a = 5.10$ Å) and thicker systems are predicted to possess similar structural configuration to bulk hematite, as revealed by computational work published by Bacaksiz et al. [73].

The magnetic behavior of bulk hematite is governed by the Fe–O–Fe superechxange, that is either antiferromagnetic (in the face-sharing octahedra) or ferromagnetic (in the edge-sharing octahedra) [53]. However, alongside with the dimensionality restriction and consequent high specific surface area, the spin-canting effects (causing weak ferromagnetic behaviour in bulk hematite above T_M) become dominant in the 2D state of hematene.

Thin hematene sheets display enhanced ferromagnetism and suppressed T_M, while in some cases of few-layered or monolayer hematene (theoretically predicted) the Morin transition completely disappears and hematene behaves as a weak ferromagnet in the entire temperature range, as evidenced by several publications [5, 72, 73, 81]. Furthermore, Mohapatra et al. [81] reported on an increased saturation magnetization (M_S) and increased coercivity (H_C) values upon cooling and a spin-glass-like transition at $T_f \approx 48$ K followed by a drop of H_C values below T_f. They ascribed the spin-glass-like transition in hematene to short range correlation of surface spin coupling with ligands.

The electronic properties were so far investigated through experimental measurements and theoretical calculations. The thin hematene sheets were mostly found to display narrower band gap compared to bulk hematite. However, the band gap values vary both in theory and experiment, depending on starting material, exfoliation conditions, sample thickness and introduced perturbations (0.8 – 1.5 eV by Padilha et al. [82]) [73, 83, 84]. The band gap narrowing can be explained by the distinct coordination and local symmetry of the Fe atoms on the surface [82]. Wei et al. [83] showed that the electronic and magnetic properties could also be modulated by a surface passivation with H/OH group. The fully hydrogenated hematene sheets were predicted to be half-metallic with a ferromagnetic groud state, whereas the sheets fully covered with OH groups were estimated as antiferromagnetic semiconductors.

These features enable hematene usage in several catalytic fields, sensors etc. Zhang et al. [85] combined hematene with Au nanoclusters for efficient glucose sensing, late Zhan et al. [86] decorated hematene with Pt to create a novel platform for methanol electrooxidation that surpasses conventional Pt/C catalysts in CO tolerance. Recently, Motlagh et al. [87] employ hematene electron and hole generation for photocatalytic decomposition of a wide spread antibiotic tetracycline to CO_2 and H_2O. In terms of optical properties, Stavrou et al. [88] described the non-linear optical behaviour of hematene and predicted its usage in photonics and optoelectronics. Recently, Monk [89] explored the hematene biocompatibility as bone tissue scaffold dopant to facilitate osteogenesis in her Master thesis, where the 2D α-Fe_2O_3 proved to be promising from the first *in vitro* experiments.

1.1.4 Preparation methods of 2D nanomaterials

The preparation of all nanomaterials regardless their dimensionality can be in general divided into two approaches: top-down and bottom-up. Top-down approach is based on reducing size or dimensionality of some parent bulk material and usually is considered as a more physical. Bottom-up means various methods of assembling individual atoms into grains and their (more) controlled growth and usually is considered as a more chemical approach [90]. A schematic depiction of the classification of preparation methods is shown in Figure 1.4.

The preparation method combined with the crystal structure, morphology, possible doping and/or defects affect the properties of the sample. Therefore, it is crucial to take into account the nature of the parent material, the requirements on the final sample and the facilities at the site to be able to find the optimal preparation conditions in a given case.

Top-down methods

If we consider the top-down approach for the preparation of 2D materials, it is the decomposition of some suitable bulk material by various methods that include:

Exfoliation This group of techniques is based on the mechanical disruption of bonds within the material in a certain direction, resulting in the formation of 2D sheets. For example, mechanical exfoliation using adhesive tape, as in the case of Novoselov and Geim's work on graphene in 2004 [3]. It can also be performed in the liquid phase using different dispersants and different energy sources (ultrasound, microwaves) to break bonding interactions as well as utilizing intercalation and expansion of molecules or ions between layers [91].

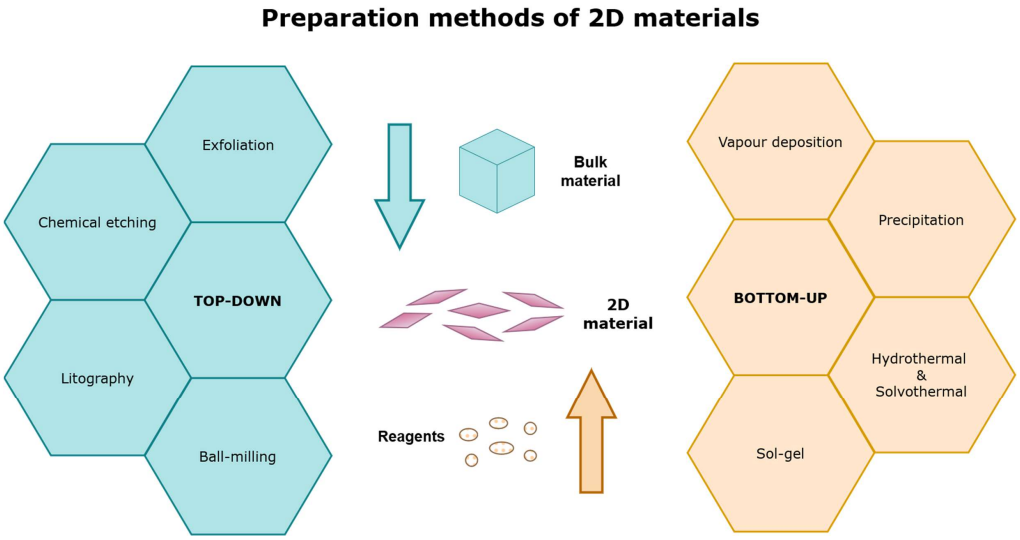

Figure 1.4: A scheme of the classification of 2D material preparation methods.

Chemical etching More advanced method utilizing a chemical reaction to selectively cleave bonds in the parent bulk material is called (chemical) etching. It is often used as the first step in the preparation of MXenes, where the MAX phase is selectively etched using a strong acid (e.g. HF) and obtained multilayers are then further delaminated by other exfoliation methods [91, 92, 93].

Litography This class of methods is based on transferring a designed pattern onto a bulk material using, for instance, photolithography or electron beam lithography, whilst the unpatterned region is then selectively etched to produce a 2D nanomaterial or a heterostructure. It is widely used in the fabrication of microchips and advanced semiconductor devices [94, 95, 96].

Ball-milling This process has been utilised as a method to prepare the bulk material prior to further exfoliation. This involves a process whereby a tangential mechanical force is applied to large crystals to disrupt their structure. In addition, the balls impact the material, leading to a reduction in the lateral dimension of the resulting sheets. This method alone is not sufficient to prepare very thin sheets and is therefore often followed by further exfoliation, e.g. chemical etching, ultrasound-assisted, etc. [36, 97].

Overall, top-down approaches to prepare 2D nanomaterials are in general inexpensive and relatively simple. However, they also have several drawbacks, such as large size distribution, possible presence of impurities and introduced defects, limited scalability, and limited yields (only a portion of the input material is fully converted into a 2D sample).

Bottom-up methods

Bottom-up preparation of 2D nanostructures is based on self-assembly of individual atoms or molecules and their controlled growth, using several possible methods:

Vapour deposition Vapour deposition is a group of techniques that rely on the transport of vapour onto a suitable substrate under controlled conditions, where the evaporated material condenses to form a solid sample ranging from 2D single crystals to continuous layers and even heterostructures. Three main vaporization techniques are recognized depending on the material to be evaporated, the vaporization method and the transfer: chemical vapour deposition, i.e. CVD (gaseous molecules are introduced into the reaction chamber), physical vapour deposition,

i.e. PVD (target material is vaporized by e.g. heating or ion sputtering) and vapour phase transport, i.e. VPT (utilizing a vapour phase transport agent) [98].

Precipitation Precipitation is a method based on crystallization from solution and subsequent grain growth that involves dynamic processes of dissolution and recrystallization.

During precipitation, so-called Ostwald ripening occurs, where large grains are favoured over small nanoparticles. In addition, spontaneous phase transformations occur during dissolution and recrystallization, with kinetics favouring the growth of thermodynamically less stable phases first, followed by recrystallization into more stable phases (a process known as Ostwald's rule of stages) [99].

Hydrothermal synthesis This method utilizes precipitation from an aqueous solution in a closed vessel known as an autoclave at elevated temperature above the boiling point of water. The properties of the resulting samples can be controlled by changes in the reaction conditions (pH, temperature, pressure, etc.). [99].

Solvothermal Solvothermal methods are similar to hydrothermal, only an organic solvent is used instead of water solution and they usually take place under elevated pressure as well as temperature [99].

Sol-gel The name of this method suggests that it will involve sol (colloidal solution) and gel (macromolecule dissolved in liquid) phases. The preparation process consists of several steps: first the solution is prepared, which is followed by gelation, or ageing, then drying and calcination. Sol-gel is not a very common way of preparing 2D materials and is scarce in the published literature [90, 100].

1.2 Introduction to the experimental techniques utilised in the thesis

The following sections provide an introduction to the experimental techniques used in the present thesis to investigate 2D nanostructures.

1.2.1 Scanning transmission electron microscopy

The usage of electron beam in microscopy is motivated by the need to image smaller objects, such as nanomaterials and nanostructures. The resolution of any microscope is given by the well known Abbe diffraction limit:

$$d \geq \frac{\lambda}{n \sin(\alpha)}, \tag{1.1}$$

where d is the spatial resolution, λ is the wavelength of the radiation/particles used, n is the refractive index of the lens and α is the angle of view. Small enough wavelengths allowing atomic resolution can be achieved via multiple different particles (e.g. X-Ray photons, neutrons, electrons, ions), yet electrons prove to be advantageous. They are readily produced, their energy and therefore wavelength can be varied by applying a potential and the path can be altered by an electromagnetic field [101].

When an electron reaches a sufficiently thin material, several phenomena can happen. It can be simply transmitted, or it can interact with the matter – be scattered. Figure 1.5 portraits possible electron and sample interactions:

Inelastic scattering Significant part of the interacting electron energy is lost through momentum transfer. The Figure 1.5 shows a collision with an inner electron of the impacted atom, which can result in the inner electron being knocked out and thus the formation of a secondary electron

(SE). The empty energy level is then filled by an electron from a higher level, releasing the characteristic X-ray emission.

Elastic scattering The incident electron interacts electrostatically either with the atomic nucleus solely (large scattering angles and backscattered electrons) or with both the nucleus and the electron shell (small scattering angles). Elastic scattering is not associated with a detectable energy change of the incident electron.

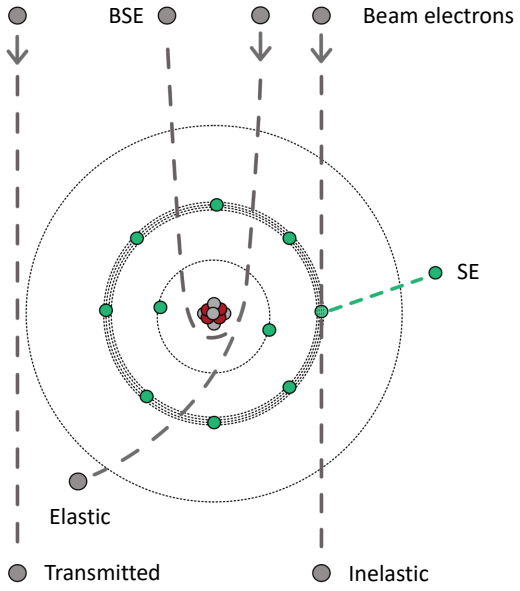

Figure 1.5: Illustration of possible interactions of a primary electron with an atom. The scheme includes back scattered electron (BSE), elastically scattered electron, secondary electron (SE) as a possible result of inelastic scattering and transmitted electron.

In scanning transmission electron microscopy (STEM), the electron beam is focused with objective lens to form a cone shaped Å -sized probe that is moved precisely by scan coils and scans the sample point by point. After elastic or

inelastic interaction with the specimen, the beam is spread with projector lens and can be detected by various detectors [101].

Two types of electrical lenses are used for modification of electron beam. Electrostatic lenses are used for extracting the electrons from electron gun and for their subsequent acceleration. Electromagnetic lenses are used for shaping the beam, however, they introduce aberrations (e.g. spherical, astigmatism, coma or chromatic aberration). As Eq. (1.1) limits optical microscopes (electron microscopy can use electron beams with different energies and therefore wavelengths), aberrations are the limiting factor in electron microscopy, and their correction is a complex process, that involves iterative measurement and subsequent correction by adjusting the electromagnetic field in the corrector [101].

Several types of detectors can be applied in STEM. A CCD (charge-coupled device) camera can be used to collect ronchigrams[3], that are convenient to navigate around the sample and especially to tune the beam (correct the aberrations and find the focal plane). Annular dark field (ADF) detectors are ring-shaped detectors used to collect elastically scattered electrons. With high enough collection angle (above 40 mrad [102]), one can exclude coherently scattered electrons and the obtained image can be dominated by the Rutherford scattering with a dependence on the atomic number. In ADF mode the heavier atoms appear brighter and vice versa providing high contrast between atoms with high and low atomic number Z, hence the term Z-contrast [101, 103].

[3]Ronchigram is a coherent convergent electron beam diffraction pattern collected with a very large objective aperture or with the aperture removed completely [101].

1.2.2 Thermal analysis

Thermal analysis is a family of destructive techniques of analytical chemistry for studying the composition of (nano)materials both quantitatively and qualitatively, their thermal stability and thermally induced behaviour by plotting measured property as a function of temperature. The most commonly used forms include thermogravimetry analysis (TGA, or just TG), differential scanning calorimetry (DSC) and secondary techniques such as evolved gas analysis (EGA). To maximize the information gained from a thermal destruction of a material, a combination of thermal analysis methods is often used at the same time. Such a set-up is called simultaneous thermal analysis (STA) [104, 105].

The principle of TG is the use of a thermo-microbalance that is able to detect sample mass change as a function of temperature. Briefly, the sample is placed in a suitable crucible in a furnace, then the temperature is increased under controlled gas flow and heating rate. The choice of atmosphere (type of gas flowing through sample chamber) for the experiment and temperature program depend on the required information about the sample. Atmosphere can be of reactive, oxidising or inert nature, which will affect the behaviour of the sample upon heating. There are three types of temperature programs: dynamic, isothermal and their non-linear combination [104].

The mass changes of the sample, i.e. mass loss or gain, may indicate several processes, including [105]:

- Evaporation of volatile constituents (drying, desorption and adsorption of gases, loss of water of crystallization).
- Oxidation of metals in air or oxygen atmosphere.
- Oxidative decomposition of organic compounds in air or oxygen atmosphere.

- Thermal decomposition in an inert atmosphere (known as pyrolysis or carbonisation for organic substances).

- Heterogeneous chemical reactions, where the starting material is taken up from experimental atmosphere (e.g. reduction under hydrogen containing gas flow).

To identify more precisely the starting and ending temperature of observed processes, a first derivative of the TGA curve, called DTG, is often performed.

When the sample is heated under a constant pressure (isobaric process), a buoyancy correction is needed due to a decrease in the gas density. For instance, dry air density changes from $1.184\,\mathrm{mg}\cdot\mathrm{mL}^{-1}$ at $25\,^{\circ}\mathrm{C}$ to $0.457\mathrm{mg}\cdot\mathrm{mL}^{-1}$ at $500\,^{\circ}$ C and even to $0.269\mathrm{mg}\cdot\mathrm{mL}^{-1}$ at $1000\,^{\circ}$ C. As a result, the sample would virtually appear heavier at increased temperature. To avoid this effect, a correction measurement (also known as a baseline or blank experiment) under the same conditions (atmosphere, temperature steps, heating rate, gas flow) with an empty crucible is necessary. The correction measurement is then subtracted from the sample measurement curve [105].

Although it is possible to gain valuable information from TG, the obtained data are indirect. Therefore, one needs to have some input information about the sample composition or utilize other techniques simultaneously. TG instrument is commonly combined with DSC that measures the heat flow from (exothermic process) or into (endothermic process) the sample as a function of temperature. When there is combined information about mass change and heat flow, one can recognize and distinguish between several phenomena, such as melting, crystallization, crystal structure rearrangement and glass transition [105].

In the material research, TGA can be used to straightforward determination of the mass percentage of functional groups, dopants and organic or

inorganic compound content. Furthermore, one can even estimate the degree of functionalization (DoF) using the following equation:

$$\mathrm{DoF} = \frac{\Delta m(\mathrm{F}) \cdot M(\mathrm{S})}{m(\mathrm{S}) \cdot M(\mathrm{F})}, \tag{1.2}$$

where $\Delta m(\mathrm{F})$ denotes the mass loss corresponding to the functionality, $M(\mathrm{S})$ is molar mass of the functionalized support material, $m(\mathrm{S})$ denotes support material residual mass, and $M(\mathrm{F})$ is molar mass of the functionality [106, 107].

To provide more information about thermal decomposition products, secondary techniques can be coupled with TG/DSC for an EGA. Usually, one of the following techniques can be used to analyse parts of the outlet gas from furnace with the sample: infrared (IR) spectroscopy, gas chromatography (GC) or mass spectrometry (MS).

1.2.3 X-ray powder diffraction

When a crystalline material is illuminated by coherent X-rays at a suitable angle, the X-rays reflected from different layers interfere according to Bragg's law:

$$n\,\lambda = 2\,d\,\sin\theta, \tag{1.3}$$

where n denotes the order of diffraction, λ is the X-ray wavelength, d is the interplanar distance and θ is the incident angle [108]. Based on the examined material, there are two main groups of X-ray crystallography methods. One is suitable for single crystals, where the obtained pattern are diffraction spots, while the other is powder X-Ray diffraction (XRD), where the diffracted beams from multiple crystallites form a cone and detected pattern is a continuous cross section of said cone.

To obtain the information about the whole crystal structure in powder XRD, one should scan the sample at different incident angles θ. When the

Bragg's law condition is fulfilled for a given angle, the beams diffracted from a certain set of planes interfere and a diffraction peak can be observed in the diffractogram. Then the relation for a certain (hkl) interplanar distance can be derived from Eq. (1.3):

$$d_{\mathrm{hkl}} = \frac{n\,\lambda}{2\,\sin\theta}. \tag{1.4}$$

Based on the positions, intensities and profiles of the peaks, several qualitative and quantitative features of the sample can be determined with numerical fitting:

- Crystal structure – from the peak positions and relative intensities.
- Lattice parameters – from peak positions.
- Quantitative phase analysis – from peak intensities.
- Crystallite sizes[4] – from peak profile.
- Micro-strain – from peak profile.
- Residual stress – from peak positions.

In order to achieve optimal measurement conditions, both beam and sample should have near-ideal properties. The beam should be coherent, collinear and perfectly focused in plane with the sample surface, which can be achieved by several optical elements such as a set of soller slits, a monochromator, a beta filter, divergent slits, anti-scatter slits, etc. The powder sample should be prepared in a way to eliminate preferential orientation (unwanted texture that accentuates some diffraction peaks over others) with a sufficiently thick layer that has a flat surface. To improve measured statistics, the sample stage is often rotated during XRD measurement.

[4]Crystallite size is usually understood as the size of coherent diffraction domains, which may be less than or equal to grain size, which may be less than or equal to particle size

Lattice strain analysis

The XRD peak profile can provide a basis for microstructural analysis of materials. The broadening of the peaks is caused mainly by a decrease in the crystallite size and by strain in the lattice [109, 110, 111]. Crystallite size can be estimated using the Scherrer equation:

$$D = \frac{K \cdot \lambda}{\beta \cdot \cos\theta}, \tag{1.5}$$

where D denotes crystallite size, K is the so-called shape (or Scherrer) factor, λ is the wavelength of the X-ray source, β denotes the peak broadening and θ corresponds to the peak position. The shape factor is a dimensionless number on the order of unity and consists of at least three contributions: (i) the definition of "breadth", which can be estimated as full width at half maximum (FWHM); (ii) the shape of crystallites and (iii) the size distribution of crystallites [112].

The advantage of Scherrer equation (i.e., (1.5)) is that the obtained data are correlated to individual peaks, so that the effects can be correlated to various crystallographic directions. However, the Scherrer equation only considers the size of the crystallites as the origin of the peak broadening. To gain some insight into the intrinsic strain, several methods have been developed, such as Williamson-Hall (W-H) method, Warren-Averbach analysis, size strain plot and their variations [110, 113]. W-H plot is simplified and straightforward, yet relatively accurate method based on following assumptions: the total peak broadening (β_{hkl}) consists of the sum of the broadening due to crystallite size (β_D) and the broadening due to strain (β_ϵ), which can be written as following equation:

$$\beta_{hkl} = \beta_D + \beta_\epsilon. \tag{1.6}$$

The size related broadening can be assigned with the Scherrer equation (1.5), and rewritten as:

$$\beta_D = \frac{K \cdot \lambda}{D \cdot \cos\theta}. \tag{1.7}$$

Then, the strain related broadening can be expressed by the following equation:

$$\beta_\epsilon = 4 \cdot \epsilon \cdot \tan\theta, \tag{1.8}$$

where ϵ denotes the intrinsic strain. After putting Eq. (1.7) and Eq. (1.8) into Eq. (1.5) and rearranging, we get:

$$\beta_{hkl} \cdot \cos\theta = \epsilon \cdot 4 \cdot \sin\theta + \frac{K \cdot \lambda}{D}. \tag{1.9}$$

The final form of Eq. (1.9) is an equation of a straight line. Therefore, after plotting β_{hkl} as a function of θ and linear fitting, we obtain the intrinsic strain directly as slope of the straight line and the crystallite size can be calculated from the intercept [110].

2 Experimental details

2.1 Syntheses of materials studied in the presented thesis

2.1.1 Graphene-polysulfide derivative and control samples

Graphene-polysulfide denoted as GPS

Graphene-polysulfide derivative (GPS) and control samples were synthesized by I. Tantis [114], based on flouorographene (FG) chemistry:

- 250 mg of FG was stirred in 15 mL of NMP (*N*-Methyl-2-pyrrolidone) for 48 h at RT, followed by exfoliation via sonication for 4 h.
- 2 g of NaPS (sodium polysulfide, see [114] for details) was added to the solution and reacted at 80 °C for 48 h under N_2 atmosphere.
- The final product was centrifuged and washed successively in NMP, distilled water, ethanol and acetone.
- The washed solution was freeze dried to obtain fine powder.

Control samples denoted as GS and EEGS

Two control samples were prepared in the scope of the study:

- GS – in the synthesis, elemental sulfur (S) was used instead of NaPS.
- EEGS – electrochemically exfoliated graphene was used instead of FG in the synthesis.

2.1.2 MXene/graphene derivative heterostructures

All the analysed samples in the span of the MXene/graphene derivative study were synthesized by V. edajová.

Graphene derivatives

N-doped graphene, denoted as GN3 was prepared following the synthesis protocol from edajová et al. [115] and charged GN3Q material was prepared with the following synthesis protocol: The measured amount of material was washed 3 times with water of pH 8, then the appropriate amount of glycidyltrimethylammonium chloride was added and allowed to react for 5 h at 40°C. The resulting product was washed thoroughly with distilled water.

Another utilized graphene derivative was graphene acid, denoted as GA, that was prepared via the synthesis reported by Bakandritsos et. al [27].

MXene samples

MAX phases and MXene samples, in particular $Ti_3C_2T_x$ were synthesized following protocol reported by Mathis et al. [116].

$Ti_3C_2T_x$/GN3 and $Ti_3C_2T_x$/GA heterostructures

To fabricate the heterostructures, the following process was performed and adjusted for different mass loadings: $Ti_3C_2T_x$ and graphene derivative were combined in a determined ratio of 99:1, respectively. The total quantity was

then adjusted to suit the specifications of the vacuum filtration setup, ensuring the desired mass loading for the resulting self-standing film.

As an example, a film with 1 mg/cm^2 mass loading, was prepared by the following protocol:

- 41.58 mg of $Ti_3C_2T_x$ in its original DI water dispersion was thoroughly mixed with 0.42 mg of GN3 in its original dispersion.
- The mixture was then diluted to 5 mL of DI water and subjected to vacuum filtration utilizing a setup with an effective filtration area of 42 cm^2. Prior to the filtration process, Celgard 3501, employed as the supporting membrane, was thoroughly washed with acetone, ethanol and DI water.
- The resulting self-standing film was carefully removed from the Celgard membrane and subsequently stored in a desiccator to ensure optimal preservation conditions.

2.1.3 Hematene-based samples

Hematene was prepared via sonochemical exfoliation of hematite ore called specularite. Two specularite species were used in the span of the work on the presented thesis:

- obtained from Moravian Museum in Brno, Czechia,
- collected at Elba, Italy.

The specularite exfoliation in DMF (samples denoted as hematene-DMF) was adapted from Purithan Balan et al. [5] and slightly modified, while exfoliation in DI water (samples denoted as hematene) was optimized by the author of the thesis. Hematene was utilized as a platform for photocatalytic ammonia

decomposition and for this purpose, a composite with RuO_2 was prepared, denoted as Ru-hematene.

Since the preparation of 2D n-vdW material – hematene – was partially developed in the span of the thesis, only the optimized protocol is described in the following paragraphs and applies to all the samples with corresponding code-name, unless stated otherwise. The optimization and comparison of different synthesis conditions (dispersant, masses and volumes, rotation and sonication times) is discussed in the section 3.2.1.

Hematene preparation in DMF

Optimized preparation of hematene in DMF dispersion consisted of the following steps:

- Specularite was ground into fine powder with a planetary ball mill (Retsch PM 100). The bulk sample was ball-milled twice for 5 minutes at 450 rpm and in between allowed to cool down to avoid undesirable sintering due to excessive heat.

- 2 g of the hematite fine powder were dispersed in 180 mL of DMF. The dispersion was then stirred in a vertical rotator (Heidolph) at 45 rpm for 96 h to achieve optimum powder wetting and subsequently the best possible transmission of ultrasonic energy to disrupt the bonds necessary for exfoliation.

- The dispersion was sonicated in a bath sonicator (Branson, power output: 130 W, frequency: 40 kHz) for 48 h.

- A successful exfoliation was indicated by the change of color from dark grey (specularite) to dark red (hematene).

- The unexfoliated hematite powder (dark grey) was collected and used again for preparation of hematene sheets.

- The exfoliated hematene was washed subsequently three times in acetone, ethanol and DI water. Exfoliated hematene sheets were separated from the supernatant by centrifugation (Sigma 4-16 K, Sigma Laborzentrifugen GmbH) at 21 000 rcf for 20 minutes after each washing step and to reach desired concentration.

- The washed hematene sheets in DI water were finally dialyzed for 3 weeks to avoid the presence of residual organic solvent.

- The aqueous hematene dispersion was then used in liquid form of known concentration or freeze dried to obtain a fine powder.

Hematene preparation in DI water

Optimized preparation of DI water derived hematene differed only in the use of DI water as a dispersant instead of toxic DMF and, as a consequence, the need for final washing and dialysis was eliminated.

Ru-hematene

Ruthenium loading was performed on hematene samples via the impregnation method, optimized by colleague S.M. Hossein Hejazi:

- A 10 mM stock solution of $RuCl_3$ in DI water was prepared.

- 10 mg of hematene was dispersed in 10 mL of DI water, defined volume of $RuCl_3$ stock solution (see Table 2.1) was added and then stirred with Teflon coated magnetic stirred for 3 h.

- The dispersion was centrifuged to separate the solid precipitates from the supernatant and washed three times with DI water to remove excessive $RuCL_3$.
- The powders were dried at 80° C for 1 h and calcined at 300 °C for 3 h in air atmosphere.

Hematene weight (mg)	Wt.% of Ru	10 mM $RuCl_3$ solution volume (μL)
10	0.1	9.9
10	0.5	49.5
10	1	98.9
10	2	197.9
10	3	296.8

Table 2.1: Volumes of $RuCl_3$ stock solution for desired wt.% of Ru loading onto hematene.

2.2 Characterization methods

2.2.1 Microscopic techniques

Microscopic techniques are divided into two sections. The first includes facilities at CATRIN – RCPTM (Palacký University), where the corresponding micrographs were acquired by instrument operators of the RCPTM microscopy research group. Second section lists STEM experimental setup at PNM group of University of Vienna, where the author of presented thesis spent her internship and obtained the data that are discussed in section 3.2.3, under the supervision of prof. Jani Kotakoski.

Transmission electron microscopy

Transmission electron microscopy images made during optimization of hematene preparation were acquired on a JEOL JEM-2100 Microscope equipped with LaB_6 type emission gun operating at 160 kV. High resolution TEM images in the presented thesis in both TEM and STEM HAADF (high angle annular dark field) mode with elemental mapping were collected with an FEI TITAN HRTEM microscope operating at 80 kV.

For these analyses, a droplet of dispersion of the material in DI water at a concentration of $\approx 0.1\,\mathrm{mg} \cdot \mathrm{mL}^{-1}$ was deposited onto a carbon-coated copper grid and dried at RT.

Scanning electron microscopy

The aqueous dispersion samples were sonicated for 2 minutes and then drop-casted on formvar-carbon supported copper grids. Powder samples were first dispersed in ethanol. The drop-casted grids were left to dry in room temperature before observation under SEM microscope JEOL 7900F operated at 3 kV.

Correlative Probe and Electron Microscopy

Scanning electron microscopy (SEM) and atomic force microscopy (AFM) analyses were performed with a FIB-SEM instrument SCIOS 2 (Thermo Fisher) equipped with an integrated AFM Litescope (NenoVision). The sample was placed on a Si wafer for analyses. The correlative probe and electron microscopy (CPEM) was used for the surface analysis, allowing simultaneous SEM and AFM data acquisition at the same place in the same coordinate system. For SEM imaging, an accelerating voltage of 2 kV, a beam current of 25 pA, and an ETD detector was deployed. The self-sensing Akiyama probe in the tapping

mode was used for the AFM measurement.

Scanning Transmission Electron Microscopy

A devoted scanning transmission electron microscope was used for atomic resolution images of hematene. The instrument utilized is a NION UltraSTEM 100 with a customized objective and sample stage, that is connected to CANVAS – an ultra-high vacuum (UHV) system built around the microscope [117]. The microscope was equipped with a 100 kV high-brightness cold field emission electron gun, a 3 rd generation C3/C5 aberration corrector with a minimum probe size of 1 – 1.3 Å at 60 – 100 kV and MAADF (medium angle annular dark field) detector in angular range of 60 – 200 mrad. A bright field CMOS camera was used as ronchigram camera for tuning and fine adjustment of the electron beam.

Sample preparation for STEM

To meet the criteria for sufficient quality imaging with NION ultraSTEM 100, an advanced sample setup had to be utilized. A sample that is placed on TEM grid to be studied with focused electron probe has to be thin enough to allow unperturbed passage of electrons and freestanding, i.e. cover the holes in the grid. However, hematene sheets that fulfil the thickness requirements, do not possess the lateral size that would allow them to cover the holes. Therefore, graphene-covered quantifoil gold grids (Graphenea) were applied for hematene samples, as depicted in Figure 2.1.

STEM data treatment

The software ImageJ was used for evaluation of STEM images. The STEM images often need to be corrected for scaling, as the field of view (FOV) set

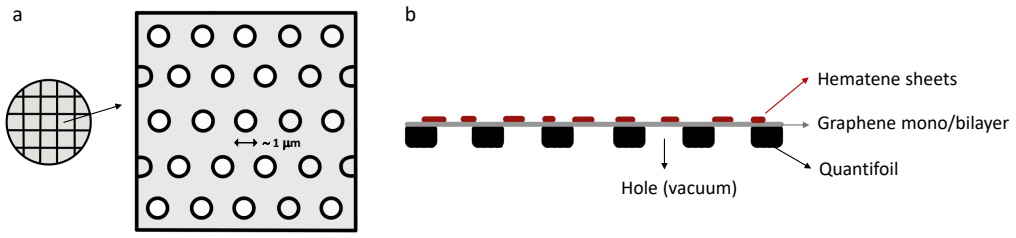

Figure 2.1: a: Schematic depiction of a TEM grid from top-view; b: schematic depiction of hematene drop-casted on graphene-covered guantifoil grid, cross sectional view.

for imaging may be several percent different.

To correct the scaling and evaluate the sample tilt, a graphene nearby studied hematene sheet was imaged, see Figure 2.2a, and used for the scaling and tilt calculations. A fast Fourier transformation (FFT) was performed from the highlighted area and the brightness and contrast were adjusted to facilitate the analysis, Figure 2.2b. Then, an ellipse was fitted into the second ring of FFT spots that corresponds to a half of the graphene (hexagonal) lattice parameter a value, see Figure 2.2c.

After at least five iterations of elliptical fitting, the major and minor axes values were averaged and used as an absolute value of frequency vector $\vec{g}$ to calculate the scaling, as it corresponds to the interplanar distance d in real space. One can calculate d using the following equation:

$$d = \frac{L}{|\vec{g}|}, \tag{2.1}$$

where L denotes the width of the original image in pixels. Furthermore, the distance d between armchair planes is equal to a half of graphene lattice parameter a, as evident from Figure 2.3. Therefore, the value of d obtained from Eq. (2.1) can be set to 1.23 Å for the actual FOV estimation. The ratio between

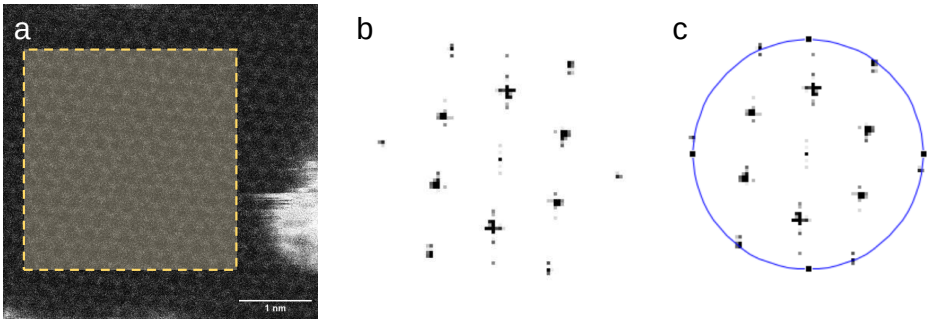

Figure 2.2: Graphene STEM image treatment to correct the scaling and evaluate the sample tilt, a: graphene STEM-MAADF image; b: FFT of the highlighted area in a; c: fitted ellipse to the second diffraction spots ring; the FFT images have inverted colours, so that the highest intensity corresponds to black colour.

actual FOV and nominal FOV (area set for imaging) of graphene image can be used for scaling of hematene images nearby, where the lattice parameter is unknown.

To evaluate the tilt of the sample, the rotation values of the fitted ellipses in FFT of graphene and hematene images were compared. If the angles had a similar value, the sample was considered to be tilted and the normalized lengths of the axes from graphene image were used to correct the tilt.

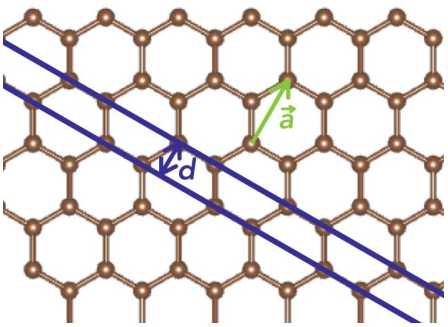

Figure 2.3: Visualisation of relation between graphene lattice vector $\vec{a}$ and the spacing d between armchair planes.

2.2.2 Thermal analysis

A Netzsch Jupyter 449C thermo-micro balance instrument was used for TGA with simultaneous evolved gas analysis (EGA). The measurements were performed with a constant heating rate of $10\,^{\circ}\mathrm{C}\cdot\mathrm{min}^{-1}$, unless stated otherwise. During experiments, a constant flow of N_2 or synthetic air at $80\,\mathrm{mL}\cdot\mathrm{min}^{-1}$ was maintained in the furnace. The masses of released gases, if EGA was performed, were determined with a Netzsch QMS 403 Aëolos instrument under synthetic air flow.

2.2.3 Powder X-Ray Diffraction

Three different diffractometers were used in the span of the presented thesis for collecting powder X-Ray Diffraction (XRD) patterns.

The diffraction patterns of graphene-polysulfide derivatives were obtained with a Malvern Panalytical X'Pert Pro, utilizing Fe-filtered CoK_α radiation – $\lambda(\mathrm{Co})=1.78901$ Å in the Bragg-Brentano geometry, with an acceleration voltage of 40 kV and a current of 30 mA. The instrument was equipped with an X'Celerator detector, programmable divergence slits and diffraction beam anti-scattering slits. The scanning step size was 0.0334°.

The diffractograms of MXene/N-doped graphene samples were collected with a Malvern Panalytical diffractometer Empyrean in the Bragg-Brentano geometry with Ni-filtered CuK_α radiation – $\lambda(\mathrm{Cu})=1.5406$ Å operated at an acceleration voltage of 45 kV and a current of 40 mA. The 2θ range of the measurements was 5° – 105°, with a step size of 0.0263°. The freestanding films were gently pressed with a glass plate into a zero background Si sample holder with a 0.2 mm deep circular area with radius of 0.75 cm. The obtained diffraction patterns were then processed using HighScore$^+$ software and the d-spacing values were calculated using the Bragg's equation (1.3).

Hematene and its bulk parent specularite samples were analysed with either Malvern Panalytical X'Pert Pro, or bench-top Aeris diffractometers. The X'Pert Pro diffractometer was in the same setup as in the study of graphene-polysulfide derivatives. The Aeris bench-top diffraction system was used in the Bragg-Brentano geometry with Fe-filtered CoK_α radiation – λ(Co)=1.78901 Å, operated at an acceleration voltage of 40 kV and a current of 15 mA. The scanning step size was 0.0217°. All the samples were gently pressed on a zero background Si slide and scanned in $2\,\theta$ range from 5° to 105°.

2.2.4 Other characterization methods

All of the following characterization methods were performed by the colleagues from CATRIN-RCPTM.

Spectroscopic measurements

The ultraviolet-visible diffuse reflectance spectra (UV-Vis DRS) of the bare hematene and hematene loaded with ruthenium oxide were obtained by a SPECORD 250 plus (Analytikjena) spectrophotometer. An integrating sphere was used to collect the spectrum. The magnesium oxide powder served as a background reference sample.

The X-Ray photoelectron spectroscopy (XPS) measurements were performed using a PHI VersaProbe II (Physical electronics) with an Al K_α source (15 kV, 50 W). The obtained spectra were deconvoluted using MultiPak software (Ulvac-PHI, Inc.)

The electron paramagnetic resonance (EPR) spectra were acquired on JEOL JES-X-320 spectrometer at X-band ($\approx 9.14 - 9.17$ GHz) at 80 K and a microwave power of 0.1 mW. A modulation width of 1 mT and a modulation frequency of 100 kHz were used. High purity quartz tubes (Suprasil, Wilmad,

$\leq$ 0.5 OD) were used as a sample holder. The accuracy of the g-values was determined by comparison with the Mn^{2+}/MgO standard (JEOL standard). All the EPR spectra were acquired with a time constant of 30 ms and a projection time of 4 min.

Magnetization measurements

Magnetization data were recorded and analysed using a Quantum Design physical properties measurement system (PPMS Dynacool system) with a vibrating magnetometer (VSM) option. Experimental data were corrected for diamagnetism and sample holder signal. The temperature dependence of magnetization was recorded in a sweep mode at 1 K/min in the zero field cooled (ZFC) and field cooled (FC) measurement modes.

Photocatalytic experiments

The photodecomposition of NH_3 was conducted in a 17.5 mL quartz reactor. After sono-dispersion of the photocatalyst in 10 mL of ammonium hydroxide, the reactor was tightly sealed with a rubber septum. Since dissolved oxygen in the solution could act as an electron scavenger, it was bubbled with argon for 15 minutes to remove the oxygen. Subsequently, the sample was illuminated under LED (Solis® High-Power LED from Thorlabs) with a power of $3\mathrm{W} \cdot \mathrm{m}^{-2}$ and wavelength of 400 – 700 nm.

To avoid the thermal decomposition of ammonia, the reactor was immersed in water bath to keep the solution temperature at 24 °C during the reaction. The photocatalytically evolved hydrogen was detected with a gas chromatograph GCMS-QP2010 SE (Shimadzu) and a Thermal conductivity detector (TCD) using Ar as carrier gas.

3 Experimental study of 2D materials

This chapter is divided into two parts. First one centres around the outcomes and findings derived from the material characterization research during the work on a co-authored publication and an ongoing project that has not been published yet. The author of the presented thesis participated in preparation of the samples to be suitable for experimental investigation with either TGA and/or XRD methods, performed the measurements and optimized the experimental conditions. After collecting the relevant data, the author evaluated them and contributed to writing the relevant part of the publication and produced the presented figures.

Second part of the chapter is focused on an extensive study of a new 2D non-van der Waals material called hematene (2D form of α-Fe_2O_3), which resulted in a shared first-authored publication. The author of the presented thesis developed a new, non-toxic synthetic approach, participated in the materials characterization, performed the XRD and STEM characterizations and subsequent analyses.

When published results are presented, they are consistently mentioned at the beginning of each subchapter and they are included in the full version in the Appendices as well.

3.1 Modern 2D materials for energy storage

In recent years, the demand for electricity has increased significantly as a result of society's growing needs. This increase can be associated with factors such as population growth, urbanization, industrialization, increasing use of electronic devices and last but not least the electrification of transport and growing popularity of electric vehicles. One of the main challenges posed by this growing demand is the need to find more efficient, safe, eco-friendly, and low-cost energy storage solutions.

Three different classes of (portable) electrical energy storage devices are recognized: batteries, capacitors and supercapacitors, that differ in working principle and consequently in their characteristics. Batteries store energy in the form of reversible chemical reactions that involve movement of Li^+ ions between two electrodes separated with electrolyte, allowing charge and discharge cycles. Therefore, they have relatively high energy density (amount of stored energy per unit volume/mass), but their power density (rate of delivering the energy) is limited by the actual movement of ions through the electrolyte and their cycle life is finite as they degrade over time and usage.

Capacitors, on the other hand, utilize physical phenomena and rely on electrostatic capacitance of two conductive plates separated by an insulator (dielectric). They have rather low energy density, but higher power density (they can store lower amount of energy, but provide it at higher rates) and almost infinite cycle life. Supercapacitors belong to the class of electrochemical capacitors. They exploit the generation of potential difference through ion-selective adsorption processes at the electrode and solid/liquid electrolyte interface. During charging, ions are adsorbed onto the electrode and form a double layer which causes an accumulation of electrical charge on the electrode. This mechanism does not involve a slow redox reaction, which is why

supercapacitors have a higher energy density compared to batteries. In recent years, novel materials have been developed that are capable of storing energy not only in the electrical double layer, as discussed above, but also in the form of redox (Faradaic) processes. These so-called pseudocapacitors fill the gap between classical double layer capacitors and batteries [118, 119, 120].

Therefore, the main challenges in energy storage depend on the type of the device: in battery development in general, it is the cost, eco-friendliness and cycle life; considering supercapacitors, it is mostly the limitation in capacity. The current boundaries are pushed with new materials developed and improved, different electrolytes, etc. [119, 121]

The sub-chapter 3.1.1 deals with TGA and XRD characterization of new cathode material for Li-sulphur batteries based on graphene-polysulfide derivative. Second sub-chapter 3.1.2 is focused on supercapacitors, namely XRD characterization of several variations of MXene/graphene derivative heterostructures.

3.1.1 Covalently interlinked graphene sheets with sulphur chains as lithium-sulphur battery cathode

Parts of the text in the following chapter are adapted from Tantis et al. [114].

Lithium-ion batteries (LIBs) currently dominate the market for energy storage systems of portable electronics. However, in their current design, they cannot keep up with the increasing demand for higher performance and lower cost [121, 122, 123]. In this respect, lithium-sulphur batteries (LSBs) could offer a promising alternative to LIBs, as they have a high theoretical capacity ($1672\,\mathrm{mA \cdot h \cdot g^{-1}}$), high specific energy ($2600\,\mathrm{W \cdot h \cdot kg^{-1}}$) and, in addition, sulphur is environmentally friendly and readily available [124, 125].

However, LSBs still suffer from some shortcomings, in particular the "shuttle-effect" of the formed lithium polysulfides, low sulphur conductivity and large volume changes. One way to address these problems is to develop functional separators and design composite cathodes featuring a sulphur-anchoring platform. However, the composites developed so far suffer from either low conductivity of the anchoring platform, low cycle life, or small amounts of anchored sulphur [125, 126].

To tackle the LSBs bottlenecks, we exploited the rich flourographene chemistry that allowed defluorination and substitution through nucleophilic attack of PS ions on the electrophilic radical FG defect centres, based on previous reports of PS attack ability on electrophilic carbons of alkylhalides [127, 128, 129]. Two conditions were crucial for successful elimination of the LSBs bottlenecks:

i) high sulphur loading to increase the full-cell specific capacity,

ii) sulphur anchoring to FG via covalent bonding.

Both criteria were confirmed with the help of TGA and STA/MS experiments performed under different atmospheres. To prove that combination of FG chemistry with PS nucleophilic attack is a unique pathway to achieve both criteria, three different samples were prepared and analysed:

- Graphene-polysulfide derivative, denoted as GPS, was the developed material via FG and PS.

- Graphene-sulfide derivative, denoted as GS, was prepared as a control using the same protocol as GPS, except elemental sulphur was utilized instead of PS.

- Electrochemically exfoliated graphene, denoted as EEGS, was used as a control to prove the role of FG (electrochemically exfoliated graphene was used instead of FG in the synthesis).

The sulphur content for each sample was determined using TGA. Since the material amount, we are interested in, is organic, we employed nitrogen atmosphere and the resulting TGA curves are plotted in Figure 3.1a. The temperature range of mass loss calculation was determined according to the DTG for each sample and verified by comparison with elemental sulphur curve. Based on the curves, 80, 85, and 5 mass% of sulphur were identified in GPS, GS, and EEGS samples, respectively. To prove that the mass losses are truly corresponding to sulphur, STA with the evolved gas analysis (EGA) by mass spectroscopy (STA/MS) experiments were performed under synthetic air, see Figure 3.1b and c. Both clearly show that the mass losses between 150 – 350 °C correspond solely to sulphur loss. Furthermore, fluorographene has been proved to be thermally stable until $\approx 400 - 450\,°C$ [130, 131].

Based on nitrogen TG curves, we estimated the DoF of S_8 in each sample and listed them in Table 3.1, together with the mass losses and graphene residual masses.

Sample	$\Delta m(S_8)$	m(C) (wt.%)	DoF (%)
GPS	80.00	14.96	25.14
GS	85.71	8.05	49.13
EEGS	5.00	86.84	0.27

Table 3.1: Calculated DoF of S_8 species in different graphene-(poly)sulfide derivatives.

The criteria i), i.e. high sulphur loading, is therefore met in samples GPS and GS, proving the important role of FG, since the EEG was able to load only 5 mass% of PS, corresponding to DoF 0.27%.

When we examine the TG curve of the GPS and GS samples after combustion in synthetic air atmospheres, Figure 3.1b,c, there are clearly visible two mass loss steps. First is between $150 - 350\,°C$ and corresponds to combustion of polysulfides, that is proved with the evolution of SO and SO_2 gasses evidenced by STA/MS. Second step between $400 - 700\,°C$ corresponds to combustion of graphene with the evolution of CO_2 species. The CO molecules are not detected, because the fragments mass-to-charge ratio would be 28 m/z, which is the same as for N_2 and therefore undetectable in the constant flow of synthetic air. The last fragment detected during the experiments was 18 m/z to monitor eventual moisture release from the samples. The small signal peak of 18 m/z fragment occurring at the second mass loss step is rather difficult to interpret, since any moisture present in the sample would be released between $100 - 120\,°C$. It could be related to defluorination of residual fluorine in fluorographene that occurs at said mass loss step. Released fluorine often forms HF, that is highly corrosive. The formed HF could then react with the quartz glass capillary inlet to the MS, via the glass-etching reaction at the elevated temperature (MS inlet is heated to 300 °C) [132]:

$$SiO_2 + 4\,HF \rightarrow SiF_4 + 2\,H_2O, \tag{3.1}$$

further corroborating lower defluorination in the GS sample related to the absence of PS nucleophilic attack on the FG defect centres.

In our experience, HF does indeed form, as extensive fluorographene experiments leading to the publications of Chronopoulos et al. [31] and Bakandritsos et al. [27] resulted in corrosive damage to the TGA furnace due to HF, which

then had to be replaced. To prevent such damage, we are limiting the initial mass of high-fluorine samples to a maximum of 3 mg.

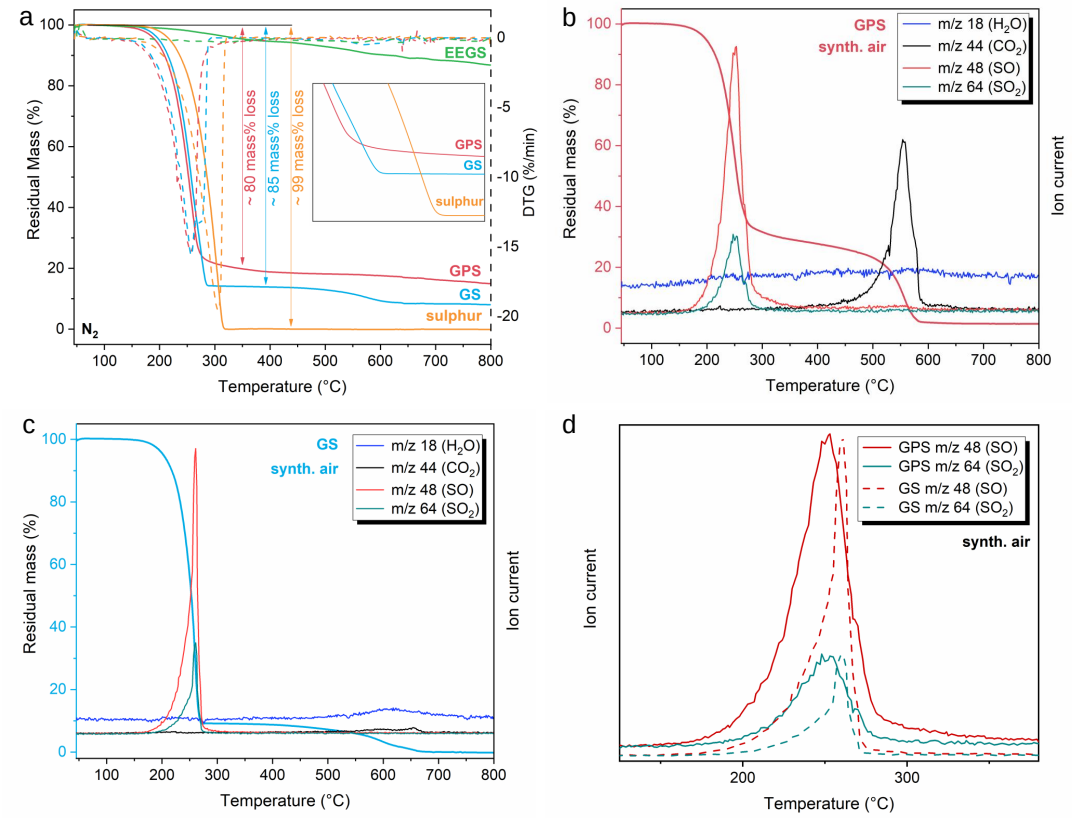

Figure 3.1: a: TGA curves in nitrogen atmosphere of GPS (red line), GS (light-blue line), EEGS (green line) and elemental sulphur (dark-yellow line) together with the corresponding DTG curves (dashed lines) and detail of TGA curves in a temperature range of 230 – 350 °C, shown in the inset; b: STA/MS results of GPS sample in synthetic air atmosphere; c: STA/MS results of the GS sample in synthetic air atmosphere; d: comparison of ion currents corresponding to SO and SO_2 fractions produced by GPS (solid lines) and GS (dashed lines) samples.

Although the sulphur loading is higher in GS than in GPS sample, the former does not fulfil the criteria ii) and there is no covalent bonding. The PS

ions in the latter are, in contrast, covalently anchored on the FG substrate. To prove this, findings of several complementary techniques were put together as a part of a puzzle. Apart from TGA, FTIR and Raman spectroscopy provided indications of bond nature in both GPS and GS samples [114].

From the TGA experiments, there are two indications of sulphur covalent anchoring. First originates from the detailed TG curves in nitrogen, where the GPS sample showed a smooth transition point to the mass-stable region after a complete loss of sulphur. In contrast, the detail of the TG curves of the GS and elemental sulphur samples showed a sharp transition point. The second indication is visible in Figure 3.1d, i.e., the release of SO and SO_2 species in STA/MS experiments in synthetic air. GPS shows broader evolution profiles of the gases than GS, indicating a stronger interaction with graphene due to covalent bonding of PS to graphene skeleton.

To shed more light on the charge/discharge processes, we performed XRD analyses of the GPS cathode material before and after electrochemical testing. First, we measured complete cathode material that consists of GPS material deposited on a carbon coated aluminium foil, which served both as a substrate and current collector, before and after cycling as well as bare substrate foil, see Figure 3.2a,b,c respectively. However, the patterns were dominated by the strong diffraction peaks of substrate foil – interestingly, the carbon coating was perturbed by the electrochemical testing accenting aluminium diffraction peaks. To obtain better information on the structures we were interested in, we performed the measurements of the pristine GPS powder before testing, Figure 3.2b, and the powder scraped off the electrode after testing, Figure 3.2c.

Solely sulphur peaks are present in the diffractogram of the GPS powder, while the diffractogram of the lithiated cathode is dominated by oxidized

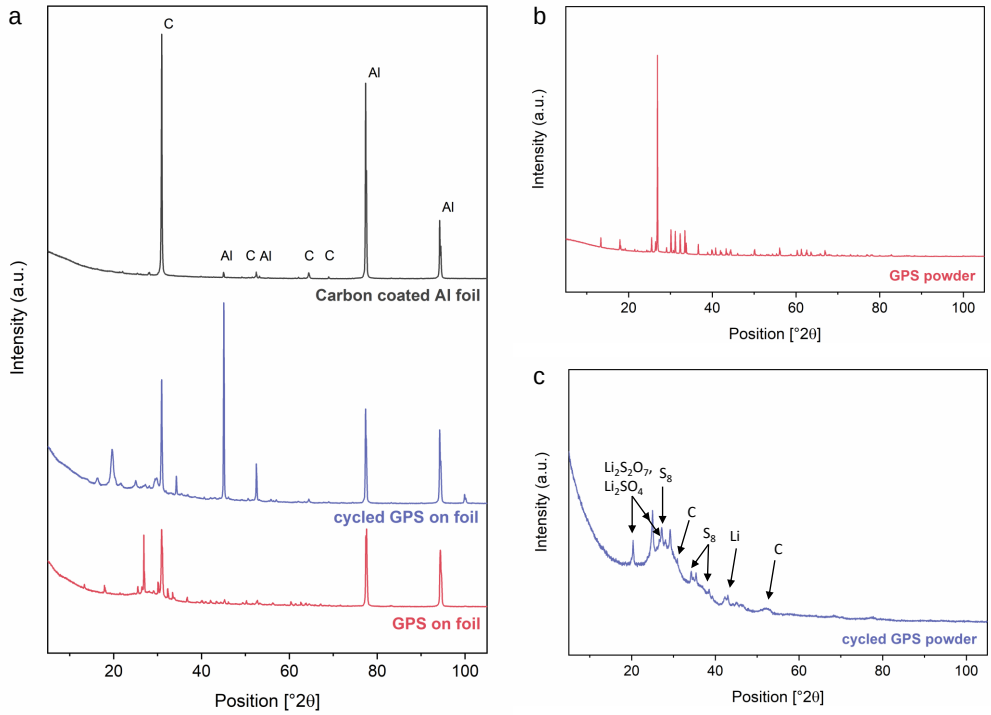

Figure 3.2: Diffractograms of: a: GPS complete cathode before testing (red line), cycled GPS cathode (purple line) and carbon coated aluminium foil, which was used as a substrate and current collector (dark grey line); b: GPS powder before testing and c: cycled GPS powder (scratched from the substrate foil).

lithium polysulfides ($Li_2S_2O_7$ and Li_2SO_4). Thus, the lithiated cathode consists of Li_2S_2/Li_2S, which are indeed expected in the lithiated state [133], but were oxidized after exposure to air; therefore, it was difficult to extract any further significant information from these experiments. To avoid cathode oxidation and to monitor underlying crystal structure changes during battery cycling, the use of in operando XRD would be preferable. However, such experiments require special equipment which is not available at our facility.

Nonetheless, the obtained XRD results are in agreement with the electrochemical testing of GPS [114]. There are two possible discharge pathways of

the GPS cathode, depending on the sulphur chains length, and they are both combined in the tested GPS discharge curve. Long chains pathway consists of two steps (discharge plateaus), where the first corresponds to solid (S_8) $\rightarrow$ liquid (Li_2S_n) transition and the second one corresponds to further reduction of Li_2S_n to Li_2S_2/Li_2S. On the other hand, short-chain sulphur cycling is via solid-solid transition from S to Li_2S associated with only one discharge plateau. As mentioned earlier, both lithiated polysulfide species in their oxidized state were identified in the cycled cathode material by XRD. Futhermore, as was shown by theoretical calculations in the published study by Tantis et al. [114], both long and short polysulfide chains can react covalently on the graphene backbone.

3.1.2 MXene/Graphene derivative heterostructure composites for supercapacitors

The following sub-chapter is based on the results obtained whilst working on a project that has not been published yet.

As the energy storage research pushes forward, supercapacitors emerge as a promising rival to LIBs, since they offer high power density (charge/discharge rate), long cycle life and independence from scarce elements. However, their applicability in industry is still limited due to their capacity, which falls significantly short compared to energy density of state of art batteries. For example, commercial supercapacitors reach a specific energy (per cell) of $10\,W \cdot h \cdot kg^{-1}$ [134, 135], while lead-acid batteries provide $20 - 35\,W \cdot h \cdot kg^{-1}$ [136] and advanced LIBs offer up to $150\,W \cdot h \cdot kg^{-1}$ [137]. Compared to LIBs, supercapacitors are superior in power density and cycle-life. To utilize the benefits of supercapacitors and facilitate their higher applicability, it is crucial to develop electrode and/or dielectric materials that surpass the current limits in energy

density and sustain the high power density as well as long service life [138].

Regarding supercapacitors electrode research, several materials have been in the spotlight during the past decades, including carbon materials with a high specific surface area, conducting polymers and transition metal oxides. Recently, the attention has been given to emerging materials such as MXenes, MOFs, metal nitride/phosphide and TMDs [138, 139]. There are plenty of aspects that play a role in the overall performance of the supercapacitors – apart from conductivity and specific energy, it is important to maximize the electrode/electrolyte interface leading to emphasis on materials with a high specific surface area (nitrogen-doped mesoporous carbon, carbon nanosheets, activated graphene, CNTs, ...) that tend to have a low mass density and eventually low energy density, which is a key performance parameter [140, 141, 142, 143].

Several strategies can be used to improve the energy density while preserving other parameters like electrode/electrolyte interaction and cycle-life, but they can in general be divided into two approaches: material improvement (compressing, element doping ect.) and composite engineering, which can allow a unique combination of different material properties to create a synergistic effect and boost the overall performance. MXenes prove to be ideal candidate for such structures, since they already possess many features favouring energy storage applications – conductivity, hydrophilic surface, ability to host various cations in the interlayer, etc., as well as some drawbacks, mainly re-stacking of the sheets, that can be minimized using an ideal counterpart [35, 144].

Here, we explore combining $Ti_3C_2T_x$ MXene with two kinds of graphene derivatives in a determined ratio of 99:1. First is nitrogen superdoped graphene that was recently reported by Sedajova et al. [115] as a supercapacitor material with unprecedented energy density, denoted here as GN3. The GN3 material

was also prepared in charged variation, denoted as GN3Q, to enhance self-assebly in the heterostructures. Second is graphene acid, that has been proven suitable for energy storage, with carboxyl boosting storage capacity, by Sedajova et al. [145], denoted here as GA. All the samples were prepared in the form of self-standing films with different mass-loading of 1, 4 and 10 $\mathrm{mg} \cdot \mathrm{cm}^{-2}$.

XRD is an important tool during the preparation and characterization of MXene materials as it is one of the first and easiest methods to confirm the successful etching of MAX phase and subsequent delamination of multilayer MXene. Original MAX phase Ti_3AlC_2 (for $Ti_3C_2T_x$) crystallizes in the hexagonal $p6_3/mmc$ space group; the typical diffraction pattern is shown in Figure 3.3. After successful etching and delamination, the diffractogram changes dramatically – only peaks corresponding to $(00l)$ planes with decreasing intensity will be present. The indices $(00l)$ are within the MXene community listed as (002), (004), (006) etc., because the MAX phases have two layers (M_3X_2) per unit cell[5], which is preserved in multilayer MXenes [147]. Although the stacking orientation becomes random for delaminated MXene films, we keep the indexing (002), (004), (006), etc. for the sake of easier comparison.

The diffraction pattern of delaminated MXene film should consist solely of six $(00l)$ peaks, ideally with decreasing intensity. If there are more peaks present, it is a sign of multilayer MXene or even a MAX phase (or some contamination). The first diffraction peak indexed as (002) is usually oriented between $2\theta \approx 7 - 10°$ (when using Cu-anode lamp as an X-Ray source) and can be used to estimate the d-spacing, c-lattice parameter and, with further experiments, also interlayer spacing, that is affected by eventually present intercalants (inorganic cations, organic molecules, water, etc.). In the case of

[5]In general, the $(00l)$ spacing indices would be typically reported as (001), (002), (003) etc. for 2D material films, since they are composed of randomly assembled flakes with identical layers and one sheet per unit cell [146].

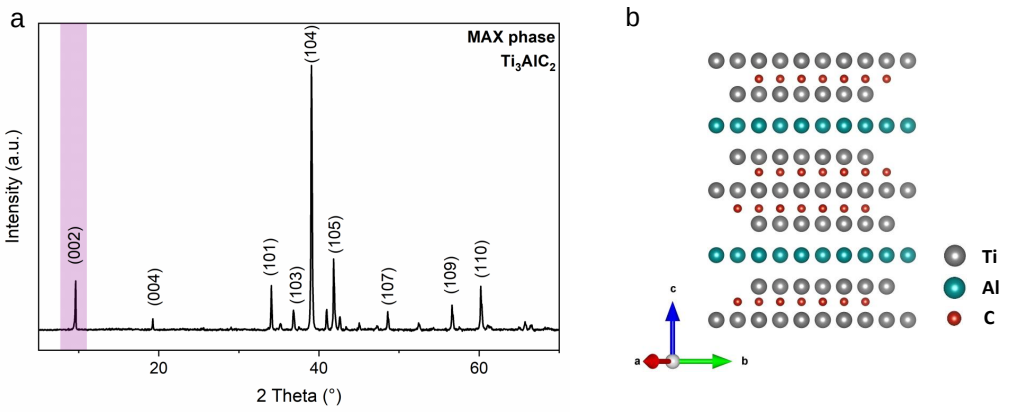

Figure 3.3: a: Diffraction pattern of Ti_3AlC_2 MAX phase; b: schematic structures of MAX phase.

MXenes, the *c*-lattice parameter is twice the d-spacing, that corresponds to the thickness of one MXene layer with surface termination T_x and intercalants on both sides.

To identify the interlayer spacing, a two step experiment should be performed. The first step consists of collecting the XRD pattern in the active state (based on particular application or experiment, e.g. self-standing film or wet multilayer powder) and the second step involves measuring the bone-dry sample with all the intercalants removed. Then, the interlayer spacing equals simply the difference between the d-spacing. However, removing all the intercalants is a challenging task that may require vacuum annealing at elevated temperature, since the intercalants are strongly bound to the MXene surface. [147]

In this study, four different samples in the form of self-standing film were prepared. Bare $Ti_3C_2T_x$ and three heterostructures with graphene derivatives: $Ti_3C_2T_x$/GN3, self-assembled $Ti_3C_2T_x$/GN3Q, and $Ti_3C_2T_x$/GA. The films were prepared with three different mass-loadings in order to test the dependence of the supercapacitor performance on the electrode thickness. The XRD

analysis was performed to confirm MXene delamination and gain more overall insight into the internal arrangement of the heterostructures. However, it was not possible to determine the interlayer spacing as the procedure requires to completely remove the intercalants and water (vacuum annealing at high temperature) would likely damage either the MXene material or the graphene derivatives causing a change in the composite properties. For instance, graphene acid starts to lose mass already above 200 °C under nitrogen flow at ambient pressure [27].

The diffraction patterns of all self-standing films, i.e. bare $Ti_3C_2T_x$ and the heterostructures, are shown in Figure 3.4. In all the diffractograms, the typical MXene orientation along the *c*-axis and hence the presence of $(00l)$ peaks is evident, confirming a successful etching of the MAX phase. Residual MAX phase would be represented in the patterns by its most intense diffraction located at $2\theta \approx 39°$, corresponding to the (104) plane [147, 148]. A negligible amount of residual MAX phase is apparently present only in the $Ti_3C_2T_x$/GA sample with a mass loading of $10\,mg \cdot cm^{-2}$, where the (104) peak of very low intensity can be observed. Furthermore, in the $Ti_3C_2T_x$/GN3 sample with a mass loading of $10\,mg \cdot cm^{-2}$ a low intensity (110) peak at $2\theta \approx 61°$ could be explained by a low amount of multilayer MXene, as has been previously reported in the literature [147].

Comparing the diffraction records of the individual materials with each other, we find that for all mass loadings of the bare $Ti_3C_2T_x$, $Ti_3C_2T_x$/GA and $Ti_3C_2T_x$/GN3, the (004) peak is distorted, very broad and of low intensity, while the (008) peak is more intense than it would be for a typical delaminated MXene, where the $(00l)$ peak intensity is gradually decreasing. These phenomena can be explained by the lower degree of stacking order along the *c*-axis caused by intercalated H_2O molecules [148]. On the other hand, the

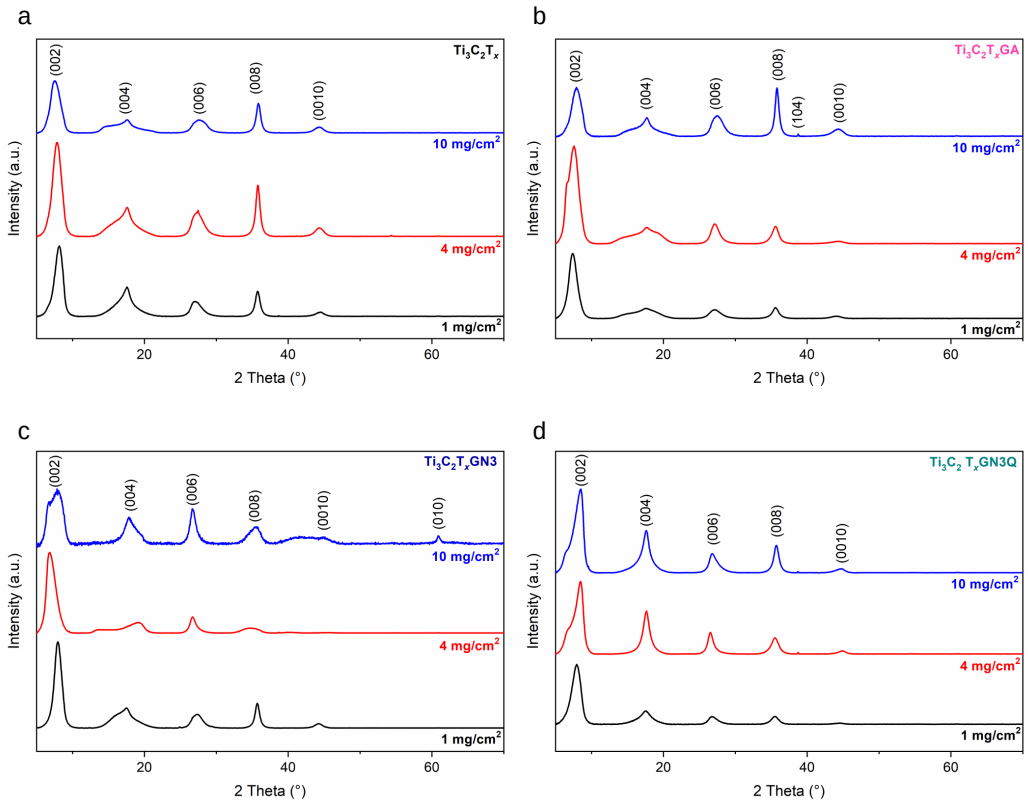

Figure 3.4: Diffraction patterns of a: bare $Ti_3C_2T_x$; b: $Ti_3C_2T_x$/GA heterostructures; c: $Ti_3C_2T_x$/GN3 heterostructures and d: $Ti_3C_2T_x$/GN3Q heterostructures.

$Ti_3C_2T_x$/GN3Q heterostructure shows all diffraction peaks of similar shape, indicating its higher uniformity. The GN3Q material is charged, leading to self-assembly of the heterostructures during synthesis and presumably enhanced ordering along the *c*-axis.

To evaluate the effect of mass loading on the self-standing film structures, we examined the d-spacing of each film from the (002) peak positions according to Bragg's law (i.e.,Eq. (1.3)) and the corresponding values are plotted in Figure 3.5. The $Ti_3C_2T_x$/GA sample with a mass loading of $4\,mg \cdot cm^{-2}$, $Ti_3C_2T_x$/GN3 sample with a mass loading of $10\,mg \cdot cm^{-2}$ and $Ti_3C_2T_x$/GN3Q

sample with a mass loading of 4 and 10 $\mathrm{mg \cdot cm^{-2}}$ have a complex (002) peak shape with a shoulder at lower 2θ angles. To obtain a sufficiently good profile fit, we assumed that it consists of contributions from multiple diffraction peaks, which could be explained by the corrugated structure of the films, as confirmed by the electron microscopy images, leading to the presence of multiple d-spacing values.

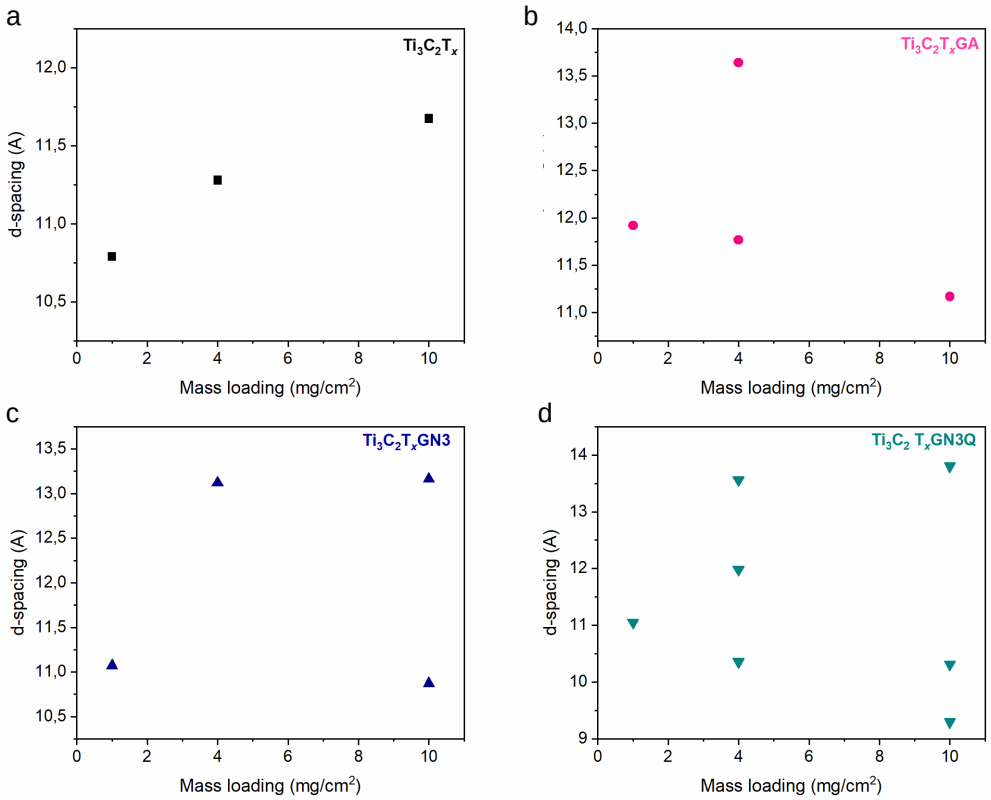

Figure 3.5: Calculated d-spacing values for different mass-loadings of a: bare $Ti_3C_2T_x$; b: $Ti_3C_2T_x$/GA heterostructures; c: $Ti_3C_2T_x$/GN3 heterostructures and d: $Ti_3C_2T_x$/GN3Q heterostructures.

The d-spacing values of bare MXene material have a nearly linear increase with increasing film thickness, which may be related to the binding of more intercalants during vacuum filtration. The MXene/GA heterostructure, on the

other hand, shows quite the opposite trend, with the more intensive peak shifting toward higher 2θ angles and d-spacing values decreasing with increasing mass loading.

The MXene/GN3 film d-spacing values do not follow any trend, there seem to be two similar stable values of d-spacing for different mass loadings, while at $10\,\mathrm{mg}\cdot\mathrm{cm}^{-2}$ both of them are present in the sample. The most interesting behaviour in the terms of d-spacing can be observed in the MXene/GN3Q self-standing films. The corrugated structure seems to be regular enough to produce three d-spacing values at higher mass loadings. The dominantly contributing peak position is shifting towards higher 2θ angles with growing mass loading, that leads to decreasing prevalent d-spacing.

Overall, the insight into the structure of the self-standing films provided by XRD confirms:

- Successful etching of the MAX phase in all the samples, except the heterostructure material $Ti_3C_2T_x$/GA with a mass loading of $10\,\mathrm{mg}\cdot\mathrm{cm}^{-2}$, where a very low intensity (104) peak at $2\theta \approx 39°$ suggests negligible amount of MAX phase Ti_3AlC_2.

- Successful delamination of the MXenes, except the $Ti_3C_2T_x$/GN3 sample with a mass loading of $10\,\mathrm{mg}\cdot\mathrm{cm}^{-2}$, where a low intensity (104) peak at $2\theta \approx 61°$ indicates presence of multilayer $Ti_3C_2T_x$.

- Corrugated structure of all the materials, with disordered stacking in the $Ti_3C_2T_x$, $Ti_3C_2T_x$/GA and $Ti_3C_2T_x$/GN3 materials.

- Regularly corrugated structure of the $Ti_3C_2T_x$/GN3Q sample, that originates probably from self-assembly of the charged graphene derivative with MXene, enabling a better adhesion between the layers.

Findings derived from XRD analyses are in agreement with electrochemical testing results, where the self-assembly in $Ti_3C_2T_x$/GN3Q heterostructures proves to be beneficial for the supercapacitors performance.

3.2 Hematene: a novel 2D non-van der Waals material

Inspired by Puthirath et al. [5], who, in 2018, reported on hematene, the first member of a new family of 2D n-vdW materials, we focused our efforts to repeat and optimize hematene preparation to be able to explore this material. First task to tackle was the optimization and scale-up of the synthesis which is described in the sub-chapter 3.2.1. Then, we could characterize the prepared material and investigate how the dimension restriction affects hematene properties, that we discuss in sub-chapter 3.2.2. Apart from material properties, we also tried to look into how the material itself changes, whether there are any modifications and lattice strain in the structure. For that, we investigated the samples with STEM and XRD while the findings are presented sub-chapter 3.2.3.

Based on properties of bulk hematite and considering the characterization of hematene, we also explored its utilization in photocatalysis. Hematene proved to be useful as a 2D platform for photocatalytic ammonia decomposition, the findings are discussed in sub-chapter 3.2.4.

Parts of text in sub-chapters 3.2.1, 3.2.2 and 3.2.4 are adapted from Dzíbelová et al. [15].

3.2.1 Synthesis optimization

The structure of n-vdW materials is complex, with strong bonds in all three directions, as explained in theoretical sub-chapter 1.1.3. Therefore, it is crucial to choose a suitable bulk parent material. When regular hematite micro/nanoparticles would be exfoliated, statistically all the morphologies should be produced and 2D flakes would not be prevalent. However, a naturally occur-

ring species of hematite exists, called specularite, that is grown with a preferred orientation and forms platelets. This mineralogical variety has a characteristic silvery black colour and (quazi)layered structure as can be seen in Figure 3.6.

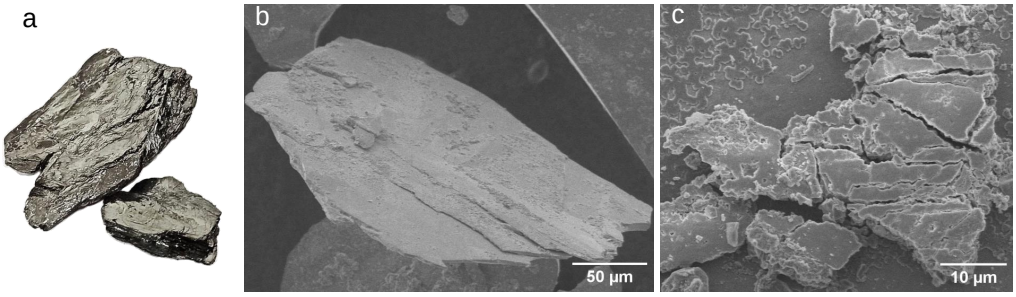

Figure 3.6: Parent material: a: photograph of iron ore specularite that was collected in Elba, Italy; b,c: SEM images of specularite.

The usage of specularite as bulk parent material facilitates exfoliation into platelets and even 2D flakes and, furthermore, it is an earth abundant, environmentally friendly material. Nevertheless, it comes with some potential drawbacks as well, mainly it often contains some other undesirable elements, such as carbon, silicon or aluminium, and it is usually not homogeneous which affects the replicability of the experiments.

Exfoliation in DMF

The exfoliation strategy reported by Puthirath et al. [5] was based on sonochemical exfoliation of specularite dispersion in an organic solvent, particularly DMF (N,N-dimethylformamide). DMF is commonly used in the preparation of graphene and its derivatives as it can penetrate the hydrophobic graphite and ensure ultrasound energy transfer. However, it is proven to be toxic to animals and humans – both acute and chronic exposure by inhalation are found to damage liver, occupational exposure can cause digestive disturbances and even potential connection between DMF and embryotoxicity and teratogenic-

ity has been suggested [149, 150]. For these reasons, the European Union is adopting regulations restricting DMF use from December 2023 onwards [151]. Therefore, it would be beneficial to develop a new synthetic approach without DMF.

At the beginning, we adopted the synthesis protocol by Puthirath et al. [5] as it was. However, due to very low starting amount of specularite (50 mg per 200 mL of DMF), the hematene yields were extremely low for any characterization apart from electron microscopy. Therefore, as an attempt to upscale the synthesis, we increased the starting specularite amount to 1 g per 60 mL of DMF, that was optimal for GF exfoliation. Prior to dispersing in DMF, specularite had to be pulverized, which was done simply with mortar and pestle and the silvery black colour changed to reddish-black when sufficiently ground.

The obtained fine powder was then dispersed in a determined amount of DMF (typically 3 g of specularite in 180 mL of DMF) and stirred for 4 days. Already after grinding and stirring in DMF, some parts of specularite begin to exfoliate, as visible in Figure 3.7a, with a relatively thin sheet of α-Fe_2O_3. After thorough mixing, the reddish-black dispersion was transferred into an ultrasound bath and sonicated for 50 h during which the colour of the dispersion changed to bright red, see Figure 3.8. Exfoliated sheets (representative TEM image in Figure 3.7b) were separated from unexfoliated black powder and then washed three times in DI water, Figure 3.7c. Subsequently, the material was dialysed for three weeks to completely remove the remaining organic impurities. The unexfoliated black specularite powder can be collected and used again for hematene preparation.

Essentially, there are three fast indications that suggest a successful exfoliation in routine experiments:

- Visible color change of the dispersion from black to red.

- EM imaging – preferably TEM, where the 2D nature is evaluated by even electron transparency throughout the sample cross-section.

- Colloidal stability – thin hematene flakes shown colloidal stability in both DMF or DI water for many hours ($8 - 24$ h)[6].

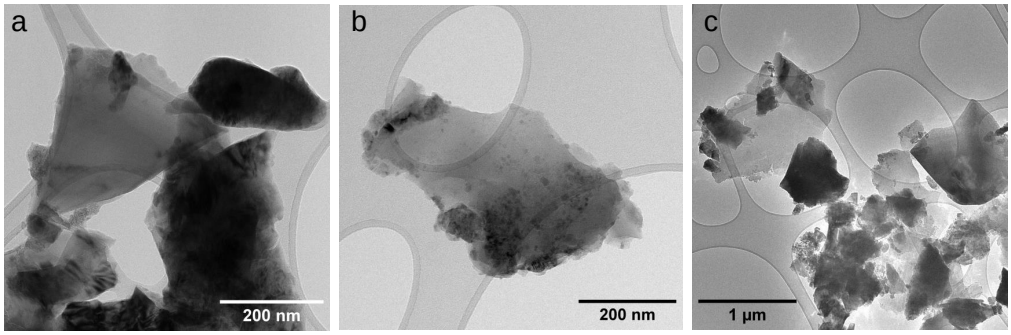

Figure 3.7: TEM images of: a: ground specularite after 4 days of stirring in DMF; b: exfoliated hematene from DMF dispersion; c: exfoliated hematene after completed washing in DI water.

Two steps of the synthesis were later adjusted: when using a magnetic stirrer for 4 days with a higher amount of specularite (5 g in 300 mL of DMF), the teflon coating of the stirred was abraded, contaminating the whole batch with teflon. Therefore, instead of stirring, vertical rotator was utilized. To minimise human influence during preparation, the grinding with mortar and pestle by hand was replaced by the use of a planetary ball mill (see sub-chapter 3.2.1 for milling details).

[6]Very small flakes with the lateral dimension of units or tens of nm are stable in dispersion for days, but they tend to have orange colour rather than red.

Figure 3.8: Scheme of exfoliation with photos of flasks with dispersions to illustrate the colour-change after sonochemical exfoliation.

Exfoliation in DI water

During characterization experiments, it was revealed that after 30 minutes of sonication of the bulk specularite in DI water, a partial color change to red occurred, indicating possible exfoliation. To test this possibility, we performed an identical synthesis using DI water instead of DMF. Even very thin hematene sheets vere possible to find with a TEM analysis after exfoliation in DI water, even though often covered with thicker platelets, see Figure 3.9a. Overall, judging by the EM contrast, it appears that very thin sheets are less common with the use of DI water and the majority of the sample is thicker, the typical appearance is shown in Figure 3.9b. The energy dispersive spectroscopy of the prevalent sheets shows that the prevalent elements in the sample are iron and oxygen, as expected for iron oxides. The Cu signal can be explained by the use of copper TEM grids, while carbon and silicon are impurities due to natural origin of specularite and their presence is confirmed also by XPS analysis, which is discussed in more detail in sub-chapter 3.2.2.

After confirming successful exfoliation of specularite in DI water, we tried to optimize the procedure for DI water. For that, we varied the dispersion

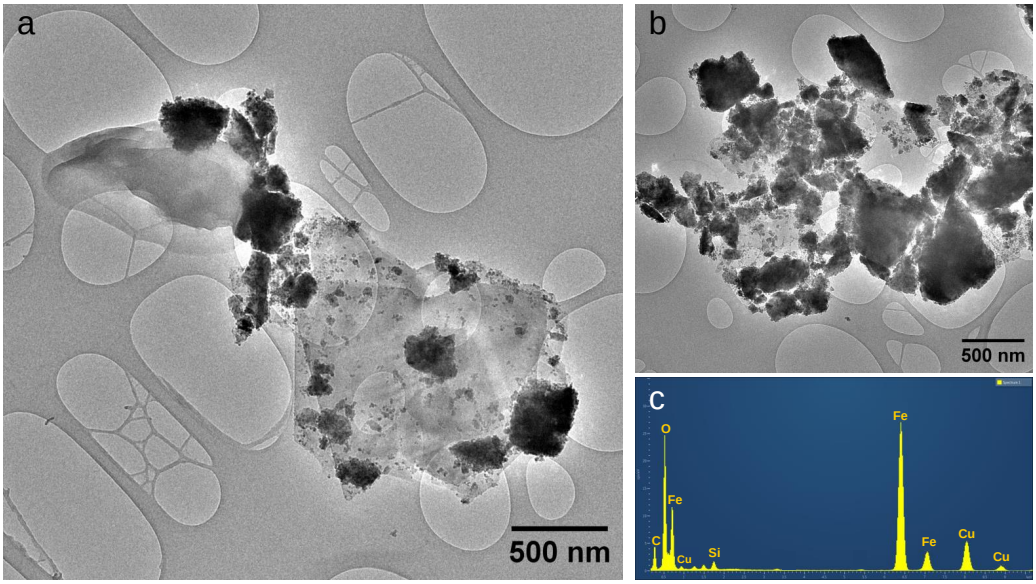

Figure 3.9: TEM images of exfoliated hematene in DI water: a: thin sheets; b: typical morphology of the sample with energy dispersive spectroscopy of the area, c.

concentration and combination of wetting in vertical rotator with sonication. Three synthetic routes were tested simultaneously:

1. Same procedure as for DMF – 1 g of specularite per 60 mL of DI water, rotated for 4 days, sonicated for 50 h.

2. Lower concentration – 1 g of specularite per 90 mL of DI water, same procedure.

3. Original concentration – 1 g of specularite per 60 mL of DI water, but after 3 days of wetting in vertical rotator, the dispersion was sonicated over night (12 h), rotated for 12 h the following day and then sonicated for remaining 38 h.

The resulting dispersions of all the samples were transferred into 50 mL vials and let to sediment over night to check the colloidal stability. According to

this, the procedure number 2 was best of the tested variations, as it was showing colloidal stability after 16 h, see Figure 3.10. Prior to sedimentation, a small amount from each batch was taken to determine the concentration precisely using TGA[7] and estimate the yield. Table 3.2 summarizes the amounts of starting material specularite, amount of obtained exfoliated hematene and the calculated yield in wt.% for each of the three synthetic routes. According to the yield as well as colloidal stability, the second synthetic procedure proves to be best out of the tested routes.

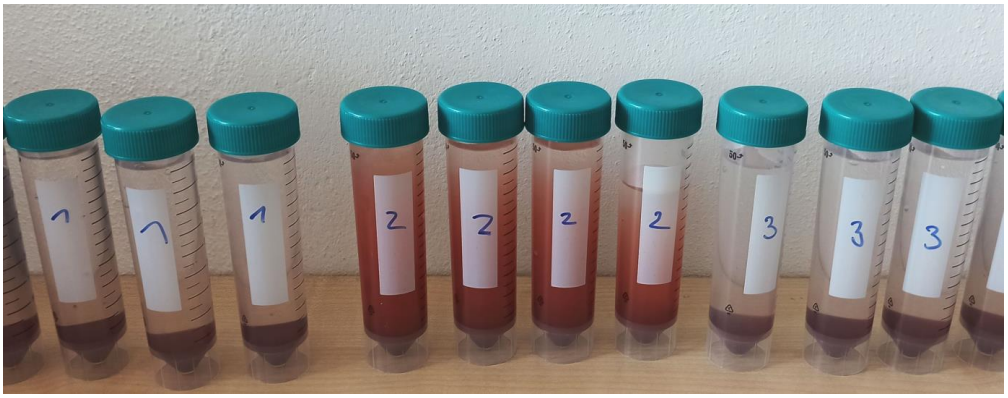

Figure 3.10: Photograph of tested synthetic variations after 16 hours of sedimentation; vials are labelled according to the synthetic procedure.

It is possible that with further optimizing and testing more conditions, a more efficient synthetic route could be found. However, with the presented preparation method, the author of the thesis was able to obtain a reasonable amount of hematene for further analyses and testing. Therefore, the second synthetic approach was adopted for hematene samples (both DMF and DI

[7]TGA utilization for concentration assessment is used in our research group for low-amount samples as follows: a known amount of the water dispersion is loaded into the crucible, heated to 120°C, let to evaporate all H_2O content and then cooled back to RT. Mass difference between the crucible with dried sample and empty crucible is used for calculation of concentration. This way, the buoyancy error of TGA is eliminated.

Synt. route	Specularite (mg)	Hematene (mg)	Yield (wt. %)
1	3000	39.9	1.3
2	2000	37.4	1.87
3	3000	19.5	0.65

Table 3.2: Comparison of different synthetic procedure yields calculated from concentrations.

water derived) in the span of the presented thesis. To illustrate the thickness of the typical sheet with a lateral dimension in a micrometer range, a correlative probe and electron microscopy (CPEM), combining SEM and atomic force microscopy (AFM) images of two different sheets derived from DI water are shown in Figure 3.11. The measured height (thickness) of hematene sheets of 3 nm corresponds to $\approx 7-9$ layers of hematene, as the thickness of molecular dynamic simulated hematene (001) and (010) planes was estimated as 3.98 Å and 3.2 Å, respectively [5].

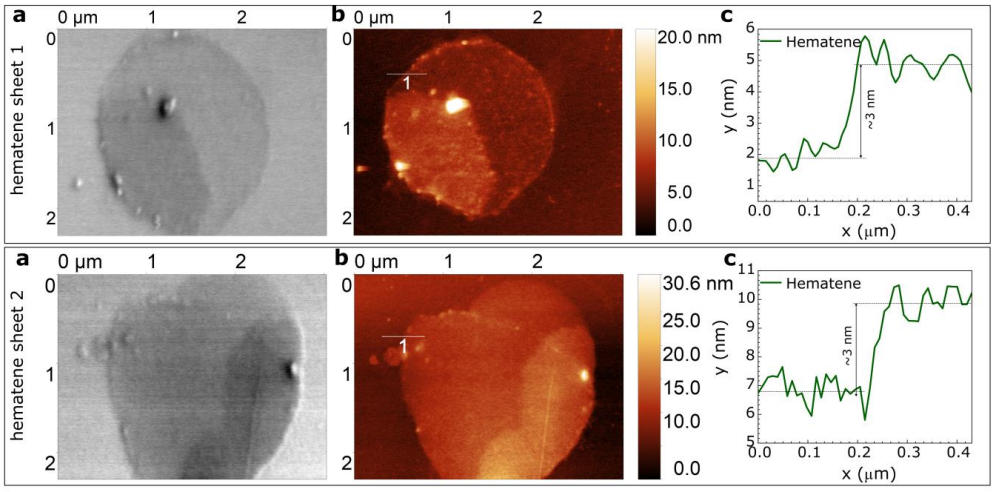

Figure 3.11: CPEM images of different hematene sheets and related height profiles; adapted from ref. [15].

Other possible variables

Apart from the effect of the dispersant, two different ultrasonication methods were tested – probe sonication and bath sonication. Probe sonication did not improve the quality of produced sheets or the exfoliation time. Furthermore, it is expected, that ultrasound power during bath sonication will affect the resulting material thickness and diameter. Unfortunately, a bath sonicator with adjustable ultrasound power was not available, so this hypothesis remained unverified.

3.2.2 Material characterization

Considering the classical (vdW) 2D materials, it is known that the dimensional restriction coming from 3D to 2D bares substantial changes in properties and behaviour of the materials, as discussed in the theoretical sub-chapter 1.1. Therefore, after successful preparation of novel 2D n-vdW material, hematene, we aimed to characterize it to study any properties differences compared to parent bulk specularite and to identify potential application directions. We focused our efforts on DI water derived hematene.

There are two main questions to be answered about hematene. The first query that comes to mind concerns the exfoliation of the specularite itself, in particular the direction of cleavage of the 3D structure. According to literature, there are two main directions [001] and [010] with the highest broken bond density in hematite, along which the crystallites should be exfoliated preferentially [5, 152]. Second question concerns the changes of properties of the material. The following sub-chapter and the sub-chapter 3.2.3 attempts to deal with both of these questions to some extent. For the sake of clarity, the following chapter is divided into several subchapters according to the studied aspects.

Structural characterization

To verify the phase composition of both bulk specularite and produced hematene, we performed XRD analysis. From XRD patterns shown in Figure 3.12, it is evident that both parent material and exfoliated hematene contain only α-Fe_2O_3 crystalline phase.

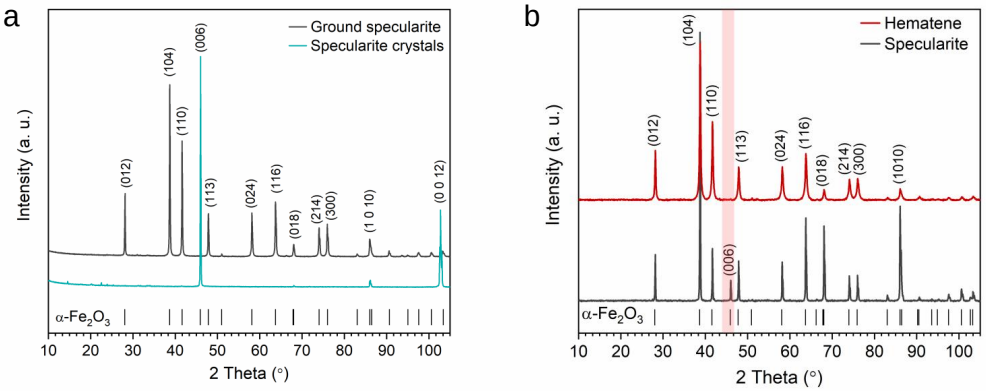

Figure 3.12: XRD patterns of: a: specularite crystals (lower cyan line) compared to ground powder (upper grey line); b: ground specularite (lower grey line) compared to exfoliated hematene (upper dark-red line).

To shed more light on the structure of specularite enabling the exfoliation, we analysed the starting material before and after grinding with mortar and pestle. It is clearly visible from Figure 3.12a, there is a preferred orientation of the specularite layer stacking leading to enhanced reflections on preferential orientation planes – (006) and (0012) – and complete suppression of other crystallographic planes. This effect is reduced after grinding the crystals into fine powder. Furthermore, after exfoliation, the reflection from (006) plane completely disappears, as evident from the highlighted area in Figure 3.12b.

The described phenomenon can be explained by the growth of the crystal in the direction perpendicular to (006) plane, that facilitates the cleavage along

[001] direction. In the exfoliated hematene, the (006) reflection would then be absent due to very low sheet thickness. These findings are further corroborating the theoretically predicted highest broken bond density in the [001] direction and exfoliation into (001) oriented sheets.

To evaluate the presence of other non-crystalline species present in the natural parent material, we performed XPS analysis of both parent and exfoliated samples, see Figure 3.13. The atomic compositions of both samples are shown in the insets of the XPS graphs and listed in Table 3.3. It is evident that the DI water and ultrasound during exfoliation partially cleanse the sample of impurities, reducing the carbon content from 30.3 at.% to 11.9 at.% and silicon from 5.7 at.% to undetectable amount.

Sample	Fe (at. %)	O (at. %)	C (at. %)	Si (at. %)
Specularite	14.4	49.6	30.3	5.7
Hematene	29.7	58.4	11.9	0.0

Table 3.3: Atomic composition of specularite and hematene according to XPS analysis.

The HR-XPS spectrum of the hematene Fe 2p region revealed two peaks at $\approx$ 712 eV and $\approx$ 725 eV, corresponding to Fe $2p_{2/3}$ and Fe $2p_{1/2}$, respectively [5, 15, 153], while the satellite peak located at $\approx$ 719 eV is indicative of the Fe^{3+} oxidation state. The HR-XPS spectrum of hematene O 1s region was fitted with three components corresponding to the lattice-incorporated oxygen at higher binding energies ($\approx$ 729.5 eV), and, at lower binding energies, to two surface present oxygen types: in a defected state and as surface oxidation [5, 15, 154, 155].

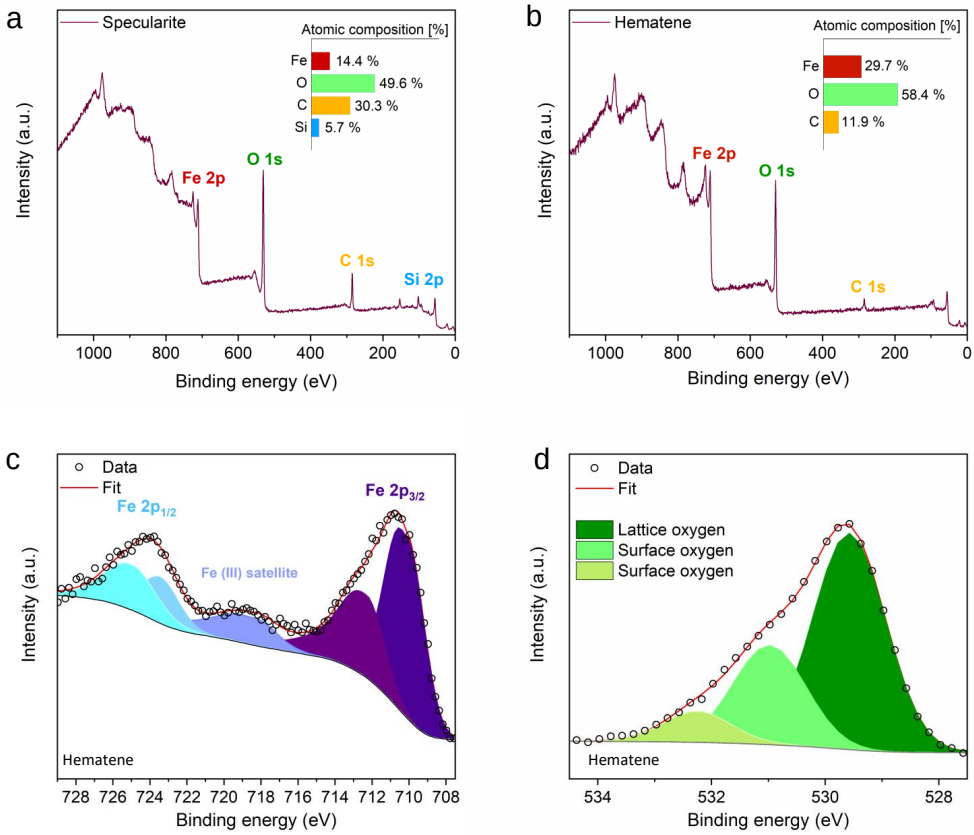

Figure 3.13: a: XPS spectrum of specularite with estimated atomic composition (inset); b: XPS spectrum of hematene with estimated atomic composition (inset); c: HR-XPS spectrum of the hematene Fe 2p and d: O 1s regions; adapted from ref. [15].

Magnetic properties

To examine the changes in magnetic behaviour in hematene after exfoliation, we measured field cooled/zero field cooled (FC/ZFC) magnetization curves of both bulk specularite and hematene, see Figure 3.14a. Furthermore, we recorded the hysteresis loops of hematene sample at 5 K and 300 K, shown in Figure 3.14b. The Morin transition temperature T_{M} of hematene is estimated

from FC/ZFC curves as ≈ 250 K and shifted towards lower temperature compared to parent specularite ($T_M \approx 265$ K). The shift can be explained by two phenomena accompanying the 2D transition: enhanced spin canting and increased lattice strain associated with the change in the exchange interactions [15]. The higher values of coercivity, magnetic remanence and saturation magnetization for 300 K hysteresis loop compared to 5 K hysteresis loop can be explained by presence of uncompensated surface spins of the 2D sheets [15].

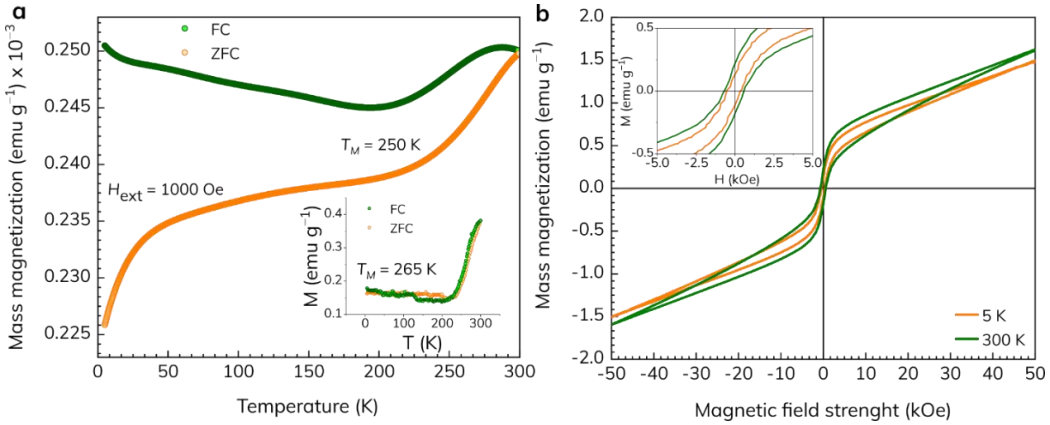

Figure 3.14: a: FC/ZFC magnetization curves of hematene sample measured in the presence of an external magnetic field of 1000 Oe and FC/ZFC magnetic curves of specularite (inset); b: magnetization hysteresis loops of hematene sample measured at 5 K (orange line) and 300 K (green line); adapted from ref. [15].

3.2.3 Intrinsic strain in hematene

Precise material characterization is crucial for understanding the properties of a nanomaterial to be able to tailor them towards specific applications. It is known that crystal structure together with its distortions, such as defects, vacancies and resulting lattice strain, affect the properties of nanomaterials.

Lattice strain as a distortion of atomic positions can influence the electronic configuration and hence the optical, electronic, electrochemical, catalytic properties etc. [156, 157, 158, 109, 159]. Methods for lattice strain evaluation provide information leading to lattice parameters of the strained sample. Among the methods using X-rays, the following are often used: extended X-ray absorption fine structure (EXAFS), synchrotron radiation XRD, HR-XRD, or there are various methods of processing powder XRD data (Williamson-Hall plot or other size-strain plot methods) [109, 160, 161, 162, 110, 163]. More local information on crystal lattice distortions can be obtained from TEM using different data acquisition and processing methods [164, 165, 166, 167, 168, 169].

Here, taking into account the available instrumental methods, we use powder XRD to get an overall idea of the lattice strain and then STEM at the atomic level of very thin sheets.

Powder XRD strain analysis

We used three different samples to evaluate the strain development with respect to exfoliation: specularite, as prepared hematene sheets and a size fraction of hematene with orange colour containing smaller flakes with a mean diameter of 120 nm (estimated by DLS), called hematene 120. The fraction was separated from heavier sheets by 48 hour sedimentation of a regular hematene batch. The XRD patterns with their corresponding W-H plots are included in Figure 3.15, while the strain values and crystallite size are listed in Table 3.4.

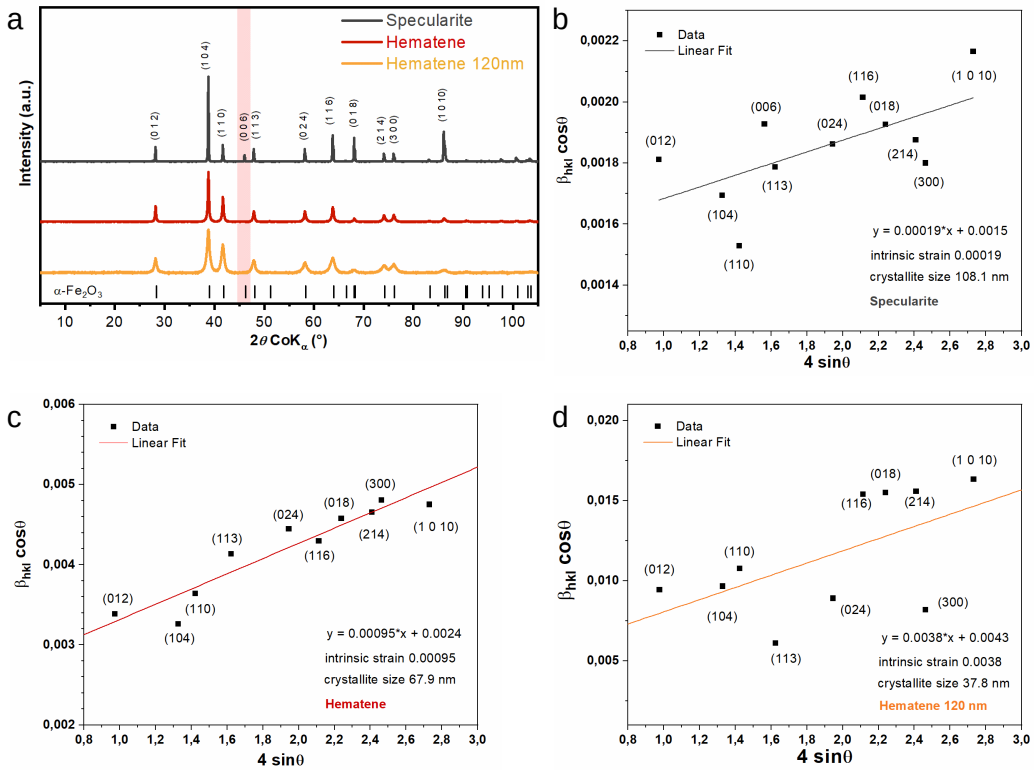

Figure 3.15: a: XRD patterns of three different samples: specularite (top grey line), as prepared hematene (middle red line) and hematene 120 (bottom orange line); corresponding W-H plots of: b: specularite; c: hematene and d: hematene 120.

Sample	Intrinsic strain (10^{-3})	Crystallite size (nm)	R^2
Specularite	0.19	108.1	0.335
Hematene	0.95	67.9	0.878
Hematene 120	3.8	37.8	0.251

Table 3.4: Values of intrinsic strain and crystallite size of specularite and hematene samples derived from the W-H plot.

It is evident from the data that the intrinsic strain values increase as exfoliation proceeds, while the crystallite size decreases, as expected. Moreover,

the positive slope indicates lattice expansion [110]. The R^2 values suggest that the conventional W-H plot is relatively suitable only in the case of as prepared hematene sheets with R^2 of 0.878, but not adequate for specularite and hematene 120, where the R^2 values were even below 0.35 and the linear fit of the data points might be questionable.

The W-H plot is nevertheless a useful tool that can reveal lattice strain in a particular crystallographic direction by patterns in outlying points. However, there are almost no trends in the data of the studied samples. If we compare the data points in all three samples, we can see that (012) diffraction peak is above the fitted line, while (104) diffraction peak lies below. The fit badness can be related to either wide crystallite size distribution or non-uniform strain in the samples.

STEM strain analysis

The STEM experiments in the following sub-chapter were carried out at University of Vienna, Austria, under the supervision of prof. Jani Kotakoski. The preparation of hematene samples for STEM imaging is described in detail in the sub-chapter 2.2.1.

The thin hematene sheets show hexagonal crystal structure, as apparent from STEM-MAADF images and the corresponding FFT[8], see Figure 3.16 and insets, further corroborating exfoliation along the [001] crystallographic direction [5]. This observation is in a good agreement with the (006) reflection disappearing from XRD pattern after exfoliation, as discussed in sub-chapter 3.2.2.

To derive the hematene lattice parameter a values within several areas

[8]The hexagonal structure is manifested by 6 FFT spots in the first and second ring of FFT spots.

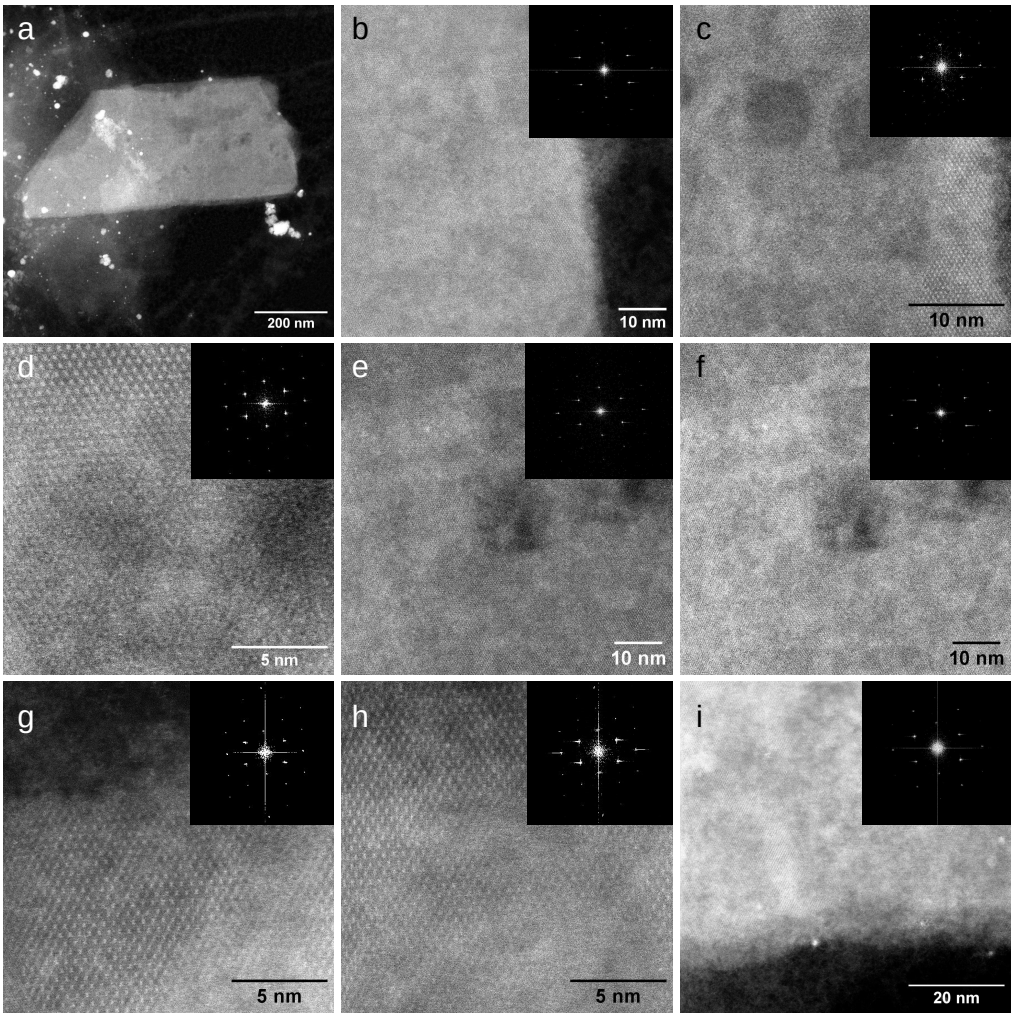

Figure 3.16: STEM-MAADF images of a: the whole hematene sheet after scanning detailed areas b – i; insets include FFT of the corresponding STEM image.

of the sheet, we used the FFT of STEM images. The second ring of FFT spots corresponds to a half of the lattice parameter value in the hexagonal structures [170]. We fitted the second ring of spots with an ellipse and used the obtained major and minor axes values and the rotation angle for the tilt correction. Then, with the lattice parameter estimated for both major and minor direction, we were able to calculate the lattice strain ϵ according to the following equation:

$$\epsilon = \frac{a - a_0}{a_0}, \tag{3.2}$$

where a_0 denotes the typical hematite lattice parameter $a_0 = 5.034$ Å. The results are listed in Table 3.5 while different areas are labelled according to letter notation in Figure 3.16.

Area	a major (Å)	a minor (Å)	ϵ major	ϵ minor
b	5.111	5.098	0.015	0.013
c	5.192	5.387	0.031	0.070
d	5.088	5.301	0.011	0.053
e	5.061	5.275	0.005	0.048
f	4.996	5.237	-0.007	0.040
g	5.205	5.398	0.034	0.072
h	5.224	5.257	0.038	0.044
i	4.995	5.014	-0.008	-0.004

Table 3.5: STEM derived values of hematene lattice parameter a in mutually perpendicular directions and corresponding lattice strain ϵ values.

The lattice parameter a values derived from multiple different areas of hematene sheet are higher compared to typical bulk hematite lattice suggesting a stretching of the hexagonal lattice in lateral dimensions. However, in areas f and i, the value of a in the major axis (in reciprocal space) is smaller, the latter area shows smaller a in both directions. Throughout the whole sheet, perturbations in the structure can be observed, probably contributing to the variations of the unit cell behaviour.

The consequent lattice strain values derived by STEM in areas with higher lattice parameter are 1 – 2 orders of magnitude higher compared to XRD W-H plot values. Unexpectedly, the lattice stretch is not the only observed phenomena, as in some areas, the lattice is shrunk in one or both directions. Therefore, it appears that hematene in-plane lattice strain is non-uniform in very thin sheets. The difference between STEM and XRD results can be explained by the fact that XRD samples contained a broad sheet diameter and thickness distribution, while STEM studied the surface of a single extremely thin flake. However, the STEM analysis would need to be performed on a larger quantity of the samples in order to draw further concrete conclusions.

Additionally, the hematene sheets were easily damaged by the electron beam, as visible from multiple areas in Figure 3.16. We hypothesize that the reason was surface contamination caused by exposure to air during the time delay between sample preparation and transferring the grids to CANVAS. Indeed, the stability was significantly improved by the immediate transfer.

3.2.4 Hematene as a platform for visible-light induced ammonia photocatalytic decomposition

The exploitation of renewable and sustainable energy sources represents one of the most important tasks for humanity, since the amount of fossil fuels is limited and the global energy consumption is predicted to at least double by the midcentury compared to the present time [171]. The newly discovered 2D n-vdW materials including hematene, magnetene (2D Fe_3O_4), ilmenene (2D $FeTiO_3$) and chromiteen (2D $FeCr_2O_4$) have proven their potential in the fields of photoelectrochemistry and electrocatalysis according to the published literature where they show excellent results in the combination with Ti nanotubes [5, 8, 172].

So far, the best results in the electrocatalysis have been achieved with noble metals, which represents a significant drawback for the scalable commercialization of these electrocatalysts, mainly due to their cost and accessibility. The development of novel materials with an enhanced electrocatalytic and/or photocatalytic activity for sustainable energy conversion is therefore highly desirable.

Hydrogen is a promising alternative to fossil fuels as it has high gravimetric energy content (120 MJ/kg) and carbon dioxide free emissions profile. However, an effective storage of hydrogen remains a challenge and a considerable research effort has focused on chemical hydrogen storage materials [173]. One of the hydrogen production approaches is ammonia decomposition leading to a release of hydrogen (fuel) and nitrogen (harmless gas). Ammonia is an ideal hydrogen carrier as it has a high gravimetric (17.8 wt.%) and volumetric (121 kg $H_2\,m^{-3}$ in liquid form) H_2 density.

The aqueous ammonia decomposition is an uphill reaction, so that an external source of the reaction energy is necessary [174]. The reaction can be induced by sunlight photons using photocatalysts. So far, only a few photoactative materials have proven to decompose the aqueous ammonia solution such as TiO_2, ZnO, ZnS, C_3N_4, graphene and other carbon based materials. However, they still suffer from several drawbacks including fast recombination of the photoinduced charge transfer, photoactivity under UV light illumination or multi-step synthesis with the help of various toxic solvents [175, 176].

Here, we explore the combination of conductive 2D hematene substrate with the catalytic surface of RuO_2 nanoparticles to obtain a sustainable platform for photocatalytic ammonia decomposition under the visible light irradiation.

Hematene composite characterization

The photocatalyst material was hematene decorated with ruthenium, hereafter denoted as Ru-hematene. We employed several experimental techniques to confirm successful loading of ruthenium species onto hematene sheets and to estimate the oxidation state of ruthenium.

The STEM-HAADF images together with elemental mapping are shown in Figure 3.17 and confirm successful loading and even spreading of ruthenium on hematene while keeping the 2D morphology of the sheets (otherwise STEM would not be possible).

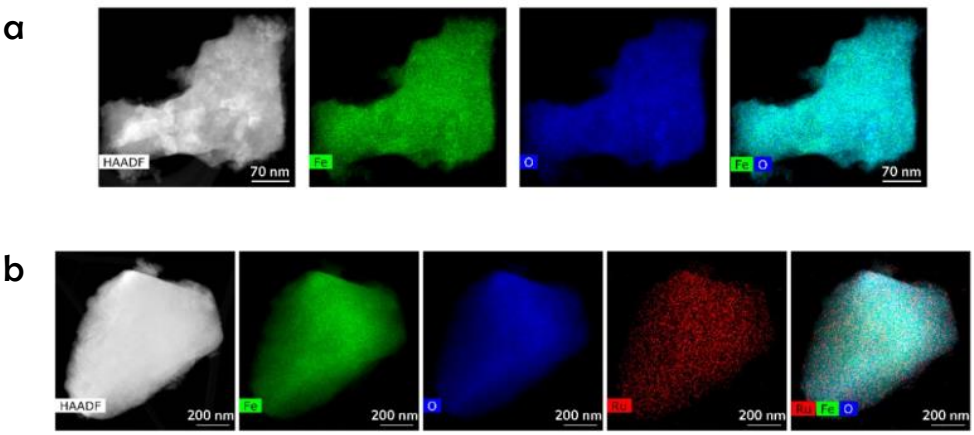

Figure 3.17: STEM-HAADF images and elemental EDS mapping of a: bare hematene; b: Ru-hematene; adapted from ref. [15].

To determine the oxidation state of ruthenium and shed more light on the electro-optical properties, a HR-XPS of the ruthenium 3d region and valence band XPS (VB-XPS) of both materials were performed as well as an electron paramagnetic resonance (EPR) study. The deconvoluted spectrum is shown in Figure 3.18a and reveals ruthenium in two different oxidation states, Ru^{4+} peak at around 280.5 eV further proves the presence of RuO_2. However, the

Ru^{3+} band below 282 eV suggests the co-presence of residual $RuCl_3$ on the sample (1.2 at.%) coming from the ruthenium loading source.

According to VB-XPS, shown in Figure 3.18b, the valence band edge remains at +1.1 eV after loading, while the density of states (DOS) showed an increasing tail at around +0.5 eV below the Fermi level. This change is related to higher photoactivity of the composite compared to the bare hematene, as these energy state levels provide orbital overlaps that facilitate the transportation of photogenerated hole to RuO_2 and oxidized ammonia to N_2. The photogenerated electrons, on the other hand, went through the hematene and reduced ammonia to H_2. Moreover, the spatial separation of charge in the place of RuO_2 and the hematene heterojunction further improved the photoactivity of the composite compared to the bare hematene. The scheme of the proposed mechanism is depicted in Figure 3.18c.

To exclude any changes in the crystal structure of hematene, that could occur during ruthenium loading and subsequent calcination on hematene at 300°C, we collected the XRD patterns of both materials, as shown in Figure 3.19a. The ruthenium in a form of crystalline RuO_2 was confirmed by a negligible diffraction peak around $32.5° \, 2\theta$ and no other phase changes were observed.

The EPR spectra reveal a major change in hematene behaviour after ruthenium loading as visible from Figure 3.19b. The EPR silence of bare hematene is in agreement with the antiferromagnetic ordering at the experimental temperature (below T_M). Furthermore, the absence of any EPR signal can be connected to the fast spin-lattice relaxation of the Fe^{3+} centres under an exchange coupled regime that became perturbed after Ru loading resulting in a broad, asymmetric resonant line in the Ru-hematene sample EPR spectrum with an average g-value of about $\approx 2,7$. We assume that the Ru ions partially altered

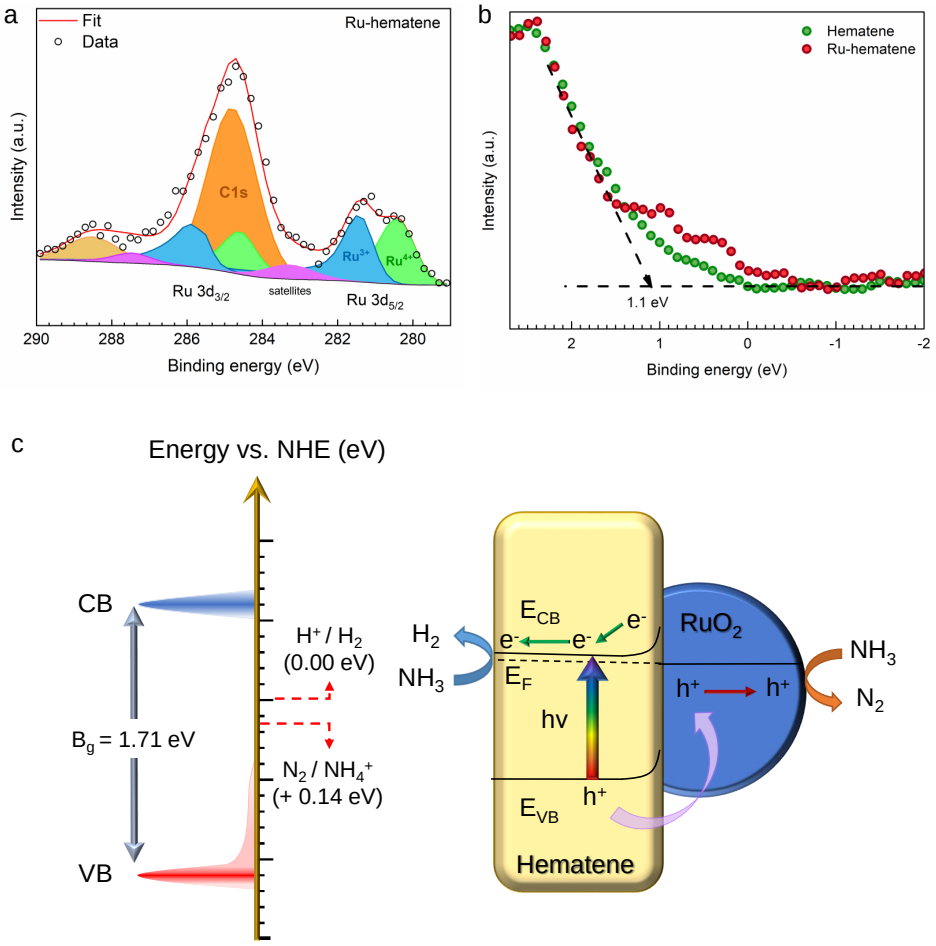

Figure 3.18: a: HR-XPS of Ru 3d region; b: VB-XPS of the bare hematene (dark green dots) and Ru-hematene (dark red dots); c: schematic depiction of DOS and band edge positions of the Ru-hematene main electronic levels relative to the energy levels of the redox couples of aqueous ammonia and the proposed mechanism of ammonia photodecomposition by the Ru-hematene photocatalyst; adapted from ref. [15].

the fraction of the Fe-O-Fe superexchange path by reacting with oxygen on top of hematene surface to form small RuO_2 nanoparticles. Furthermore, a weak modulation of the Fe^{3+} envelope was observed at $g \approx 2.09$ corresponding to the

signal of Ru^{3+} in the resonant line of $RuCl_3$. Since the Ru loading was very low (0.5 wt.%), we could only detect the Ru^{3+} species via EPR and part of these fragments may also indicate a residual $RuCl_3$ in the composite as observed by XPS.

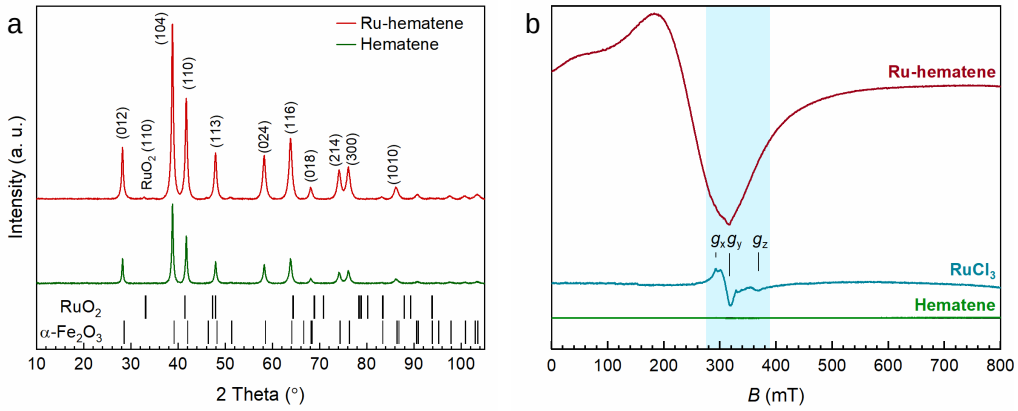

Figure 3.19: a: XRD patterns of bare hematene (dark green line) and Ru-hematene (dark red line); b: X-band CW EPR spectra of bare hematene (lower dark green line), $RuCl_3$ (middle blue line) and Ru-hematene (upper dark red line) recorded in frozen DI water dispersion ($T = 80\,\mathrm{K}$); adapted from ref. [15].

Photocatalytic activity

Both hematene and Ru-hematene suitability for ammonia photodecomposition was tested by means of UV-Vis diffuse reflectance spectroscopy (UV-Vis DRS), see Figure 3.20a, b. The band edge absorption for both samples was around 729 nm proving that these materials can absorb UV and visible part of the light spectrum. The amount of light absorbed, especially in the visible region was highly increased in the Ru-hematene sample – one of the main conditions for an ideal photocatalyst. The optical band gap energy of hematene and Ru-hematene calculated by the Tauc plot [177] based on the Kubelka-

Munk [178] theory was 1.70 eV and 1.71 eV respectively – almost the same in spite of the huge difference in the absorbed light.

The control experiments under dark conditions showed almost zero catalytic activity of both materials for ammonia decomposition. Furthermore, the photodecomposition of ammonia without the presence of photocatalyst at 24°C was zero.

After confirming ruthenium as an ideal co-catalyst for hematene to decompose ammonia, several optimization were performed. The testing of different Ru loading amount is shown in Figure 3.20c, where the optimum amount of Ru proves to be 0.5 wt.% and leads to continuously increasing amount of H_2 within 24 h. In lower amounts of Ru, the charge separation was not effective enough to produce H_2. Higher amounts of Ru provided recombination centres at the hematene surface. Another optimization concerned the mass of photocatalyst against the photoactivity, as it is not necessarily proportional due to limitation of light absorption and diffusion conditions [179, 180]. The loading of 2 mg of the photocatalyst was optimal for both materials, as visible from Figure 3.20d.

Finally, the reusability of optimal photocatalyst amount was tested, see Figure 3.20e. The Ru-hematene decreased in the activity by 11% after five photocatalytic runs (24 h per run) for the total of 120 h. The decrease can be associated with the loss of photocatalyst caused by an attachment to the reactor or magnetic stirrer or by passivation with reactants, products or intermediate species, as the catalyst was not washed after each photoreaction run.

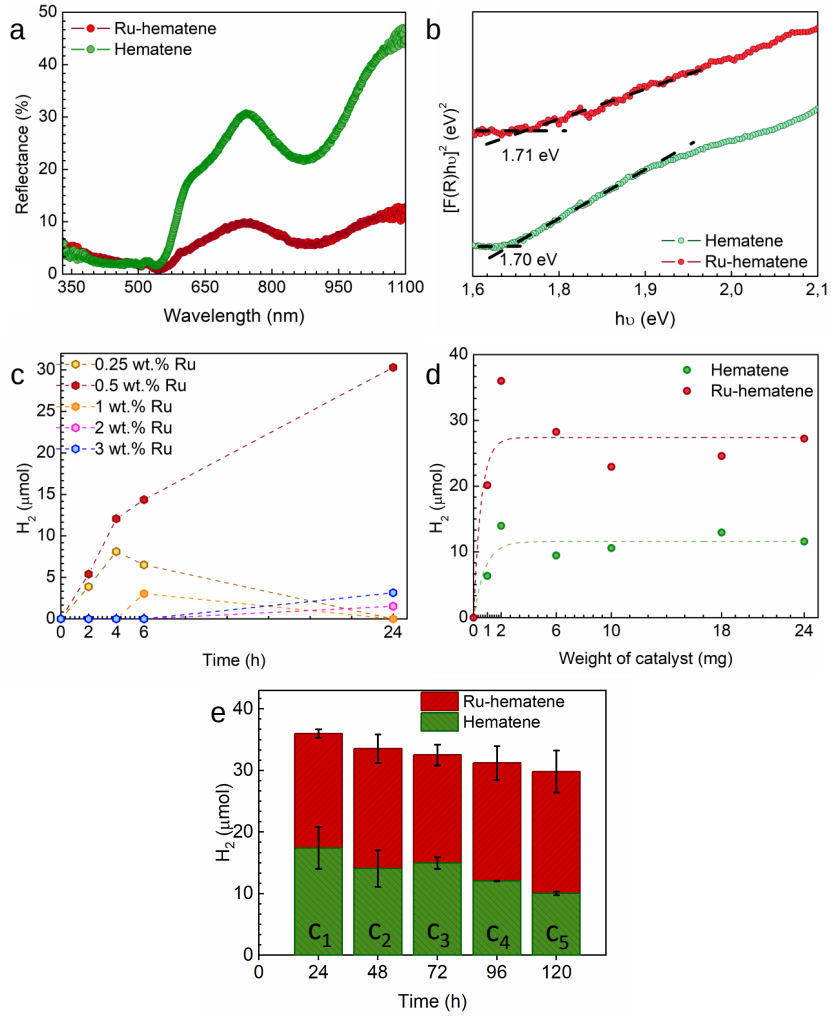

Figure 3.20: a: UV-Vis DRS of hematene and Ru-hematene and b: corresponding Tauc plot based on Kubelka-Munk model; c: optimization of Ru co-catalyst loading amount (reactors were loaded with 8 mg of photocatalyst); d: the amount of evolved H_2 from photodecomposition of ammonia with different loading amount of the pristine hematene and Ru-hematene (reactors were under illumination for 24 hours); e: reusability of 2 mg of hematene and Ru-hematene for H_2 evolution from ammonia photo decomposition demonstrated by consecutive cycles (c_1–c_5). After each cycle, the solution was sonicated and bubbled with Ar for 15 min. In all the cases, the reactor was under visible LED illumination (wavelength 400 – 700 nm, power 3 W $\cdot$ m^{-2}); adapted from ref. [15].

4 Conclusion

The presented dissertation thesis focused on the investigation of three different 2D materials whose unique properties allowed them to be applied in the fields of energy storage and photocatalysis. We demonstrated the key role of TGA and XRD in the description of advanced 2D systems based on graphene derivatives and MXenes. The techniques contributed to the understanding of the internal structure, quantity and bonding interactions of the functionalities, which was essential to properly explain the performance of the materials in energy storage. The graphene polysulfide derivative based on fluorographene chemistry showed outstanding results as LSB cathode with capacity of 800 $\mathrm{mAh\,g^{-1}}$ (3 times higher than conventionally sulphurized graphene). The MXene/graphene derivative heterostructures proved to have variable adhesion between the layers that enabled better supercapacitor efficiency.

In the field of (quasi) 2D non-van der Waals (n-vdW) materials, we showed that their preparation does not rely on the use of toxic solvent such as DMF and that, when compromising with the reachable thickness (down to 3–5 layers), hematene can be prepared via exfoliation in DI water dispersion. Then, we investigated lattice strain in hematene via XRD and STEM and revealed that the stress in the hematene lattice generally increases with decreasing layer thickness at long-range level. However, in very thin sheets the strain is non-uniform. An understanding of the intrinsic strain is crucial for tailoring hematene properties for the desired application.

Hematene possesses distinct properties compared to its bulk counterpart, for example a narrower band gap, which leads to easier formation of electrons and holes. By decorating the hematene sheets with RuO_2 nanoparticles, we created a synergistic system able to decompose ammonia via photocatalysis induced by visible light, that could lead to future production of hydrogen as a fuel. This way, we presented hematene as a low cost, eco friendly (quasi) 2D material, that can be applied in numerous fields on its own or serve as a platform for single atom engineering.

Furthermore, we started to explore the iron oxide transitions for converting hematene to other iron oxides while keeping the 2D morphology. By doing so, we can open the door towards other 2D iron oxide based materials that might be more difficult to prepare by exfoliation. To illustrate this, we show preliminary results of electrochemical reduction of hematene via lithium intercalation in Figure 4.1.

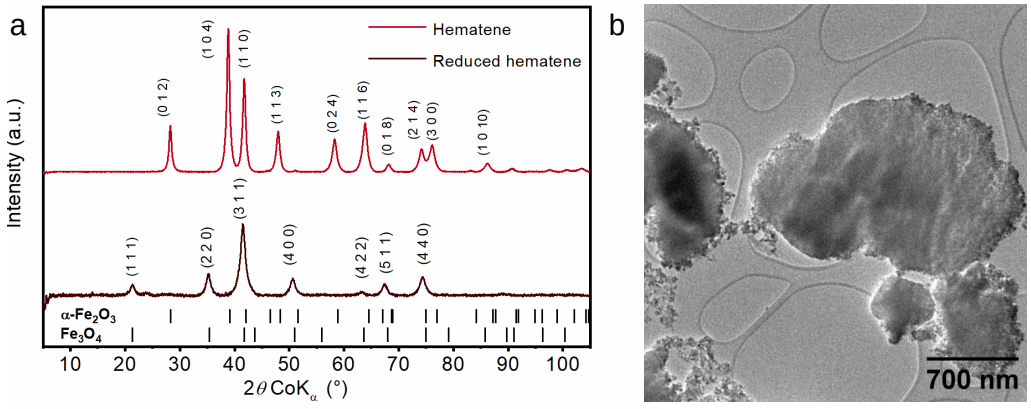

Figure 4.1: Preliminary results of electrochemical reduction of hematene: a: XRD patterns of hematene and sample after electrochemical treatment; b: TEM image of electrochemically treated sample.

Bibliography

[1] P. R. Wallace, "The Band Theory of Graphite," *Phys. Rev.*, vol. 71, no. 9, pp. 622–634, May 1947.

[2] C. Oshima and A. Nagashima, "Ultra-thin epitaxial films of graphite and hexagonal boron nitride on solid surfaces," *J. Phys.: Condens. Matter*, vol. 9, no. 1, p. 1, Jan. 1997.

[3] K. S. Novoselov, A. K. Geim, S. V. Morozov, D. Jiang, Y. Zhang, S. V. Dubonos, I. V. Grigorieva, and A. A. Firsov, "Electric Field Effect in Atomically Thin Carbon Films," *Science*, vol. 306, no. 5696, pp. 666–669, Oct. 2004.

[4] P. Miró, M. Audiffred, and T. Heine, "An atlas of two-dimensional materials," *Chem. Soc. Rev.*, vol. 43, no. 18, pp. 6537–6554, Aug. 2014.

[5] A. Puthirath Balan, S. Radhakrishnan, C. F. Woellner, S. K. Sinha, L. Deng, C. Reyes, B. M. Rao, M. Paulose, R. Neupane, A. Apte, V. Kochat, R. Vajtai, A. R. Harutyunyan, C.-W. Chu, G. Costin, D. S. Galvao, A. A. Martí, P. A. Aken, O. K. Varghese, C. S. Tiwary, A. Malie Madom Ramaswamy Iyer, and P. M. Ajayan, "Exfoliation of a non-van der Waals material from iron ore hematite," *Nat. Nanotechnol.*, vol. 13, no. 7, pp. 602–609, Jul. 2018.

[6] P. Serles, T. Arif, A. B. Puthirath, S. Yadav, G. Wang, T. Cui, A. P. Balan, T. P. Yadav, P. Thibeorchews, N. Chakingal, G. Costin, C. V. Singh, P. M. Ajayan, and T. Filleter, "Friction of magnetene, a non–van der Waals 2D material," *Science Advances*, vol. 7, no. 47, p. eabk2041, Nov. 2021.

[7] T. P. Yadav, S. N. Shirodkar, N. Lertcumfu, S. Radhakrishnan, F. N. Sayed, K. D. Malviya, G. Costin, R. Vajtai, B. I. Yakobson, C. S. Tiwary, and P. M. Ajayan,

"Chromiteen: A New 2D Oxide Magnetic Material from Natural Ore," *Advanced Materials Interfaces*, vol. 5, no. 19, p. 1800549, Oct. 2018.

[8] A. Puthirath Balan, S. Radhakrishnan, R. Kumar, R. Neupane, S. K. Sinha, L. Deng, C. A. Reyes, A. Apte, B. M. Rao, M. Paulose, R. Vajtai, C. W. Chu, G. Costin, A. A. Martí, O. K. Varghese, A. K. Singh, C. S. Tiwary, M. R. Anantharaman, and P. M. Ajayan, "A Non-van der Waals Two-Dimensional Material from Natural Titanium Mineral Ore Ilmenite," *Chem. Mater.*, vol. 30, no. 17, pp. 5923–5931, Sep. 2018.

[9] R. Friedrich, M. Ghorbani-Asl, S. Curtarolo, and A. V. Krasheninnikov, "Data-Driven Quest for Two-Dimensional Non-van der Waals Materials," *Nano Lett.*, vol. 22, no. 3, pp. 989–997, Feb. 2022.

[10] K. V. Larionov, D. G. Kvashnin, and P. B. Sorokin, "2D FeO: A New Member in 2D Metal Oxide Family," *J. Phys. Chem. C*, vol. 122, no. 30, pp. 17 389–17 394, Aug. 2018.

[11] A. B. Puthirath, S. N. Shirodkar, G. Gao, F. C. R. Hernandez, L. Deng, R. Dahal, A. Apte, G. Costin, N. Chakingal, A. P. Balan, L. M. Sassi, C. S. Tiwary, R. Vajtai, C.-W. Chu, B. I. Yakobson, and P. M. Ajayan, "Scale-Enhanced Magnetism in Exfoliated Atomically Thin Magnetite Sheets," *Small*, vol. 16, no. 45, p. 2004208, 2020.

[12] C. Jin and L. Kou, "Two-dimensional non-van der Waals magnetic layers: Functional materials for potential device applications," *J. Phys. D: Appl. Phys.*, vol. 54, no. 41, p. 413001, Jun. 2021.

[13] P. Kumbhakar, C. Chowde Gowda, P. L. Mahapatra, M. Mukherjee, K. D. Malviya, M. Chaker, A. Chandra, B. Lahiri, P. M. Ajayan, D. Jariwala, A. Singh, and C. S. Tiwary, "Emerging 2D metal oxides and their applications," *Materials Today*, vol. 45, pp. 142–168, May 2021.

[14] I. Tantis, S. Talande, V. Tzitzios, G. Basina, V. Shrivastav, A. Bakandritsos, and R. Zboril, "Non-van der Waals 2D Materials for Electrochemical Energy Storage," *Advanced Functional Materials*, vol. n/a, no. n/a, p. 2209360.

[15] J. Dzíbelová, S. M. H. Hejazi, V. Šedajová, D. Panáček, P. Jakubec, Z. Baďura, O. Malina, J. Kašlík, J. Filip, Š. Kment, M. Otyepka, and R. Zbořil, "Hematene: A sustainable 2D conductive platform for visible-light-driven photocatalytic ammonia decomposition," *Applied Materials Today*, vol. 34, p. 101881, Oct. 2023.

[16] G. Yang, L. Li, W. B. Lee, and M. C. Ng, "Structure of graphene and its disorders: A review," *Science and Technology of Advanced Materials*, vol. 19, no. 1, pp. 613–648, Dec. 2018.

[17] J. C. Meyer, A. K. Geim, M. I. Katsnelson, K. S. Novoselov, T. J. Booth, and S. Roth, "The structure of suspended graphene sheets," *Nature*, vol. 446, no. 7131, pp. 60–63, Mar. 2007.

[18] H. Huang, Y. Xu, J. Wang, and W. Duan, "Emerging topological states in quasi-two-dimensional materials," *WIREs Computational Molecular Science*, vol. 7, no. 4, p. e1296, 2017.

[19] A. P. Balan, A. B. Puthirath, S. Roy, G. Costin, E. F. Oliveira, M. A. S. R. Saadi, V. Sreepal, R. Friedrich, P. Serles, A. Biswas, S. A. Iyengar, N. Chakingal, S. Bhattacharyya, S. K. Saju, S. C. Pardo, L. M. Sassi, T. Filleter, A. Krasheninnikov, D. S. Galvao, R. Vajtai, R. R. Nair, and P. M. Ajayan, "Non-van der Waals quasi-2D materials; recent advances in synthesis, emergent properties and applications," *Materials Today*, vol. 58, pp. 164–200, Sep. 2022.

[20] A. K. Geim, "Graphene: Status and Prospects," *Science*, vol. 324, no. 5934, pp. 1530–1534, Jun. 2009.

[21] Y. Gogotsi, Ed., *Nanomaterials Handbook*, 2nd ed. Boca Raton: CRC Press, Feb. 2017.

[22] D. Akinwande, C. J. Brennan, J. S. Bunch, P. Egberts, J. R. Felts, H. Gao, R. Huang, J.-S. Kim, T. Li, Y. Li, K. M. Liechti, N. Lu, H. S. Park, E. J. Reed, P. Wang, B. I. Yakobson, T. Zhang, Y.-W. Zhang, Y. Zhou, and Y. Zhu, "A review on mechanics and mechanical properties of 2D materials—Graphene and beyond," *Extreme Mechanics Letters*, vol. 13, pp. 42–77, May 2017.

[23] A. H. Castro Neto, F. Guinea, N. M. R. Peres, K. S. Novoselov, and A. K. Geim, "The electronic properties of graphene," *Rev. Mod. Phys.*, vol. 81, no. 1, pp. 109–162, Jan. 2009.

[24] A. Bianco, H.-M. Cheng, T. Enoki, Y. Gogotsi, R. H. Hurt, N. Koratkar, T. Kyotani, M. Monthioux, C. R. Park, J. M. D. Tascon, and J. Zhang, "All in the graphene family – A recommended nomenclature for two-dimensional carbon materials," *Carbon*, vol. 65, pp. 1–6, Dec. 2013.

[25] J. Sturala, J. Luxa, M. Pumera, and Z. Sofer, "Chemistry of Graphene Derivatives: Synthesis, Applications, and Perspectives," *Chemistry – A European Journal*, vol. 24, no. 23, pp. 5992–6006, 2018.

[26] M. Inagaki and F. Kang, "Graphene derivatives: Graphane, fluorographene, graphene oxide, graphyne and graphdiyne," *J. Mater. Chem. A*, vol. 2, no. 33, pp. 13 193–13 206, Jul. 2014.

[27] A. Bakandritsos, M. Pykal, P. Błoński, P. Jakubec, D. D. Chronopoulos, K. Poláková, V. Georgakilas, K. Čépe, O. Tomanec, V. Ranc, A. B. Bourlinos, R. Zbořil, and M. Otyepka, "Cyanographene and Graphene Acid: Emerging Derivatives Enabling High-Yield and Selective Functionalization of Graphene," *ACS Nano*, vol. 11, no. 3, pp. 2982–2991, Mar. 2017.

[28] I. Tantis, A. Bakandritsos, D. Zaoralová, M. Medveď, P. Jakubec, J. Havláková, R. Zbořil, and M. Otyepka, "Covalently Interlinked Graphene Sheets with Sulfur-Chains Enable Superior Lithium–Sulfur Battery Cathodes at Full-Mass Level," *Advanced Functional Materials*, vol. 31, no. 30, p. 2101326, 2021.

[29] T. M. Magne, T. de Oliveira Vieira, L. M. R. Alencar, F. F. M. Junior, S. Gemini-Piperni, S. V. Carneiro, L. M. U. D. Fechine, R. M. Freire, K. Golokhvast, P. Metrangolo, P. B. A. Fechine, and R. Santos-Oliveira, "Graphene and its derivatives: Understanding the main chemical and medicinal chemistry roles for biomedical applications," *J Nanostruct Chem*, vol. 12, no. 5, pp. 693–727, Oct. 2022.

[30] V. Šedajová, A. Bakandritsos, P. Błoński, M. Medveď, R. Langer, D. Zaoralová, J. Ugolotti, J. Dzíbelová, P. Jakubec, V. Kupka, and M. Otyepka, "Nitrogen doped graphene with diamond-like bonds achieves unprecedented energy density at high power in a symmetric sustainable supercapacitor," *Energy Environ. Sci.*, vol. 15, no. 2, pp. 740–748, Feb. 2022.

[31] D. D. Chronopoulos, A. Bakandritsos, M. Pykal, R. Zbořil, and M. Otyepka, "Chemistry, properties, and applications of fluorographene," *Applied Materials Today*, vol. 9, pp. 60–70, Dec. 2017.

[32] V. Mazánek, O. Jankovský, J. Luxa, D. Sedmidubský, Z. Janoušek, F. Šembera, M. Mikulics, and Z. Sofer, "Tuning of fluorine content in graphene: Towards large-scale

production of stoichiometric fluorographene," *Nanoscale*, vol. 7, no. 32, pp. 13 646–13 655, Aug. 2015.

[33] R. Zbořil, F. Karlický, A. B. Bourlinos, T. A. Steriotis, A. K. Stubos, V. Georgakilas, K. Šafářová, D. Jančík, C. Trapalis, and M. Otyepka, "Graphene Fluoride: A Stable Stoichiometric Graphene Derivative and its Chemical Conversion to Graphene," *Small*, vol. 6, no. 24, pp. 2885–2891, 2010.

[34] V. Hrubý, L. Zdražil, J. Dzíbelová, V. Šedajová, A. Bakandritsos, P. Lazar, and M. Otyepka, "Unveiling the true band gap of fluorographene and its origins by teaming theory and experiment," *Applied Surface Science*, vol. 587, p. 152839, Jun. 2022.

[35] H. Tang, Q. Hu, M. Zheng, Y. Chi, X. Qin, H. Pang, and Q. Xu, "MXene–2D layered electrode materials for energy storage," *Progress in Natural Science: Materials International*, vol. 28, no. 2, pp. 133–147, Apr. 2018.

[36] M. Naguib, M. Kurtoglu, V. Presser, J. Lu, J. Niu, M. Heon, L. Hultman, Y. Gogotsi, and M. W. Barsoum, "Two-Dimensional Nanocrystals Produced by Exfoliation of Ti3AlC2," *Advanced Materials*, vol. 23, no. 37, pp. 4248–4253, 2011.

[37] G. Deysher, C. E. Shuck, K. Hantanasirisakul, N. C. Frey, A. C. Foucher, K. Maleski, A. Sarycheva, V. B. Shenoy, E. A. Stach, B. Anasori, and Y. Gogotsi, "Synthesis of Mo4VAlC4 MAX Phase and Two-Dimensional Mo4VC4 MXene with Five Atomic Layers of Transition Metals," *ACS Nano*, vol. 14, no. 1, pp. 204–217, Jan. 2020.

[38] R. E. Ustad, S. Kundale, K. A. Rokade, S. Patil, V. D. Chavan, K. D. Kadam, H. Patil, S. P. Patil, R. K. Kamat, D.-k. Kim, and T. Dongale, "Recent progress in energy, environment and electronic applications of MXene nanomaterials," *Nanoscale*, 2023.

[39] Y. Gogotsi and B. Anasori, "The Rise of MXenes," *ACS Nano*, vol. 13, no. 8, pp. 8491–8494, Aug. 2019.

[40] U. Amara, I. Hussain, M. Ahmad, K. Mahmood, and K. Zhang, "2D MXene-Based Biosensing: A Review," *Small*, vol. 19, no. 2, p. 2205249, 2023.

[41] M. Shekhirev, C. E. Shuck, A. Sarycheva, and Y. Gogotsi, "Characterization of MXenes at every step, from their precursors to single flakes and assembled films," *Progress in Materials Science*, vol. 120, p. 100757, Jul. 2021.

[42] "Introduction to the Iron Oxides," in *The Iron Oxides*. John Wiley & Sons, Ltd, 2003, ch. 1, pp. 1–7.

[43] "Crystal Structure," in *The Iron Oxides*. John Wiley & Sons, Ltd, 2003, ch. 2, pp. 9–38.

[44] J. Tuček, L. Machala, S. Ono, A. Namai, M. Yoshikiyo, K. Imoto, H. Tokoro, S.-i. Ohkoshi, and R. Zbořil, "Zeta-Fe2O3 – A new stable polymorph in iron(III) oxide family," *Sci Rep*, vol. 5, no. 1, p. 15091, Oct. 2015.

[45] R. K. Sharma, S. Dutta, S. Sharma, R. Zboril, R. S. Varma, and M. B. Gawande, "Fe 3 O 4 (iron oxide)-supported nanocatalysts: Synthesis, characterization and applications in coupling reactions," *Green Chemistry*, vol. 18, no. 11, pp. 3184–3209, 2016.

[46] K. Hola, Z. Markova, G. Zoppellaro, J. Tucek, and R. Zboril, "Tailored functionalization of iron oxide nanoparticles for MRI, drug delivery, magnetic separation and immobilization of biosubstances," *Biotechnology Advances*, vol. 33, no. 6, Part 2, pp. 1162–1176, Nov. 2015.

[47] M. Kilianová, R. Prucek, J. Filip, J. Kolařík, L. Kvítek, A. Panáček, J. Tuček, and R. Zbořil, "Remarkable efficiency of ultrafine superparamagnetic iron(III) oxide nanoparticles toward arsenate removal from aqueous environment," *Chemosphere*, vol. 93, no. 11, pp. 2690–2697, Nov. 2013.

[48] J. Tuček, K. C. Kemp, K. S. Kim, and R. Zbořil, "Iron-Oxide-Supported Nanocarbon in Lithium-Ion Batteries, Medical, Catalytic, and Environmental Applications," *ACS Nano*, vol. 8, no. 8, pp. 7571–7612, Aug. 2014.

[49] L. Lv, M. Peng, L. Wu, Y. Dong, G. You, Y. Duan, W. Yang, L. He, and X. Liu, "Progress in Iron Oxides Based Nanostructures for Applications in Energy Storage," *Nanoscale Res Lett*, vol. 16, no. 1, p. 138, Aug. 2021.

[50] Y. Lee, J. Kwon, J. Lim, W. Shin, S. Park, E. Hwang, J. Shin, H. Cho, J. Jung, H.-J. Kim, S. Han, H. Lee, Y. Son, C. W. Ha, P. Prabhakaran, J. Yeo, S. H. Ko, and S. Hong, "Digital Laser Micropainting for Reprogrammable Optoelectronic Applications," *Advanced Functional Materials*, vol. 31, no. 1, p. 2006854, 2021.

[51] S. D. Roy, K. C. Das, and S. S. Dhar, "Conventional to green synthesis of magnetic iron oxide nanoparticles; its application as catalyst, photocatalyst and toxicity: A short review," *Inorganic Chemistry Communications*, vol. 134, p. 109050, Dec. 2021.

[52] R. Zboril, M. Mashlan, and D. Petridis, "Iron(III) Oxides from Thermal ProcessesSynthesis, Structural and Magnetic Properties, Mössbauer Spectroscopy Characterization, and Applications," *Chem. Mater.*, vol. 14, no. 3, pp. 969–982, Mar. 2002.

[53] "Electronic, Electrical and Magnetic Properties and Colour," in *The Iron Oxides*. John Wiley & Sons, Ltd, 2003, ch. 6, pp. 111–137.

[54] D. Kubániová, L. Kubíčková, T. Kmječ, K. Závěta, D. Nižňanský, P. Brázda, M. Klementová, and J. Kohout, "Hematite: Morin temperature of nanoparticles with different size," *Journal of Magnetism and Magnetic Materials*, vol. 475, pp. 611–619, Apr. 2019.

[55] P. J. Besser, A. H. Morrish, and C. W. Searle, "Magnetocrystalline Anisotropy of Pure and Doped Hematite," *Phys. Rev.*, vol. 153, no. 2, pp. 632–640, Jan. 1967.

[56] D. Schroeer and R. C. Nininger, "Morin Transition in α - Fe 2 O 3 Microcyrstals," *Phys. Rev. Lett.*, vol. 19, no. 11, pp. 632–634, Sep. 1967.

[57] R. D. Zysler, D. Fiorani, A. M. Testa, L. Suber, E. Agostinelli, and M. Godinho, "Size dependence of the spin-flop transition in hematite nanoparticles," *Phys. Rev. B*, vol. 68, no. 21, p. 212408, Dec. 2003.

[58] J. Leland and A. Bard, "Photochemistry of Colloidal Semiconducting Iron-Oxide Polymorphs," *J. Phys. Chem.*, vol. 91, no. 19, pp. 5076–5083, Sep. 1987.

[59] X. Zhang, H. Li, S. Wang, F.-R. F. Fan, and A. J. Bard, "Improvement of Hematite as Photocatalyst by Doping with Tantalum," *J. Phys. Chem. C*, vol. 118, no. 30, pp. 16 842–16 850, Jul. 2014.

[60] J. Xie, W. Liu, J. Xin, F. Lei, L. Gao, H. Qu, X. Zhang, and Y. Xie, "Dual Effect in Fluorine-Doped Hematite Nanocrystals for Efficient Water Oxidation," *ChemSusChem*, vol. 10, no. 22, pp. 4465–4471, Nov. 2017.

[61] P. C. L. Muraro, S. R. Mortari, B. S. Vizzotto, G. Chuy, C. dos Santos, L. F. W. Brum, and W. L. da Silva, "Iron oxide nanocatalyst with titanium and silver nanoparticles: Synthesis, characterization and photocatalytic activity on the degradation of Rhodamine B dye," *Sci Rep*, vol. 10, no. 1, p. 3055, Feb. 2020.

[62] X. Hu, S. Han, and Y. Zhu, "Facet-controlled synthesis of polyhedral hematite/carbon composites with enhanced photoactivity," *Appl. Surf. Sci.*, vol. 443, pp. 227–235, Jun. 2018.

[63] M. P. Cardona, M. Li, W. Li, J. McCall, D. Wang, Y. Li, and C. Yang, "The role of graphene as an overlayer on nanostructured hematite photoanodes for improved solar water oxidation," *Mater. Today Energy*, vol. 8, pp. 8–14, Jun. 2018.

[64] O. F. S. Khasawneh, P. Palaniandy, and L. P. Teng, "Large-scale study for the photocatalytic degradation of paracetamol using Fe2O3/TiO2 nanocomposite catalyst and CPC reactor under natural sunlight radiations," *MethodsX*, vol. 6, pp. 2735–2743, 2019.

[65] Y. H. Chen and C. C. Lin, "Effect of nano-hematite morphology on photocatalytic activity," *Phys Chem Minerals*, vol. 41, no. 10, pp. 727–736, Nov. 2014.

[66] F. C. Voogt, T. Hibma, P. J. M. Smulders, L. Iesen, and T. Fujii, "MBE-Growth of Iron and Iron Oxide Thin Films on MgO(100), using NO2, NO, and N2O as Oxidising Agents," *MRS Online Proceedings Library*, vol. 474, no. 1, pp. 211–216, Dec. 1997.

[67] B. K. McMillin, P. Biswas, and M. R. Zachariah, "In situ characterization of vapor phase growth of iron oxide-silica nanocomposites: Part I. 2-D planar laser-induced fluorescence and Mie imaging," *Journal of Materials Research*, vol. 11, no. 6, pp. 1552–1561, Jun. 1996.

[68] Y. Wang, P. Wang, H. Wang, B. Xu, H. Li, M. Cheng, W. Feng, R. Du, L. Song, X. Wen, X. Li, J. Yang, Y. Cai, J. He, Z. Wang, and J. Shi, "Room-Temperature Magnetoelectric Coupling in Atomically Thin ϵ-Fe2O3," *Advanced Materials*, vol. 35, no. 7, p. 2209465, 2023.

[69] Y. Li, X. Zhao, Y. Cui, F. Yang, and X. Bao, "Oxidation-induced structural transition of two-dimensional iron oxide on Au(111)," *J. Phys. D: Appl. Phys.*, vol. 54, no. 20, p. 204003, Mar. 2021.

[70] R. Singla, T. A. Hackett, S. Kumar, J. Sharma, and M. K. Kashyap, "Curie temperature engineering in a novel 2D analog of iron ore (hematene) via strain," *Nanoscale Advances*, vol. 2, no. 12, pp. 5890–5896, 2020.

[71] J. Shi, W. Ren, X. Ren, Y. Shang, R. Pang, and S. Li, "Edge-state-induced magnetism in two-dimensional hematene," *Journal of Materials Chemistry A*, vol. 10, no. 34, pp. 17 766–17 772, 2022.

[72] A. Bandyopadhyay, N. C. Frey, D. Jariwala, and V. B. Shenoy, "Engineering Magnetic Phases in Two-Dimensional Non-van der Waals Transition-Metal Oxides," *Nano Lett.*, vol. 19, no. 11, pp. 7793–7800, Nov. 2019.

[73] C. Bacaksiz, M. Yagmurcukardes, F. M. Peeters, and M. V. Milošević, "Hematite at its thinnest limit," *2D Mater.*, vol. 7, no. 2, p. 025029, Feb. 2020.

[74] Y. Xu, L. Wang, and Y. Li, "Regulating Magnetic Behavior of Fe in Hematene by Defects to Improve Oxygen Evolution Reaction," *J. Phys. Chem. Lett.*, vol. 13, no. 33, pp. 7629–7635, Aug. 2022.

[75] Y. Wei, M. Ghorbani-Asl, and A. V. Krasheninnikov, "Tailoring the Electronic and Magnetic Properties of Hematene by Surface Passivation: Insights from First-Principles Calculations," *J. Phys. Chem. C*, vol. 124, no. 41, pp. 22 784–22 792, 2020.

[76] A. Kumar, R. Zhang, M. Venkatesan, P. Stamenov, and J. M. D. Coey, "Exfoliation of hematite: Morphological, structural and magnetic investigations," *Journal of Magnetism and Magnetic Materials*, vol. 542, p. 168507, Jan. 2022.

[77] A. Thejas Prasannakumar, B. C, R. R, R. F. U, R. Philip, and S. J Varma, "Hematene Nanoflakes: A Non-van der Waals Material with Superior Nonlinear Optical Properties," *ACS Appl. Opt. Mater.*, Nov. 2022.

[78] A. Koutsioukis, G. Florakis, N. Samartzis, S. N. Yannopoulos, M. Stavrou, D. Theodoropoulou, N. Chazapis, S. Couris, A. Kolokithas-Ntoukas, G. Asimakopoulos, D. P. Gournis, V. Tzitzios, E. Sakellis, S. F. Tombros, S. Kokkalas, and V. Georgakilas, "Green synthesis of ultrathin 2D nanoplatelets, hematene and magnetene, from mineral ores in water, with strong optical limiting performance," *Journal of Materials Chemistry C*, vol. 11, no. 9, pp. 3244–3251, 2023.

[79] B. Mohanty, Y. Wei, M. Ghorbani-Asl, A. V. Krasheninnikov, P. Rajput, and B. Kumar Jena, "Revealing the defect-dominated oxygen evolution activity of hematene," *Journal of Materials Chemistry A*, vol. 8, no. 14, pp. 6709–6716, 2020.

[80] Z. Zhang, M. Ye, E. J. Harvey, and G. Merle, "Editors' Choice—Methanol Electrooxidation with Platinum Decorated Hematene Nanosheet," *J. Electrochem. Soc.*, vol. 166, no. 4, p. H135, Feb. 2019.

[81] J. Mohapatra, A. Ramos, J. Elkins, J. Beatty, M. Xing, D. Singh, E. C. La Plante, and J. Ping Liu, "Ferromagnetism in 2D α-Fe2O3 nanosheets," *Applied Physics Letters*, vol. 118, no. 18, p. 183102, May 2021.

[82] A. C. M. Padilha, M. Soares, E. R. Leite, and A. Fazzio, "Theoretical and Experimental Investigation of 2D Hematite," *J. Phys. Chem. C*, vol. 123, no. 26, pp. 16 359–16 365, Jul. 2019.

[83] Y. Wei, M. Ghorbani-Asl, and A. V. Krasheninnikov, "Tailoring the Electronic and Magnetic Properties of Hematene by Surface Passivation: Insights from First-Principles Calculations," *The Journal of Physical Chemistry C*, vol. 124, no. 41, pp. 22 784–22 792, Oct. 2020.

[84] C. Gao and C. V. Singh, "Mechanical properties and magnetic and electronic properties tuned via strain in two-dimensional non-van der Waals hematene," *Nuclear Analysis*, vol. 2, no. 1, p. 100061, Mar. 2023.

[85] Z. Zhang, D. Vieira, J. E. Barralet, and G. Merle, "2D hematene, a bioresorbable electrocatalytic support for glucose oxidation," *2D Materials*, vol. 7, no. 2, p. 025044, Mar. 2020.

[86] Z. Zhang, M. Ye, E. J. Harvey, and G. Merle, "Editors' Choice—Methanol Electrooxidation with Platinum Decorated Hematene Nanosheet," *Journal of The Electrochemical Society*, vol. 166, no. 4, pp. H135–H139, 2019.

[87] P. Yekan Motlagh, A. Khataee, A. Hassani, and Y. Orooji, "Facile and environmentally friendly synthesis of highly efficient two-dimensional hematene nanosheets for photocatalytic applications," *Journal of Industrial and Engineering Chemistry*, vol. 126, pp. 465–479, Oct. 2023.

[88] M. Stavrou, N. Chazapis, V. Arapakis, V. Georgakilas, and S. Couris, "Strong Ultrafast Saturable Absorption and Nonlinear Refraction of Some Non-van der Waals 2D Hematene and Magnetene Nanoplatelets for Ultrafast Photonic Applications," *ACS Appl. Mater. Interfaces*, vol. 15, no. 29, pp. 35 391–35 399, Jul. 2023.

[89] R. Monk, "Novel Bioresorbable Hematene-Doped Monetite Scaffold for Bone Repair," M.Sc., 2022.

[90] N. Abid, A. M. Khan, S. Shujait, K. Chaudhary, M. Ikram, M. Imran, J. Haider, M. Khan, Q. Khan, and M. Maqbool, "Synthesis of nanomaterials using various top-down and bottom-up approaches, influencing factors, advantages, and disadvantages: A review," *Advances in Colloid and Interface Science*, vol. 300, p. 102597, Feb. 2022.

[91] S. Hao, X. Zhao, Q. Cheng, Y. Xing, W. Ma, X. Wang, G. Zhao, and X. Xu, "A Mini Review of the Preparation and Photocatalytic Properties of Two-Dimensional Materials," *Frontiers in Chemistry*, vol. 8, 2020.

[92] B. Cho and Y. Kim, "Preparation and Properties of 2D Materials," *Nanomaterials*, vol. 10, no. 4, p. 764, Apr. 2020.

[93] H. Cui, Y. Guo, W. Ma, and Z. Zhou, "2 D Materials for Electrochemical Energy Storage: Design, Preparation, and Application," *ChemSusChem*, vol. 13, no. 6, pp. 1155–1171, 2020.

[94] H. Schift, "Nanoimprint lithography: 2D or not 2D? A review," *Appl. Phys. A*, vol. 121, no. 2, pp. 415–435, Nov. 2015.

[95] M. V. Pugachev, A. I. Duleba, A. A. Galiullin, and A. Y. Kuntsevich, "Micromask Lithography for Cheap and Fast 2D Materials Microstructures Fabrication," *Micromachines*, vol. 12, no. 8, p. 850, Aug. 2021.

[96] W. Song, L. Kong, Q. Tao, Q. Liu, X. Yang, J. Li, H. Duan, X. Duan, L. Liao, and Y. Liu, "High-Resolution Van der Waals Stencil Lithography for 2D Transistors," *Small*, vol. 17, no. 29, p. 2101209, 2021.

[97] G. Wu, M. Yi, G. Xiao, Z. Chen, J. Zhang, and C. Xu, "A novel method for producing boron nitride nanosheets via synergistic exfoliation with pure shear ball milling and ultrasonication," *Ceramics International*, vol. 45, no. 17, Part B, pp. 23 841–23 848, Dec. 2019.

[98] Z. Cai, B. Liu, X. Zou, and H.-M. Cheng, "Chemical Vapor Deposition Growth and Applications of Two-Dimensional Materials and Their Heterostructures," *Chem. Rev.*, vol. 118, no. 13, pp. 6091–6133, Jul. 2018.

[99] F. Wang and X. Wang, "Mechanisms in the solution growth of free-standing two-dimensional inorganic nanomaterials," *Nanoscale*, vol. 6, no. 12, pp. 6398–6414, 2014.

[100] R. Sui, J. M. H. Lo, C. B. Lavery, C. E. Deering, K. G. Wynnyk, N. Chou, and R. A. Marriott, "Sol–Gel-Derived 2D Nanostructures of Aluminum Hydroxide Acetate: Toward the Understanding of Nanostructure Formation," *J. Phys. Chem. C*, vol. 122, no. 9, pp. 5141–5150, Mar. 2018.

[101] R. Erni, *Aberration-Corrected Imaging In Transmission Electron Microscopy: An Introduction (2nd Edition)*. World Scientific Publishing Company, Mar. 2015.

[102] A. Howie, "Image Contrast And Localized Signal Selection Techniques," *Journal of Microscopy*, vol. 117, no. 1, pp. 11–23, 1979.

[103] S. J. Pennycook and D. E. Jesson, "High-resolution Z-contrast imaging of crystals," *Ultramicroscopy*, vol. 37, no. 1, pp. 14–38, Aug. 1991.

[104] "Handbook of Thermal Analysis | Wiley," https://www.wiley.com/en-us/Handbook+of+Thermal+Analysis-p-9780471983637.

[105] P. Gabbott, "A Practical Introduction to Differential Scanning Calorimetry," in *Principles and Applications of Thermal Analysis*. John Wiley & Sons, Ltd, 2008, ch. 1, pp. 1–50.

[106] M. Schirowski, F. Hauke, and A. Hirsch, "Controlling the Degree of Functionalization: In-Depth Quantification and Side-Product Analysis of Diazonium Chemistry on SWCNTs," *Chemistry – A European Journal*, vol. 25, no. 55, pp. 12 761–12 768, 2019.

[107] F. G. Brunetti, M. A. Herrero, J. d. M. Muñoz, A. Díaz-Ortiz, J. Alfonsi, M. Meneghetti, M. Prato, and E. Vázquez, "Microwave-Induced Multiple Functionalization of Carbon Nanotubes," *J. Am. Chem. Soc.*, vol. 130, no. 25, pp. 8094–8100, Jun. 2008.

[108] J. H. Williams, *Crystal Engineering: How Molecules Build Solids*. Morgan & Claypool Publishers, Sep. 2017.

[109] E. Westsson, S. Picken, and G. Koper, "The effect of lattice strain on catalytic activity," *Chem. Commun.*, vol. 55, no. 9, pp. 1338–1341, Jan. 2019.

[110] D. Nath, F. Singh, and R. Das, "X-ray diffraction analysis by Williamson-Hall, Halder-Wagner and size-strain plot methods of CdSe nanoparticles- a comparative study," *Materials Chemistry and Physics*, vol. 239, p. 122021, Jan. 2020.

[111] M. De and S. P. S. Gupta, “Lattice imperfection studies in polycrystalline materials by x-ray diffraction line-profile analysis,” *Pramana - J Phys*, vol. 23, no. 6, pp. 721–744, Dec. 1984.

[112] J. I. Langford and A. J. C. Wilson, “Scherrer after sixty years: A survey and some new results in the determination of crystallite size,” *Journal of Applied Crystallography*, vol. 11, no. 2, pp. 102–113, 1978.

[113] S. Das Bakshi, D. Sinha, and S. Ghosh Chowdhury, “Anisotropic broadening of XRD peaks of A'-Fe: Williamson-Hall and Warren-Averbach analysis using full width at half maximum (FWHM) and integral breadth (IB),” *Materials Characterization*, vol. 142, pp. 144–153, Aug. 2018.

[114] I. Tantis, A. Bakandritsos, D. Zaoralová, M. Medveď, P. Jakubec, J. Havláková, R. Zbořil, and M. Otyepka, “Covalently Interlinked Graphene Sheets with Sulfur-Chains Enable Superior Lithium–Sulfur Battery Cathodes at Full-Mass Level,” *Adv Funct Materials*, vol. 31, no. 30, p. 2101326, Jul. 2021.

[115] V. Šedajová, A. Bakandritsos, P. Błoński, M. Medveď, R. Langer, D. Zaoralová, J. Ugolotti, J. Dzíbelová, P. Jakubec, V. Kupka, and M. Otyepka, “Nitrogen doped graphene with diamond-like bonds achieves unprecedented energy density at high power in a symmetric sustainable supercapacitor,” *Energy Environ. Sci.*, vol. 15, no. 2, pp. 740–748, 2022.

[116] T. S. Mathis, K. Maleski, A. Goad, A. Sarycheva, M. Anayee, A. C. Foucher, K. Hantanasirisakul, C. E. Shuck, E. A. Stach, and Y. Gogotsi, “Modified MAX Phase Synthesis for Environmentally Stable and Highly Conductive Ti3C2 MXene,” *ACS Nano*, vol. 15, no. 4, pp. 6420–6429, Apr. 2021.

[117] C. Mangler, J. Meyer, A. Mittelberger, K. Mustonen, T. Susi, and J. Kotakoski, “A Materials Scientist’s CANVAS: A System for Controlled Alteration of Nanomaterials in Vacuum Down to the Atomic Scale,” *Microscopy and Microanalysis*, vol. 28, no. S1, pp. 2940–2942, Aug. 2022.

[118] M. S. Guney and Y. Tepe, “Classification and assessment of energy storage systems,” *Renewable and Sustainable Energy Reviews*, vol. 75, pp. 1187–1197, Aug. 2017.

[119] J. Xie and Y.-C. Lu, “A retrospective on lithium-ion batteries,” *Nat Commun*, vol. 11, no. 1, p. 2499, May 2020.

[120] Q. Zhu, D. Zhao, M. Cheng, J. Zhou, K. A. Owusu, L. Mai, and Y. Yu, "A New View of Supercapacitors: Integrated Supercapacitors," *Advanced Energy Materials*, vol. 9, no. 36, p. 1901081, 2019.

[121] T. Kim, W. Song, D.-Y. Son, L. K. Ono, and Y. Qi, "Lithium-ion batteries: Outlook on present, future, and hybridized technologies," *Journal of Materials Chemistry A*, vol. 7, no. 7, pp. 2942–2964, 2019.

[122] J. Liu, Z. Bao, Y. Cui, E. J. Dufek, J. B. Goodenough, P. Khalifah, Q. Li, B. Y. Liaw, P. Liu, A. Manthiram, Y. S. Meng, V. R. Subramanian, M. F. Toney, V. V. Viswanathan, M. S. Whittingham, J. Xiao, W. Xu, J. Yang, X.-Q. Yang, and J.-G. Zhang, "Pathways for practical high-energy long-cycling lithium metal batteries," *Nat Energy*, vol. 4, no. 3, pp. 180–186, Mar. 2019.

[123] M. Armand, P. Axmann, D. Bresser, M. Copley, K. Edström, C. Ekberg, D. Guyomard, B. Lestriez, P. Novák, M. Petranikova, W. Porcher, S. Trabesinger, M. Wohlfahrt-Mehrens, and H. Zhang, "Lithium-ion batteries – Current state of the art and anticipated developments," *Journal of Power Sources*, vol. 479, p. 228708, Dec. 2020.

[124] S. Evers and L. F. Nazar, "New Approaches for High Energy Density Lithium–Sulfur Battery Cathodes," *Acc. Chem. Res.*, vol. 46, no. 5, pp. 1135–1143, May 2013.

[125] Z. Wang, Y. Dong, H. Li, Z. Zhao, H. Bin Wu, C. Hao, S. Liu, J. Qiu, and X. W. D. Lou, "Enhancing lithium–sulphur battery performance by strongly binding the discharge products on amino-functionalized reduced graphene oxide," *Nat Commun*, vol. 5, no. 1, p. 5002, Sep. 2014.

[126] X. Ji, K. T. Lee, and L. F. Nazar, "A highly ordered nanostructured carbon–sulphur cathode for lithium–sulphur batteries," *Nature Mater*, vol. 8, no. 6, pp. 500–506, Jun. 2009.

[127] M. Medveď, G. Zoppellaro, J. Ugolotti, D. Matochová, P. Lazar, T. Pospíšil, A. Bakandritsos, J. Tuček, R. Zbořil, and M. Otyepka, "Reactivity of fluorographene is triggered by point defects: Beyond the perfect 2D world," *Nanoscale*, vol. 10, no. 10, pp. 4696–4707, Mar. 2018.

[128] D. Matochová, M. Medved', A. Bakandritsos, T. Steklý, R. Zbořil, and M. Otyepka, "2D Chemistry: Chemical Control of Graphene Derivatization," *J. Phys. Chem. Lett.*, vol. 9, no. 13, pp. 3580–3585, Jul. 2018.

[129] R. Steudel, "Sulfur: Organic Polysulfanes," in *Encyclopedia of Inorganic Chemistry*. John Wiley & Sons, Ltd, 2007.

[130] Y. Yang, G. Lu, Y. Li, Z. Liu, and X. Huang, "One-Step Preparation of Fluorographene: A Highly Efficient, Low-Cost, and Large-Scale Approach of Exfoliating Fluorographite," *ACS Appl. Mater. Interfaces*, vol. 5, no. 24, pp. 13 478–13 483, Dec. 2013.

[131] X. Wang, Y. Dai, W. Wang, M. Ren, B. Li, C. Fan, and X. Liu, "Fluorographene with High Fluorine/Carbon Ratio: A Nanofiller for Preparing Low-κ Polyimide Hybrid Films," *ACS Appl. Mater. Interfaces*, vol. 6, no. 18, pp. 16 182–16 188, Sep. 2014.

[132] Y. Ono, Y. Hayashi, S.-h. Urashima, and H. Yui, "Glass etching with gaseous hydrogen fluoride: Rapid management of surface nano-roughness," *International Journal of Applied Glass Science*, vol. 13, no. 4, pp. 676–683, 2022.

[133] R. Fang, S. Zhao, Z. Sun, D.-W. Wang, H.-M. Cheng, and F. Li, "More Reliable Lithium-Sulfur Batteries: Status, Solutions and Prospects," *Advanced Materials*, vol. 29, no. 48, p. 1606823, 2017.

[134] J. Yan, Q. Wang, T. Wei, and Z. Fan, "Recent Advances in Design and Fabrication of Electrochemical Supercapacitors with High Energy Densities," *Advanced Energy Materials*, vol. 4, no. 4, p. 1300816, 2014.

[135] Q. Wang, J. Yan, and Z. Fan, "Carbon materials for high volumetric performance supercapacitors: Design, progress, challenges and opportunities," *Energy Environ. Sci.*, vol. 9, no. 3, pp. 729–762, Mar. 2016.

[136] B. Hariprakash, A. U. Mane, S. K. Martha, S. A. Gaffoor, S. A. Shivashankar, and A. K. Shukla, "A Low-Cost, High Energy-Density Lead/Acid Battery," *Electrochem. Solid-State Lett.*, vol. 7, no. 3, p. A66, Jan. 2004.

[137] P. Albertus, S. Babinec, S. Litzelman, and A. Newman, "Status and challenges in enabling the lithium metal electrode for high-energy and low-cost rechargeable batteries," *Nat Energy*, vol. 3, no. 1, pp. 16–21, Jan. 2018.

[138] J. Sun, B. Luo, and H. Li, "A Review on the Conventional Capacitors, Supercapacitors, and Emerging Hybrid Ion Capacitors: Past, Present, and Future," *Advanced Energy and Sustainability Research*, vol. 3, no. 6, p. 2100191, 2022.

[139] X. He and X. Zhang, "A comprehensive review of supercapacitors: Properties, electrodes, electrolytes and thermal management systems based on phase change materials," *Journal of Energy Storage*, vol. 56, p. 106023, Dec. 2022.

[140] T. Lin, I.-W. Chen, F. Liu, C. Yang, H. Bi, F. Xu, and F. Huang, "Nitrogen-doped mesoporous carbon of extraordinary capacitance for electrochemical energy storage," *Science*, vol. 350, no. 6267, pp. 1508–1513, Dec. 2015.

[141] J. Hou, C. Cao, F. Idrees, and X. Ma, "Hierarchical Porous Nitrogen-Doped Carbon Nanosheets Derived from Silk for Ultrahigh-Capacity Battery Anodes and Supercapacitors," *ACS Nano*, vol. 9, no. 3, pp. 2556–2564, Mar. 2015.

[142] Y. Zhu, S. Murali, M. D. Stoller, K. J. Ganesh, W. Cai, P. J. Ferreira, A. Pirkle, R. M. Wallace, K. A. Cychosz, M. Thommes, D. Su, E. A. Stach, and R. S. Ruoff, "Carbon-Based Supercapacitors Produced by Activation of Graphene," *Science*, vol. 332, no. 6037, pp. 1537–1541, Jun. 2011.

[143] A. Izadi-Najafabadi, S. Yasuda, K. Kobashi, T. Yamada, D. N. Futaba, H. Hatori, M. Yumura, S. Iijima, and K. Hata, "Extracting the Full Potential of Single-Walled Carbon Nanotubes as Durable Supercapacitor Electrodes Operable at 4 V with High Power and Energy Density," *Advanced Materials*, vol. 22, no. 35, pp. E235–E241, 2010.

[144] H. Saini, N. Srinivasan, V. Šedajová, M. Majumder, D. P. Dubal, M. Otyepka, R. Zbořil, N. Kurra, R. A. Fischer, and K. Jayaramulu, "Emerging MXene@Metal–Organic Framework Hybrids: Design Strategies toward Versatile Applications," *ACS Nano*, vol. 15, no. 12, pp. 18 742–18 776, Dec. 2021.

[145] V. Šedajová, P. Jakubec, A. Bakandritsos, V. Ranc, and M. Otyepka, "New Limits for Stability of Supercapacitor Electrode Material Based on Graphene Derivative," *Nanomaterials*, vol. 10, no. 9, p. 1731, Sep. 2020.

[146] B. E. Warren, "X-Ray Diffraction in Random Layer Lattices," *Phys. Rev.*, vol. 59, no. 9, pp. 693–698, May 1941.

[147] M. Shekhirev, C. E. Shuck, A. Sarycheva, and Y. Gogotsi, "Characterization of MXenes at every step, from their precursors to single flakes and assembled films," *Progress in Materials Science*, vol. 120, p. 100757, Jul. 2021.

[148] M. Anayee, N. Kurra, M. Alhabeb, M. Seredych, M. Nejib Hedhili, A.-H. Emwas, H. N. Alshareef, B. Anasori, and Y. Gogotsi, "Role of acid mixtures etching on the

surface chemistry and sodium ion storage in Ti 3 C 2 T x MXene," *Chemical Communications*, vol. 56, no. 45, pp. 6090–6093, 2020.

[149] D. K. Craig, R. J. Weir, W. Wagner, and D. Groth, "Subchronic Inhalation Toxicity of Dimethylformamide in Rats and Mice," *Drug and Chemical Toxicology*, vol. 7, no. 6, pp. 551–571, Jan. 1984.

[150] T. H. Kim and S. G. Kim, "Clinical Outcomes of Occupational Exposure to N,N-Dimethylformamide: Perspectives from Experimental Toxicology," *Safety and Health at Work*, vol. 2, no. 2, pp. 97–104, Jun. 2011.

[151] "COMMISSION REGULATION (EU) 2021/2030," Nov. 2021.

[152] Z.-y. Gao, W. Sun, and Y.-h. Hu, "Mineral cleavage nature and surface energy: Anisotropic surface broken bonds consideration," *Transactions of Nonferrous Metals Society of China*, vol. 24, no. 9, pp. 2930–2937, Sep. 2014.

[153] T. Fujii, F. M. F. Groot, G. A. Sawatzky, F. C. Voogt, T. Hibma, and K. Okada, "In situ XPS analysis of various iron oxide films grown by ${\mathrm{NO}}_{2}$-assisted molecular-beam epitaxy," *Phys. Rev. B*, vol. 59, no. 4, pp. 3195–3202, Jan. 1999.

[154] X. Lu, Y. Zeng, M. Yu, T. Zhai, C. Liang, S. Xie, M.-S. Balogun, and Y. Tong, "Oxygen-Deficient Hematite Nanorods as High-Performance and Novel Negative Electrodes for Flexible Asymmetric Supercapacitors," *Adv. Mater.*, vol. 26, no. 19, pp. 3148–3155, 2014.

[155] S. Chahal, S. M. Kauzlarich, and P. Kumar, "Microwave Synthesis of Hematene and Other Two-Dimensional Oxides," *ACS Mater. Lett.*, vol. 3, no. 5, pp. 631–640, May 2021.

[156] A. M. Smith, A. M. Mohs, and S. Nie, "Tuning the optical and electronic properties of colloidal nanocrystals by lattice strain," *Nature Nanotech*, vol. 4, no. 1, pp. 56–63, Jan. 2009.

[157] S. Maiti, K. Maiti, M. T. Curnan, K. Kim, K.-J. Noh, and J. Woo Han, "Engineering electrocatalyst nanosurfaces to enrich the activity by inducing lattice strain," *Energy & Environmental Science*, vol. 14, no. 7, pp. 3717–3756, 2021.

[158] S. Wang, T. Zhao, J. Chen, A. Missyul, L. Simonelli, L. Liu, F. Li, X. Kong, and W. Hua, "Accumulated Lattice Strain as an Intrinsic Trigger for the First-Cycle Voltage Decay in Li-Rich 3d Layered Oxides," *ACS Appl. Mater. Interfaces*, vol. 15, no. 16, pp. 20 200–20 207, Apr. 2023.

[159] L. Hou, Z. Li, H. Jang, Y. Wang, X. Cui, X. Gu, M. G. Kim, L. Feng, S. Liu, and X. Liu, "Electronic and Lattice Engineering of Ruthenium Oxide towards Highly Active and Stable Water Splitting," *Advanced Energy Materials*, vol. 13, no. 22, p. 2300177, 2023.

[160] B. Gilbert, F. Huang, H. Zhang, G. A. Waychunas, and J. F. Banfield, "Nanoparticles: Strained and Stiff," *Science*, vol. 305, no. 5684, pp. 651–654, Jul. 2004.

[161] J. Srisuriyachot, S. A. M. McNair, Y. Chen, T. Barthelay, R. Gray, J. Bénézech, I. P. Dolbnya, R. Butler, and A. J. G. Lunt, "Carbon fibre lattice strain mapping via microfocus synchrotron X-ray diffraction of a reinforced composite," *Carbon*, vol. 200, pp. 347–360, Nov. 2022.

[162] M. K. Ozturk, E. Arslan, İ. Kars, S. Ozcelik, and E. Ozbay, "Strain analysis of the GaN epitaxial layers grown on nitridated Si(111) substrate by metal organic chemical vapor deposition," *Materials Science in Semiconductor Processing*, vol. 16, no. 1, pp. 83–88, Feb. 2013.

[163] K. R. Desai, S. T. Alone, S. R. Wadgane, S. E. Shirsath, K. M. Batoo, A. Imran, E. H. Raslan, M. Hadi, M. F. Ijaz, and R. H. Kadam, "X-ray diffraction based Williamson–Hall analysis and rietveld refinement for strain mechanism in Mg–Mn co-substituted CdFe2O4 nanoparticles," *Physica B: Condensed Matter*, vol. 614, p. 413054, Aug. 2021.

[164] B. Goris, J. De Beenhouwer, A. De Backer, D. Zanaga, K. J. Batenburg, A. Sánchez-Iglesias, L. M. Liz-Marzán, S. Van Aert, S. Bals, J. Sijbers, and G. Van Tendeloo, "Measuring Lattice Strain in Three Dimensions through Electron Microscopy," *Nano Lett.*, vol. 15, no. 10, pp. 6996–7001, Oct. 2015.

[165] G. Argentero, A. Mittelberger, M. Reza Ahmadpour Monazam, Y. Cao, T. J. Pennycook, C. Mangler, C. Kramberger, J. Kotakoski, A. K. Geim, and J. C. Meyer, "Unraveling the 3D Atomic Structure of a Suspended Graphene/hBN van der Waals Heterostructure," *Nano Lett.*, vol. 17, no. 3, pp. 1409–1416, Mar. 2017.

[166] A. Ishizuka, M. Hytch, and K. Ishizuka, "STEM moiré analysis for 2D strain measurements," *Journal of Electron Microscopy*, vol. 66, no. 3, pp. 217–221, Jun. 2017.

[167] L. Jones, S. Wenner, M. Nord, P. H. Ninive, O. M. Løvvik, R. Holmestad, and P. D. Nellist, "Optimising multi-frame ADF-STEM for high-precision atomic-resolution strain mapping," *Ultramicroscopy*, vol. 179, pp. 57–62, Aug. 2017.

[168] Y. L. Tang, Y. L. Zhu, and X. L. Ma, "On the benefit of aberration-corrected HAADF-STEM for strain determination and its application to tailoring ferroelectric domain patterns," *Ultramicroscopy*, vol. 160, pp. 57–63, Jan. 2016.

[169] U. Ludacka, M. R. A. Monazam, C. Rentenberger, M. Friedrich, U. Stefanelli, J. C. Meyer, and J. Kotakoski, "In situ control of graphene ripples and strain in the electron microscope," *npj 2D Mater Appl*, vol. 2, no. 1, pp. 1–6, Aug. 2018.

[170] J. C. Meyer, A. K. Geim, M. I. Katsnelson, K. S. Novoselov, T. J. Booth, and S. Roth, "The structure of suspended graphene sheets," *Nature*, vol. 446, no. 7131, pp. 60–63, Mar. 2007.

[171] N. S. Lewis and D. G. Nocera, "Powering the planet: Chemical challenges in solar energy utilization," *Proc. Natl. Acad. Sci.*, vol. 103, no. 43, pp. 15 729–15 735, Oct. 2006.

[172] H. Wang, J. Chen, Y. Lin, X. Wang, J. Li, Y. Li, L. Gao, L. Zhang, D. Chao, X. Xiao, and J.-M. Lee, "Electronic Modulation of Non-van der Waals 2D Electrocatalysts for Efficient Energy Conversion," *Adv. Mater.*, vol. 33, no. 26, p. 2008422, Jul. 2021.

[173] W. I. F. David, J. W. Makepeace, S. K. Callear, H. M. A. Hunter, J. D. Taylor, T. J. Wood, and M. O. Jones, "Hydrogen Production from Ammonia Using Sodium Amide," *J. Am. Chem. Soc.*, vol. 136, no. 38, pp. 13 082–13 085, Sep. 2014.

[174] A. Iwase, K. Ii, and A. Kudo, "Decomposition of an aqueous ammonia solution as a photon energy conversion reaction using a Ru-loaded ZnS photocatalyst," *Chem. Commun.*, vol. 54, no. 48, pp. 6117–6119, 2018.

[175] M. Reli, M. Edelmannová, M. Šihor, P. Praus, L. Svoboda, K. K. Mamulová, H. Otoupalíková, L. Čapek, A. Hospodková, L. Obalová, and K. Kočí, "Photocatalytic H2 generation from aqueous ammonia solution using ZnO photocatalysts prepared by different methods," *Intl. J. Hydrog. Energy*, vol. 40, no. 27, pp. 8530–8538, Jul. 2015.

[176] Y. Shu, J. Ji, M. Zhou, S. Liang, Q. Xie, S. Li, B. Liu, J. Deng, J. Cao, S. Liu, and H. Huang, "Selective photocatalytic oxidation of gaseous ammonia at ppb level over Pt and F modified TiO2," *Appl. Catal. B*, vol. 300, p. 120688, Jan. 2022.

[177] J. Tauc, R. Grigorovici, and V. Vancu, "Optical properties and electronic structure of amorphous germanium," *Phys. Status Solidi*, vol. 15, pp. 627–637, 1966.

[178] P. Makuła, M. Pacia, and W. Macyk, "How To Correctly Determine the Band Gap Energy of Modified Semiconductor Photocatalysts Based on UV–Vis Spectra," *J. Phys. Chem. Lett.*, vol. 9, no. 23, pp. 6814–6817, Dec. 2018.

[179] S. Cao and L. Piao, "Considerations for a More Accurate Evaluation Method for Photocatalytic Water Splitting," *Angew. Chem.*, vol. 132, no. 42, pp. 18 468–18 476, Oct. 2020.

[180] M. Qureshi and K. Takanabe, "Insights on Measuring and Reporting Heterogeneous Photocatalysis: Efficiency Definitions and Setup Examples," *Chem. Mater.*, vol. 29, no. 1, pp. 158–167, Jan. 2017.

Appendix A

RESEARCH ARTICLE

ADVANCED FUNCTIONAL MATERIALS
www.afm-journal.de

Covalently Interlinked Graphene Sheets with Sulfur-Chains Enable Superior Lithium–Sulfur Battery Cathodes at Full-Mass Level

Iosif Tantis, Aristides Bakandritsos, Dagmar Zaoralová, Miroslav Medveď, Petr Jakubec, Jana Havláková, Radek Zbořil,* and Michal Otyepka**

Sulfur represents a low-cost, sustainable, and high theoretical capacity cathode material for lithium–sulfur batteries, which can meet the growing demand in portable power sources, such as in electric vehicles and mobile information technologies. However, the shuttling effect of the formed lithium polysulfides, as well as their low conductivity, compromise the electrochemical performance of lithium–sulfur cells. To tackle this challenge, a so far unexplored cathode, composed of sulfur covalently bonded directly on graphene is developed. This is achieved by leveraging the nucleophilicity of polysulfide chains, which react readily with the electrophilic centers in fluorographene, as experimental and theoretical data unveil. The reaction leads to the formation of carbon–sulfur covalent bonds and a particularly high sulfur content of 80 mass%. Owing to these features, the developed cathode exhibits excellent performance with only 5 mass% of conductive carbon additive, delivering very high full-cathode-mass capacities and rate capability, combined with superior cycling stability. In combination with a fluorinated ether as electrolyte additive, the capacity persists at ≈700 mAh g^{-1} after 100 cycles at 0.1 C, and at ≈644 mAh g^{-1} after 250 cycles at 0.2 C, keeping ≈470 mAh g^{-1} even after 500 cycles.

1. Introduction

Lithium–ion batteries are electrochemical rechargeable energy storage systems leading the battery market of portable electronics for telecommunications and information processing since the 1990's, after the first commercial cell was introduced by Sony corporation.[1,2] With the rapid development and broad application of mobile devices, electric and unmanned vehicles, as well as with the rise of smart grids and networks for "the internet of things," the demand for batteries with higher performance and lower cost is rapidly growing.[3,4] Lithium–sulfur batteries (LSBs) could offer a promising alternative for energy storage because of the high theoretical capacity (1672 mAh g^{-1}) and specific energy (2600 Wh kg^{-1}).[5–8] Moreover, sulfur is environmentally friendly and a key byproduct of the petroleum industry, with attractive features for commercialization, such as abundance and low cost.[9–12] However, several bottlenecks hamper the practical development of the LSBs,[13,14] including the sulfur's poor conductivity, its large volume change, and the "shuttling-effect" of lithium polysulfides (PSs), formed during the charge/discharge process.[15] The dissolution of these lithium PSs (Li_2S_n, $n \geq 4$) into the liquid electrolyte leads to low Coulombic efficiency, poor sulfur utilization, fast capacity fading, and other parasitic reactions with the Li anode.[16,17]

To address these challenges, different strategies emerged in the past few years for the development of advanced composite cathodes designed for high sulfur utilization and stability. In particular, pinning of sulfur in engineered materials acting as

Dr. I. Tantis, Dr. A. Bakandritsos, D. Zaoralová, Dr. M. Medveď, Dr. P. Jakubec, J. Havláková, Prof. R. Zbořil, Prof. M. Otyepka
Regional Centre of Advanced Technologies and Materials
Czech Advanced Technology and Research Institute
Palacký University
Křížkovského 511/8, Olomouc 77900, Czech Republic
E-mail: a.bakandritsos@upol.cz; radek.zboril@upol.cz
michal.otyepka@upol.cz

The ORCID identification number(s) for the author(s) of this article can be found under https://doi.org/10.1002/adfm.202101326.

DOI: 10.1002/adfm.202101326

Dr. A. Bakandritsos, Prof. R. Zbořil
Nanotechnology Centre
Centre of Energy and Environmental Technologies
VŠB-Technical University of Ostrava
17. listopadu 2172/15, Ostrava-Poruba 70800, Czech Republic

D. Zaoralová
Department of Physical Chemistry
Faculty of Science
Palacký University Olomouc
17. listopadu 1192/12, Olomouc 77900, Czech Republic

J. Havláková
Department of Experimental Physics
Faculty of Science
Palacký University Olomouc
17. listopadu 1192/12, Olomouc 77900, Czech Republic

high-affinity hosts for sulfur and development of functional separators which hinder the shuttling of lithium PSs have been pursued.[18–22] In this frame, nanostructured carbon-based materials are intensively explored as sulfur hosts because of their lightweight nature, good electrical conductivity, large surface area, and excellent mechanical properties.[23–25] In a pioneering work, an ordered mesoporous carbon was exploited to encapsulate sulfur in order to improve its utilization and restrain the shuttling-effect of the lithium-PS species.[12] However, such pure carbon hosts, although being porous, suffer from sluggish cycling stability due to the weak interactions between the PSs and the carbon surface. Therefore, the design and development of new nanocarbons with sulfur-binding surface groups is essential.[26,27] Such functional groups can offer strong anchoring sites for the robust immobilization of the sulfur and PS species, effectively limiting the shuttling-effect during charging/discharging for long and stable lifecycle.[28,29] In addition, nanocarbons, especially carbon nanotubes and graphene, may not only act as sulfur hosts, but can also mitigate its low electrical conductivity and improve the mechanical properties.[30–34] However, most of the reported strongly immobilized or covalently-bonded sulfur cathodes have achieved low cycle-life, low sulfur loading contents, or were obtained on nonconductive matrices (e.g., polymers or amorphous carbons), necessitating the addition of high amounts of conductive, but electrochemically inactive additives, and thus, eventually, limiting the true (i.e., total mass-based) cathode capacities (Table S1, Supporting Information). Therefore, the strong covalent bonding of sulfur on conductive materials, affording cathodes with appropriately high sulfur loading, is challenging but essential for leveraging the full potential of LSBs and high utilization of sulfur.

In this work, we report the successful development of a graphene-sulfur cathode with very high sulfur loading, whereby the sulfur chains are immobilized by covalent bonding to graphene. The loading in covalent-sulfur reached an unprecedented 80 mass%, increasing the full-cell specific capacity and, importantly, limiting the shuttling-effect even at very low specific currents, thus ascribing outstanding cycling stability. Moreover, achieving such a high covalent-sulfur loading on graphene instead of graphene oxide or porous/amorphous carbons did not compromise the cathode's electrical conductivity and thus allowed operation with a very low content of conductive, but electrochemically inactive additives. Accessing such highly and covalently sulfur-derivatized graphene was only possible via the rich chemistry of fluorographene (FG),[35,36] exploiting the high electrophilicity and chain-propagating reactivity of its carbon-centered radicals.[36,37] Remarkably, the use of sodium polysulfide (NaPS) and FG (instead of elemental sulfur, metal sulfides, or graphene) was discovered as a unique pathway, offering adequately nucleophilic centers at the PS chain ends, reacting effectively and extensively with the respective electrophilic carbon sites developed through defluorination of FG, affording a densely sulfurized graphene cathode.

2. Results and Discussion

Recently, it was shown that the use of strong nucleophiles in aprotic solvents is a very effective way of FG functionalization through nucleophilic attack, initiated on the electrophilic radical centers at the defect sites of FG.[37,38] Because the nucleophile delivers a negative charge, the neighboring C—F bonds become susceptible to heterolytic cleavage, promoting the next step of defluorination and substitution.[37,38] Here, we explored the strong nucleophilicity of PS ions (demonstrated by their ability to attack the electrophilic carbons of alkylhalides[39,40] according to the [X–R–X + Na_2S_x accord$_n$ + 2NaX] pathway), but applied for the first time in the reaction with FG in *N*-methyl-2-pyrrolidone (NMP) at 80 °C (**Figure 1**a, and Experimental Section). FT-IR analysis of the purified reaction product (graphene-polysulfide, GPS), unveiled the development of covalent C—S bonds, and the extensive defluorination of FG (Figure 1b). In particular, the C—F band of FG at ≈1200 cm^{-1} decreased and a new band at ≈1580 cm^{-1} emerged in GPS due to the aromatic ring stretching, indicating the successful defluorination and the formation of conjugated C=C bonds, respectively.[41] Importantly, the band at ≈1150 cm^{-1} demonstrated the development of covalent C—S bonds (stretching vibration).[42] In contrast, the spectrum of a control sample obtained after a reaction of FG with elemental sulfur (GS, Figure 1b) showed a very intense C—F band and no C—S vibrations, while the strong S—S bands originated from deposited elemental sulfur. The high sulfur content in the GS control sample, as IR suggests, is only due to weak sulfur interactions with FG. Indeed, a treatment of GS with carbon disulfide—a very good solvent for sulfur—clearly demonstrated the sulfur-leaching in GS, unlike covalent GPS (Figure S1a, Supporting Information). A dramatic difference on the stability was also clearly demonstrated in the electrochemical testing of the two materials, as discussed later. The spectra of the starting NaPS and sulfur are also shown in Figure 1b, confirming the absence of the C—S vibration band at 1150 cm^{-1} which was only observed in the case of the GPS product.

The sulfur content for each sample was determined via thermogravimetric analysis (TGA, Figure 1c), based on the mass loss between 200 and 350 °C.[43] Accordingly, ≈80 and ≈85 mass% of sulfur was found for GPS and GS, respectively. Lower sulfur loading could be achieved by reaction of FG with a lower amount of NaPS with respect to the FG and/or by a shorter reaction time. On the other hand, the lower content in PSs would also lead to higher content in fluorine atoms, since both processes, that is, defluorination and substitution, occur simultaneously (as discussed below). The higher content in fluorine atoms is, however, undesirable because C—F bonds increase the band gap of graphene and hinder the material's electrical conductivity.[44] Another control reaction (identical to the reaction for obtaining GPS but using electrochemically exfoliated graphene instead of FG) showed only 5 at.% sulfur content (product EEGS, Figure S1b, Supporting Information), corroborating the important role of FG for developing covalent bonding of NaPS chains to graphene. Evolved gas analysis (EGA) with mass spectroscopy for the GS and GPS materials during TGA under air (Figure 1d) showed that the SO and SO_2 evolution profiles were wider for GPS than for GS, indicating stronger interaction with graphene in the former case, due to the covalent bonding of PSs on the graphene skeleton, in line with the IR analysis. Furthermore, the TGA thermogram from GPS showed a smooth transition point to the mass-stable

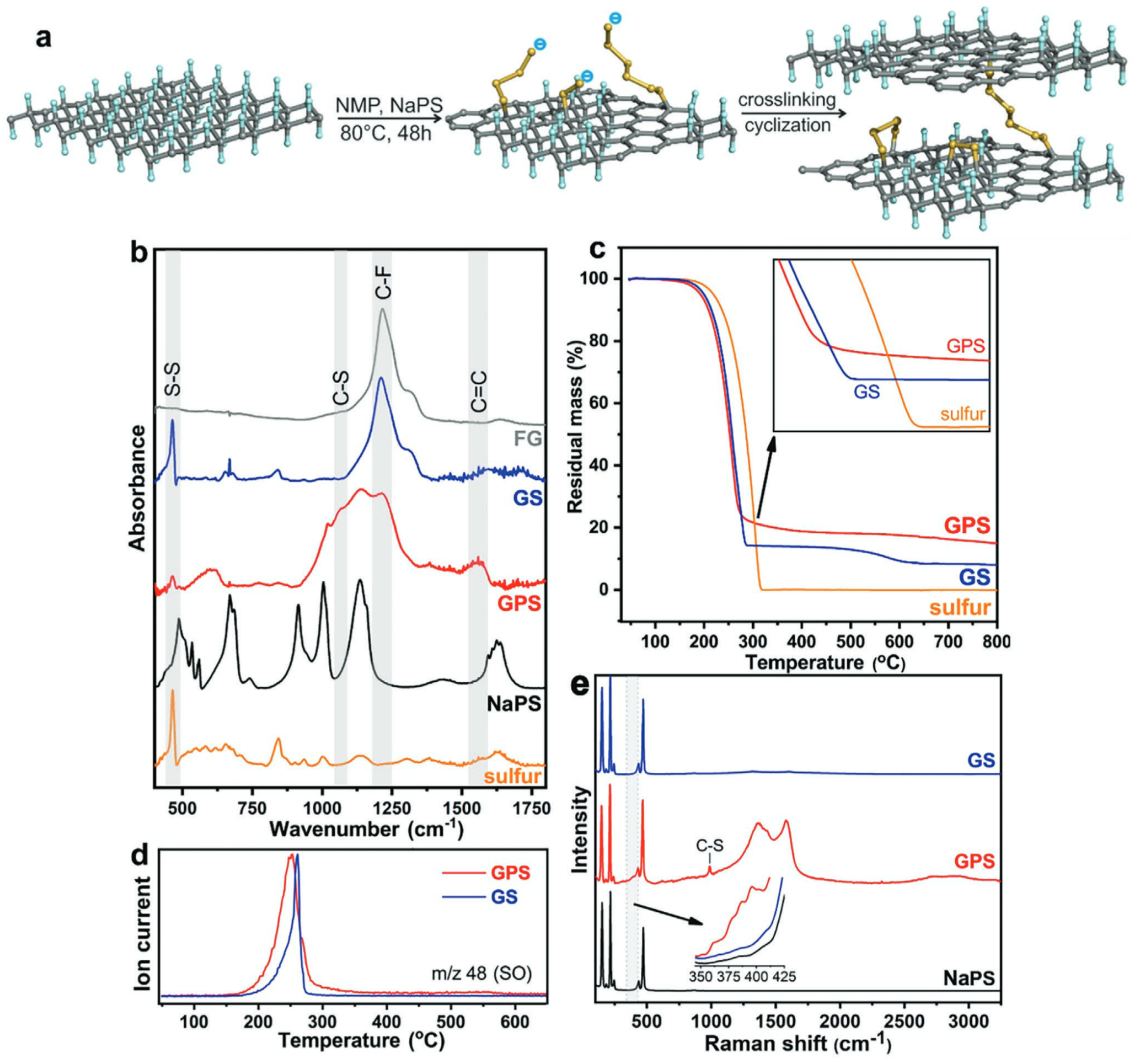

Figure 1. a) Reaction scheme for covalent binding of sodium polysulfide (NaPS) to fluorographene (FG) leading to graphene-polysulfide (GPS), b) FTIR spectra for elemental sulfur, NaPS, GPS, the sulfur-reacted FG derivative (GS), and the starting FG, c) thermograms of sulfur, GS, and GPS. d) Evolved gas analysis with mass spectrometry for SO and SO_2 fragments during TGA of GS and GPS (normalized ion currents at maximum) and e) Raman spectra of GS, GPS, and NaPS.

region after total sulfur loss, in contrast to a sharp transition point observed for GS and elemental sulfur samples (Figure 1c, and inset). The smooth transition point is an indirect evidence of sulfur trapping or covalent immobilization on surfaces,[32,45] corroborating the direct evidence of the C—S bonds obtained from the IR spectra.

The successful covalent sulfur-functionalization of FG via its reaction with NaPS was also confirmed by Raman spectroscopy (Figure 1e). The GS, GPS, and NaPS spectra showed the characteristic S—S bonds from the NaPS chains at 149, 212, and 470 cm^{-1} (ref. [46]), while in EEGS the S—S bonds were present only at noise level (Figure S1c, Supporting Information). It is noted that FG does not have any Raman peaks due to the absence of aromatic rings and high fluorescence.[36] Importantly, GPS showed two peaks at 395 and 987 cm^{-1} (Figure 1e, and inset), corresponding to covalent C—S bending and stretching vibrations, respectively.[47,48] In contrast, they were absent in NaPS and GS, verifying further the presence of covalent C—S bonds between the PS chain ends on the graphenic skeleton of GPS. Furthermore, GPS exhibited the characteristic D and G bands at around 1330 and 1580 cm^{-1}, respectively, due to the restoration of the aromatic network[49] after the defluorination. The ratio of I_D and I_G band intensities for GPS was 0.96, which along with the broadening of the bands, demonstrated a high degree of graphene functionalization.[50]

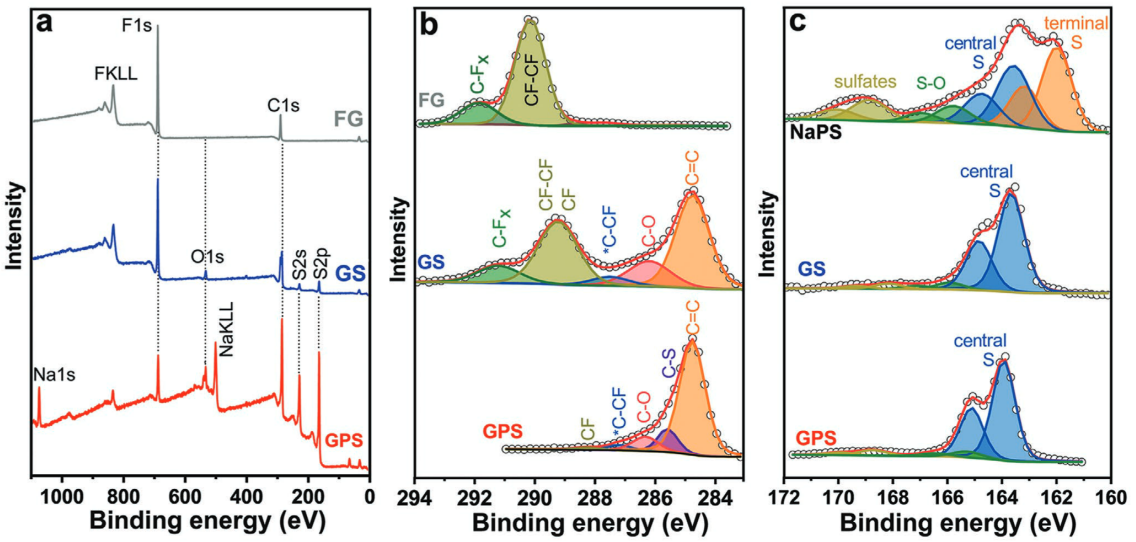

Figure 2. a) XPS survey spectra of GPS, GS, and pristine FG, b) C 1s HR-XPS spectra of pristine FG, GPS, and GS, respectively and c) S 2p HR-XPS spectra of pristine NaPS, GPS, and GS, respectively.

X-ray photoelectron spectroscopy (XPS) spectra confirmed the high sulfur content in GPS and the drastically reduced F 1s peak, indicated the efficacy of the reaction through the substitution–defluorination propagation pathway (**Figure 2**a,b). The Na 1s peak was also observed due to a few unreacted PS chain ends, as discussed below. More specifically, the deconvoluted C 1s spectra of pristine FG (Figure 2b) displayed two components at 290.1 eV due to CF—CF and at ≈291.8 eV due to C—F_x.[44,51] On the other hand, the C 1s region of GPS showed a dominant component at 284.8 eV corresponding to graphitic sp^2 carbons, while the C—F components practically disappeared, explaining the low F content (Table S2, Supporting Information). Another component emerged at 285.6 eV corresponding to carbons covalently bonded to sulfur.[32] In antithesis, the various covalent CF components were preserved at a significantly high extent in GS (Figure 2b), indicating that sulfur did not effectively react with FG in this case, but mostly deposited on the surface through weak interactions.[52] The S 2p spectrum of GPS, indicated strong modification of the electronic density distribution of the PS chains after the functionalization reaction, in comparison to the starting NaPS (Figure 2c). In particular, NaPS displayed four doublets at 162.0 eV (terminal S atoms), 163.5 eV (central S atoms), and 165.8 and 168.9 eV due to small amount of oxidized sulfur and sulfates, respectively.[53] On the other hand, the terminal S component was drastically reduced in GPS, indicating that a cyclization and crosslinking reaction took place, retaining only a few unmodified PS ends in the product. Control samples confirmed the extremely low sulfur content in EEGS (1.6. at.%, Table S2 and Figure S1d, Supporting Information), further indicating the necessity of the synergy between the strong nucleophilic centers in NaPS and reactive electrophilic sites in FG, for the reaction to proceed.[54]

The morphology of GPS corresponded to few-layered graphene sheets densely covered by sulfur, as observed with scanning electron microscopy (SEM, **Figure 3**a). Further inspection with high-resolution transmission electron microscopy (HR-TEM, Figure 3b) showed few-layered graphene sheets with high content of sulfur, as energy-dispersive X-ray spectroscopy (EDS, Figure 3b, inset) and chemical mapping (Figure 3c,d) indicated. It is also worth noting that the sulfur/carbon rich and poor regions perfectly coincided (e.g., arrows in Figure 3e,f), providing further evidence that sulfur was intimately bonded to graphene, without forming independent sulfur-rich areas. Even after 250 charge/discharge cycles and thorough washing, the SEM of the cathode showed that the distribution of sulfur on the sheets was fully preserved (Figure 3g,h).

To provide mechanistic insight into the formation of covalent C—S bonds during the reaction of NaPS with FG, the nucleophilic attack of short PS chains (S_x^{2-}, $x = 2$, 4, and 6) on various FG structures (**Figure 4**a-c; Figures S2-S4, Supporting Information) was explored by density functional theory (DFT) calculations. Interestingly, unlike in the case of smaller nucleophiles,[37,38] a direct attack of PS on single atomic radical centers in highly fluorinated graphenes was not found energetically favorable, due to sterical hindrance from the neighboring fluorine atoms carrying partial negative charge. However, the low ionization energy of PS chains and relatively high electron affinity of the FG radical centers (Table S3, Supporting Information) suggest that a defluorination reaction can be initiated by electron transfer from the PS chains to the radical centers of FG.[37] NMP solvent can also trigger defluorination of FG,[55] as also shown here in the FT-IR and Raman spectra of the pristine FG and the FG after 24 h treatment in NMP at 80 °C (Figure S5a,b, Supporting Information). Indeed, the nucleophilic attack of PS chains became more favorable on the larger defluorinated graphene domains (Figure 4a–c; Figures S2–S4, Supporting Information), which exhibit electrophilic character in the vicinity of C—F bonds showing increasing susceptibility of FG to the

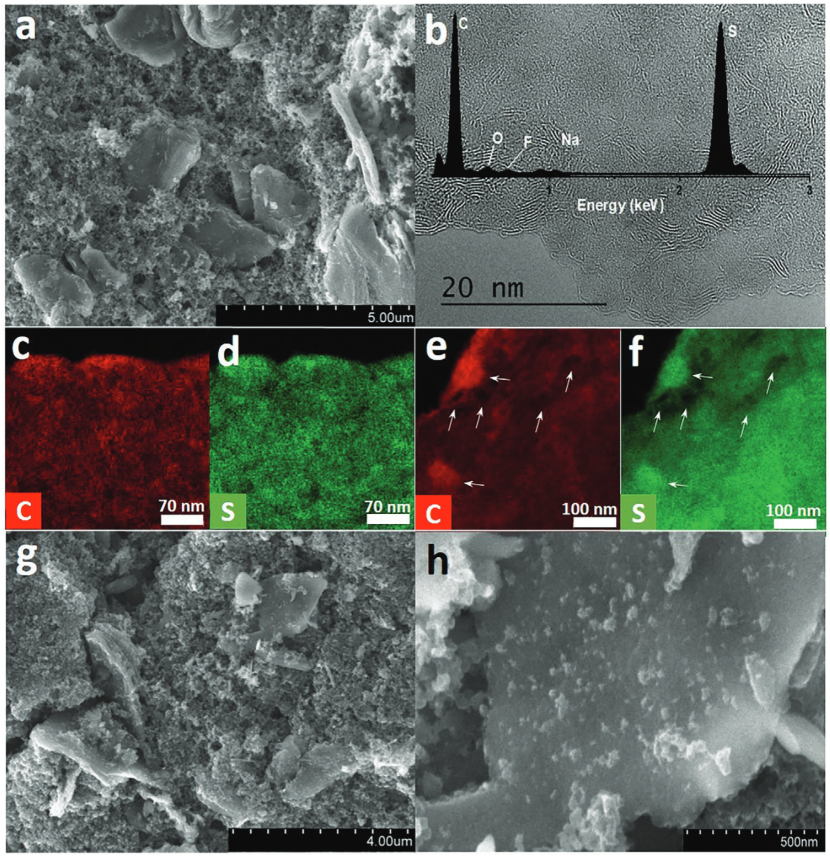

Figure 3. a) SEM image of a GPS electrode before testing and b) HR-TEM image of the GPS material (with EDS spectra in inset). c–f) Carbon and sulfur EDS maps of GPS at two different areas. Arrows on panels e,f) highlight the perfect overlap of sulfur and carbon rich or poor regions. g,h) SEM images of the GPS material after testing 250 charge per discharge cycles.

PS nucleophilic attack with decreasing fluorine content. The formation of a C—S bond and the charge transfer from PS to FG caused spontaneous detachment of a fluoride ion from the substrate. Importantly, the free end of the PS chain could act as a nucleophile in subsequent reaction steps leading either to crosslinking of graphene sheets (in the case of longer chains) or to cyclization (in the case of short chains, Figure 4d).

In order to evaluate the electrochemical performance of GPS, cathode electrodes were prepared by doctor blading of a paste containing 90% GPS as active material. Since GPS contains few-layered graphene (rather than graphene oxide or other non-conductive carbon matrices), the need of conductive additive was limited to only 5 mass%, which is of key importance toward high full-cathode-mass capacities. The final cathode was evaluated against lithium metal in an 1 M lithium bis(trifluoromethanesulfonyl)imide (LiTFSI) electrolyte dissolved in dioxolane (DOL) mixture with a fluorinated ether (TTE, 1,1,2,2-tetrafluoroethyl 2,2,3,3-tetrafluoropropyl ether, known to limit the solubility of lithium PSs[56]). Cyclic voltammetry of GPS (**Figure 5**a) at 0.1, 0.2, and 0.5 mV s^{-1} showed a broad anodic peak during charging, and a two-step sulfur reduction, similar to DOL/DME (dimethoxy ethane, Figure S6, Supporting Information). The oxidation of the cathode was completed in two stages, with the broad peak at ≈2.45 V representing the conversion of Li_2S_{1-2} to Li_2S_n ($n > 2$) and the formation of elemental sulfur. The reduction was also completed in two clearly separated steps: the peak at 2.25 V is ascribed at the reduction of elemental sulfur to Li_2S_n ($4 \le n \le 8$) while the peak at 1.7 V corresponds to the subsequent reduction of Li_2S_n to Li_2S_{1-2}.[57] A typical charge/discharge curve of a LSB consists of two plateaus during discharge. The first one corresponds to a solid (S_8) → liquid (Li_2S_n) transition with a theoretical capacity of 418 mAh g^{-1} while the second discharge plateau corresponds to further reduction of lithium PSs to Li_2S_2/Li_2S with a theoretical capacity of 1254 mAh g^{-1}.[58] On the other hand, short sulfur chain cycling is performed through a solid-solid phase transition from S to Li_2S having only one discharge plateau at ≈1.8 V.[59] In the present case the discharge curve of GPS combines the typical long-sulfur-chain LSB characteristics with the short sulfur chain discharge plateau (Figure 5b). Interestingly, as it was shown by the theoretical calculations, both short and longer chains of PSs can react covalently with the

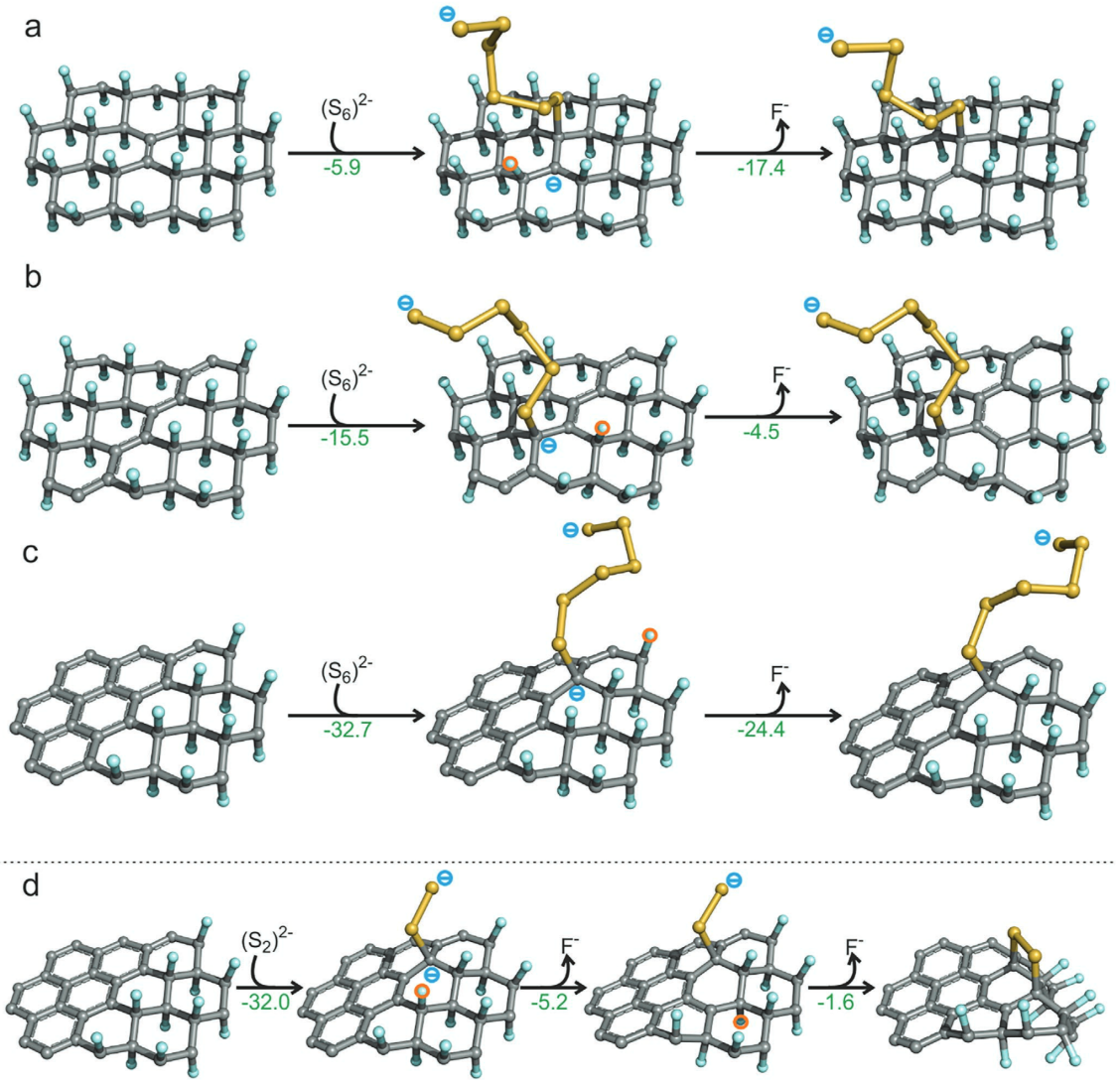

Figure 4. a–c) Nucleophilic attack of $(S_6)^{2-}$ on FG with different level of defluorination. d) Nucleophilic attack of $(S_2)^{2-}$ on the edge of fluorinated and defluorinated areas of FG resulting in a cyclized structure of the PS chain. Fluorine atoms detached in the next reaction step are marked by an orange circle. Reaction energies are in kcal·mol^{-1}. Carbon atoms are grey, fluorine blue, and sulfur yellow. Hydrogen atoms on edges of model molecules are hidden for clarity.

graphene backbone (Figure 4). Therefore, the discharge plateaus at 2.3 and ≈2 V are related with the longer sulfur chains while the discharge plateau at ≈1.8 V corresponds to the short sulfur chain phase transition ($S_{2-4} \rightarrow S^{2-}$). The reduction peak potential values are down-shifted compared to DOL/DME solvent due to the low lithium PS solubility in TTE, leading to controlled Li_2S precipitation.[60] The electrochemical profiles recorded during the galvanostatic charging/discharging of the GPS cathode were well maintained for more than 50 cycles at a specific current of 0.1 C (167 mA g^{-1}, Figure 5b), owing to the high electrochemical reversibility. Upon cycling, the plateau contribution from the short sulfur chains increased at the expense of the long sulfur chains, indicating a disproportionation of the long chains to shorter ones, along with some Li_2S_n losses in the electrolyte. This can also account for the small capacity fade in the subsequent cycles. The stability of GPS was outstanding for both high and low specific currents; the initial capacities of 636 mAh g^{-1} (1 C), 930 mAh g^{-1} (0.2 C), and 920 mAh g^{-1} (0.1 C) were maintained at 470 mAh g^{-1} after 500 cycles, 644 mAh g^{-1} after 250 cycles, and >700 mAh g^{-1} after

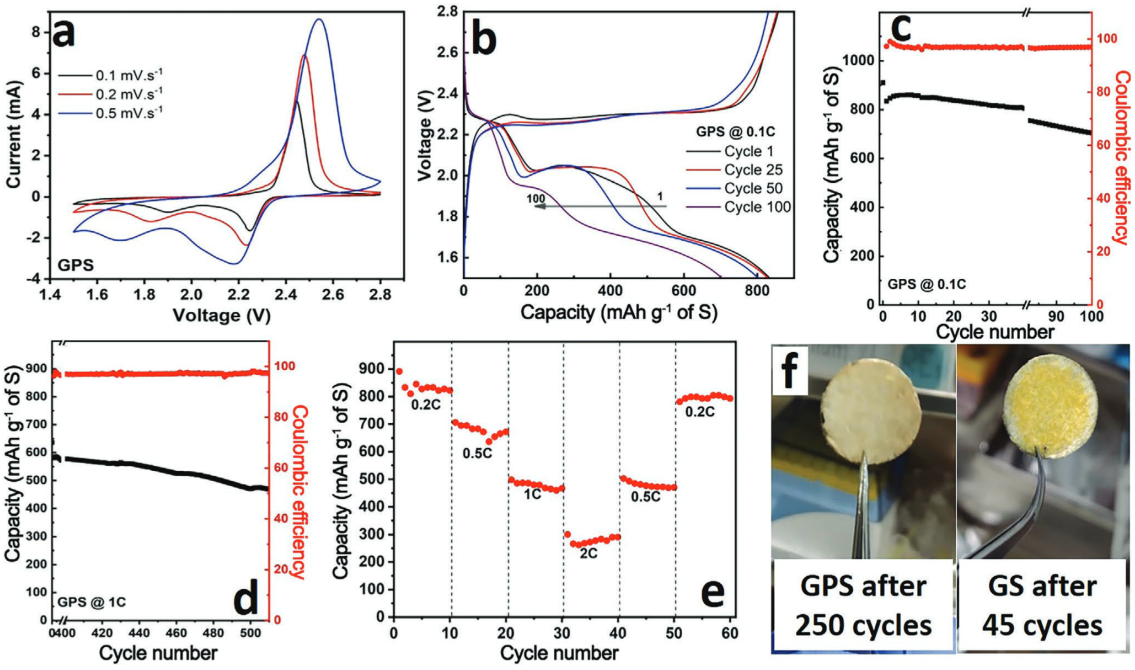

Figure 5. Electrochemical performance of the GPS cathode against lithium metal in 1 M LiTFSI in 1:1 DOL:TTE electrolyte. a) CV curves at 0.1, 0.2, and 0.5 mV g^{-1}, b) charge/discharge profiles at 0.1 C, c,d) cycling performance at different C-rates, e) rate capability at rates varied from 0.2 to 2 C, and f) photos of the glass fiber separator after cycling for the GPS and GS cathodes (1 C = 1672 mA g^{-1}). The specific capacities in the figure refer to the sulfur-based mass.

100 cycles, respectively (Figure 5c,d; Figure S7, Supporting Information). The 700 mAh g^{-1} value corresponds to 630 mAh g^{-1} with respect to the active material (90% GPS content), and 507 mAh g^{-1} with respect to the whole cathode material mass (Table S1, Supporting Information). The cathode was also endowed with excellent rate capability (Figure 5e), with capacities of 485 mAh g^{-1} at 1 C (1.67 A g^{-1}) and 290 mAh g^{-1} even at 2 C (3.3 A g^{-1}). Importantly, after the rate capability test, the cathode regained its initial capacity of ≈800 mAh g^{-1}, when the C-rate returned back at 0.2 C (Figure 5e).

The above results were attainable only in the case of GPS, since the non-covalent GS derivative obtained with elemental sulfur showed very low initial capacity of 380 and ≈260 mAh g^{-1} after only 15 cycles at 1 C (Figure S8, Supporting Information), tested under the same conditions as the GPS cathode. Moreover, the initial Coulombic efficiency was 108%, indicating a very strong shuttling-effect during the first charge.[61] The dissolution of the yellow elemental sulfur was also clearly visible in the glass fiber separator after 45 cycles of the GS cathode (Figure 5f), in contrast to the case of GPS.

To interpret the results in perspective with the current state of the art, a comparison between the GPS cathode and other sulfur-based materials studied in LSBs was necessary (Table S1, Supporting Information). The capacity values were calculated with respect to the total mass of the cathode material containing all additives and non-active components, at the last recorded cycle, which is beneficial for evaluating better their practical application potential. Most of the so far developed cathodes required high amounts of conductive additives (e.g., 20 mass%, ref. [62–65] 10 mass%, ref. [66–69]), or/and could sustain only low sulfur loadings,[25,63,64,66–70] thus compromising the full-cathode-mass capacity. For example, Zhou et al.[67] achieved 600 mAh g^{-1} at 0.5 C, which translated into 220 mAh g^{-1} with respect to full cathode mass, since the sulfur content was limited at 46 mass%. Similarly, Zheng et al.[71] reported an outstanding capacity of 775 mAh g^{-1} after 150 cycles, but this value reduced to 400 mAh g^{-1} with respect to full cathode mass. In another instance, carbonized metal organic framework crystals to trap sulfur in the pores, interwoven with carbon nanotubes to increase conductivity, delivered 650 mAh g^{-1} at 0.2 C, but only 260 mAh g^{-1} with respect to full cathode mass.[25] In addition, the use of nonconductive metal oxides (MgO,[62] or $BaTiO_3$[64]) to capture the lithium PSs resulted to 60–66% sulfur loading, but a 20% conductive binder was necessary. Furthermore, quite often, multistep and high temperature procedures were required, increasing the cost and environmental impact of the products.[24,29,70,72–75] For example, Zhang et al.[29] reported carbon nanocages as a sulfur host achieving 77 mass% sulfur loading and good electrochemical performance. However, the synthetic procedure required the preparation of graphene oxide, reduction with hydrazine, immobilization of a polymer, growth of iron oxide nanoparticles, high temperature hydrothermal treatment for 15 h, calcination at 800 °C, and acidic dissolution of the inorganic particles, before the loading of sulfur

through additional steps. Therefore, the herein GPS cathode presented very high full-cathode-mass capacities and rate capability combined with outstanding cycling stability (464 mAh g^{-1} after 250 cycles at 0.2 C), attained through a particularly simple, one-step procedure, via the chemical reaction of FG with NaPS in NMP at 80 °C. Importantly, these features were attained at a controlled low-temperature of 25 °C, unlike other top-rated materials whose performance is not yet connected with specific temperature conditions.[32,74–76] This is of particular importance since the usually fluorinated electrolytes or additives used in LSBs are of high viscosity, thus small temperature differences induce dramatic changes on the capacities recorded.[77,78] It should be emphasized that for the reaction there was no size-selection procedure after the sonication of bulk graphite fluoride, leading to full material economy, which is of significant importance for the cost and applicability of the cathode. This is further strengthened considering that graphite fluoride, first synthesized in 1934[79,80] and heavily explored since the 70's as a primary lithium battery electrode[81,82] (Matsushita Electric Co. 1975[83]), is easily accessible on the market and produced in large quantities as an industrial lubricant.[84–86]

3. Conclusion

An efficient and straightforward approach to prepare a highly and covalently sulfurized graphene cathode for LSBs is reported, exploiting the nucleophilicity of PS anions and the electrophilic centers in FG. The chemical reaction affords an electrochemically active cathode material with a remarkably high covalent sulfur content of 80 mass%. The covalent bonding was clearly observed and verified with infrared and Raman spectroscopies, as well as with theoretical calculations unveiling the mechanism of the nucleophilic attack of the PSs chains primarily on carbons adjacent to fluorinated areas. Electrochemical cycling of the sulfurized-graphene material against metallic lithium exhibited top-rated performance with only 5 mass% of conductive additives and at a low temperature of 25 °C. The cathode showed high sulfur utilization and specific capacities at both low and high current rates, excellent cycling stability, and high rate capabilities. The described methodology offers an effective pathway for the development and study of previously unexplored cathode materials for LSBs, exploiting the alkylhalide-like and elegant chemistry of fluorinated carbon matrices. The simple, eco-friendly, and cost-effective cathode combined with the very high sulfur loading could represent a strong candidate for practically efficient LSBs.

4. Experimental Section

Sodium Polysulfide Preparation: 1 M of sodium sulfide nonahydrate ($Na_2S{\cdot}9H_2O$) was dissolved in a water-ethanol mixed solvent (1:1 volume ratio) and 1 M of sulfur (S) was added subsequently. The solution turned from yellow to dark orange indicating the gradually increasing chain-length of the PSs while reacting at 30 °C for 3 h (Figure S9, Supporting Information).[34] The solvent was vacuum dried and the residue was milled in a mortar to create a fine powder.

GPS Preparation and Control Samples: To prepare the covalently modified graphene with sulfur (GPS), FG (250 mg) was stirred in NMP (15 mL) for 48 h at room temperature, followed by further exfoliation via sonication for 4 h. After the exfoliation, NaPS (2 g) was added and the mixture reacted at 80 °C under reflux for 48 h, in N_2 atmosphere. The final product (GPS) was centrifuged, washed with NMP, distilled water, ethanol, and acetone and finally it was freeze dried to form a fine powder.

The same procedure was repeated using electrochemically exfoliated graphene[87] (instead of FG) and NaPS, affording the control sample EEGS, which contained very low sulfur amount. The reaction between elemental sulfur (instead of NaPS) and FG afforded the control sample GS, with high amount of sulfur, in which C—S covalent bonds were not detected. In both control samples the same mass ratios of C:S were used during the synthesis, as in the main GPS product.

Structural and Chemical Characterization: FT-IR spectra were recorded on an iS5 FTIR spectrometer (Thermo Nicolet) using the KBr pellet accessory. Spectra were recorded by summing 50 scans, using pure KBr for the background acquisition. Baseline corrections were applied to the collected spectra. TGA with EGA was performed with a Netzsch STA 449 C Jupiter thermo-microbalance instrument at a heating rate of 10 °C min^{-1} under an N_2 flow in the furnace. The masses of released gases over the range 18–64 m/z were determined with a QMS 403 Aëolos instrument (Netzsch) under a synthetic air flow. To avoid overloading the spectrometer with adsorbed water, a heating to 100 °C and consequent cooling to room temperature was performed prior to the EGA measurements. Raman spectra were collected using a DXR Raman spectroscope (Thermo Scientific) equipped with a laser operating at a wavelength of 633 nm. XPS was carried out with a PHI VersaProbe II (Physical Electronics) spectrometer using an Al Ka source (15 kV, 50 W). The obtained data were evaluated and deconvoluted with the MultiPak (Ulvac-PHI, Inc.) software package. The spectral analysis included Shirley background subtraction and peak deconvolution employing mixed Gaussian-Lorentzian functions. Electron microscopy images were obtained using a JEOL 2010 TEM equipped with a LaB_6 type emission gun operating at 160 kV. EDS was recorded on an Oxford x-MAX 80T (SSD) at 200 kV accelerating voltage. Scanning transmission electron microscopy high-angle annular dark-field imaging analyses for EDS mapping of elemental distributions on the products were performed with an FEI Titan HRTEM microscope operating at 80 kV.

Theoretical Calculations: To explore possible reaction mechanism of sulfur covalent binding to graphene, DFT calculations were performed to model the nucleophilic attack of short PS chains (S_x^{2-}, $x = 2$, 4, and 6) on various FG structures. Ground state structures of all investigated species were optimized at the ωB97X-D/6-31++G(d,p) level of theory[88,89] using Gaussian16 software.[90] Solvent effects were taken into account by the universal continuum solvation model based on electron density (SMD).[91] Ovalene molecule with three different levels of fluorination was used as a model of partially defluorinated FG (Figures S2–S4, Supporting Information).

Electrochemical Characterization: The slurries were prepared by mixing the active material (GPS), Ketjen black and polyvinylidene fluoride (polymer binder) with a weight ratio of 90:5:5 (total mass 40 mg), using NMP as solvent (around 0.4 mL). The homogenization of the slurries was performed in a ultrasonicating bath for 2 h to break any agglomerates and then using a planetary mixer (Thinky ARV-310LED) for 10 min at 2000 rpm under vacuum. This procedure was repeated three times.

After homogenization, the slurries were casted, on a carbon coated Al foil, which was used as a substrate and current collector, using a 180 µm stainless steel doctor blade. After casting, the electrodes were dried at 80 °C under vacuum overnight. The mass loading of total material on an 18 mm diameter coin was ≈4 mg (≈1.6 or 1.15 mg cm^{-2} of sulfur). The electrodes were tested in sealed electrochemical cells (El-cell) using lithium foil as the counter electrode, and a glass fiber separator (0.26 mm, El-cell). The electrolyte contained 1 M LiTFSI (Aldrich) in a mixed solvent of 1,3-dioxolane (DOL, Aldrich) and dimethoxy ethane (DME, Aldrich) or TTE (TCI) (DOL:DME or DOL/TTE, 1:1 by volume) and 100 µL of the electrolyte was introduced in each cell.

The cells were assembled in Ar-filled glovebox (both H_2O and O_2 contents were below 1.0 ppm). Galvanostatic discharge/charge test was

carried out on a battery test system (BCS-810, Biologic) in the range of 1.5–2.8 V at 25 °C. Cyclic voltammetry was performed at different scan rates from 0.1 to 0.5 mV s^{-1}. All the current densities, C-rates, and specific capacities were based on the weight of sulfur (unless otherwise stated).

Supporting Information

Supporting Information is available from the Wiley Online Library or from the author.

Acknowledgements

The work was supported by the ERDF/ESF project "Nano4Future" (No. CZ.02.1.01/0.0/0.0/16_019/0000754). I.T. acknowledges the support by the Operational Programme Research, Development and Education—Project No. CZ.02.1.01/0.0/0.0/15_003/0000416 of the Ministry of Education, Youth and Sports of the Czech Republic. R.Z. and A.B. acknowledge the funding from the Czech Science Foundation, project GA CR—EXPRO, 19-27454X. M.O. acknowledges the ERC grand 2D-CHEM, No 683024 from H2020. Operation of XPS and TEM facilities were partly funded from by the Research Infrastructure NanoEnviCz, supported by the Ministry of Education, Youth and Sports of the Czech Republic under Project No. LM2018124. D.Z. thanks the Student project by Palacký University Olomouc (IGA_PrF_2021_031). J.H. thanks the Student project by Palacký University Olomouc (IGA_PrF_2020_011). The authors thank V. Šedajová for XPS, J. Stráská and O. Tomanec for TEM/HR-TEM, E. Ioannou and C. M. Reyes Pérez for SEM, and K. Štymplová for Raman measurements.

Conflict of Interest

A European patent application is currently under consideration.

Data Availability Statement

Data available from the authors upon request

Keywords

covalent functionalization, crosslinking, fluorographene, graphene, lithium–sulfur batteries, sodium polysulfide

Received: February 7, 2021
Revised: March 31, 2021
Published online: April 15, 2021

[1] M. Armand, J.-M. Tarascon, *Nature* **2008**, *451*, 652.
[2] N.-S. Choi, Z. Chen, S. A. Freunberger, X. Ji, Y.-K. Sun, K. Amine, G. Yushin, L. F. Nazar, J. Cho, P. G. Bruce, *Angew. Chem., Int. Ed.* **2012**, *51*, 9994.
[3] J. Liu, Z. Bao, Y. Cui, E. J. Dufek, J. B. Goodenough, P. Khalifah, Q. Li, B. Y. Liaw, P. Liu, A. Manthiram, Y. S. Meng, V. R. Subramanian, M. F. Toney, V. V. Viswanathan, M. S. Whittingham, J. Xiao, W. Xu, J. Yang, X.-Q. Yang, J.-G. Zhang, *Nat. Energy* **2019**, *4*, 180.
[4] N. Nitta, F. Wu, J. T. Lee, G. Yushin, *Mater. Today* **2015**, *18*, 252.
[5] S. Evers, L. F. Nazar, *Acc. Chem. Res.* **2013**, *46*, 1135.
[6] Y.-X. Yin, S. Xin, Y.-G. Guo, L.-J. Wan, *Angew. Chem., Int. Ed.* **2013**, *52*, 13186.
[7] H.-J. Peng, J.-Q. Huang, X.-B. Cheng, Q. Zhang, *Adv. Energy Mater.* **2017**, *7*, 1700260.
[8] Y.-S. Su, Y. Fu, T. Cochell, A. Manthiram, *Nat. Commun.* **2013**, *4*, 2985.
[9] J. D. V. Hamme, A. Singh, O. P. Ward, *Microbiol. Mol. Biol. Rev.* **2003**, *67*, 503.
[10] D. Peramunage, S. Licht, *Science* **1993**, *261*, 1029.
[11] P. G. Bruce, S. A. Freunberger, L. J. Hardwick, J.-M. Tarascon, *Nat. Mater.* **2012**, *11*, 19.
[12] X. Ji, K. T. Lee, L. F. Nazar, *Nat. Mater.* **2009**, *8*, 500.
[13] A. Bhargav, J. He, A. Gupta, A. Manthiram, *Joule* **2020**, *4*, 285.
[14] A. Manthiram, Y. Fu, Y.-S. Su, *Acc. Chem. Res.* **2013**, *46*, 1125.
[15] Y. V. Mikhaylik, J. R. Akridge, *J. Electrochem. Soc.* **2004**, *151*, A1969.
[16] Z. W. Seh, W. Li, J. J. Cha, G. Zheng, Y. Yang, M. T. McDowell, P.-C. Hsu, Y. Cui, *Nat. Commun.* **2013**, *4*, 1331.
[17] X. Ji, S. Evers, R. Black, L. F. Nazar, *Nat. Commun.* **2011**, *2*, 325.
[18] W. G. Chong, J.-Q. Huang, Z.-L. Xu, X. Qin, X. Wang, J.-K. Kim, *Adv. Funct. Mater.* **2017**, *27*, 1604815.
[19] G. Zhou, L. Li, D.-W. Wang, X. Shan, S. Pei, F. Li, H.-M. Cheng, *Adv. Mater.* **2015**, *27*, 641.
[20] Y. He, Y. Qiao, H. Zhou, *Dalton Trans.* **2018**, *47*, 6881.
[21] B. Liu, R. Bo, M. Taheri, I. Di Bernardo, N. Motta, H. Chen, T. Tsuzuki, G. Yu, A. Tricoli, *Nano Lett.* **2019**, *19*, 4391.
[22] L. Xiao, Y. Cao, J. Xiao, B. Schwenzer, M. H. Engelhard, L. V. Saraf, Z. Nie, G. J. Exarhos, J. Liu, *Adv. Mater.* **2012**, *24*, 1176.
[23] W. Qian, Q. Gao, Z. Li, W. Tian, H. Zhang, Q. Zhang, *ACS Appl. Mater. Interfaces* **2017**, *9*, 28366.
[24] Y. Liu, G. Li, J. Fu, Z. Chen, X. Peng, *Angew. Chem., Int. Ed.* **2017**, *56*, 6176.
[25] Y. Mao, G. Li, Y. Guo, Z. Li, C. Liang, X. Peng, Z. Lin, *Nat. Commun.* **2017**, *8*, 14628.
[26] J. Wang, Y.-S. He, J. Yang, *Adv. Mater.* **2015**, *27*, 569.
[27] B. Wang, T. Ruan, Y. Chen, F. Jin, L. Peng, Y. Zhou, D. Wang, S. Dou, *Energy Storage Mater.* **2020**, *24*, 22.
[28] R. Fang, K. Chen, L. Yin, Z. Sun, F. Li, H.-M. Cheng, *Adv. Mater.* **2019**, *31*, 1800863.
[29] J. Zhang, C.-P. Yang, Y.-X. Yin, L.-J. Wan, Y.-G. Guo, *Adv. Mater.* **2016**, *28*, 9539.
[30] J. Li, J. Zhou, T. Wang, X. Chen, Y. Zhang, Q. Wan, J. Zhu, *Nanoscale* **2020**, *12*, 8991.
[31] L. Fan, R. Ma, Y. Yang, S. Chen, B. Lu, *Nano Energy* **2016**, *28*, 304.
[32] G. Li, J. Sun, W. Hou, S. Jiang, Y. Huang, J. Geng, *Nat. Commun.* **2016**, *7*, 10601.
[33] F. Liu, J. Liang, C. Zhang, L. Yu, J. Zhao, C. Liu, Q. Lan, S. Chen, Y.-C. Cao, G. Zheng, *Results Phys.* **2017**, *7*, 250.
[34] Y. Zhang, Y. Peng, Y. Wang, J. Li, H. Li, J. Zeng, J. Wang, B. J. Hwang, J. Zhao, *Sci. Rep.* **2017**, *7*, 11386.
[35] A. Bakandritsos, M. Pykal, P. Błoński, P. Jakubec, D. D. Chronopoulos, K. Poláková, V. Georgakilas, K. Čépe, O. Tomanec, V. Ranc, A. B. Bourlinos, R. Zbořil, M. Otyepka, *ACS Nano* **2017**, *11*, 2982.
[36] D. D. Chronopoulos, A. Bakandritsos, M. Pykal, R. Zbořil, M. Otyepka, *Appl. Mater. Today* **2017**, *9*, 60.
[37] M. Medveď, G. Zoppellaro, J. Ugolotti, D. Matochová, P. Lazar, T. Pospíšil, A. Bakandritsos, J. Tuček, R. Zbořil, M. Otyepka, *Nanoscale* **2018**, *10*, 4696.
[38] D. Matochová, M. Medveď, A. Bakandritsos, T. Steklý, R. Zbořil, M. Otyepka, *J. Phys. Chem. Lett.* **2018**, *9*, 3580.
[39] R. Steudel, in *Encyclopedia of Inorganic Chemistry*, Wiley, Hoboken, NJ **2007**.
[40] H. Becker, W. Berger, G. Domschke, *Organicum: Practical Handbook of Organic Chemistry*, Elsevier, Amsterdam **2013**.
[41] D. D. Chronopoulos, M. Medveď, G. Potsi, O. Tomanec, M. Scheibe, M. Otyepka, *Chem. Commun.* **2020**, *56*, 1936.
[42] S. S. Zhang, *Front. Energy Res.* **2013**, *1*, 10.

[43] S. W. Shin, J. H. Han, J. Y. Lee, Y. C. Park, G. L. Agawane, A. V. Moholkar, M.-G. Gang, C. H. Jeong, J. H. Kim, J. H. Yun, *Appl. Surf. Sci.* **2013**, *270*, 572.
[44] E. C. Vermisoglou, P. Jakubec, A. Bakandritsos, M. Pykal, S. Talande, R. Zboril, *Chem. Mater.* **2019**, *31*, 4698.
[45] Y. Z. Zhang, S. Liu, G. C. Li, G. R. Li, X. P. Gao, *J. Mater. Chem. A* **2014**, *2*, 4652.
[46] A. T. Ward, *J. Phys. Chem.* **1968**, *72*, 4133.
[47] M. Hagen, P. Schiffels, M. Hammer, S. Dörfler, J. Tübke, M. J. Hoffmann, H. Althues, S. Kaskel, *J. Electrochem. Soc.* **2013**, *160*, A1205.
[48] X. Yu, J. Xie, J. Yang, H. Huang, K. Wang, Z. Wen, *J. Electroanal. Chem.* **2004**, *573*, 121.
[49] A. C. Ferrari, D. M. Basko, *Nat. Nanotechnol.* **2013**, *8*, 235.
[50] J. M. Englert, P. Vecera, K. C. Knirsch, R. A. Schäfer, F. Hauke, A. Hirsch, *ACS Nano* **2013**, *7*, 5472.
[51] A. Kouloumpis, D. D. Chronopoulos, G. Potsi, M. Pykal, J. Vlček, M. Scheibe, M. Otyepka, *Chem. - Eur. J.* **2020**, *26*, 6518.
[52] F. Karlický, E. Otyepková, R. Lo, M. Pitoňák, P. Jurečka, M. Pykal, P. Hobza, M. Otyepka, *J. Chem. Theory Comput.* **2017**, *13*, 1328.
[53] M. Fantauzzi, *RSC Adv.* **2015**, *5*, 75953.
[54] V. Urbanová, K. Holá, A. B. Bourlinos, K. Čépe, A. Ambrosi, A. H. Loo, M. Pumera, F. Karlický, M. Otyepka, R. Zbořil, *Adv. Mater.* **2015**, *27*, 2305.
[55] X. Wang, W. Wang, Y. Liu, M. Ren, H. Xiao, X. Liu, *Phys. Chem. Chem. Phys.* **2016**, *18*, 3285.
[56] W. Weng, V. G. Pol, K. Amine, *Adv. Mater.* **2013**, *25*, 1608.
[57] M.-Q. Zhao, Q. Zhang, J.-Q. Huang, G.-L. Tian, J.-Q. Nie, H.-J. Peng, F. Wei, *Nat. Commun.* **2014**, *5*, 3410.
[58] R. Fang, S. Zhao, Z. Sun, D.-W. Wang, H.-M. Cheng, F. Li, *Adv. Mater.* **2017**, *29*, 1606823.
[59] S. Xin, L. Gu, N.-H. Zhao, Y.-X. Yin, L.-J. Zhou, Y.-G. Guo, L.-J. Wan, *J. Am. Chem. Soc.* **2012**, *134*, 18510.
[60] M. Cuisinier, P.-E. Cabelguen, B. D. Adams, A. Garsuch, M. Balasubramanian, L. F. Nazar, *Energy Environ. Sci.* **2014**, *7*, 2697.
[61] R. Elazari, G. Salitra, A. Garsuch, A. Panchenko, D. Aurbach, *Adv. Mater.* **2011**, *23*, 5641.
[62] X. Tao, J. Wang, C. Liu, H. Wang, H. Yao, G. Zheng, Z. W. Seh, Q. Cai, W. Li, G. Zhou, C. Zu, Y. Cui, *Nat. Commun.* **2016**, *7*, 11203.
[63] S.-K. Park, J. Lee, T. Hwang, Y. Piao, *J. Mater. Chem. A* **2017**, *5*, 975.
[64] K. Xie, Y. You, K. Yuan, W. Lu, K. Zhang, F. Xu, M. Ye, S. Ke, C. Shen, X. Zeng, X. Fan, B. Wei, *Adv. Mater.* **2017**, *29*, 1604724.
[65] D. Cai, M. Lu, L. Li, J. Cao, D. Chen, H. Tu, J. Li, W. Han, *Small* **2019**, *15*, 1902605.
[66] Z. Xu, J. Wang, J. Yang, X. Miao, R. Chen, J. Qian, R. Miao, *Angew. Chem., Int. Ed.* **2016**, *55*, 10372.
[67] Y. Zhou, C. Zhou, Q. Li, C. Yan, B. Han, K. Xia, Q. Gao, J. Wu, *Adv. Mater.* **2015**, *27*, 3774.
[68] Q. Sun, B. He, X.-Q. Zhang, A.-H. Lu, *ACS Nano* **2015**, *9*, 8504.
[69] M. Yu, J. Ma, M. Xie, H. Song, F. Tian, S. Xu, Y. Zhou, B. Li, D. Wu, H. Qiu, R. Wang, *Adv. Energy Mater.* **2017**, *7*, 1602347.
[70] X. Yang, L. Zhang, F. Zhang, Y. Huang, Y. Chen, *ACS Nano* **2014**, *8*, 5208.
[71] J. Zheng, G. Ji, X. Fan, J. Chen, Q. Li, H. Wang, Y. Yang, K. C. DeMella, S. R. Raghavan, C. Wang, *Adv. Energy Mater.* **2019**, *9*, 1803774.
[72] R. Fang, S. Zhao, S. Pei, X. Qian, P.-X. Hou, H.-M. Cheng, C. Liu, F. Li, *ACS Nano* **2016**, *10*, 8676.
[73] X. Liang, Y. Rangom, C. Y. Kwok, Q. Pang, L. F. Nazar, *Adv. Mater.* **2017**, *29*, 1603040.
[74] G. Hu, C. Xu, Z. Sun, S. Wang, H.-M. Cheng, F. Li, W. Ren, *Adv. Mater.* **2016**, *28*, 1603.
[75] H. Zhang, W. Zhao, M. Zou, Y. Wang, Y. Chen, L. Xu, H. Wu, A. Cao, *Adv. Energy Mater.* **2018**, *8*, 1800013.
[76] H.-J. Peng, J.-Q. Huang, M.-Q. Zhao, Q. Zhang, X.-B. Cheng, X.-Y. Liu, W.-Z. Qian, F. Wei, *Adv. Funct. Mater.* **2014**, *24*, 2772.
[77] C.-W. Lee, Q. Pang, S. Ha, L. Cheng, S.-D. Han, K. R. Zavadil, K. G. Gallagher, L. F. Nazar, M. Balasubramanian, *ACS Cent. Sci.* **2017**, *3*, 605.
[78] C. V. Amanchukwu, Z. Yu, X. Kong, J. Qin, Y. Cui, Z. Bao, *J. Am. Chem. Soc.* **2020**, *142*, 7393.
[79] O. Ruff, O. Bretschneider, *Z. Anorg. Allg. Chem* **1934**, *217*, 1.
[80] Y. Liu, L. Jiang, H. Wang, H. Wang, W. Jiao, G. Chen, P. Zhang, D. Hui, X. Jian, *Nanotechnol. Rev.* **2019**, *8*, 573.
[81] J. Liu, Y. Wan, W. Liu, Z. Ma, S. Ji, J. Wang, Y. Zhou, P. Hodgson, Y. Li, *J. Mater. Chem. A* **2013**, *1*, 1969.
[82] N. F. Watanabe, US3700502A **1972**.
[83] M. Fukuda, T. Iijima, in *Power Sources 5*, (Ed: D. H. Collins) Academic Press, New York **1975**, *5*, p. 713.
[84] X. Ye, L. Ma, Z. Yang, J. Wang, H. Wang, S. Yang, *ACS Appl. Mater. Interfaces* **2016**, *8*, 7483.
[85] R. L. Fusaro, H. E. Sliney, *A. S. L. E. Trans.* **1970**, *13*, 56.
[86] N. Watanabe, T. H. Nakajima Touhara, in *Graphite Fluorides: Studies in Inorganic Chemistry*, Vol. *8*, Elsevier, Amsterdam **1988**.
[87] H. Barès, A. Bakandritsos, M. Medveď, J. Ugolotti, P. Jakubec, O. Tomanec, S. Kalytchuk, R. Zbořil, M. Otyepka, *Carbon* **2019**, *145*, 251.
[88] J.-D. Chai, M. Head-Gordon, *Phys. Chem. Chem. Phys.* **2008**, *10*, 6615.
[89] R. Ditchfield, W. J. Hehre, J. A. Pople, *J. Chem. Phys.* **1971**, *54*, 724.
[90] M. J. Frisch, G. W. Trucks, H. B. Schlegel, G. E. Scuseria, M. A. Robb, J. R. Cheeseman, G. Scalmani, V. Barone, G. A. Petersson, H. Nakatsuji, X. Li, M. Caricato, A. Marenich, J. Bloino, B. G. Janesko, R. Gomperts, B. Mennucci, H. P. Hratchian, J. V. Ortiz, A. F. Izmaylov, J. L. Sonnenberg, D. Williams-Young, F. Ding, F. Lipparini, F. Egidi, J. Goings, B. Peng, A. Petrone, T. Henderson, D. Ranasinghe, et al, *Gaussian 09, Revision A.02*, Gaussian, Inc., Wallingford CT **2016**.
[91] A. V. Marenich, C. J. Cramer, D. G. Truhlar, *J. Phys. Chem. B* **2009**, *113*, 6378.

Appendix B

ADVANCED FUNCTIONAL MATERIALS

Supporting Information

for *Adv. Funct. Mater.,* DOI: 10.1002/adfm.202101326

Covalently Interlinked Graphene Sheets with Sulfur-Chains Enable Superior Lithium–Sulfur Battery Cathodes at Full-Mass Level

Iosif Tantis, Aristides Bakandritsos, Dagmar Zaoralová, Miroslav Medveď, Petr Jakubec, Jana Havláková, Radek Zbořil,* and Michal Otyepka**

WILEY-VCH

Supporting Information

Covalently Interlinked Graphene Sheets with Sulfur-Chains Enable Superior Lithium-Sulfur Battery Cathodes at Full-Mass Level.

Iosif Tantis, Aristides Bakandritsos, Dagmar Zaoralová, Miroslav Medved', Petr Jakubec, Jana Havláková, Radek Zbořil*, Michal Otyepka**

Dr. Iosif Tantis, Dr. Aristides Bakandritsos, Dagmar Zaoralová, Dr. Miroslav Medved', Dr. Petr Jakubec, Jana Havláková, Prof. Radek Zbořil, Prof. Michal Otyepka
Regional Centre of Advanced Technologies and Materials, Czech Advanced Technology and Research Institute, Palacký University, Olomouc, Křížkovského 511/8, 77 900 Czech Republic
E-mail: a.bakandritsos@upol.cz; michal.otyepka@upol.cz; radek.zboril@upol.cz

Dr. Aristides Bakandritsos, Prof. Radek Zbořil
Nanotechnology Centre, Centre of Energy and Environmental Technologies, VŠB–Technical University of Ostrava, 17. listopadu 2172/15, 708 00 Ostrava-Poruba, Czech Republic

Dagmar Zaoralová
Department of Physical Chemistry, Faculty of Science, Palacký University Olomouc, 17. listopadu 1192/12, 77 900 Olomouc, Czech Republic

Jana Havláková
Department of Experimental Physics, Faculty of Science, Palacký University Olomouc, 17. listopadu 1192/12, 77 900 Olomouc, Czech Republic

Keywords: lithium-sulfur batteries, fluorographene, graphene, sodium polysulfide, covalent

functionalization, crosslinking

Table S1. Literature comparison of the capacity of the GPS cathode with state-of-the-art reported materials based on LSBs. All values are also calculated using the mass of the full cathode material.

Material	Sulfur content [wt.%]	Cond. additive [%]	Max. cycles	Rate [C]	C_{Smass} at last cycle [mAh g^{-1}]	C_{full} at last cycle [mAh g^{-1}]	Ref.
S@C	65	10	150	~0.06	775	403	[1]
MgO decorated carbon flakes	66	20	300	0.1	~900	416	[2]
MXene/CNT composite	80	10	250	0.2	~750	480	[3]
Holey-CNT/S/ZrO	46	10	200	0.5	~600	221	[4]
Core-shell carbon spheres	70	15	200	0.5	920	483	[5]
Freestanding and sandwich-structured electrode	55	10	500	0.5	550	242	[6]
MCNC/G-S	60	20	100	0.5	525	220	[7]
S@$Ni_3(HITP)_2$	65.5	20	100	0.2	878	399	[8]
C/S + $BaTiO_3$	60	20	100	0.2	835	351	[9]
SWCNs@MOFs	40	0	500	0.2	650	260	[10]
Layered graphene/porous carbon	68	0	100	0.5	597	365	[11]
Graphene foam	83	0	350	0.2	645	535	[12]
CNT@large-ZIF8	64	0	500	1.0	750	480	[13]
Graphene/CNT@porous carbon	50	0	150	1.0	877	395	[14]
GPS (covalently sulfurized graphene)	80	5	100	0.1	704	507	**This work**
	80	5	250	0.2	644	464	
	80	5	500	1.0	470	339	

Table S2. Elemental composition (at. %) from XPS analysis for the EEGS (electrochemically exfoliated graphene reacted with NaPS), GPS (fluorographene reacted with NaPS) and GS (fluorographene reacted with sulfur) products.

	C	O	F	S	N	Na
GF	43.6	0.1	55.8	-	0.5	-
EEGS	88.0	8.2	-	1.6	1.9	0.3
GPS	55.8	9.3	7.4	18.5	1.0	8.0
GS	55.4	2.8	37	3.6[a)]	1.2	-

[a)]The atomic ratio of sulfur in GS was lower than the expected from TGA because this material, having no strong interaction between the sulfur and the FG, suffered from phase separation. Thus, we observed that FG enriched the surface of the dried material, leading to the underestimation of sulfur with this technique (Table S2).

Table S3. Adiabatic ionization energies of PS (IE) and electron affinity (EA) of FG radical center in NMP (kcal·mol^{-1}, ωB97X-D/6-31++G(d,p)/SMD level of theory).

	IE
S_2^{2-}	66.6
S_4^{2-}	86.4
S_6^{2-}	82.1
	EA
FG radical center (model molecule)	119.5

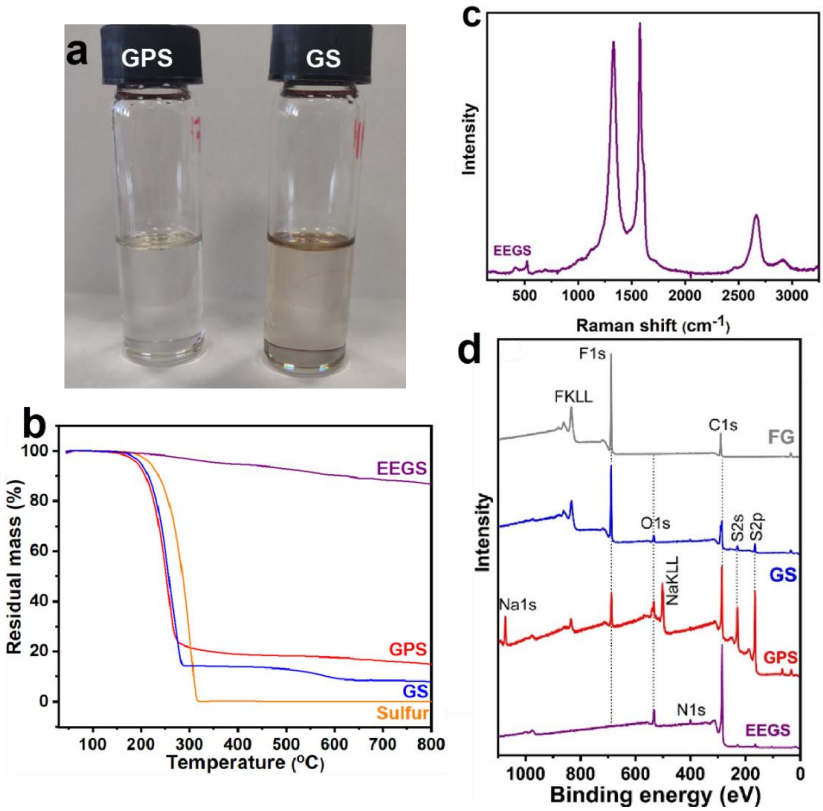

Figure S1. (a) Photos of the CS_2 extracted sulfur from GS and GPS. (b) TGA profile, (c) Raman spectrum and, (d) XPS survey spectrum of EEGS (the respective data of the other samples are also displayed for direct comparison).

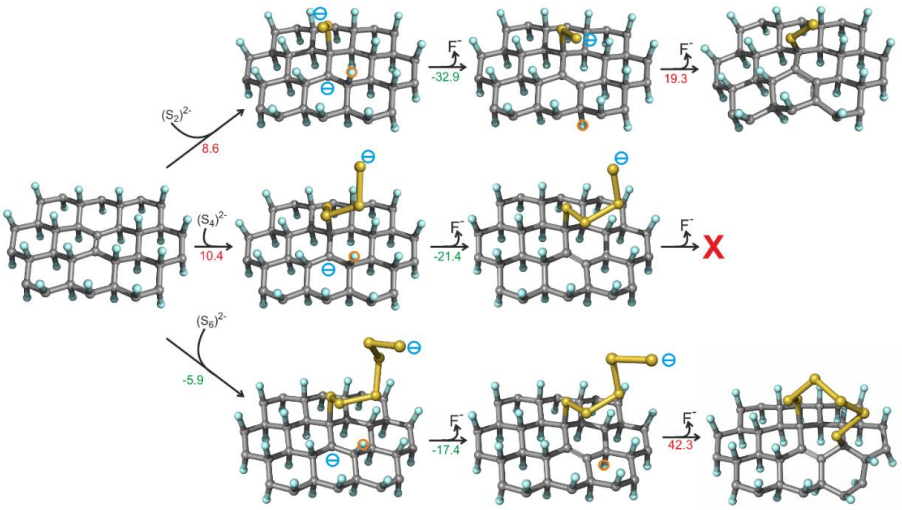

Figure S2. Nucleophilic attack of S_x^{2-} (x = 2, 4, 6) on the C=C bond in partially defluorinated FG. Fluorine atoms detached in the next reaction step are marked by orange circles. Reaction energies are in kcal·mol^{-1}. Carbon atoms are grey, fluorine blue and sulfur yellow. Hydrogen atoms on edges of model molecules are hidden for clarity.

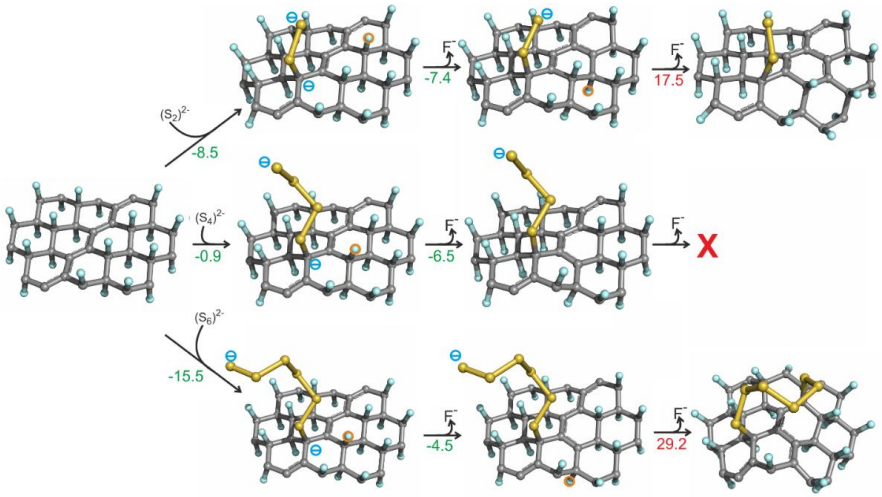

Figure S3. Nucleophilic attack of S_x^{2-} (x = 2, 4, 6) on a π-conjugated chain of C=C bonds (zigzag motif) in partially defluorinated FG. Fluorine atoms detached in the next reaction step are marked by orange circles. Reaction energies are in kcal·mol^{-1}. Carbon atoms are grey, fluorine blue and sulfur yellow. Hydrogen atoms on edges of model molecules are hidden for clarity.

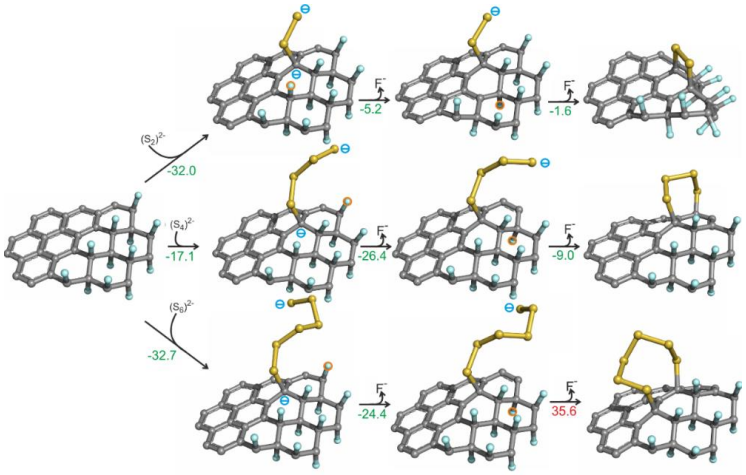

Figure S4. Nucleophilic attack of S_x^{2-} (x = 2, 4, 6) on an edge of fluorinated and defluorinated areas of partially defluorinated FG. Fluorine atoms detached in the next reaction step are marked by orange circles. Reaction energies are in kcal·mol^{-1}. Carbon atoms are grey, fluorine blue and sulfur yellow. Hydrogen atoms on edges of model molecules are hidden for clarity.

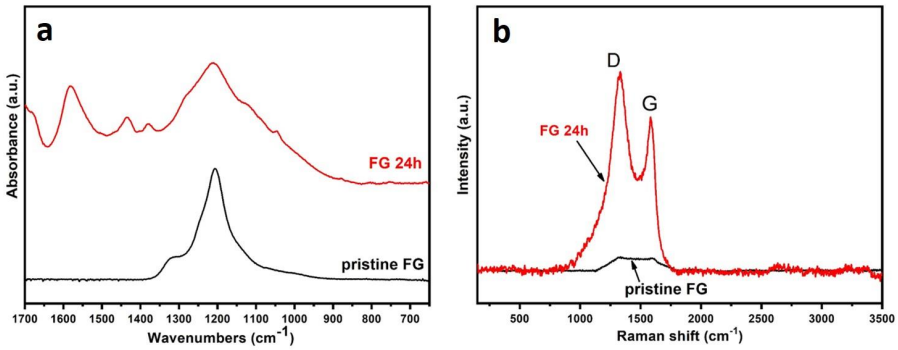

Figure S5. (a) FTIR spectra for elemental pristine FG and FG after 24h treatment with NMP at 80 °C and (b) Raman spectra of the same samples.

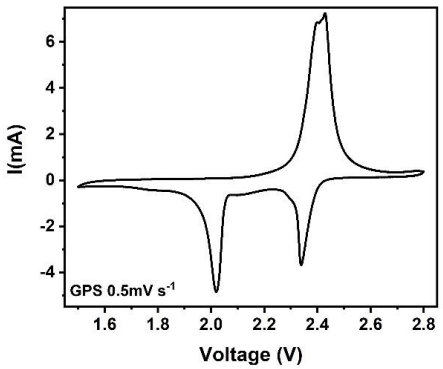

Figure S6. CV curve of GPS as a LSB cathode at 0.5 mV g^{-1} using 1 M LiTFSI in 1:1 DOL:DME +1 wt. % $LiNO_3$ as an electrolyte.

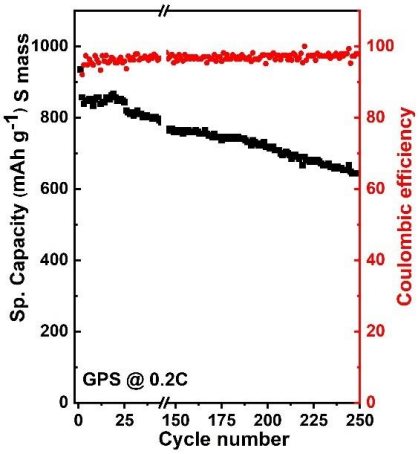

Figure S7. Cycling performance of GPS as a LSB cathode in in 1 M LiTFSI in 1:1 DOL:TTE electrolyte at 0.2 C (1 C=1672 mAh g^{-1})

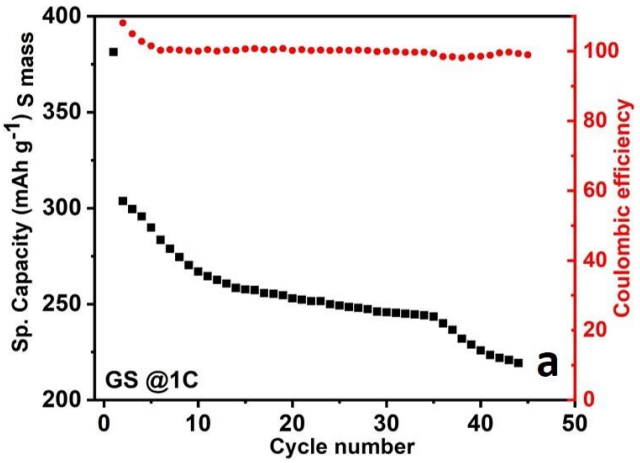

Fugure S8. Cycling performance of GS as a LSB cathode in 1 M LiTFSI in 1:1 DOL:TTE electrolyte at 1 C.

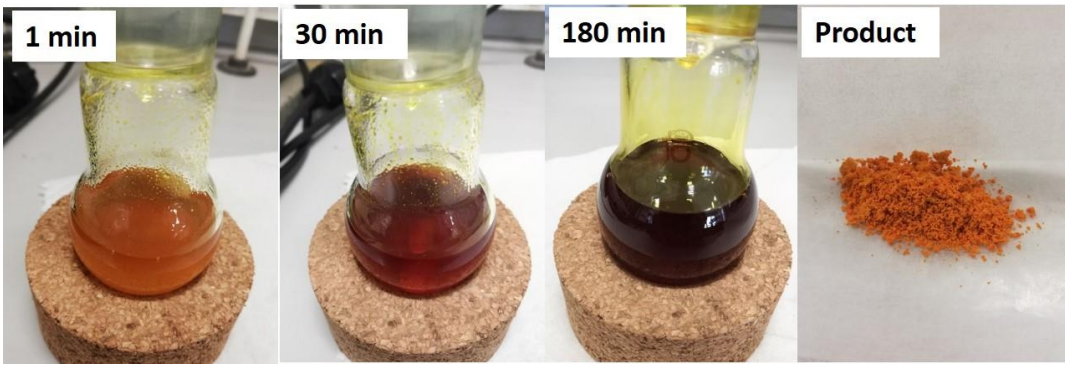

Figure S9. Photos of the NaPS preparation in different reaction progress time.

Supplemental References

[1] J. Zheng, G. Ji, X. Fan, J. Chen, Q. Li, H. Wang, Y. Yang, K. C. DeMella, S. R. Raghavan, C. Wang, *Adv. Energy Mater.* **2019**, *9*, 1803774.

[2] X. Tao, J. Wang, C. Liu, H. Wang, H. Yao, G. Zheng, Z. W. Seh, Q. Cai, W. Li, G. Zhou, C. Zu, Y. Cui, *Nat. Commun.* **2016**, *7*, 11203.

[3] X. Liang, Y. Rangom, C. Y. Kwok, Q. Pang, L. F. Nazar, *Adv. Mater.* **2017**, *29*, 1603040.

[4] Y. Zhou, C. Zhou, Q. Li, C. Yan, B. Han, K. Xia, Q. Gao, J. Wu, *Adv. Mater.* **2015**, *27*, 3774.

[5] Q. Sun, B. He, X.-Q. Zhang, A.-H. Lu, *ACS Nano* **2015**, *9*, 8504.

[6] M. Yu, J. Ma, M. Xie, H. Song, F. Tian, S. Xu, Y. Zhou, B. Li, D. Wu, H. Qiu, R. Wang, *Adv. Energy Mater.* **2017**, *7*, 1602347.

[7] S.-K. Park, J. Lee, T. Hwang, Y. Piao, *J. Mater. Chem. A* **2017**, *5*, 975.

[8] D. Cai, M. Lu, L. Li, J. Cao, D. Chen, H. Tu, J. Li, W. Han, *Small* **2019**, *15*, 1902605.

[9] K. Xie, Y. You, K. Yuan, W. Lu, K. Zhang, F. Xu, M. Ye, S. Ke, C. Shen, X. Zeng, X. Fan, B. Wei, *Adv. Mater.* **2017**, *29*, 1604724.

[10] Y. Mao, G. Li, Y. Guo, Z. Li, C. Liang, X. Peng, Z. Lin, *Nat. Commun.* **2017**, *8*, 14628.

[11] X. Yang, L. Zhang, F. Zhang, Y. Huang, Y. Chen, *ACS Nano* **2014**, *8*, 5208.

[12] G. Hu, C. Xu, Z. Sun, S. Wang, H.-M. Cheng, F. Li, W. Ren, *Adv. Mater.* **2016**, *28*, 1603.

[13] H. Zhang, W. Zhao, M. Zou, Y. Wang, Y. Chen, L. Xu, H. Wu, A. Cao, *Adv. Energy Mater*. **2018**, *8*, 1800013.

[14] H.-J. Peng, J.-Q. Huang, M.-Q. Zhao, Q. Zhang, X.-B. Cheng, X.-Y. Liu, W.-Z. Qian, F. Wei, *Adv. Funct. Mater.* **2014**, *24*, 2772.

Appendix C

Applied Materials Today 34 (2023) 101881

Contents lists available at ScienceDirect

Applied Materials Today

journal homepage: www.elsevier.com/locate/apmt

Hematene: A sustainable 2D conductive platform for visible-light-driven photocatalytic ammonia decomposition

Jana Dzíbelová [a,b,1], S.M. Hossein Hejazi [a,c,1], Veronika Šedajová [a], David Panáček [a], Petr Jakubec [a,*], Zdeněk Baďura [a,b], Ondřej Malina [a], Josef Kašlík [a], Jan Filip [a], Štěpán Kment [a,c], Michal Otyepka [a,d,*], Radek Zbořil [a,c,*]

[a] Regional Centre of Advanced Technologies and Materials, Czech Advanced Technology and Research Institute (CATRIN), Palacký University Olomouc, Šlechtitelů 241/27, Olomouc 779 00, Czech Republic
[b] Department of Experimental Physics, Faculty of Science, Palacký University Olomouc, 17. listopadu 1192/12, Olomouc 779 00, Czech Republic
[c] Nanotechnology Centre, Centre of Energy and Environmental Technologies, VŠB–Technical University of Ostrava, 17. listopadu 2172/15, Poruba, Ostrava 708 00, Czech Republic
[d] IT4Innovations, VŠB–Technical University of Ostrava, 17. listopadu 2172/15-Poruba, Ostrava 708 00, Czech Republic

ARTICLE INFO

Keywords:
Hematene
Ammonia
Hydrogen Production
Photocatalytic decomposition

ABSTRACT

The emerging class of 2D non-van der Waals (n-vdW) materials, including 2D iron oxides, possesses unique properties and high applicability, making them attractive for various technological applications. However, the synthesis of these materials through a scalable and eco-friendly method remains a challenge, as most known chemical exfoliation processes require toxic organic solvents. In this study, we report a green synthesis of 2D hematene (α-Fe_2O_3) using an ultrasound-supported exfoliation method of earth-abundant iron oxide ore in a pure aqueous solution. The resulting hematene sheets, only a few nanometers thick, exhibit superior electrochemical performance in terms of charge transfer processes, making them ideal for photocatalytic applications. By doping a conductive hematene substrate with ruthenium, we demonstrate a synergistic effect for generating electrons and holes under visible light irradiation. Using this approach, we successfully decomposed ammonia into hydrogen and nitrogen, highlighting the potential of this novel class of environmentally-friendly photocatalysts for clean energy production. Overall, our water-assisted scalable synthesis of hematene offers a promising strategy for producing efficient and sustainable photocatalysts.

1. Introduction

The discovery of two-dimensional (2D) materials has kindled immense interest among scientists as they exhibit unique chemical, physical, and electronic properties, compared to their 3D counterparts [1]. Their properties can be exploited in various applications, including electronics [2,3], sensors [4–6], energy storage [7–9], and spintronics [10,11]. Owing to their bonding nature, 2D materials can be sorted into two main classes: i) van-der Waals (vdW) 2D materials, such as graphene, black phosphorus (BP), transition metal dichalcogenides, metal-organic frameworks (MOFs), or MXenes, where the strong chemical bonding is located in-plane and the weak vdW bonding out-of-plane; and ii) non-van-der Waals (n-vdW) 2D materials like metal chalcogenides, oxides, nitrides, and phosphides, which exhibit strong chemical bonding in all three directions [12]. The n-vdW materials have a layered structure with an overall thickness of around 10 nm and encompass high energy surfaces [13].

Methodologies used for the synthesis of n-vdW materials include a self-assembly approach [14–16], exfoliation [17], lamellar intermediate exfoliation [18,19], and topochemical transformation [12,20,21]. The exfoliation process has been adopted as the most convenient strategy for the preparation of iron oxide derived n-vdW 2D materials such as hematene (2D α-Fe_2O_3), magnetene (2D Fe_3O_4), ilmenene (2D $FeTiO_3$), and chromiteen (2D $FeCr_2O_4$) [22]. All these materials were prepared from natural ores in organic solvents (typically DMF; N, N-dimethylformamide), deploying ultrasonication, with that being the

* Corresponding authors at: Regional Centre of Advanced Technologies and Materials, Czech Advanced Technology and Research Institute (CATRIN), Palacký University Olomouc, Šlechtitelů 241/27, Olomouc 779 00, Czech Republic.
E-mail addresses: p.jakubec@upol.cz (P. Jakubec), michal.otyepka@upol.cz (M. Otyepka), radek.zboril@upol.cz (R. Zbořil).
[1] These authors contributed equally.

https://doi.org/10.1016/j.apmt.2023.101881
Received 31 March 2023; Received in revised form 30 June 2023; Accepted 13 July 2023
Available online 29 July 2023

main drawback of these exfoliation processes due to the inherent toxicity of DMF and unwanted surface functionalization [23]. Because of the DMF toxicity [24,25], the European Union is adopting regulations restricting its use from December 2023 onwards [26]; hence the need for the development of alternative exfoliation processes in nontoxic solvents.

Since the amount of fossil fuels is limited, alongside the fact that global energy consumption is estimated to increase at least twice by the midcentury compared to the present time [27], the exploitation of renewable and sustainable energy sources represents one of the most important tasks. Previously published reports show that n-vdW materials such as hematene (2D α-Fe_2O_3), magnetene (2D Fe_3O_4), ilmenene (2D $FeTiO_3$), and chromiteen (2D $FeCr_2O_4$) have strong potential in the field of photoelectrochemistry, where the combination of these allotropes with Ti nanotubes shows excellent results [28,29]. N-vdW materials also hold great potential in various electrocatalytic applications targeting the energy conversion processes, including water splitting (HER and OER reactions), CO_2 reduction reaction (CRR), nitrogen reduction and oxidation reactions (NRR and NOR), NO_x reduction and NH_3 oxidation [12]. Up to now, the highest electrocatalytic activity is achieved with noble metals, which represents the main drawback for the scalable application of these electrocatalysts on the commercial level, mainly due to their price and availability. Thus, the development of novel materials with enhanced electrocatalytic and/or photocatalytic activity towards sustainable energy conversion is highly desired.

An ammonia decomposition reaction is a promising alternative to fossil fuels that leads to the release of hydrogen and nitrogen, thus overcoming the challenges of hydrogen storage [30,31]. Ammonia is an ideal hydrogen carrier since it has a high gravimetric (17.8 wt. % H_2) and volumetric (121 kg H_2 m^{-3} in the liquid form) H_2 density and produces a high amount of CO_x free hydrogen after decomposition [30, 32]. Therefore, a clean process based on renewable energy sources to convert NH_3 to H_2 (as a fuel) and N_2 (as a harmless gas) is an important scientific challenge. The aqueous ammonia decomposition (1) is an uphill reaction and the required reaction energy can be provided by the sun light photons using photocatalyst materials [33].

$$NH_3(aq.) \rightarrow 3/2H_2(g) + 1/2N_2(g) \quad (1)$$

$$\Delta G_{298K} = 27 \text{ kJ mol}^{-1}$$

Currently, only a few photoactive materials are found to be able to decompose the aqueous ammonia solution, including TiO_2 [34–38], ZnO [39,40], ZnS [33], C_3N_4 [41], graphene, and other carbon based materials [42]. However, all these materials suffer from several drawbacks limiting their wide application in practice. TiO_2 is a very popular photoactive material that has relatively low cost, high chemical stability, and good light conversion efficiency. However, the efficiency is still relatively low because of the fast recombination of the photoinduced charge transfer. Another handicap is that TiO_2, for instance, works only under the UV illumination [34,39,40]. The complicated multiple-step synthesis of the photocatalysts using various toxic solvents (e.g., DMF) [40,42] limits the practical applicability of other photocatalysts. Therefore, the preparation of photocatalysts by green chemistry principles while relying on cheap and eco-friendly transition metal oxides as successful N_2 activators remains one of the major challenges in the field of photocatalytic decomposition of ammonia.

In this work, we show that the two-dimensional hematene can be synthesized by a green environmentally friendly scalable method from an earth abundant raw material—iron oxide ore specularite. The hematene sheets were a few nanometers in thickness and gave a satisfactory electrochemical performance in terms of the charge transfer limiting processes. Reflecting these properties, we exploited the combination of a conductive 2D hematene substrate with the catalytic surface of RuO_2 nanoparticles to test them as a photocatalytical platform suitable for the production of hydrogen under the visible light irradiation. The obtained results clearly proved that this nanocomposite exhibited a synergic effect in terms of the generation of electrons and holes. In this case, the holes oxidized the already absorbed ammonia through the quasi-metallic ruthenium oxide and left the electrons in hematene for the reduction of ammonia under the visible light irradiation. The excellent photocatalytic performance of the ruthenium oxide-loaded hematene supported by the fact that the entire photocatalyst can be prepared by environmentally friendly and scalable ways indicates that the developed strategy is viable for the fabrication of a novel class of photocatalysts suitable for the production of hydrogen.

2. Experimental

2.1. Common reagents

Potassium ferricyanide (p.a.) was purchased from Lachema (Brno, Czech Republic) and potassium chloride (p.a.) was obtained from Penta. Iron oxide ore specularite was obtained from the Moravian Museum (Brno, Czech Republic). The $RuCl_3.xH_2O$ (content of Ru: 38% min) and ammonium hydroxide (28 % NH_3) were purchased from Alfa Aesar. The magnesium oxide powder was purchased from Sigma Aldrich. Deionized water (DI) was used for the preparation of all aqueous solutions and dispersions.

2.2. Synthesis of hematene and loading with ruthenium

The hematite ore specularite was ground into a fine powder using a Retsch Planetary Ball Mill PM 100. The bulk sample was ball milled for 5 minutes, allowed to cool down to avoid excessive heating that might have led to undesirable effects, e.g., sintering, and then ball milled again for another 5 minutes. The ensued fine hematite powder (2 g) was dispersed in 180 mL of DI water, mixed thoroughly with a vertical rotator (Heidolph) at 45 rpm for 96 h, and sonicated in a bath sonicator (Branson; power output: 130 W, frequency: 40 kHz) for 48 h. The exfoliated hematene sheets were separated by sedimentation from the unexfoliated specularite and further processed to the desired concentration using centrifugation (centrifuge Sigma 4–16 K, Sigma Laborzentrifugen GmbH, Osterode am Harz, Germany) at 21 000 rcf. The unexfoliated powder of hematite was collected and used again for the preparation of hematene sheets.

The ruthenium loading was done via the impregnation method. First, the hematene powders were separated from the solution by centrifugation and dried at 80 °C for 1 h. After preparing the predefined concentration of $RuCl_3$ in DI water, the measured amount of dried hematene was added to the solution and stirred for 3 hours. Then the emulsion was centrifuged to separate the solid precipices from the supernatant. The centrifugation was repeated twice while it was washed with DI water to remove the extra amount of $RuCl_3$. Then, the powders were dried at 80 °C for 1 h and calcined at 300 °C for 3 h in air atmosphere.

2.3. Microscopic techniques

Scanning electron microscopy (SEM) and atomic force microscopy (AFM) analyses were performed with a FIB-SEM instrument SCIOS 2 (Thermo Fisher) equipped with an integrated AFM Litescope (NenoVision). The sample was analyzed on a Si wafer. The correlative probe and electron microscopy (CPEM) was used for the surface analysis, allowing simultaneous SEM and AFM data acquisition at the same place in the same coordinate system. For SEM imaging, an accelerating voltage of 2 kV, a beam current of 25 pA, and an ETD detector was deployed. The self-sensing Akiyama probe in the tapping mode was used for the AFM measurement. High-resolution TEM (HRTEM) images including STEM-HAADF (high-angle annular dark-field imaging) analyses for elemental mapping of the products were collected with an FEI Titan HRTEM microscope using an operating voltage of 80 kV. For these analyses, a droplet of dispersion of the material in ultrapure H_2O at a concentration of ~0.1 mg mL^{-1} was deposited onto a carbon-coated copper grid and

dried.

2.4. Spectroscopic measurements

The X-ray photoelectron spectroscopy (XPS) measurements were carried out by a PHI VersaProbe II probe (Physical Electronics) with an Al Ka source (15 kV, 50 W). The measured spectra were deconvoluted using the MultiPak software (Ulvac-PHI, Inc.). The Raman spectra for all the samples were recorded on a DXR Raman microscope using a diode laser with an excitation line of 633 nm. The EPR spectra were collected on a X-band (~9.14–9.17 GHz) spectrometer JEOL JES-X-320 equipped with a variable He temperature set-up ES-CT470 apparatus. The experimental temperature was set to 80 K. The quality factor (Q) was kept above 6000 for all measurements to make the spectra comparable. High purity quartz tubes (Suprasil, Wilmad, ≤0.5 OD) were used as a sample holder. The accuracy of the *g*-values was determined by comparing them with a Mn^{2+}/MgO standard (JEOL standard). The microwave power was set to 1.0 mW to avoid any power saturation effects. A modulation width of 1 mT and a modulation frequency of 100 kHz were used. All the EPR spectra were collected with a time constant of 30 ms and a sweep time of 4 min.

2.5. Structural and phase analysis

X-ray diffraction (XRD) patterns of bulk iron ore and exfoliated hematene samples were collected on a PANalytical X'Pert PRO diffractometer (iron-filtered Co Kα radiation: λ = 0.178901 nm, 40 kV and 30 mA) in a Bragg-Brentano geometry equipped with an X'Celerator detector, programmable divergence, and diffraction beam anti-scattering slits. Each sample was placed on a zero-background Si slide, gently pressed, and scanned in the 2θ range from 5° to 105° The phase identification was performed using PANalytical HighScore Plus software with PDF-4+ and ICSD databases.

2.6. Electrochemical measurements

All the electrochemical measurements in a three-electrode set-up were performed at ambient room temperature (22 ± 2 °C) using the Metrohm Autolab PGSTAT128N potentiostat (MetrohmAutolab B.V., Netherlands). The obtained electrochemical data sets were evaluated by the NOVA software package (version 1.11.2). The system comprised a glassy carbon electrode (GCE) serving as the working electrode, a platinum wire electrode used as the counter electrode and an Ag/AgCl (3 M KCl) electrode as the reference electrode. The GCE was modified as follows: a 10 μL drop of a sample dispersion in DI water (concentration of ≈ 1 mg mL^{-1}) was coated onto the surface of the GCE electrode and allowed to dry at ambient temperature to form a thin film. Potassium chloride (c = 1 mol L^{-1}) containing potassium ferricyanide (c = 5 mmol L^{-1}) as a redox probe served as a supporting electrolyte for impedance measurements. Individual settings for impedance spectroscopy measurements (EIS) are given in the Figure legends.

2.7. Photocatalyst characterization and photodecomposition of ammonia

The ultraviolet-visible diffuse reflectance spectra (UV–Vis DRS) of the synthesized samples were obtained by a Specord 250 plus (Analytik Jena, Jena, Germany) spectrophotometer. An integrating sphere was used to collect the spectrum. The magnesium oxide powder served as a background reference sample.

The photodecomposition of NH_3 was conducted in a 17.5 mL quartz reactor. After sono-dispersion of the photocatalyst in 10 mL of ammonium hydroxide, the rector was tightly sealed with a rubber septum. Since dissolved oxygen in a solution could act as an electron scavenger, it was bubbled with argon for 15 min to remove the oxygen. Then, the sample was illuminated under LED (Solis® High-Power LED from Thorlabs) with the power of 3 W·m^{-2} and a wavelength of 400–700 nm.

To avoid the thermal decomposition of ammonia, the reaction was conducted in a water bath to keep the temperature of the solution at 24 °C during the reaction. The photocatalytically evolved hydrogen was detected with a gas chromatograph GCMS-QP2010 SE (Shimadzu, Kyoto, Japan) and a TCD (Thermal conductivity detector) using Ar as carrier gas.

3. Results and discussion

3.1. Structural, morphological, and (electro)chemical characterization of hematene

Multi-layered hematene sheets were prepared via an exfoliation process from an (ultra)pure water dispersion of specularite, as discussed earlier in the experimental section. The morphology of the hematene sample was evaluated by a CPEM technique (combination of SEM and AFM analysis) and a HRTEM analysis, as shown in Fig. 1a–f and Fig. S1a–c. It is evident that the exfoliated sample was of a 2D-like nature with the lateral sizes in units of micrometers (Fig. 1a–c). Homogenous distribution of the individual elements such as iron or oxygen (Fig. S1b) implied high purity of the prepared hematene sample, which was affirmed by an EDAX analysis (Fig. S1c), ultimately confirming the dominant presence of these elements; the appearance of the copper element related to the grid used for the HRTEM analysis. The AFM analysis (Fig. 1b,c) and the related height profile (Fig. 1d) revealed that the thickness of the representative sheet was of around 5 nm. The thickness of the molecular dynamic simulated hematene (001) and (010) planes was estimated as 3.98 Å and 3.2 Å, respectively, corroborating a previously published report [28]. Thus, the thickness of 5 nm represented ≈ 12 hematene layers in the final product. A higher number of layers validates the theory that the selection of a chemical solvent decidedly affects the possibility of exfoliating the sample by ultrasonic irradiation up to individual layers [43]. As expected, the sonochemical preparation strategy of hematene from (ultra)pure water did not enable to provide a mono or two-layered system. To prove the size and thickness of the hematene material, CPEM images with related height profiles were collected from different sheets, and are depicted in Fig. S2. The 2D structure of the hematene sample was also confirmed from magnetic data measurements. Details of those experiments and related discussion are provided in the ESI. The composition of the product was also supported by XPS, as shown in the box (Fig. 1e,f). The obtained HR-XPS spectrum of the Fe 2p region (Fig. 1e) revealed two peaks at around 712 and 725 eV, corresponding to Fe $2p_{3/2}$ and Fe $2p_{1/2}$, respectively [28,44]. The satellite peak located at around 719 eV further indicated the Fe^{3+} oxidation state [44]. As evident from the deconvolution, both spin-orbit components were fitted with two peaks. These fitted peaks served more as a reference, indicating a trend based on already published studies [45,46]; the transition metals in their 2p states should be fitted by multiple components, representing the multiplet splitting. The HR-XPS spectrum of the O 1 s region (Fig. 1f) was fitted in three components, based on previous reports [47,48], corresponding to the lattice incorporated oxygen at higher binding energies and the surface present oxygen (in a defect state and as surface oxidation [28,47,48]) at lower binding energies, respectively.

The nature of the hematene sample was also evaluated by means of Raman spectroscopy. Fig. 2a shows the Raman spectra of original specularite ore in comparison with the hematene sample. The positions of the most important bands were found at around 224 and 495 cm^{-1} (A_{1g} modes) and 249, 290, 409, 611 cm^{-1} (E_g modes). The broad intense band visible at around 1318 cm^{-1} was connected with the scattering of two magnons in the structure of the hematite ore [49]. As expected, the hematene showed the position of the most important bands, similarly to specularite. Nevertheless, the additional band was observed at 663 cm^{-1}, which can be assigned to the structural disorders inside the crystal lattice (E_u modes) related to the 2D crystal structure [28,48,50,51]. The crystalline structure and chemical phase purity of both the original

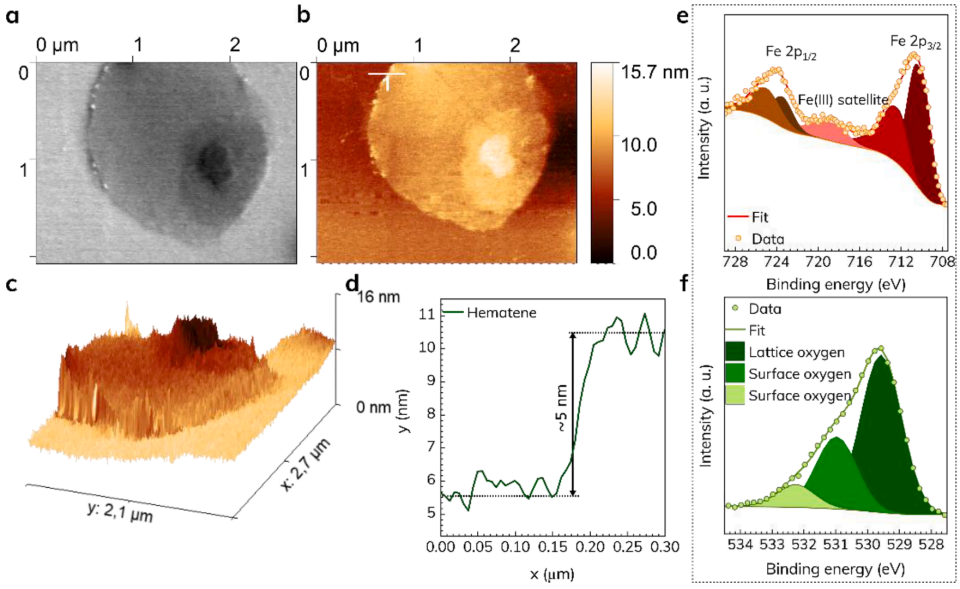

Fig. 1. (a–c) CPEM images of hematene sheet and related height profile (d); (e) HR-XPS spectrum of Fe 2p and (f) O 1 s region.

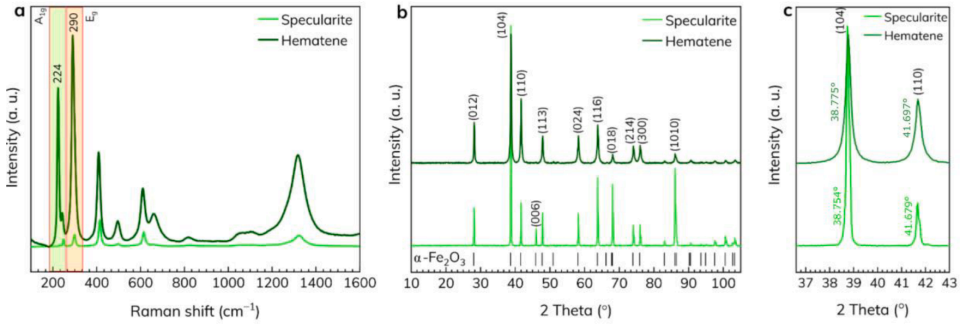

Fig. 2. (a) Raman spectra of specularite and hematene; (b) XRD patterns of specularite and hematene; (c) detail of XRD patterns showing the broadening and shift of hematene diffraction peaks compared to parent specularite.

specularite and the exfoliated hematene were additionally evaluated by XRD measurements (Fig. 2b). The collected patterns illustrate that both samples contained only the α-Fe_2O_3 phase of the corundum crystal structure (JCPDS card 01–089–0599, rhombohedral structure, space group R-3c), which rules out the presence of any other crystalline phases. The diffraction pattern of hematene (lattice parameters: a = 5.035 Å and c = 13.745 Å) showed that the diffraction peaks were slightly broadened and slightly shifted in their position, compared to the original specularite (lattice parameters: a = 5.034 Å and c = 13.742 Å). These effects are visible in Fig. 2c, providing a detail about the positions of the two diffraction peaks, where the diffraction on the (104) plane is typically dominant for the α-Fe_2O_3 structure. Such observation is consistent with the exfoliation of hematite in previous studies [28,52], where the broadening of the lines is related to the reduction in crystallite size [17, 53].

Prior to the modification of the hematene with ruthenium, the electrochemical performance of specularite and its 2D analogue was evaluated by means of impedance spectroscopy (EIS). Fig. 3a illustrates the EIS spectra as the Nyquist plot of a bare glassy carbon electrode (GCE) and GCE modified with the specularite precursor and the hematene sample. As visible in Fig. 3b, all EIS spectra should be fitted with a simple Randles circuit, which illustrates the non-complicated electrochemical behavior of all the tested materials. In general, resistance R_S located at point A (see Fig. 3b) was assigned to the solution resistance or the so-called ESR resistance (known also as the internal resistance), whereas the diameter of the semicircle $R_{AB} = R_B - R_A$ represented the sum of the electrode and contact resistance and the charge transfer resistance (R_{ct}) [54,55]. A magnified version of the Nyquist plot (inset of Fig. 3a) revealed that the charge transfer resistance (R_{ct}) increased significantly when the working electrode (R_{ct} = 40.4 Ω) was modified either with the specularite (R_{ct} = 222 Ω) or the hematene (R_{ct} = 173 Ω). Such behavior suggested the successful immobilization of both materials on the surface of the working electrode. It is perfectly clear that the diameter of the semicircle was smaller in favor of the hematene (inset of Fig. 3a), which reflected a better contact of the hematene film with the surface of the working electrode and thus a lower impact on the charge transfer limiting processes. Therefore, it can be expected that the electron transfer was enhanced in that case.

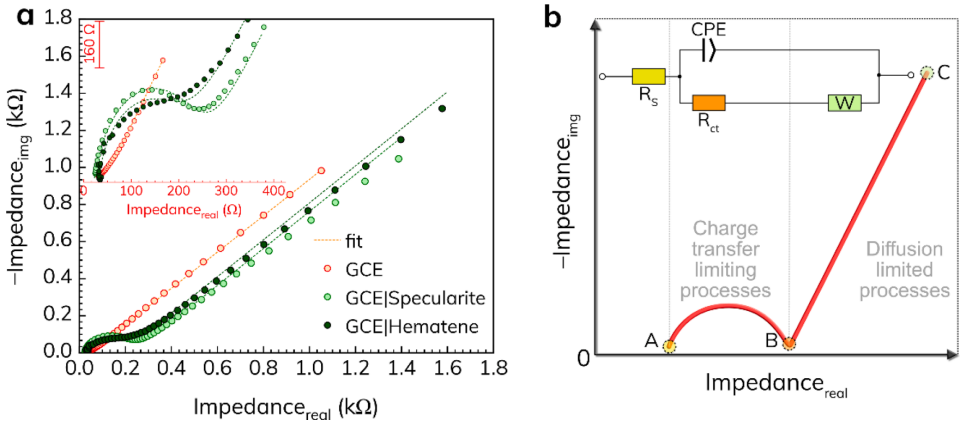

Fig. 3. (a) Nyquist plot of bare GCE and GCE modified with specularite and hematene; parameters of EIS: frequency range from 100 kHz to 0.1 Hz, the amplitude of 10 mV and half-wave potential of 0.24 V; (b) visualization of Nyquist plot and related equivalent circuit used for the data evaluation.

3.2. *Photocatalyst characterization*

Fig. 4 shows the HRTEM images of the hematene and the Ru-hematene together with the elemental analysis. The dominant crystal plane distance in the hematene was 2.7 Å, which was related to the (104) plane, while the presence of ruthenium oxide was confirmed by its dominant crystal plane distance 3.2 Å related to the (110) plane. Both structures in Ru-hematene were also identified by XRD (Fig. S6).

The EDS elemental analysis of the Ru-hematene showed a well dispersed ruthenium oxide particles without any sign of agglomeration at the surface of the hematene structure as catalyst sites for ammonia oxidation. This uniform dispersion of ruthenium oxide helped to increase the charge separation and therefore its photoactivity.

The XPS technique was employed to determine the oxidation states of the ruthenium in the Ru-hematene sample. As shown in Fig. 5a, the HR-XPS Ru 3d region was analyzed and deconvoluted to reveal two oxidation states of ruthenium. The Ru^{4+} peak at around 280.5 eV further proved the presence of RuO_2 species [56–58], which was in agreement with the EPR observations (Fig. 5d), and was reasonable to expect due to the heat treatment of the sample at 300 °C. The adjacent Ru^{3+} band below 282 eV indicated the existence of the Ru(III) [56,57,59] atoms, which can be further explained by the co-presence of the chlorine in this sample (1.2 at.% coming from the precursor) (Fig. S5). The carbon content (C 1 s peak) is intrinsic to the hematene itself and was not fully eliminated during the heating process. These XPS observations confirmed the previous characterization techniques as well as the photocatalytic activity [58–62]. Fig. 5b shows the valence band XPS (VB-XPS) of the hematene and the Ru-hematene. The position of the valence band edge of the hematene did not change after loading with ruthenium (+1.1 eV), while the density of states (DOS) showed an increase at around +0.5 eV below the Fermi level within the band gap. This tail was possibly due to the presence of the RuO_2 species, creating heterojunction at the surface of hematene, which provided a mid-band gap energy state levels around +0.5 eV below the hematene Fermi level (Fig. 5c). These energy state levels were able to facilitate the photogenerated hole transportation from the hematene to RuO_2 and oxidize ammonia to N_2 by providing orbital overlaps [63]. On the other hand, the photogenerated electrons went through the hematene and reduced the ammonia to hydrogen (Fig. 5c). This spatial charge separation in the place of RuO_2 and the hematene heterojunction resulted in higher photoactivity of this photocatalyst in comparison with the bare hematene.

To obtain more detailed information about the structure and the nature of the Ru coupling mechanism on hematene, we carried out an electron paramagnetic resonance (EPR) study at low temperature (T = 80 K). In a neat hematene, in spite of assuming the presence of a large number of spin-containing defects located on the edges of individual flakes, the recorded spectrum in a frozen water matrix was indeed EPR

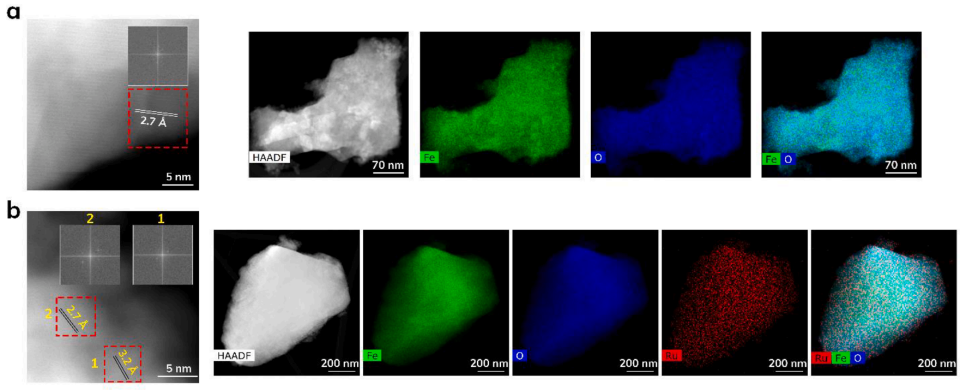

Fig. 4. HRTEM image (left), STEM-HAADF images and elemental EDS mapping (right) of (a) hematene and (b) Ru-hematene. The insets show the FFT patterns of the shown area by dashed red rectangle.

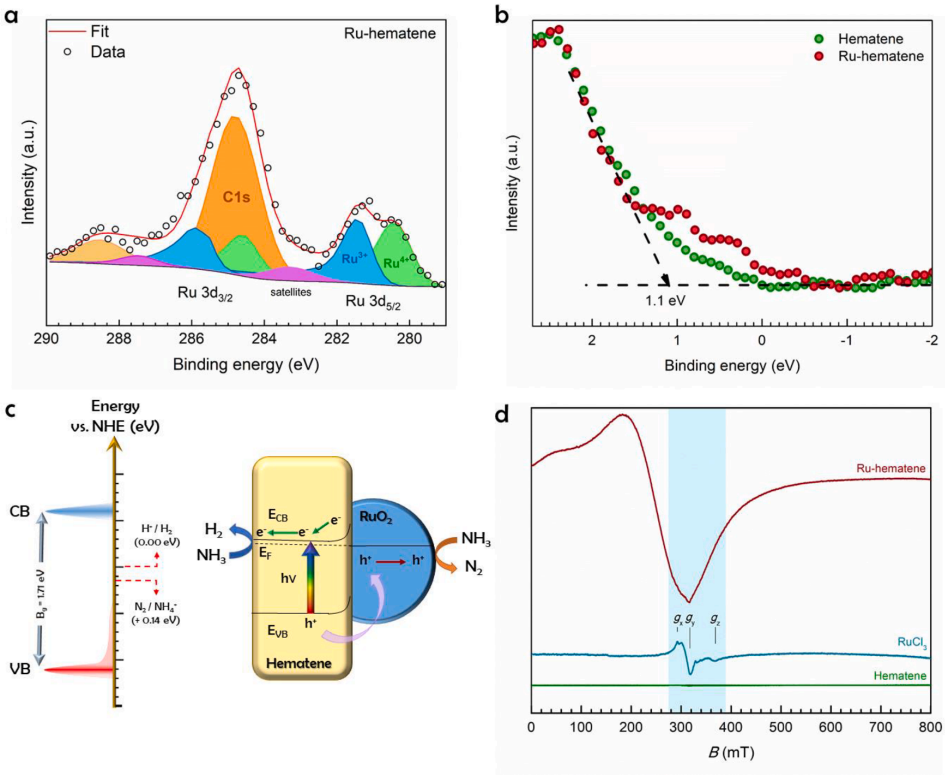

Fig. 5. (a) Deconvolution of HR-XPS of Ru 3d orbital of Ru-hematene photocatalyst; (b) Valence band XPS (VB-XPS) of hematene and Ru-hematene; (c) Schematic density of states (DOS) and band edge positions of the main electronic levels of Ru-hematene relative to the energy levels of the redox couples of aqueous ammonia (left) and the proposed mechanism of ammonia photodecomposition by Ru-hematene photocatalyst (right). (d) X-band CW EPR spectra of neat hematene (green line), $RuCl_3$ (blue spectrum) and EPR envelope of hematene decorated by RuO_2 nanoparticles (red curve), dispersed in DI H_2O and recorded in the frozen solution (T = 80 K).

silent (green line in Fig. 5d). Since, this material exhibited antiferromagnetic ordering at T below 250 K, this phenomenon was not unexpected. Nevertheless, a statistical percentage of an effective spin moment ($d\chi^{II}/dB \neq 0$) should be left at 80 K, which raises a question why these effective spins cannot be observed at X-band frequency. The reasoning can be back traced in the fast spin-lattice relaxation of the Fe^{3+} centers under an exchange coupled regime, and in the large zero-field splitting term arising from the coupling scheme, which renders the system to be more likely a non-Kramer multiplet.

The resulting EPR spectrum of $RuCl_3$ as the metal-salt source for the decoration of the hematene flakes is shown for comparison in Fig. 5d (blue line). The rhombic resonant line of Ru cations in +3 oxidation state showed small g-tensor anisotropy, with components at $g_x = 2.220$, $g_y = 2.094$ and $g_z = 1.802$. These g-values are typical for Ru^{3+} ions, however, here, they were slightly smaller than in the Ru^{3+} complexes coordinated to the organic frameworks [64] because of the absence of a strong ligand field. In Fig. 5d (red spectrum), the EPR envelope of Ru-hematene showed significant differences compared with the EPR spectra of the two previous reference samples. In the EPR spectrum of the composite Ru-hematene material, a very broad and asymmetric resonant line became dominant. This line exhibited an average g-value of about ~ 2.7, which was fully consistent with clustered Fe^{3+} cations on the layered surface that became perturbed by the Ru cations in a way that their antiferromagnetically coupling interaction, as seen in the neat hematene, was strongly weakened and therefore EPR detectable. We assume that the Ru ions reacted with oxygen on the top of the hematene surface to form small RuO_2 nanoparticles, and by doing so, they partially altered the fraction of the Fe-O-Fe superexchange path. Therefore, the observed effect on the resonance spectrum, combined with clear asymmetry in the broad resonance, suggests this was a surface localization of these defects, which is in full agreement with the 2D structure of the hematene flakes and the TEM analysis (Fig. S1a). Furthermore, in the area highlighted in blue in the EPR spectrum of the Ru-hematene (Fig. 5d), a weak modulation of an Fe^{3+} envelope around 310 mT was observed. It was positioned at $g \sim 2.09$, a value that is in line with the signal of Ru^{3+}, and probably located on the surface of the RuO_2 nanoparticles, as usually observed [65]. Since the Ru loading was very low, and we could detect only the Ru^{3+} species via EPR, the signal of Ru was observed as weak modulation in the broad resonant line of Fe^{3+}. However, part of the Ru^{3+} fragments in the EPR spectrum can also be an indicator of a small amount of residual $RuCl_3$ salt in the resulting material, which was also observed in XPS.

3.3. *Photocatalytic decomposition of HN_3 via ruthenium loaded hematene*

Prior to photocatalytical experiments, both pristine and Ru-hematene were evaluated by means of UV–VIS spectroscopy to assess the suitability of both materials for photodecomposition of ammonia. The band edge absorption for both samples was around 729 nm, as shown in Fig. 6a. Therefore, these materials can absorb both UV and a visible part of the light spectrum. The reason for the dark red color in the samples is also related to this wide absorption region. The amount of

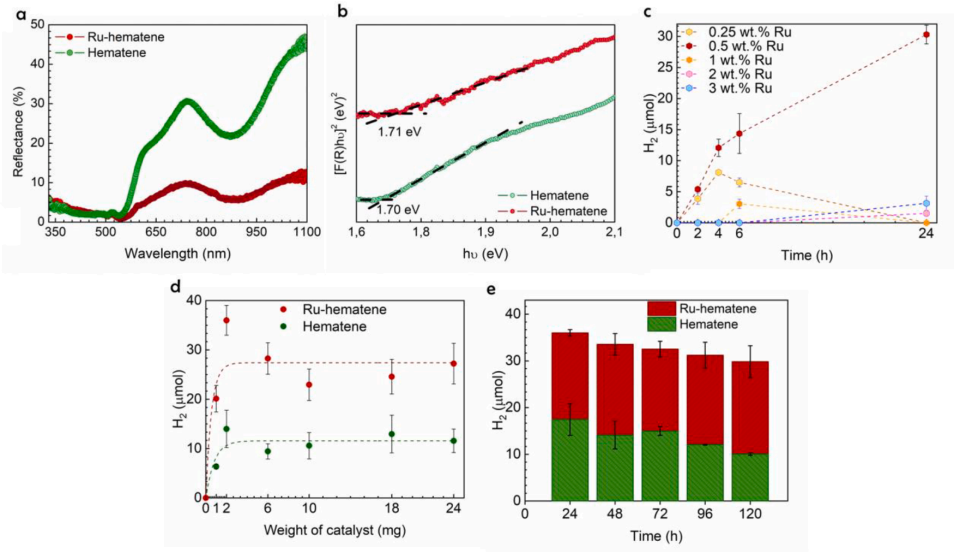

Fig. 6. (a) UV–VIS DRS of hematene and Ru-hematene and (b) corresponding Tauc plot based on Kubelka-Munk model to calculate the optical band gap of hematene and Ru-hematene; (c) Optimizing the loading amount of Ru co-catalyst for H_2 evolution of ammonia photodecomposition. The reactors were loaded with 8 mg of photocatalyst; (d) The amount of evolved H_2 from photodecomposition of ammonia with different loading amount of pristine hematene and Ru-hematene. The reactors were under illumination for 24 hours; (e) Reusability of 2 mg of hematene and Ru-hematene for H_2 evolution from ammonia photo decomposition. After each cycle, the solution was sonicated and bubbled with Ar for 15 min. In all cases, the reactor was under visible LED illumination (wavelength from 400 to 700 nm, power 3 $W{\cdot}m^{-2}$).

light absorption (especially in the visible region) was highly increased after adding ruthenium. This huge increase in visible light absorption fulfills one of the main conditions of an ideal photocatalyst for photocatalytic reactions. To highlight this unique property of current photocatalysts, all of the photoreactions in this work were conducted under the visible part of the light (wavelength 400–700 nm). The optical band gap energy of the hematene and the Ru-hematene calculated by the Tauc plot [66] based on the Kubelka-Munk [67] theory was 1.70 and 1.71 eV, respectively (Fig. 6b). It should be noted that in spite of the huge difference in absorbed light, the band gap of the photocatalysts was almost the same.

As discussed in detail, the presence of RuO_2 was proved by the surface XPS analysis (Fig. 5a). This oxidation occurred probably during the calcination step at 300 °C. Nagaoka and coworkers [68] reported that RuO_2 produces a catalytic surface for exothermic adsorption of NH_3. This chemisorption of ammonia decreased the overall thermodynamic energy needed for its decomposition. Then, the subsequent photo absorption by hematene resulted in the generation of electrons and holes. The holes were able to oxidize the already absorbed NH_3 through the quasi-metallic ruthenium oxide and left the electrons in the hematene for the reduction of the ammonia.

The control experiments show that the catalytic activity of hematene and ruthenium loaded hematene for decomposition of ammonia under dark condition is almost zero. Furthermore, the photodecomposition of ammonia as ammonium hydroxide without the presence of photocatalyst at 24 °C is zero.

After the ruthenium oxide was confirmed as a proper co-catalyst for hematene to decompose the ammonia, the loading optimization of Ru was performed. Fig. 6c shows that loading the hematene with the optimum amount of Ru—0.5 wt. %—led to a continuously increased amount of H_2. In lower amounts of the Ru loading, the charge separation was not effective enough to produce hydrogen, while a higher amount of Ru was able to produce charge recombination centers at the surface of the hematene [68]. All the characterization was done while loading the hematene with 0.5 wt.% of Ru, labelled as Ru-hematene.

To have a fair and reliable comparison between the photoactivity of the hematene and the Ru-hematene, the mass of the photocatalyst had to be optimized against the photoactivity (Fig. 6d and Fig. S4). The reason is that the amount of the H_2 production during the photocatalytic reaction is not necessarily proportional to the mass of the photocatalyst due to the limitation of light absorption and diffusion conditions [69, 70]. It is obvious from Fig. 6d that the loading of 2 mg of the photocatalyst in both cases was able to produce the optimum amount of the product. This plot shows that the Ru-hematene photocatalyst produced 2.5 times more H_2 than the pristine hematene under optimum conditions.

The Ru-hematene showed an 11% decrease in activity after five photocatalytic runs for the total of 120 h (Fig. 6e). A constant decrease in activity after each run could be correlated to a loss in the photocatalyst caused by the attachment to the reactor walls and even to the magnet stirrer. Additionally, as the catalyst was not washed after each run of the photoreaction, the surface of the catalyst could have been passivated by reactants, products or intermediate species.

4. Conclusions

A non-van der Waals 2D material, hematene, was simply prepared via the exfoliation of iron oxide ore specularite, deploying an (ultra)pure water solution. Using this strategy, the prepared material exhibited favorable electrochemical properties in terms of charge transfer and diffusion limiting processes. As a proof-of-concept, we have amply demonstrated that this pure n-vdW material can be easily modified with ruthenium oxide nanoparticles and can serve as a catalytic eco-friendly platform for the photocatalytic decomposition of an aqueous solution of ammonia in order to produce hydrogen via the visible light irradiation. The obtained results proved that the combination of RuO_2 catalytic surface with the conductive 2D hematene substrate exhibited a synergic effect in terms of the generation of electrons and holes. Based on the results, the holes were able to oxidize the already absorbed ammonia through the quasi-metallic ruthenium oxide and left the electrons in the

hematene for the reduction of ammonia. Experimental data indicate that the optimum dosage of ruthenium was around 0.5 wt %, yielding the maximum amount of hydrogen after 24 hours. With respect to the pristine hematene, a co-doped material provided at least 2.5 times better photocatalytic response towards hydrogen evolution. Without any cleaning steps, the Ru-hematene photocatalyst exhibited only 11 % of the photocatalytic reaction decrease after five successful photocatalytic runs, predisposing it for practical application. The discovery opens up possibilities for creating robust and effective photocatalysts for a wide range of applications using non-van der Waals 2D materials and metal oxide nanoparticles.

CRediT authorship contribution statement

Jana Dzíbelová: Investigation, Writing – original draft, Writing – review & editing. **S.M. Hossein Hejazi:** Conceptualization, Investigation, Writing – original draft, Writing – review & editing. **Veronika Šedajová:** Investigation, Writing – original draft. **David Panáček:** Investigation, Writing – original draft. **Petr Jakubec:** Conceptualization, Writing – original draft, Writing – review & editing. **Zdeněk Baďura:** Investigation, Writing – original draft. **Ondřej Malina:** Investigation, Writing – original draft, Writing – review & editing. **Josef Kašlík:** Investigation. **Jan Filip:** Conceptualization. **Štěpán Kment:** Conceptualization. **Michal Otyepka:** Conceptualization, Writing – review & editing. **Radek Zbořil:** Conceptualization, Writing – original draft, Writing – review & editing.

Declaration of Competing Interest

The authors declare that they have no known competing financial interests or personal relationships that could have appeared to influence the work reported in this paper.

Data availability

Data will be made available on request.

Acknowledgments

R.Z. acknowledges the support from the Czech Science Foundation, project No. 19–27454X. P.J. acknowledges the Research Infrastructure NanoEnviCz, supported by the Ministry of Education, Youth and Sports of the Czech Republic under Project No. LM2018124. We also acknowledge the support from ERDF/ESF "Nano4Future" (No. CZ.02.1.01/0.0/0.0/16_019/0000754) and the Technology Agency of the Czech Republic, Program TREND (GEFSEM, FW01010183). The authors gratefully thank Ondřej Tomanec (HR-TEM); Jiří Hošek (CPEM); Kateřina Roháčová (Raman); and Jan Pauswang (part of electrochemical testing).

Supplementary materials

Supplementary material associated with this article can be found, in the online version, at doi:10.1016/j.apmt.2023.101881.

References

[1] A. Gupta, T. Sakthivel, S. Seal, Recent development in 2D materials beyond graphene, Prog. Mater. Sci. 73 (2015) 44–126, https://doi.org/10.1016/j.pmatsci.2015.02.002.
[2] Z. Lin, Y. Liu, U. Halim, M. Ding, Y. Liu, Y. Wang, C. Jia, P. Chen, X. Duan, C. Wang, F. Song, M. Li, C. Wan, Y. Huang, X. Duan, Solution-processable 2D semiconductors for high-performance large-area electronics, Nature 562 (2018) 254–258, https://doi.org/10.1038/s41586-018-0574-4.
[3] Q.A. Vu, Y.S. Shin, Y.R. Kim, V.L. Nguyen, W.T. Kang, H. Kim, D.H. Luong, I. M. Lee, K. Lee, D.S. Ko, J. Heo, S. Park, Y.H. Lee, W.J. Yu, Two-terminal floating-gate memory with van der Waals heterostructures for ultrahigh on/off ratio, Nat. Commun. 7 (2016) 12725, https://doi.org/10.1038/ncomms12725.
[4] S. Jiao, L. Liu, J. Wang, K. Ma, J. Lv, A novel biosensor based on molybdenum disulfide (MoS_2) modified porous anodic aluminum oxide nanochannels for ultrasensitive microRNA-155 detection, Small 16 (2020), 2001223, https://doi.org/10.1002/smll.202001223.
[5] X. Chen, Y.J. Park, M. Kang, S.K. Kang, J. Koo, S.M. Shinde, J. Shin, S. Jeon, G. Park, Y. Yan, M.R. MacEwan, W.Z. Ray, K.M. Lee, J.A. Rogers, J.H. Ahn, CVD-grown monolayer MoS_2 in bioabsorbable electronics and biosensors, Nat. Commun. 9 (2018) 1690, https://doi.org/10.1038/s41467-018-03956-9.
[6] T. Kaewmaraya, L. Ngamwongwan, P. Moontragoon, W. Jarernboon, D. Singh, R. Ahuja, A. Karton, T. Hussain, Novel green phosphorene as a superior chemical gas sensing material, J. Hazard. Mater. 401 (2021), 123340, https://doi.org/10.1016/j.jhazmat.2020.123340.
[7] D. Kundu, B.D. Adams, V. Duffort, S.H. Vajargah, L.F. Nazar, A high-capacity and long-life aqueous rechargeable zinc battery using a metal oxide intercalation cathode, Nat. Energy 1 (2016) 16119, https://doi.org/10.1038/nenergy.2016.119.
[8] M. Jana, R. Xu, X.B. Cheng, J.S. Yeon, J.M. Park, J.Q. Huang, Q. Zhang, H.S. Park, Rational design of two-dimensional nanomaterials for lithium–sulfur batteries, Energy Environ. Sci. 13 (2020) 1049–1075, https://doi.org/10.1039/C9EE02049G.
[9] A.S. Agnihotri, A. Varghese, N. M, Transition metal oxides in electrochemical and bio sensing: a state-of-art review, Appl. Surf. Sci. Adv. 4 (2021), 100072, https://doi.org/10.1016/j.apsadv.2021.100072.
[10] C. Gong, L. Li, Z. Li, H. Ji, A. Stern, Y. Xia, T. Cao, W. Bao, C. Wang, Y. Wang, Z. Q. Qiu, R.J. Cava, S.G. Louie, J. Xia, X. Zhang, Discovery of intrinsic ferromagnetism in two-dimensional van der Waals crystals, Nature 546 (2017) 265–269, https://doi.org/10.1038/nature22060.
[11] B. Huang, G. Clark, E. Navarro-Moratalla, D.R. Klein, R. Cheng, K.L. Seyler, D. Zhong, E. Schmidgall, M.A. McGuire, D.H. Cobden, W. Yao, D. Xiao, P. Jarillo-Herrero, X. Xu, Layer-dependent ferromagnetism in a van der Waals crystal down to the monolayer limit, Nature 546 (2017) 270–273, https://doi.org/10.1038/nature22391.
[12] H. Wang, J. Chen, Y. Lin, X. Wang, J. Li, Y. Li, L. Gao, L. Zhang, D. Chao, X. Xiao, J.-M. Lee, Electronic modulation of non-van der Waals 2D electrocatalysts for efficient energy conversion, Adv. Mater. 33 (2021), 2008422, https://doi.org/10.1002/adma.202008422.
[13] Y. Wang, Z. Zhang, Y. Mao, X. Wang, Two-dimensional nonlayered materials for electrocatalysis, Energy Environ. Sci. 13 (2020) 3993–4016, https://doi.org/10.1039/D0EE01714K.
[14] X. Huang, S. Tang, X. Mu, Y. Dai, G. Chen, Z. Zhou, F. Ruan, Z. Yang, N. Zheng, Freestanding palladium nanosheets with plasmonic and catalytic properties, Nat. Nanotechnol. 6 (2011) 28–32, https://doi.org/10.1038/nnano.2010.235.
[15] M. Luo, Z. Zhao, Y. Zhang, Y. Sun, Y. Xing, F. Lv, Y. Yang, X. Zhang, S. Hwang, Y. Qin, J.Y. Ma, F. Lin, D. Su, G. Lu, S. Guo, PdMo bimetallene for oxygen reduction catalysis, Nature 574 (2019) 81–85, https://doi.org/10.1038/s41586-019-1603-7.
[16] H. Duan, N. Yan, R. Yu, C.R. Chang, G. Zhou, H.S. Hu, H. Rong, Z. Niu, J. Mao, H. Asakura, T. Tanaka, P.J. Dyson, J. Li, Y. Li, Ultrathin rhodium nanosheets, Nat. Commun. 5 (2014) 3093, https://doi.org/10.1038/ncomms4093.
[17] A. Zavabeti, J.Z. Ou, B.J. Carey, N. Syed, R. Orrell-Trigg, E.L.H. Mayes, C. Xu, O. Kavehei, A.P. O'Mullane, R.B. Kaner, K. Kalantar-zadeh, T. Daeneke, A liquid metal reaction environment for the room-temperature synthesis of atomically thin metal oxides, Science 358 (2017) 332–335, https://doi.org/10.1126/science.aao4249.
[18] Y. Dou, J. Xu, B. Ruan, Q. Liu, Y. Pan, Z. Sun, S.X. Dou, Atomic layer-by-Layer Co_3O_4/graphene composite for high performance lithium-ion batteries, Adv. Energy Mater. 6 (2016), 1501835, https://doi.org/10.1002/aenm.201501835.
[19] S. Qamar, F. Lei, L. Liang, S. Gao, K. Liu, Y. Sun, W. Ni, Y. Xie, Ultrathin TiO_2 flakes optimizing solar light driven CO_2 reduction, Nano Energy 26 (2016) 692–698, https://doi.org/10.1016/j.nanoen.2016.06.029.
[20] J. Cao, T. Li, H. Gao, Y. Lin, X. Wang, H. Wang, T. Palacios, X. Ling, Realization of 2D crystalline metal nitrides via selective atomic substitution, Sci. Adv. 6 (2020) eaax8784, https://doi.org/10.1126/sciadv.aax8784.
[21] H. Wu, X. Lu, G. Zheng, G.W. Ho, Topotactic engineering of ultrathin 2D nonlayered nickel selenides for full water electrolysis, Adv. Energy Mater. 8 (2018), 1702704, https://doi.org/10.1002/aenm.201702704.
[22] C. Jin, L. Kou, Two-dimensional non-van der Waals magnetic layers: functional materials for potential device applications, J. Phys. Appl. Phys. 54 (2021), 413001, https://doi.org/10.1088/1361-6463/ac08ca.
[23] R. Ramírez-Jiménez, M. Franco, E. Rodrigo, R. Sainz, R. Ferritto, A.M. Lamsabhi, J. L. Aceña, M.B. Cid, Unexpected reactivity of graphene oxide with DBU and DMF, J. Mater. Chem. A 6 (2018) 12637–12646, https://doi.org/10.1039/C8TA03529F.
[24] J. Mráz, H. Cross, A. Gescher, M.D. Threadgill, J. Flek, Differences between rodents and humans in the metabolic toxification of N,N-dimethylformamide, Toxicol. Appl. Pharmacol. 98 (1989) 507–516, https://doi.org/10.1016/0041-008X(89)90179-8.
[25] G. Groth, K. Kronauer, K.J. Freundt, Effects of N,N-dimethylformamide and its degradation products in zebrafish embryos, Toxicol. *In Vitro* 8 (1994) 401–406, https://doi.org/10.1016/0887-2333(94)90161-9.
[26] Commission Regulation (EU) 2021/2030 of 19 November 2021 amending Annex XVII to Regulation (EC) No 1907/2006 of the European Parliament and of the Council concerning the Registration, Evaluation, Authorisation and Restriction of Chemicals (REACH) as regards N,N-dimethylformamide (Text with EEA relevance). Document 32021R2030. https://eur-lex.europa.eu/legal-content/EN/TXT/PDF/?uri=CELEX:32021R2030&from=EN.

[27] N.S. Lewis, D.G. Nocera, Powering the planet: chemical challenges in solar energy utilization, Proc. Natl. Acad. Sci. 103 (2006) 15729–15735, https://doi.org/10.1073/pnas.0603395103.

[28] A. Puthirath Balan, S. Radhakrishnan, C.F. Woellner, S.K. Sinha, L. Deng, C. de los Reyes, B.M. Rao, M. Paulose, R. Neupane, A. Apte, V. Kochat, R. Vajtai, A. R. Harutyunyan, C.W. Chu, G. Costin, D.S. Galvao, A.A. Martí, P.A. van Aken, O. K. Varghese, C.S. Tiwary, A. Malie Madom Ramaswamy Iyer, P.M. Ajayan, Exfoliation of a non-van der Waals material from iron ore hematite, Nat. Nanotechnol. 13 (2018) 602–609, https://doi.org/10.1038/s41565-018-0134-y.

[29] A. Puthirath Balan, S. Radhakrishnan, R. Kumar, R. Neupane, S.K. Sinha, L. Deng, C.A. Reyes, A. Apte, B.M. Rao, M. Paulose, R. Vajtai, C.W. Chu, G. Costin, A. A. Martí, O.K. Varghese, A.K. Singh, C.S. Tiwary, M.R. Anantharaman, P. M. Ajayan, A non-van der Waals two-dimensional material from natural titanium mineral ore Ilmenite, Chem. Mater. 30 (2018) 5923–5931, https://doi.org/10.1021/acs.chemmater.8b01935.

[30] F. Schüth, R. Palkovits, R. Schlögl, D.S. Su, Ammonia as a possible element in an energy infrastructure: catalysts for ammonia decomposition, Energy Environ. Sci. 5 (2012) 6278–6289, https://doi.org/10.1039/C2EE02865D.

[31] S. Zhang, Z. He, X. Li, J. Zhang, Q. Zang, S. Wang, Building heterogeneous nanostructures for photocatalytic ammonia decomposition, Nanoscale. Adv. 2 (2020) 3610–3623, https://doi.org/10.1039/D0NA00161A.

[32] W.I.F. David, J.W. Makepeace, S.K. Callear, H.M.A. Hunter, J.D. Taylor, T.J. Wood, M.O. Jones, Hydrogen production from ammonia using sodium amide, J. Am. Chem. Soc. 136 (2014) 13082–13085, https://doi.org/10.1021/ja5042836.

[33] A. Iwase, K. Ii, A. Kudo, Decomposition of an aqueous ammonia solution as a photon energy conversion reaction using a Ru-loaded ZnS photocatalyst, Chem. Commun. 54 (2018) 6117–6119, https://doi.org/10.1039/C8CC02639D.

[34] A. Utsunomiya, A. Okemoto, Y. Nishino, K. Kitagawa, H. Kobayashi, K. Taniya, Y. Ichihashi, S. Nishiyama, Mechanistic study of reaction mechanism on ammonia photodecomposition over Ni/TiO_2 photocatalysts, Appl. Catal. B Environ. 206 (2017) 378–383, https://doi.org/10.1016/j.apcatb.2017.01.045.

[35] K. Obata, K. Kishishita, A. Okemoto, K. Taniya, Y. Ichihashi, S. Nishiyama, Photocatalytic decomposition of NH_3 over TiO_2 catalysts doped with Fe, Appl. Catal. B Environ. 160–161 (2014) 200–203, https://doi.org/10.1016/j.apcatb.2014.05.033.

[36] E. Bahadori, F. Conte, A. Tripodi, G. Ramis, I. Rossetti, Photocatalytic selective oxidation of ammonia in a semi-batch reactor: unravelling the effect of reaction conditions and metal co-catalysts, Catalysts 11 (2021) 209, https://doi.org/10.3390/catal11020209.

[37] H. Yuzawa, T. Mori, H. Itoh, H. Yoshida, Reaction mechanism of ammonia decomposition to nitrogen and hydrogen over metal loaded titanium oxide photocatalyst, J. Phys. Chem. C 116 (2012) 4126–4136, https://doi.org/10.1021/jp209795t.

[38] Y. Shu, J. Ji, M. Zhou, S. Liang, Q. Xie, S. Li, B. Liu, J. Deng, J. Cao, S. Liu, H. Huang, Selective photocatalytic oxidation of gaseous ammonia at ppb level over Pt and F modified TiO_2, Appl. Catal. B Environ. 300 (2022), 120688, https://doi.org/10.1016/j.apcatb.2021.120688.

[39] M. Reli, M. Edelmannová, M. Šihor, P. Praus, L. Svoboda, K.K. Mamulová, H. Otoupalíková, L. Čapek, A. Hospodková, L. Obalová, K. Kočí, Photocatalytic H_2 generation from aqueous ammonia solution using ZnO photocatalysts prepared by different methods, Int. J. Hydrog. Energy. 40 (2015) 8530–8538, https://doi.org/10.1016/j.ijhydene.2015.05.004.

[40] Z. Mohammadi, S. Sharifnia, Y. Shavisi, Photocatalytic degradation of aqueous ammonia by using TiO2ZnO/LECA hybrid photocatalyst, Mater. Chem. Phys. 184 (2016) 110–117, https://doi.org/10.1016/j.matchemphys.2016.09.031.

[41] H. Wang, Y. Su, H. Zhao, H. Yu, S. Chen, Y. Zhang, X. Quan, Photocatalytic oxidation of aqueous ammonia using atomic single layer graphitic-C_3N_4, Environ. Sci. Technol. 48 (2014) 11984–11990, https://doi.org/10.1021/es503073z.

[42] R. Wang, T. Xie, Z. Sun, T. Pu, W. Li, J.P. Ao, Graphene quantum dot modified g-C_3N_4 for enhanced photocatalytic oxidation of ammonia performance, RSC Adv. 7 (2017) 51687–51694, https://doi.org/10.1039/C7RA07988E.

[43] H. Xu, B.W. Zeiger, K.S. Suslick, Sonochemical synthesis of nanomaterials, Chem. Soc. Rev. 42 (2013) 2555–2567, https://doi.org/10.1039/C2CS35282F.

[44] T. Fujii, F.M.F. de Groot, G.A. Sawatzky, F.C. Voogt, T. Hibma, K. Okada, In situ XPS analysis of various iron oxide films grown by NO_2-assisted molecular-beam epitaxy, Phys. Rev. B 59 (1999) 3195–3202, https://doi.org/10.1103/PhysRevB.59.3195.

[45] R.P. Gupta, S.K. Sen, Calculation of multiplet structure of core p -vacancy levels. II, Phys. Rev. B 12 (1975) 15–19, https://doi.org/10.1103/PhysRevB.12.15.

[46] M.C. Biesinger, B.P. Payne, A.P. Grosvenor, L.W.M. Lau, A.R. Gerson, R.S.C. Smart, Resolving surface chemical states in XPS analysis of first row transition metals, oxides and hydroxides: Cr, Mn, Fe, Co and Ni, Appl. Surf. Sci. 257 (2011) 2717–2730, https://doi.org/10.1016/j.apsusc.2010.10.051.

[47] X. Lu, Y. Zeng, M. Yu, T. Zhai, C. Liang, S. Xie, M.-S. Balogun, Y. Tong, Oxygen-deficient hematite nanorods as high-performance and novel negative electrodes for flexible asymmetric supercapacitors, Adv. Mater. 26 (2014) 3148–3155, https://doi.org/10.1002/adma.201305851.

[48] S. Chahal, S.M. Kauzlarich, P. Kumar, Microwave synthesis of hematene and other two-dimensional oxides, ACS Mater. Lett. 3 (2021) 631–640, https://doi.org/10.1021/acsmaterialslett.1c00102.

[49] D.L.A. de Faria, S. Venâncio Silva, M.T. de Oliveira, Raman microspectroscopy of some iron oxides and oxyhydroxides, J. Raman Spectrosc. 28 (1997) 873–878, https://doi.org/10.1002/(SICI)1097-4555(199711)28:11<873::AID-JRS177>3.0.CO;2-B.

[50] A. Thejas Prasannakumar, B. C, R. R, R.F. U, R. Philip, S.J Varma, Hematene nanoflakes: a non-van der Waals material with superior nonlinear optical properties, ACS Appl. Opt. Mater. (2022), https://doi.org/10.1021/acsaom.2c00071.

[51] S.-H. Shim, T.S. Duffy, Raman spectroscopy of Fe_2O_3 to 62GPa, Am. Mineral. 87 (2002) 318–326, https://doi.org/10.2138/am-2002-2-314.

[52] Z. Zhang, M. Ye, E.J. Harvey, G. Merle, Editors' choice—methanol electrooxidation with platinum decorated hematene nanosheet, J. Electrochem. Soc. 166 (2019) H135, https://doi.org/10.1149/2.0661904jes.

[53] U. Holzwarth, N. Gibson, The Scherrer equation versus the "Debye-Scherrer equation, Nat. Nanotechnol. 6 (2011) 534, https://doi.org/10.1038/nnano.2011.145.

[54] B.-Y. Chang, S.-M. Park, Electrochemical impedance spectroscopy, Annu. Rev. Anal. Chem. 3 (2010) 207–229, https://doi.org/10.1146/annurev.anchem.012809.102211.

[55] A.R.C. Bredar, A.L. Chown, A.R. Burton, B.H. Farnum, Electrochemical impedance spectroscopy of metal oxide electrodes for energy applications, ACS Appl. Energy Mater. 3 (2020) 66–98, https://doi.org/10.1021/acsaem.9b01965.

[56] D.J. Morgan, Resolving ruthenium: XPS studies of common ruthenium materials, Surf. Interface Anal. 47 (2015) 1072–1079, https://doi.org/10.1002/sia.5852.

[57] J.Y. Shen, A. Adnot, S. Kaliaguine, An ESCA study of the interaction of oxygen with the surface of ruthenium, Appl. Surf. Sci. 51 (1991) 47–60, https://doi.org/10.1016/0169-4332(91)90061-N.

[58] S. Hao, M. Liu, J. Pan, X. Liu, X. Tan, N. Xu, Y. He, L. Lei, X. Zhang, Dopants fixation of Ruthenium for boosting acidic oxygen evolution stability and activity, Nat. Commun. 11 (2020) 5368, https://doi.org/10.1038/s41467-020-19212-y.

[59] S. Cattaneo, H. Naslhajian, F. Somodi, C. Evangelisti, A. Villa, L. Prati, Ruthenium on carbonaceous materials for the selective hydrogenation of HMF, Molecules 23 (2018) 2007, https://doi.org/10.3390/molecules23082007.

[60] R. Bavand, A. Yelon, E. Sacher, X-ray photoelectron spectroscopic and morphologic studies of Ru nanoparticles deposited onto highly oriented pyrolytic graphite, Appl. Surf. Sci. 355 (2015) 279–289, https://doi.org/10.1016/j.apsusc.2015.06.202.

[61] N. Chakroune, G. Viau, S. Ammar, L. Poul, D. Veautier, M.M. Chehimi, C. Mangeney, F. Villain, F. Fiévet, Acetate- and Thiol-Capped Monodisperse Ruthenium Nanoparticles: XPS, XAS, and HRTEM Studies, Langmuir 21 (2005) 6788–6796, https://doi.org/10.1021/la050706c.

[62] Q. Liu, B. Lu, F. Nichols, J. Ko, R. Mercado, F. Bridges, S. Chen, Rapid preparation of carbon-supported ruthenium nanoparticles by magnetic induction heating for efficient hydrogen evolution reaction in both acidic and alkaline media, SusMat 2 (2022) 335–346, https://doi.org/10.1002/sus2.66.

[63] S.M.H. Hejazi, M. Shahrezaei, P. Błoński, M. Allieta, P.M. Sheverdyaeva, P. Moras, Z. Baďura, S. Kalytchuk, E. Mohammadi, R. Zbořil, Š. Kment, M. Otyepka, A. Naldoni, P. Fornasiero, Defect engineering over anisotropic brookite toward substrate-specific photo-oxidation of alcohols, Chem. Catal. 2 (2022) 1177–1190, https://doi.org/10.1016/j.checat.2022.03.015.

[64] Y. Gao, J.K. Kuncheria, H.A. Jenkins, R.J. Puddephatt, G.P.A. Yap, The interconversion of formic acid and hydrogen/carbon dioxide using a binuclear ruthenium complex catalyst, J. Chem. Soc. Dalton Trans. (2000) 3212–3217, https://doi.org/10.1039/b004234j.

[65] M. Lin, L.X. Dai, J. Gu, L.Q. Kang, Y.H. Wang, R. Si, Z.Q. Zhao, W.C. Liu, X. Fu, L. D. Sun, Y.W. Zhang, C.H. Yan, Moderate oxidation levels of Ru nanoparticles enhance molecular oxygen activation for cross-dehydrogenative-coupling reactions via single electron transfer, RSC Adv. 7 (2017) 33078–33085, https://doi.org/10.1039/C7RA05726A.

[66] J. Tauc, R. Grigorovici, V. Vancu, Optical properties and electronic structure of amorphous germanium, Phys. Stat. Sol. 15 (1966) 627–637.

[67] P. Makuła, M. Pacia, W. Macyk, How to correctly determine the band gap energy of modified semiconductor photocatalysts based on UV–Vis spectra, J. Phys. Chem. Lett. 9 (2018) 6814–6817, https://doi.org/10.1021/acs.jpclett.8b02892.

[68] K. Nagaoka, T. Eboshi, Y. Takeishi, R. Tasaki, K. Honda, K. Imamura, K. Sato, Carbon-free H_2 production from ammonia triggered at room temperature with an acidic RuO_2/γ-Al_2O_3 catalyst, Sci. Adv. 3 (2017), e1602747, https://doi.org/10.1126/sciadv.1602747.

[69] S. Cao, L. Piao, Considerations for a more accurate evaluation method for photocatalytic water splitting, Angew. Chem. 132 (2020) 18468–18476, https://doi.org/10.1002/ange.202009633.

[70] M. Qureshi, K. Takanabe, Insights on measuring and reporting heterogeneous photocatalysis: efficiency definitions and setup examples, Chem. Mater. 29 (2017) 158–167, https://doi.org/10.1021/acs.chemmater.6b02907.

Appendix D

Electronic Supporting Information

To

Hematene: A Sustainable 2D Conductive Platform for Visible-Light-Driven Photocatalytic Ammonia Decomposition

Jana Dzíbelová[a,b,‡], S. M. Hossein Hejazi[a,c,‡], Veronika Šedajová[a], David Panáček[a], Petr Jakubec[a*], Zdeněk Baďura[a,b], Ondřej Malina[a], Josef Kašlík[a], Jan Filip[a], Štěpán Kment[a,c], Michal Otyepka[a,d*], Radek Zbořil[a,c*]

[a]Regional Centre of Advanced Technologies and Materials, Czech Advanced Technology and Research Institute (CATRIN), Palacký University Olomouc, Šlechtitelů 241/27, 779 00 Olomouc, Czech Republic

[b]Department of Experimental Physics, Faculty of Science, Palacký University Olomouc, 17. listopadu 1192/12, 779 00 Olomouc, Czech Republic

[c]Nanotechnology Centre, Centre of Energy and Environmental Technologies, VŠB–Technical University of Ostrava, 17. listopadu 2172/15, Poruba, 708 00 Ostrava, Czech Republic

[d]IT4Innovations, VŠB–Technical University of Ostrava, 17. listopadu 2172/15, 708 00 Ostrava-Poruba, Czech Republic

[‡]These authors contributed equally

*Corresponding author. E-mail: michal.otypka@upol.cz, p.jakubec@upol.cz, radek.zboril@upol.cz

1. Characterization methods

1.1 Magnetic measurements

The magnetic data were collected and analyzed deploying a Quantum Design Physical Properties Measurement System (PPMS Dynacool system) with the vibrating sample magnetometer (VSM) option. The experimental data were corrected for the diamagnetism and signal of the sample holder. The temperature dependence of the magnetization was recorded in a sweep mode of 1 K/min in the zero-field-cooled (ZFC) and field-cooled (FC) measuring regimes.

2. Supporting figures and data

2.1 Microscopic data

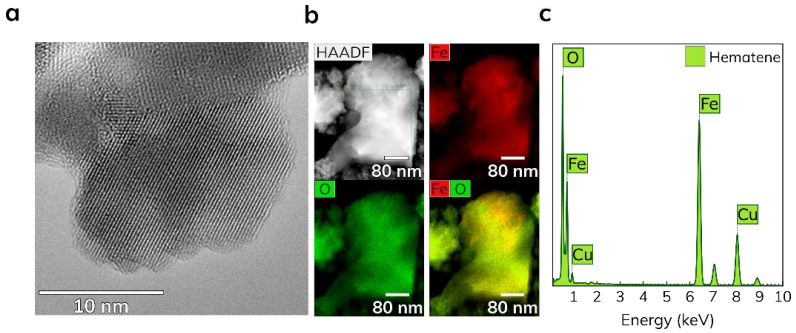

Fig. S1. (a) HRTEM image of hematene sheet with elemental mapping of individual elements (b); (c) EDAX analysis of hematene sheet.

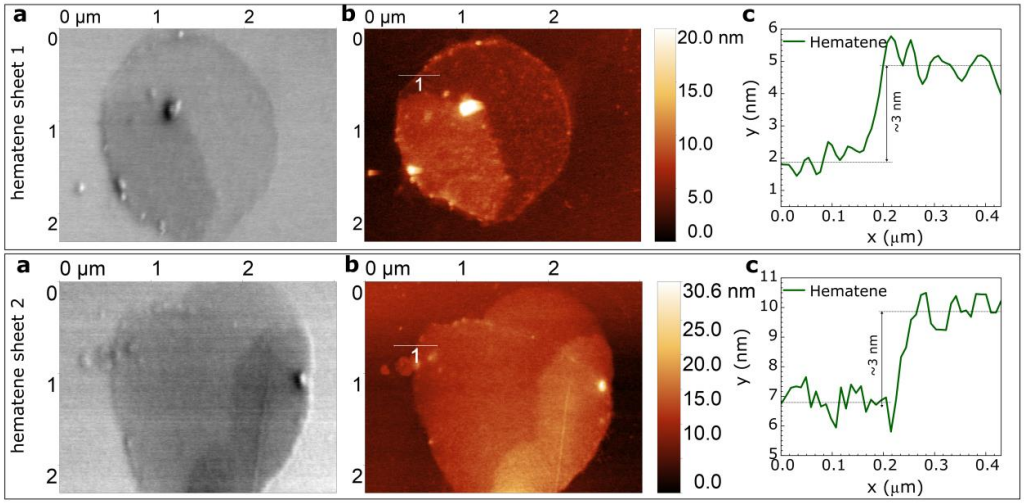

Fig. S2. (a) SEM images of two different hematene sheets; (b) AFM images of two different hematene sheets with related high profiles (c)

2.2 Magnetic properties of hematene

To shed more light on the nature of the hematene allotrope, we conducted magnetic measurements. It is well known that the magnetic properties of bulk hematite are mainly controlled by strong antiferromagnetic super-exchange interactions mediated through oxygen atoms [1–5]. At low temperature, hematite possesses antiferromagnetic ordering with perfect collinear orientation of magnetic sub-lattices, while at room temperature it exhibits weak ferromagnetic ordering due to the existence of canted spins [1–5]. The transition temperature from antiferromagnetic ordering to weak ferromagnetism is known as the Morin transition (T_M = 268 K), which is a thermodynamic transition where the spins undergo reorientation by 90 ° [1–5]. The T_M is largely dependent on the particle size distribution, alongside their morphology, presence of foreign metals, vacancies, and structural defects of the lattice [6–8].

The magnetic properties of hematene flakes are shown in Fig. S3a,b. The temperature-dependent magnetization (Fig. S3a) shows a sharp rise in the magnetization values around the temperature T_M = 250 K, which corresponds to the Morin transition temperature. The shift in the value of the Morin transition temperature indirectly confirms the 2D character of the hematene nanoparticles since the exfoliation process during the preparation influences the exchange interactions and subsequently leads to the enhancement of the lattice strain.

Moreover, the spin canting is more pronounced in 2D materials, resulting in a significant shift in the Morin transition temperature. The magnetic response of the specularite precursor is shown in inset Fig. S3a, and the analysis proves a higher value of the Morin temperature in the specularite sample (T_M = 265 K).

The hysteresis loops measured at 5 and 300 K are depicted in Fig. S3b and are in good agreement with ZFC-FC curves. The higher values of coercivity, magnetic remanence, and saturation magnetization at 300 K, compared to those at 5 K, relate to the presence of uncompensated surface spins of the 2D sheets.

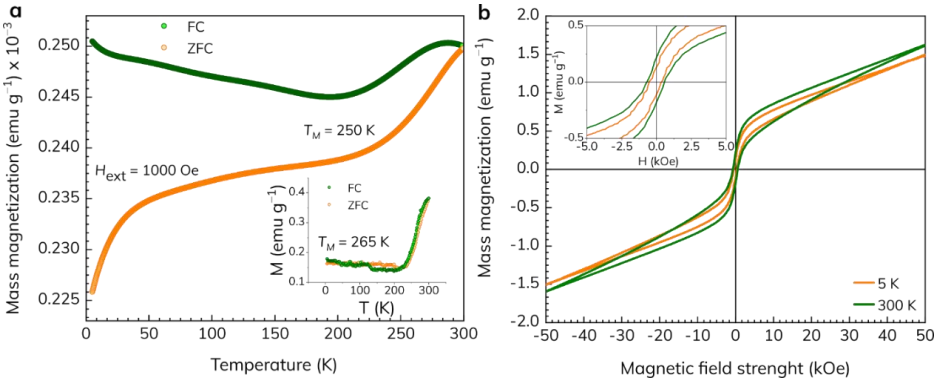

Fig. S3. (a) ZFC/FC magnetization curves measured for the hematene sample in the presence of an external magnetic field 1000 Oe, inset showing the ZFC/FC magnetization curves for the parent material, specularite; (b) hysteresis loops measured for the hematene sample at 5 and 300 K.

2.3 Photocatalytic activity

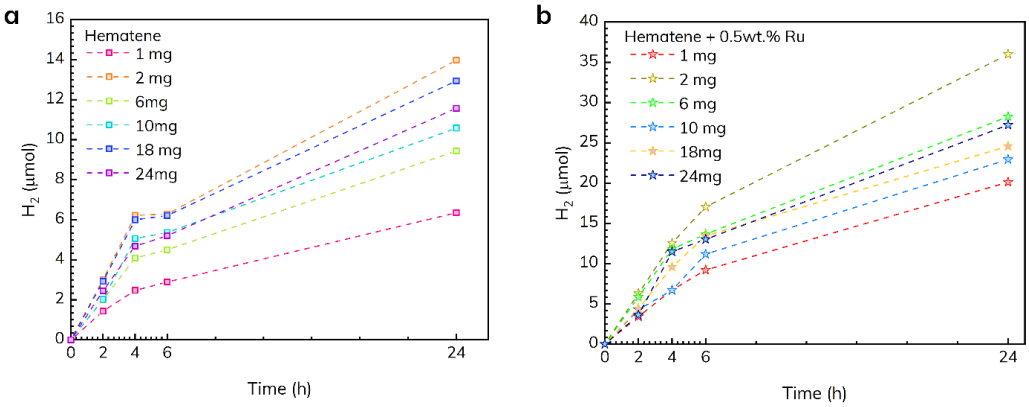

Fig. S4. Time course evolution of H_2 over (a) pristine hematene and (b) Ru-hematene with different amount of photocatalyst loading. The reactor was under visible light LED illumination (wavelength 400-700 nm, power 3 $W.m^{-2}$).

2.4 XPS survey

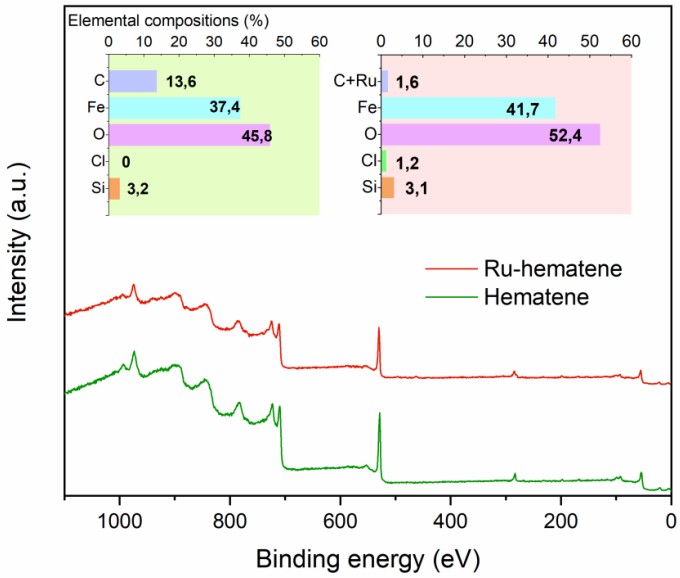

Fig. S5. XPS survey and elemental composition of hematene and Ru-hematene

2.5 XRD characterization before and after Ruthenium loading

To check the composition of the photocatalyst and to rule out major changes in the structure during ruthenium loading, XRD measurements of the hematene and Ru-hematene samples were performed, Figure S6. Table S1 shows the positions of the most significant hematene diffraction peaks and lattice parameters of both samples. The parameters remained essentially unchanged, clearly showing that no structural modifications of hematene occurred during the RuO_2 anchoring.

Furthermore, XRD measurement confirms the successful loading with ruthenium, where a low intensity peak at $2\vartheta \sim 32.75°$ is evident, corresponding to the most intense diffraction of RuO_2 (110) plane.

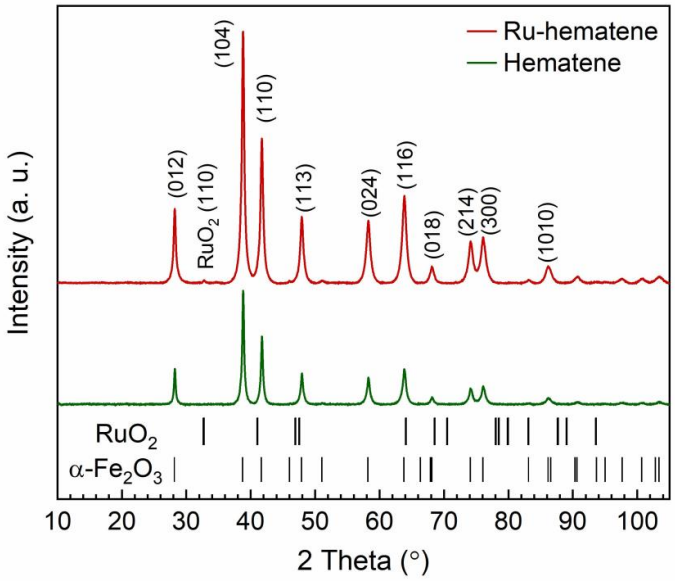

Fig. S6. XRD patterns of hematene and Ru-hematene

Table S1. Positions of significant hematene diffraction peaks and lattice parameters

Sample	Position 2ϑ (°) (1 0 4)	Position 2ϑ (°) (1 1 0)	Lattice parameter *a* (Å)	Lattice parameter *c* (Å)
Hematene	38.797	41.719	5.036	13.752
Ru-hematene	38.776	41.695	5.037	13.753

Supporting literature

[1] I. Dzyaloshinsky, A thermodynamic theory of "weak" ferromagnetism of antiferromagnetics, J. Phys. Chem. Solids. 4 (1958) 241–255. https://doi.org/10.1016/0022-3697(58)90076-3.

[2] T. Moriya, Anisotropic Superexchange Interaction and Weak Ferromagnetism, Phys. Rev. 120 (1960) 91–98. https://doi.org/10.1103/PhysRev.120.91.

[3] R. Zboril, M. Mashlan, D. Petridis, Iron(III) Oxides from Thermal ProcessesSynthesis, Structural and Magnetic Properties, Mössbauer Spectroscopy Characterization, and Applications, Chem. Mater. 14 (2002) 969–982. https://doi.org/10.1021/cm0111074.

[4] F.J. Morin, Magnetic Susceptibility of α-Fe_2O_3 and α-Fe_2O_3 with Added Titanium, Phys. Rev. 78 (1950) 819–820. https://doi.org/10.1103/PhysRev.78.819.2.

[5] R.M. Cornell, U. Schwertmann, The Iron Oxides Structure, Properties, Reactions, Occurrences and Uses, 2nd ed., Wiley, 2006. https://nbn-resolving.org/urn:nbn:de:101:1-2014081514273.

[6] D. Kubániová, L. Kubíčková, T. Kmječ, K. Závěta, D. Nižňanský, P. Brázda, M. Klementová, J. Kohout, Hematite: Morin temperature of nanoparticles with different size, J. Magn. Magn. Mater. 475 (2019) 611–619. https://doi.org/10.1016/j.jmmm.2018.11.126.

[7] D. Schroeer, R.C. Nininger, Morin Transition in α-Fe_2O_3 Microcrystals, Phys. Rev. Lett. 19 (1967) 632–634. https://doi.org/10.1103/PhysRevLett.19.632.

[8] R.D. Zysler, D. Fiorani, A.M. Testa, M. Godinho, E. Agostinelli, L. Suber, Size effects in the spin–flop transition of hematite nanoparticles, J. Magn. Magn. Mater. 272–276 (2004) 1575–1576. https://doi.org/10.1016/j.jmmm.2003.12.1128.

Faculty of Science, Palacký University

Olomouc

Department of Experimental Physics

2D Materials for Energy Storage and Photocatalysis: View into Intriguing Properties

PRESENTATION OF DOCTORAL THESIS

Mgr. Jana Dzíbelová

supervisor:

Mgr. Jan Filip, Ph.D.

Olomouc 2023

Author's first name and surmane:	Jana Dzíbelová
Supervisor:	Mgr. Jan Filip, Ph.D.
Study programme:	P 1703
Field of study:	Applied Physics
Form of study:	Full-time study
Oponents:	doc. RNDr. Libor Machala, Ph.D.
	prof. Dimitrios Gournis

Place and date of the defense:

The dissertation and opinions will be available at the library of Faculty of Science, Palacký University, at least 14 days before the defense.

List of Publications to which the Author of This Dissertation Has Contributed as Main Author or Co-Author During Her Doctoral Studies (2017 - 2023)

i. **Havláková, J.**, Tuek, J., Zboil, R.: *Stoichiometry issue of Iron(III) oxide nanomaterials by mossbauer spectroscopy*, NANOCON 2018 - Conference Proceedings, 10th Anniversary International Conference on Nanomaterials - Research and Application, 2019, pp. 93-99

ii. Tantis, I., Bakandritsos, A., Zaoralová, D., Medve, M., Jakubec, P., **Havláková, J.**, Zboil, R., Otyepka, M.: *Covalently Interlinked Graphene Sheets with Sulfur-Chains Enable Superior LithiumSulfur Battery Cathodes at Full-Mass Level*, **Advanced Functinoal Materials**, 2021

iii. edajová, V., Bakandritsos, A., Boski, P., Medve, M., Langer, R., Zaoralová, D., Ugolotti, J., **Dzíbelová, J.**, Jakubec, P., Kupka, V., Otyepka, M.: *Nitrogen doped graphene with diamond-like bonds achieves unprecedented energy density at high power in a symmetric sustainable supercapacitor*, **Energy Environmental Science**, 2022

iv. Karagiannaki, A., Konidakis, I., Kourmoulakis, G., Demeridou, I., **Dzíbelová, J.**, Bakandritsos, A., Stratakis, E.: *Probing the effect of a glass network on the synthesis and luminescence properties of composite perovskite glasses*, **Optical Material Express**, 2022

v. Hrubý, V., Zdrail, L., **Dzíbelová, J.**, edajová, V., Bakandritsos, A., Lazar. P., Otyepka, M.: *Unveiling the true band gap of fluorographene and its origins by teaming theory and experiment*, **Applied Surface Science**, 2022

vi. **Dzíbelová, J.**, Hejazi, H.S.M., edajová, V., Panáek, D., Jakubec, P., Baura, Z., Malina, O., Kalík, J., Filip, J., Kment, ., Otyepka, M., Zboil, R.: *Hematene: A Sustainable 2D Conductive Platform for Visible-Light-Driven Photocatalytic Ammonia Decomposition*, **Applied Materials Today**, 2023

Contents

Introduction

The material science community faces a major challenge considering growing society demand for sustainable energy sources and next generation energy storage devices. As a result, novel advanced materials are developed, explored and tested in the fields of energy storage and (photo)catalysis. The class of two-dimensional (2D) materials has gained significant attention in the past decade thanks to their attractive properties that are distinct compared to their bulk/three-dimensional (3D) material counterparts.

The present dissertation deals with study of advanced 2D materials, in particular for energy storage and photocatalysis, using thermogravimetric analysis (TGA), powder X-Ray diffraction (XRD) and scanning transmission electron microscopy (STEM) techniques, which provide insight into the quantitative composition, structure and microstructure of nanomaterials.

There are three main aims in the present thesis: (i) study of different graphene derivatives and MXene heterostructure for energy storage by means of TGA and powder XRD to provide better understanding of the functionalization, structural properties and their effect on the material applicability; (ii) preparation of novel 2D α-Fe_2O_3 material (hematene) with a focus on synthesis optimization in terms of sustainability; (iii) subsequent study of the prepared hematene with a focus on the structure, change of properties with reduced dimensionality and exploration of possible application.

1 Theoretical part

1.1 Two-dimensional van der Waals and non-van der Waals systems

1.1.1 Graphene and its derivatives

Graphene, as was proven in 2004, has many superlative features, such as superior mechanical strength, giant charge carrier intrinsic mobility and record thermal conductivity [1]. These qualities make graphene interesting from the point of view of both fundamental research on quantum phenomena and practical applications. However, there are some drawbacks limiting the applicability of pristine graphene, mainly relatively low reactivity, zero bandgap and hydrophobicity [2, 3].

Graphene consists of a single, freestanding layer of carbon atoms with sp^2 hybridization in honeycomb-like hexagonal structure, as depicted in figure 1.1a. Adjacent carbon atoms are bonded both by an in-plane σ-bonding and by π-bonding of delocalized electrons in the plane perpendicular to graphene, see Figure 1.1b. The structure and bonding type are responsible for graphene's superlative properties [4, 5].

To overcome the challenges caused by graphene drawbacks, surface modification and tailored functionalization of graphene are often utilized.

Graphene derivatives

Among other graphene derivatives, fluorographene has a prominent place, as its extensive chemistry allows for new synthetic routes to various functionalities of excellent quality in terms of their yield and uniform distribution. The synthetic approaches utilize controlled partial/complete defluorination and/or substitution, enabling func-

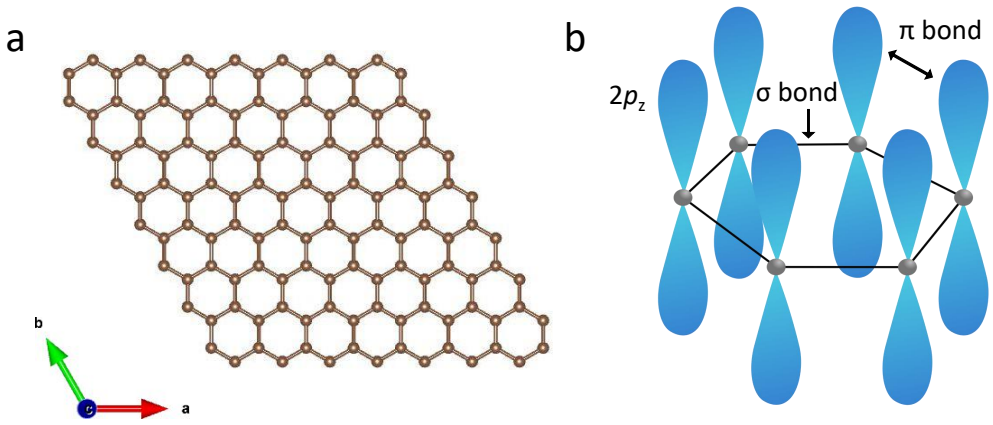

Figure 1.1: Scheme of graphene structure, a: graphene structure from top-view; b: graphene p_z orbitals with σ and π bonds.

tionalization that cannot be achieved via plain graphene [14].

Fluorographene is a monolayer of graphite fluoride, that can be prepared both by fluorination of graphene [15] or exfoliation of graphite fluoride [16]. Even a small amount of introduced fluorine atoms changes the structure and therefore the properties of graphene. It expands its band gap and changes the hybridization of the carbon atoms from sp^2 to sp^3, thus improving the applicability in electronics, significantly increasing reactivity and paving the way for the adoption of additional functionalities. [17]. Therefore, it is of course necessary not only to know how to prepare these derivatives, but also to characterize them correctly and to know the actual amount of functional groups. Among other experimental methods, TGA has proved to be particularly suitable for this purpose, as it can provide information not only about the thermal stability but also about the amount of functional groups or dopants. In terms of studying the structure of the material, powder XRD is a key technique.

1.1.2 MXenes

MXenes, first described in 2011, are a relatively new group of 2D materials based on cleaving the MAX phase – a ternary carbide or nitride with the general formula

$M_{n+1}AX_n$, where M stands for an early transition metal (e.g. Ti, Nb, V, Cr, Mo, Ta), A is (mostly) 13 and 14 group element and X denotes carbon and/or nitrogen. The so-called MAX phase forms a hexagonal laminated structure (space group $P6_3/mmc$) with two formula units per unit cell. The M and X elements form planes of near close-packed M_6X octahedras, while interleaved by weaker (longer) bonds with pure A-group element layers, as can be seen in Figure 1.2 [18].

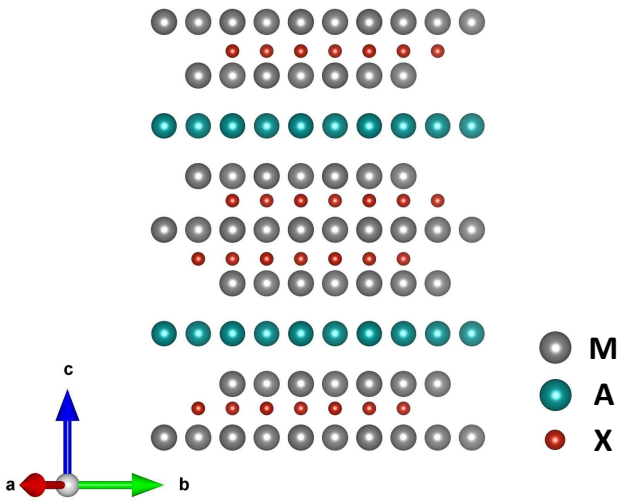

Figure 1.2: Schematic structure of typical MAX phase, where M (metal) atoms are in grey, A (13 and 14 group element) atoms are in cyan and X atoms (C or N) are in red-brown.

The relatively weak connection via A layers is used for selective etching that leads to multilayered MXene (without the A-group element), that is later delaminated into single flakes. Produced MXenes have a general formula $M_{n+1}X_nT_x$, where T_x represents the surface termination groups (e.g. $-$OH, $=$O, $-$F) [18, 19]. As their formula suggests, MXenes are among the most versatile 2D materials, of which more than 30 stoichiometric structures are known today [20]. The composition fundamentally influences the properties of these materials and thus their applicability. MXenes exhibit a rather unique combination of properties – they are highly conductive, possess the mechanical properties of transition metal carbides/nitrides and their surface functional groups in turn provide hydrophilicity and binding capacity. As a result, they have ap-

plication potential in many industries, ranging from energy storage, electronics, optics, bioapplications, catalysis, environmental applications, sensors, etc. [20, 21, 22].

The versatility of MXenes comes along with the need to properly characterize them in terms of composition, structure and properties. This is important in terms of possible applications and, moreover, in terms of replicability in materials science [23]. Approaches to the investigation of MXenes, in particular using powder XRD, will be discussed later in this thesis.

1.1.3 Iron oxides

Iron oxides generally form a large group including oxides, hydroxides or oxide-hydroxides, i.e. compounds consisting of Fe and/or OH. Iron oxides are Earth-abundant in both bulk and nanometric form and moreover, they can be easily prepared in the laboratory. Their accessibility, combined with their attractive properties, makes them an object of interest for a wide range of fields of mankind [24]. However, for the purposes of this thesis, solely the non-hydrated forms of iron oxides will be considered hereafter.

Crystal structure

There are three different non-hydrated iron oxides – FeO, Fe_3O_4 and Fe_2O_3, that consist of Fe^{2+} and/or Fe^{3+} cations and O^{2-} anions with radii of approximately 0.82 Å, 0.65 Å, and 1.4 Å, respectively. As evident, the O^{2-} ions are larger and therefore their arrangement determines the crystal structure of the whole compound, see Figure 1.3. As a result, there are also two basic ways of defining the crystal structure of iron oxides. One can describe either the arrangement of the anions (packing) or the link between the octa/tetrahedra formed by the cation centre and the nearest anions [25]. With respect to the anion arrangement, all the three different iron oxides consist of stacked O^{2-} planes with interlayers of iron cations in different polyhedral coordination.

Since crystal structure governs the material magnetic, electric, optical and chemical properties, each iron oxide with different lattice arrangement has distinct features. Various iron oxides are utilized in medicine, (photo)catalysis, biosensors, en-

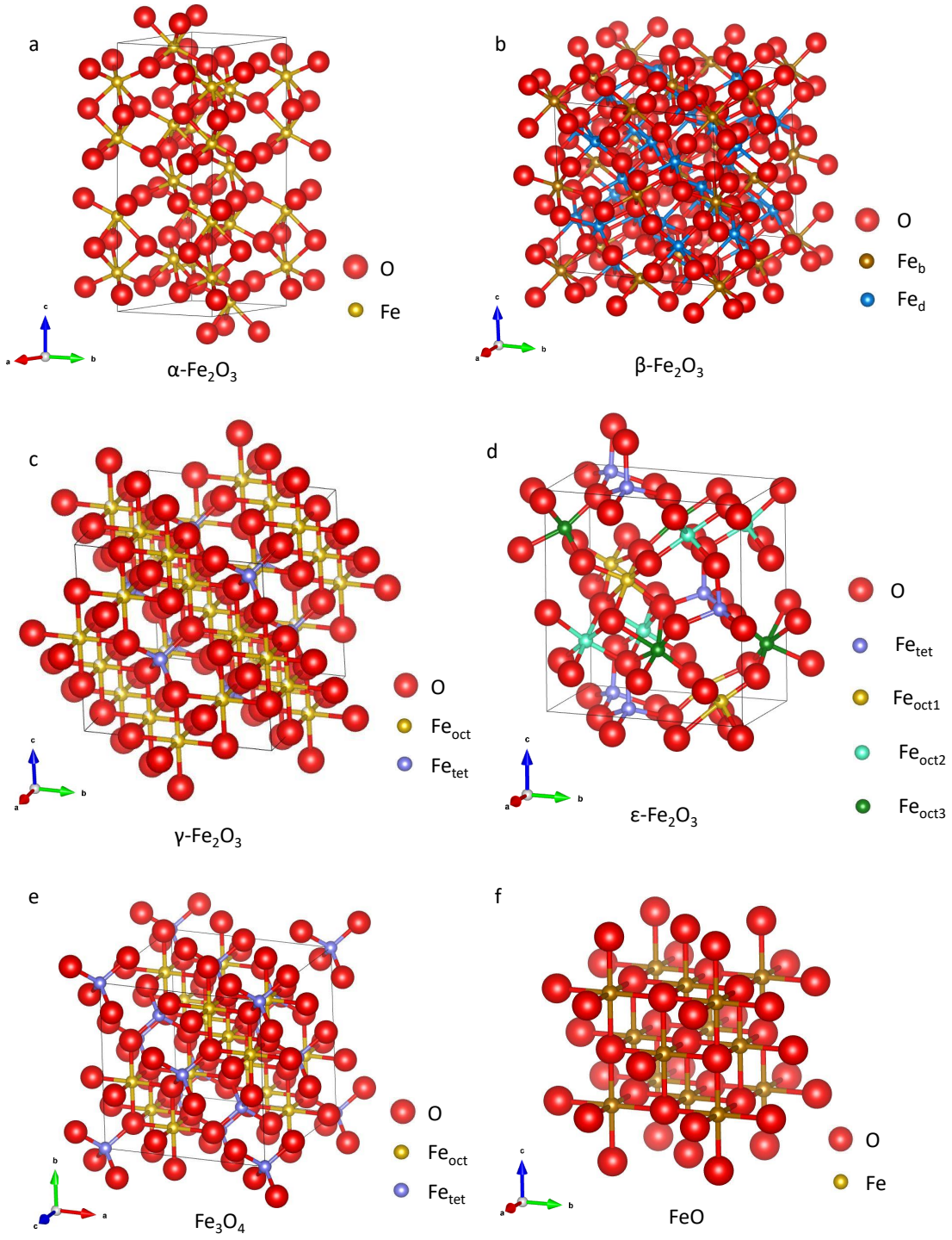

Figure 1.3: Schematic crystal structures of all iron oxide phases.

ergy storage, optoelectronics, environmental technologies and magnetic data storage [33, 34, 35, 36, 37, 38, 39].

2D iron oxides

Iron oxides display a complex variety of crystal structures with strong chemical bonding in all three directions and therefore can be referred to as non-van der Waals materials. Early indications of 2D iron oxides were based on thin films or layers grown by different vapor deposition methods (CVD, MBE, etc.) on various substrates and have been studied since the 1990s [40, 41, 42, 43]. However, the first freestanding 2D iron oxide – α-Fe_2O_3, so-called hematene – was introduced in 2018 by Puthirath et al. [44]. Soon after this pioneering work Puthirath et al. followed with report on ilmenene (2D $FeTiO_3$) in 2018 [45] and Serles et al. introducing magnetene (2D Fe_3O_4) in 2021 [46].

The studies published so far suggest that 2D iron oxides open up a new class of interesting materials and the possibility of studying physical phenomena (especially magnetism) in 2D nanostructures. With respect to hematene, interesting features have been predicted [47, 48, 49, 50, 51, 52] and some so far observed - for example, a decrease in the Morin temperature (T_M) of the transition from the antiferromagnetic to the weakly ferromagnetic state [44, 53], interesting optical properties - nonlinear optical behaviour suitable for protective devices [54, 55], and from a chemical point of view, the large surface to volume ratio combined with potential defect structure appears to have the prospect for various chemical reactions [56, 57].

2 Experimental study of 2D materials

2.1 Modern 2D materials for energy storage

In recent years, the demand for electricity has increased significantly as a result of society's growing needs. This increase can be associated with factors such as population growth, urbanization, industrialization, increasing use of electronic devices and last but not least the electrification of transport and growing popularity of electric vehicles. One of the main challenges posed by this growing demand is the need to find more efficient, safe, eco-friendly and low-cost energy storage solutions.

Three different classes of (portable) electrical energy storage devices are recognized: batteries, capacitors and supercapacitors, that differ in working principle and consequently in their characteristics.

Therefore, the main challenges in energy storage depend on the type of the device: in battery development in general it is the cost, eco-friendliness and cycle life; considering supercapacitors it is mostly the limitation in capacity. The current boundaries are pushed with new materials developed and improved, different electrolytes, etc. [83, 85]

The sub-chapter 2.1.1 deals with TGA and XRD characterization of new cathode material for Li-sulphur batteries based on graphene-polysulfide derivative. Second sub-chapter 2.1.2 is focused on supercapacitors, namely XRD characterization of several variations of MXene/graphene derivative heterostructures.

2.1.1 Covalently interlinked graphene sheets with sulphur chains as lithium-sulphur battery cathode

Parts of the text in the following chapter are adapted from Tantis et al. [86].

Lithium-ion batteries (LIBs) currently dominate the market for energy storage systems of portable electronics. However, in their current design, they cannot keep up with the increasing demand for higher performance and lower cost [85, 87, 88]. In this respect, lithium-sulphur batteries (LSBs) could offer a promising alternative to LIBs, as they have a high theoretical capacity ($1672\,\mathrm{mA \cdot h \cdot g^{-1}}$), high specific energy ($2600\,\mathrm{W \cdot h \cdot kg^{-1}}$) and, in addition, sulphur is environmentally friendly and readily available [89, 90].

However, LSBs still suffer from some shortcomings, in particular the "shuttle-effect" of the formed lithium polysulfides, low sulphur conductivity and large volume changes. One way to address these problems is to develop functional separators and design composite cathodes featuring a sulphur anchoring platform. However, the composites developed so far suffer from either low conductivity of the anchoring platform, low cycle life, or small amounts of anchored sulphur [90, 91].

To tackle the LSBs bottlenecks, we exploited the rich flourographene chemistry that allowed defluorination and substitution through nucleophilic attack of PS ions on the electrophilic radical FG defect centres, based on previous reports of PS attack ability on electrophilic carbons of alkylhalides. [92, 93, 94]. Two conditions were crucial for successful elimination of the LSBs bottlenecks:

i) high sulphur loading to increase the full-cell specific capacity,

ii) sulphur anchoring to FG via covalent bonding.

Both criteria were confirmed with the help of TGA and STA/MS experiments performed under different atmospheres. To prove that combination of FG chemistry with PS nucleophilic attack is a unique pathway to achieve both criteria, three different samples were prepared and analyzed:

- Graphene-polysulfide derivative, denoted as GPS, was the developed material via FG and PS.

- Graphene-sulfide derivatice, denoted as GS, was prepared as a control using the same protocol as GPS, except elemental sulphur was utilized instead of PS.

- Electrochemically exfoliated graphene, denoted as EEGS, was used as a control to prove the role of FG (electrochemically exfoliated graphene was used instead of FG in the synthesis).

The sulphur content for each sample was determined with the help of TGA, see Figure 2.1. Based on the TG curves obtained under N_2 flow, 80, 85 and 5 mass% of sulphur were identified in GPS, GS and EEGS samples, respectively. To prove that the mass losses are truly corresponding to sulphur, STA/MS experiments were performed under synthetic air, see Figure 2.1b and c. Both clearly show, that the mass losses between 150 – 350 °C correspond solely to sulphur loss. Furthermore, fluorographene has been proved to be thermally stable until $\approx 400 - 450\,°C$ [95, 96].

Based on nitrogen TG curves, we estimated the DoF of S_8 in each sample and listed them in Table 2.1, together with mass losses and graphene residual masses.

Sample	$\Delta m(S_8)$	m(C) (wt.%)	DoF (%)
GPS	80.00	14.96	25.14
GS	85.71	8.05	49.13
EEGS	5.00	86.84	0.27

Table 2.1: Calculated DoF of S_8 species in different graphene-(poly)sulfide derivatives.

The criteria i), i.e. high sulphur loading, is therefore met in samples GPS and GS, proving the important role of FG, since the EEG was able to load only 5 mass% of PS, corresponding to DoF 0.27%.

Although the sulphur loading is higher in GS than in GPS sample, the former does not fulfil the criteria ii) and there is no covalent bonding. The PS ions in the latter are, in contrast, covalently anchored on the FG substrate. To prove this, findings of several complementary techniques were put together as a part of a puzzle. Apart from TGA, FTIR and and Raman spectroscopy provided indications of bond nature in both GPS and GS samples [86].

To shed more light on the charge/discharge processes, we performed XRD analyses of the GPS cathode material before and after electrochemical testing, see Figure 2.2.

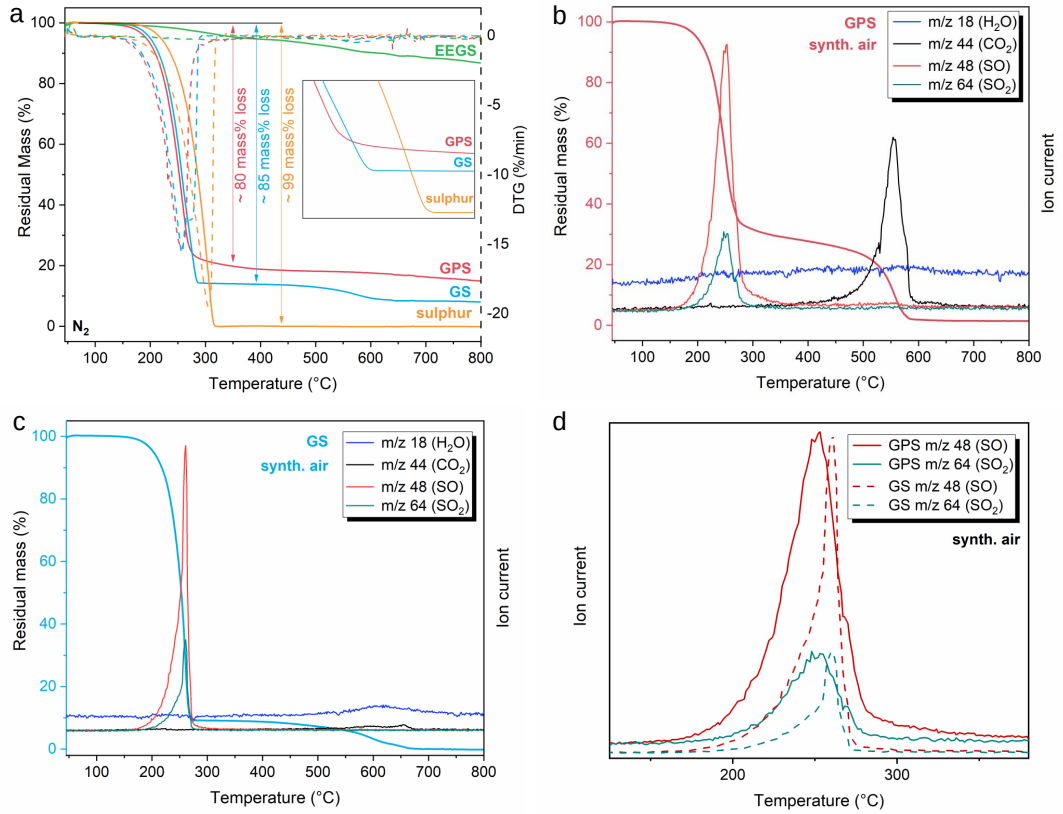

Figure 2.1: a: TGA curves in nitrogen atmosphere of GPS (red line), GS (light-blue line), EEGS (green line) and elemental sulphur (dark-yellow line) together with the corresponding DTG curves (dashed lines) and detail of TGA curves in temperature range of 230 – 350 °C, shown in the inset; b: STA/MS results of GPS sample in synthetic air atmosphere; c: STA/MS results of GS sample in synthetic air atmosphere; d: comparison of ion currents corresponding to SO and SO_2 fractions produced by GPS (solid lines) and GS (dashed lines) samples.

Solely sulphur peaks are present in the diffractogram of the GPS powder, while the diffractogram of the lithiated cathode is dominated by oxidized lithium polysulfides ($Li_2S_2O_7$ and Li_2SO_4). Thus, the lithiated cathode consists of Li_2S_2/Li_2S, which are indeed expected in the lithiated state [98], but were oxidized after exposure to air, therefore it was difficult to extract any further significant information from these experiments. To avoid cathode oxidation and to monitor underlying crystal structure changes during battery cycling, the use of in operando XRD would be preferable. How-

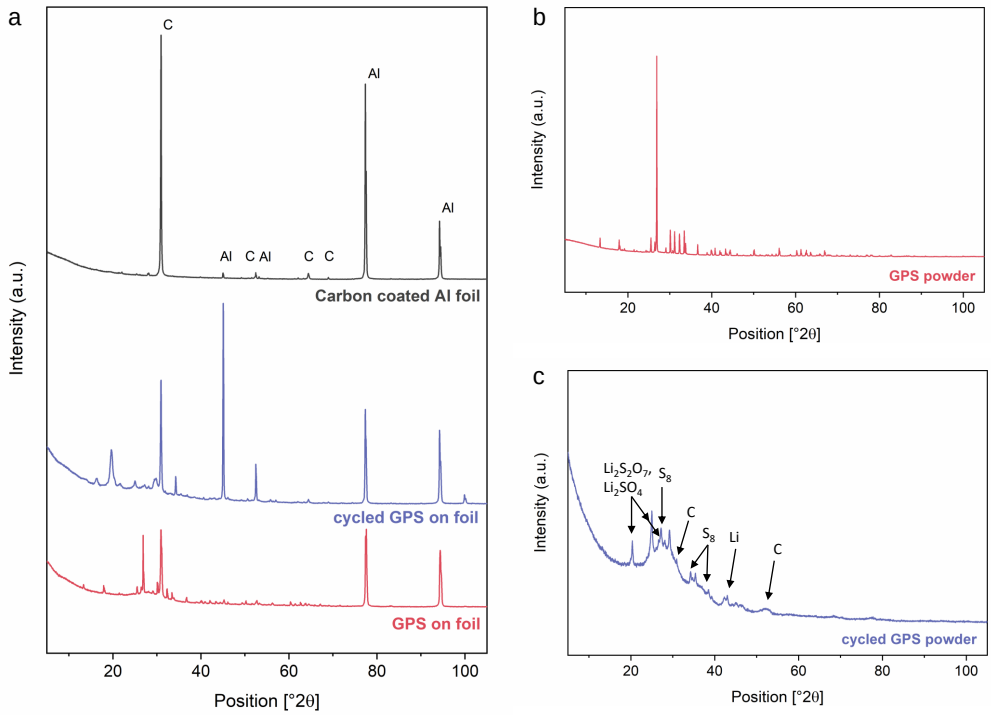

Figure 2.2: Diffractograms of: a: GPS complete cathode before testing (red line), cycled GPS cathode (purple line) and carbon coated aluminium foil, which was used as a substrate and current collector (dark grey line); b: GPS powder before testing and c: cycled GPS powder (scratched from the substrate foil).

ever, such experiments require special equipment which is not available at our facility.

2.1.2 MXene/Graphene derivative heterostructure composites for supercapacitors

The following sub-chapter is based on the results obtained whilst working on a project that has not been published yet.

As the energy storage research pushes forward, supercapacitors emerge as a promising rival to LIBs, since they offer high power density (charge/discharge rate), long cycle life and independence from scarce elements. However, their applicability in industry is still limited due to their capacity, which falls significantly short compared to energy density of state of art batteries. For example, commercial supercapacitors reach specific energy (per cell) of $10\,\mathrm{W}\cdot\mathrm{h}\cdot\mathrm{kg}^{-1}$ [99, 100], while lead-acid batteries provide 20 –

$35\,\mathrm{W \cdot h \cdot kg^{-1}}$ [101] and advanced LIBs offer up to $150\,\mathrm{W \cdot h \cdot kg^{-1}}$ [102]. Compared to LIBs, supercapacitors are superior in power density and cycle-life. To utilize the benefits of supercapacitors and facilitate their higher applicability, it is crucial to develop electrode and/or dielectric materials that surpass the current limits in energy density and sustain the high power density as well as long service life [103].

Here, we explore combining $Ti_3C_2T_x$ MXene with two kinds of graphene derivatives in determined ratio 99:1. First is recently reported nitrogen superdoped graphene that was recently reported by Sedajova et al. as supercapacitor material with unprecedented energy density [111], denoted here as GN3. The GN3 material was also prepared in charged variation, denoted as GN3Q, to enhance self-assebly in the heterostructures. Second is graphene acid, that has been proven suitable for energy storage, with carboxyl boosting storage capacity, by Sedajova et al. [112], denoted here as GA. All samples were prepared in the form of self-standing films with different mass-loading of 1, 4 and $10\ \mathrm{mg \cdot cm^{-2}}$.

The diffraction patterns of all self-standing films, i.e. bare $Ti_3C_2T_x$ and the heterostructures, are shown in Figure 2.3.

To evaluate the effect of mass loading on the self-standing film structures, we examined the d-spacing of each film from the (002) peak positions and the corresponding values are plotted in Figure 2.4. The samples $Ti_3C_2T_x$/GA with mass loading of $4\,\mathrm{mg \cdot cm^{-2}}$, $Ti_3C_2T_x$/GN3 with mass loading of $10\,\mathrm{mg \cdot cm^{-2}}$ and $Ti_3C_2T_x$/GN3Q with mass loading of 4 and $10\,\mathrm{mg \cdot cm^{-2}}$ have a complex (002) peak shape with a shoulder at lower 2θ angles. To obtain a sufficiently good profile fit, we assumed that it consists of contributions from multiple diffraction peaks, which could be explained by the corrugated structure of the films, as confirmed by the electron microscopy images, leading to the presence of multiple d-spacing values.

Overall, the insight into the structure of the self-standing films provided by XRD confirms:

- Successful etching of the MAX phase in all samples, except the heterostructure material $Ti_3C_2T_x$/GA with mass loading of $10\,\mathrm{mg \cdot cm^{-2}}$, where a very low inten-

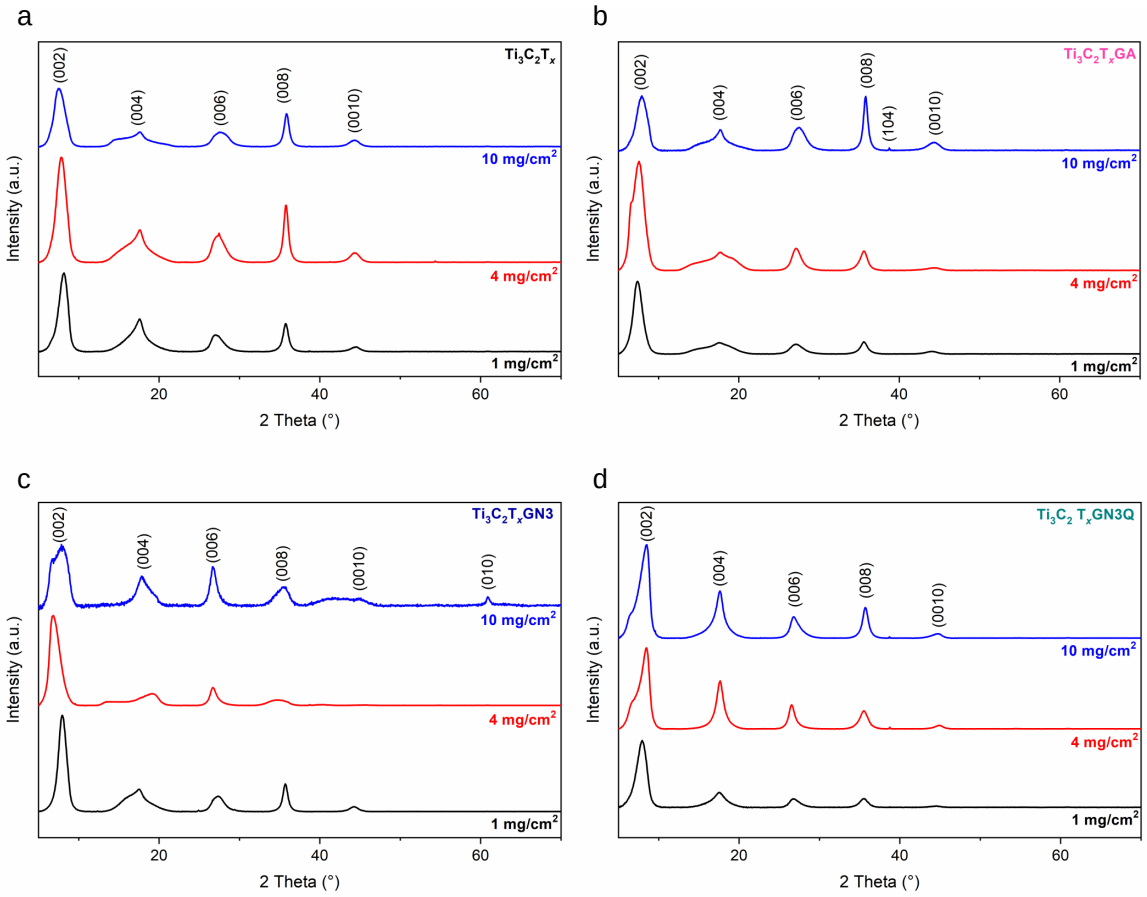

Figure 2.3: Diffraction patterns of a: bare $Ti_3C_2T_x$; b: $Ti_3C_2T_x$/GA heterostructures; c: $Ti_3C_2T_x$/GN3 heterostructures and d: $Ti_3C_2T_x$/GN3Q heterostructures.

sity (104) peak at $2\theta \approx 39°$ suggests negligible amount of MAX phase Ti_3AlC_2.

- Successful delamination of the MXenes, except the $Ti_3C_2T_x$/GN3 sample with mass loading of $10\,mg \cdot cm^{-2}$, where a low intensity (104) peak at $2\theta \approx 61°$ indicates presence of multilayer $Ti_3C_2T_x$.

- Corrugated structure of all the materials, with disordered stacking in the $Ti_3C_2T_x$, $Ti_3C_2T_x$/GA and $Ti_3C_2T_x$/GN3 materials.

- Regularly corrugated structure of the $Ti_3C_2T_x$/GN3Q sample, that originates probably from self-assembly of the charged graphene derivative with MXene, enabling a better adhesion between the layers.

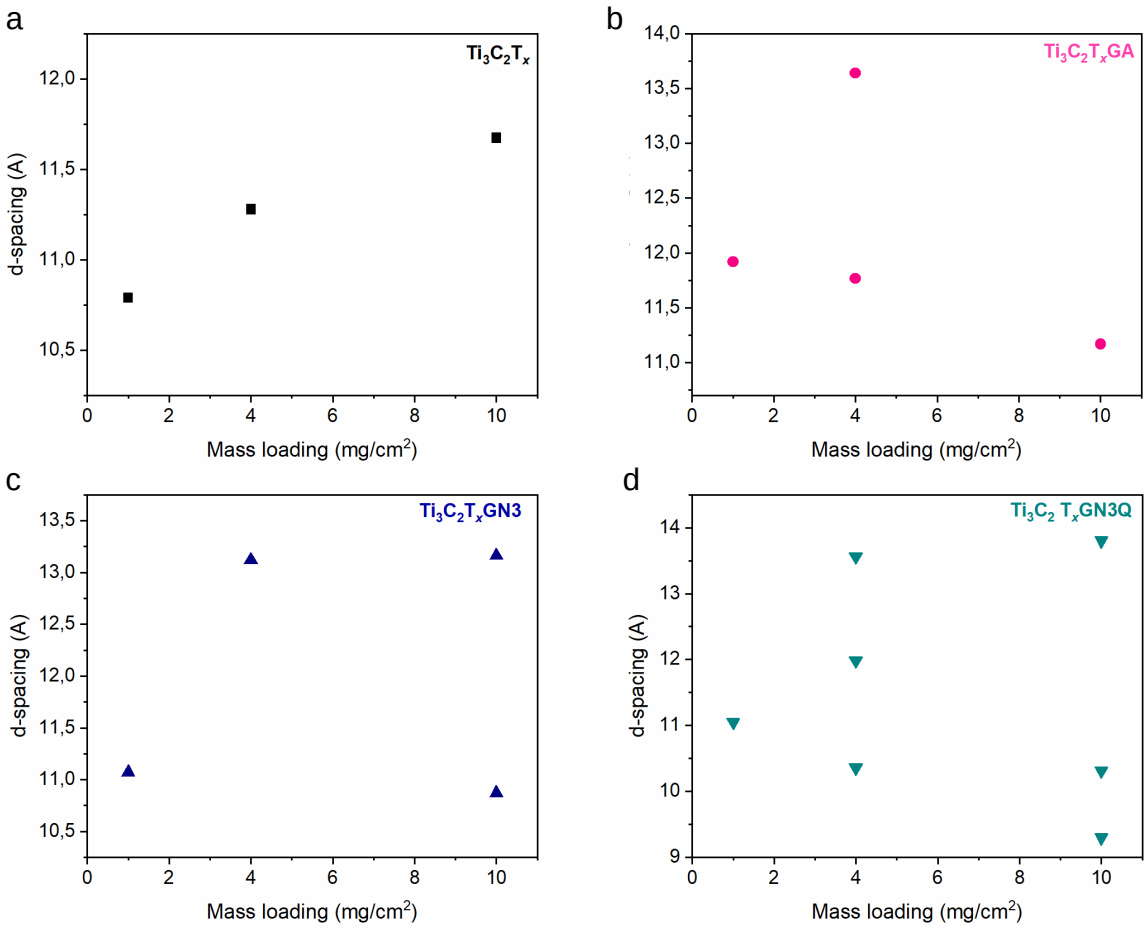

Figure 2.4: Calculated d-spacing values for different mass-loading of a: bare $Ti_3C_2T_x$; b: $Ti_3C_2T_x$/GA heterostructures; c: $Ti_3C_2T_x$/GN3 heterostructures and d: $Ti_3C_2T_x$/GN3Q heterostructures.

Findings derived from XRD analyses are in agreement with electrochemical testing results, where the self-assembly in $Ti_3C_2T_x$/GN3Q heterostructures proves to be beneficial for the supercapacitors performance.

2.2 Hematene: a novel 2D non-van der Waals material

Inspired by Puthirath et al., who, in 2018, reported on hematene [44], the first member of a new family of 2D n-vdW materials, we focused our efforts to repeat and

optimize hematene preparation to be able to explore this material. The exfoliation relies on the use of a suitable starting material, in this case an iron oxide ore called specularite, grown in a lamellar quasi layered structure, see Figure 2.5. The schematic of the exfoliation is shown in Figure 2.6.

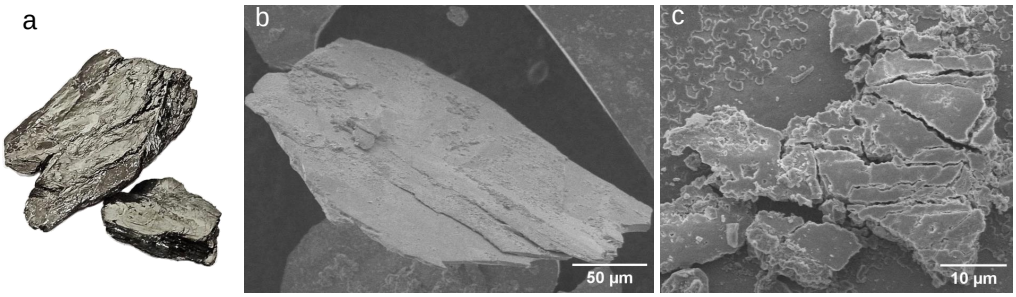

Figure 2.5: Parent material: a: photograph of iron ore specularite that was collected in Elba, Italy; b,c: SEM images of specularite.

Figure 2.6: Scheme of exfoliation with photos of flasks with dispersions to illustrate the colour-change after sonochemical exfoliation.

2.2.1 Material characterization

Considering the classical (vdW) 2D materials, it is known that the dimensional restriction coming from 3D to 2D bares substantial changes in properties and behaviour of the materials, as discussed in the theoretical sub-chapter 1.1. Therefore, after successful preparation of novel 2D n-vdW material, hematene, we aimed to characterize it to study any properties differences compared to parent bulk specularite and to identify

potential application directions. We focused our efforts on DI water derived hematene.

There are two main questions to ask about hematene. The first query that comes to mind concerns the exfoliation of the specularite itself, in particular the direction of cleavage of the 3D structure. According to literature, there are two main directions [001] and [010] with highest broken bond density in hematite, along which the crystallites should be exfoliated preferentially [44, 120]. Second question concerns the changes of properties of the material. The following sub-chapter and the sub-chapter 2.2.2 attempts to deal with both of these questions to some extent. For the sake of clarity, the following chapter is divided into several sub-chapters according to the studied aspects.

Structural characterization

To verify the phase composition of both bulk specularite and produced hematene, we performed XRD analysis. From XRD patterns shown in Figure 2.7 it is evident that both parent material and exfoliated hematene contain only α-Fe_2O_3 crystalline phase.

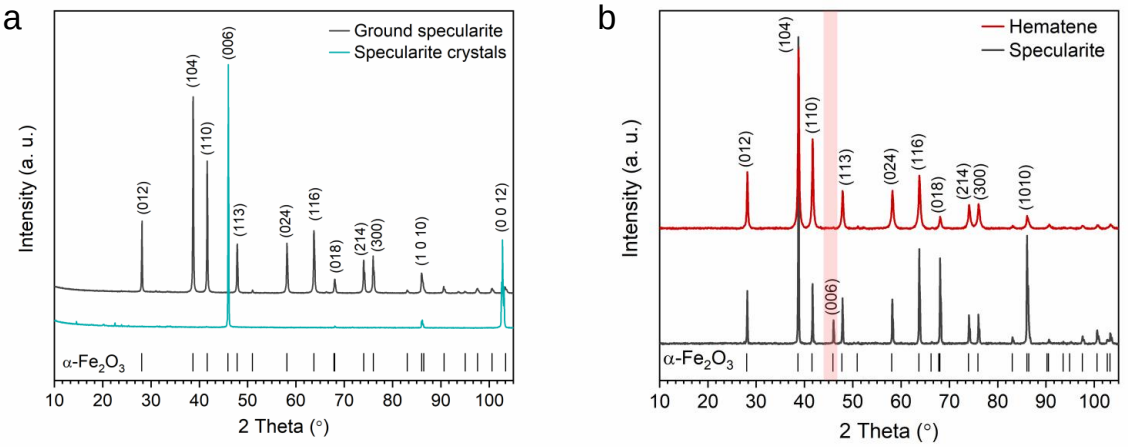

Figure 2.7: XRD patterns of: a: specularite crystals (lower cyan line) compared to ground powder (upper grey line); b: ground specularite (lower grey line) compared to exfoliated hematene (upper dark-red line).

The parent material was analysed before and after grinding with mortar and pestle and as clearly visible from Figure 2.7a, there is a preferred orientation of the specularite

layer stacking leading to enhanced reflections on preferential orientation planes – (006) and (0012) – and complete suppression of other crystallographic planes. This effect is reduced after grinding the crystals into fine powder. Furthermore, after exfoliation, the reflection from (006) plane completely disappears, as evident from Figure 2.7b. The described phenomenon can be explained by the growth of the crystal in the direction perpendicular to (006) plane, that facilitates the cleavage along [001] direction. In the exfoliated hematene, the (006) reflection would then be absent due to very low sheet thickness. To evaluate the presence of other non-crystalline species present in the natural parent material, we performed XPS analysis of both parent and exfoliated samples, see Figure 2.8. The atomic compositions of both samples are shown in the insets of the XPS graphs and listed in Table 2.2.

Sample	Fe (at. %)	O (at. %)	C (at. %)	Si (at. %)
Specularite	14.4	49.6	30.3	5.7
Hematene	29.7	58.4	11.9	0.0

Table 2.2: Atomic composition of specularite and hematene according to XPS analysis.

2.2.2 Intrinsic strain in hematene

Precise material characterization is crucial for understanding the properties of a nanomaterial to be able to tailor them towards specific applications. It is known, that crystal structure together with its distortions, such as defects, vacancies and resulting lattice strain, affect the properties of nanomaterials. Lattice strain as a distortion of atomic positions can influence the electronic configuration and hence the optical, electronic, electrochemical, catalytic properties etc. [124, 125, 126, 77, 127].

Here, taking into account the available instrumental methods, we use powder XRD to get an overall idea of the lattice strain and then STEM at the atomic level of very thin sheets.

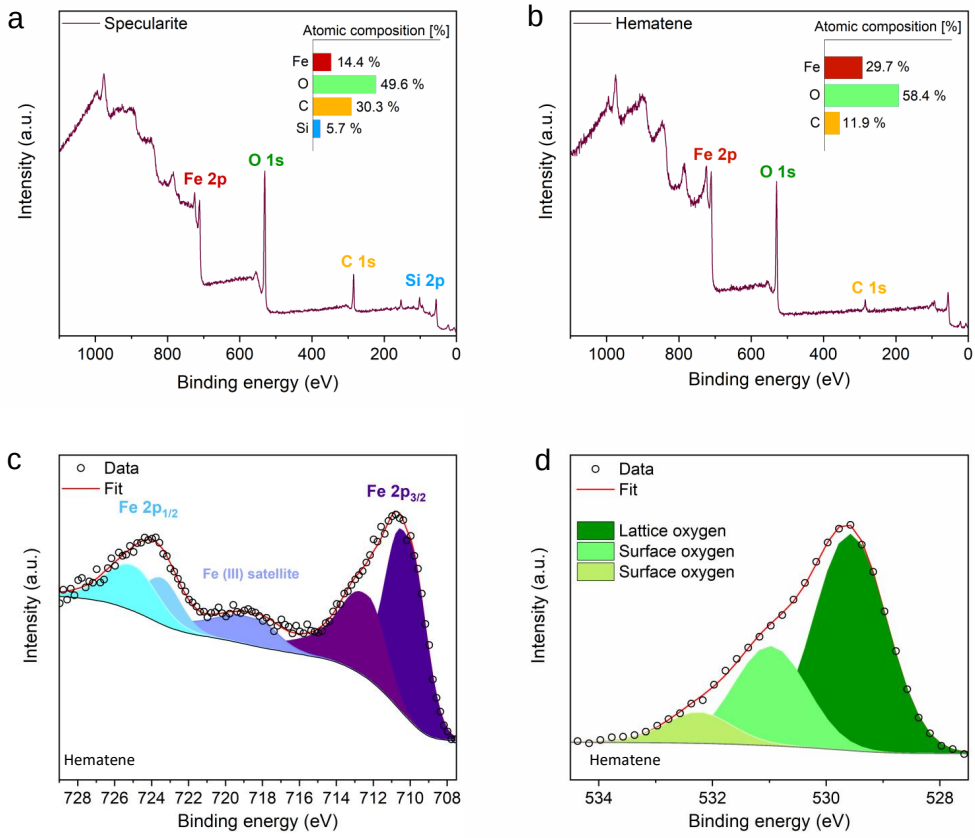

Figure 2.8: a: XPS spectrum of specularite with estimated atomic composition (inset); b: XPS spectrum of hematene with estimated atomic composition (inset); c: HR-XPS spectrum of the hematene Fe 2p and d: O 1s regions; adapted from ref. [116].

Powder XRD strain analysis

We used three different samples to evaluate the strain development with respect to exfoliation: specularite, as prepared hematene sheets and a size fraction of hematene with mean diameter of 120 nm (estimated by DLS), called hematene 120. The XRD patterns with their corresponding W-H plots are included in Figure 2.9, while the strain values and crystallite size are listed in Table 2.3.

It is evident from the data, that the intrinsic strain values increase as exfoliation proceeds, while the crystallite size decreases, as expected. Moreover, the positive slope indicates lattice expansion [78]. The R^2 values suggest, that conventional W-H plot is relatively suitable only in the case of as prepared hematene sheets with R^2 of 0.878,

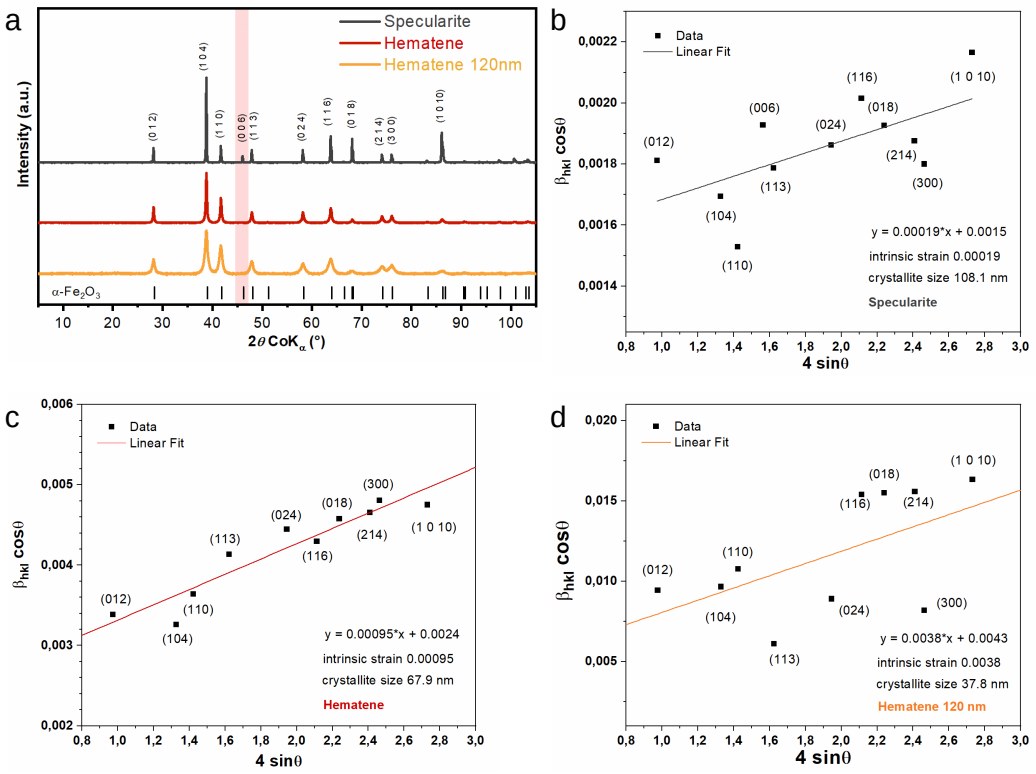

Figure 2.9: a: XRD patterns of three different samples: specularite (top grey line), as prepared hematene (middle red line) and hematene 120 (bottom orange line); corresponding W-H plots of: b: specularite; c: hematene and d: hematene 120.

Sample	Intrinsic strain (10^{-3})	Crystallite size (nm)	R^2
Specularite	0.19	108.1	0.335
Hematene	0.95	67.9	0.878
Hematene 120	3.8	37.8	0.251

Table 2.3: Values of intrinsic strain and crystallite size of specularite and hematene samples derived from the W-H plot.

but not adequate for specularite and hematene 120, where the R^2 values were even below 0.35 and linear fit of the data points might be questionable.

The W-H plot is nevertheless a useful tool that can reveal lattice strain in a particular crystallographic direction by patterns in outlying points. However, there are almost no trends in the data of the studied samples. If we compare the data points

in all three samples, we can see that (012) diffraction peak is above the fitted line, while (104) diffraction peak lies below. The fit badness can be related to either wide crystallite size distribution or non-uniform strain in the samples.

STEM strain analysis

The STEM experiments in the following sub-chapter were carried out at University of Vienna, Austria, under the supervision of prof. Jani Kotakoski.

The thin hematene sheets show hexagonal crystal structure, as apparent from STEM-MAADF images and the corresponding FFT, see Figure 2.10 and insets, suggesting exfoliation along the [001] crystallographic direction [44]. This observation is in a good agreement with the (006) reflection disappearing from XRD pattern after exfoliation, as discussed in sub-chapter 2.2.1.

To derive the hematene lattice parameter a values within several areas the sheet, we used the FFT of STEM images. The second ring of FFT spots corresponds to a half of the lattice parameter value in hexagonal structures [138]. We fitted the second ring of spots with an ellipse and used the obtained major and minor axes values and the rotation angle for the tilt correction. Then, with the lattice parameter estimated for both major and minor direction, we were able to calculate the lattice strain ϵ according to the following equation:

$$\epsilon = \frac{a - a_0}{a_0}, \tag{2.1}$$

where a_0 denotes the typical hematite lattice parameter $a_0 = 5.034$ Å. The results are listed in Table 2.4 while different areas are labelled according to letter notation in Figure 2.10.

The difference between STEM and XRD results can be explained by the fact, that XRD samples contained a broad sheet diameter and thickness distribution, while STEM studied the surface of a single extremely thin flake. However, the STEM analysis would need to be performed on a larger quantity of samples in order to draw further concrete conclusions.

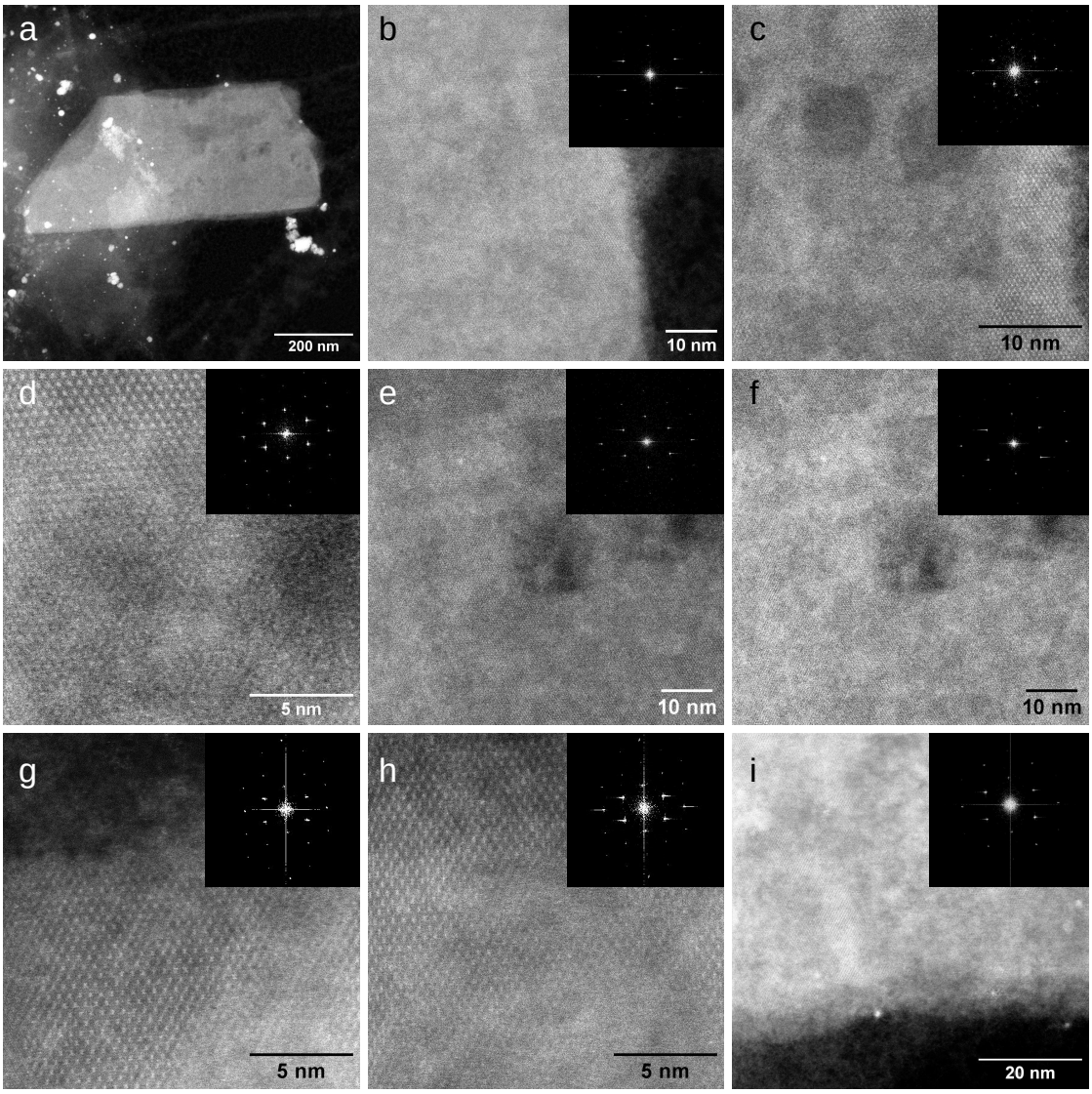

Figure 2.10: STEM-MAADF images of a: the whole hematene sheet after scanning detailed areas b – i; insets include FFT of the corresponding STEM image.

2.2.3 Hematene as a platform for visible-light induced ammonia photo-catalytic decomposition

The exploitation of renewable and sustainable energy sources represents one of the most important tasks for humanity, since the amount of fossil fuels is limited and the global energy consumption is predicted to at least double by the midcentury compared to present time [139]. The newly discovered 2D n-vdW materials including hematene, magnetene (2D Fe_3O_4), ilmenene (2D $FeTiO_3$) and chromiteen (2D $FeCr_2O_4$)

Area	a major (Å)	a minor (Å)	ϵ major	ϵ minor
b	5.111	5.098	0.015	0.013
c	5.192	5.387	0.031	0.070
d	5.088	5.301	0.011	0.053
e	5.061	5.275	0.005	0.048
f	4.996	5.237	-0.007	0.040
g	5.205	5.398	0.034	0.072
h	5.224	5.257	0.038	0.044
i	4.995	5.014	-0.008	-0.004

Table 2.4: STEM derived values of hematene lattice parameter a in mutually perpendicular directions and corresponding lattice strain ϵ values.

have proven their potential in the fields of photoelectrochemistry and electrocatalysis according to published literature where they show excellent results in the combination with Ti nanotubes [44, 45, 140].

Here, we explore the combination of conductive 2D hematene substrate with the catalytic surface of RuO_2 nanoparticles to obtain a sustainable platform for photocatalytic ammonia decomposition under the visible light irradiation.

Hematene composite characterization

The photocatalyst material was hematene decorated with ruthenium, hereafter denoted as Ru-hematene. We employed several experimental techniques to confirm successful loading of ruthenium species onto hematene sheets and to estimate the oxidation state of ruthenium.

The STEM-HAADF images together with elemental mapping are shown in Figure 2.11 and confirm successful loading and even spreading of ruthenium on hematene while keeping the 2D morphology of the sheets (otherwise STEM would not be possible).

To determine the oxidation state of ruthenium and shed more light on the electro-optical properties, a HR-XPS of the ruthenium 3d region and valence band XPS (VB-

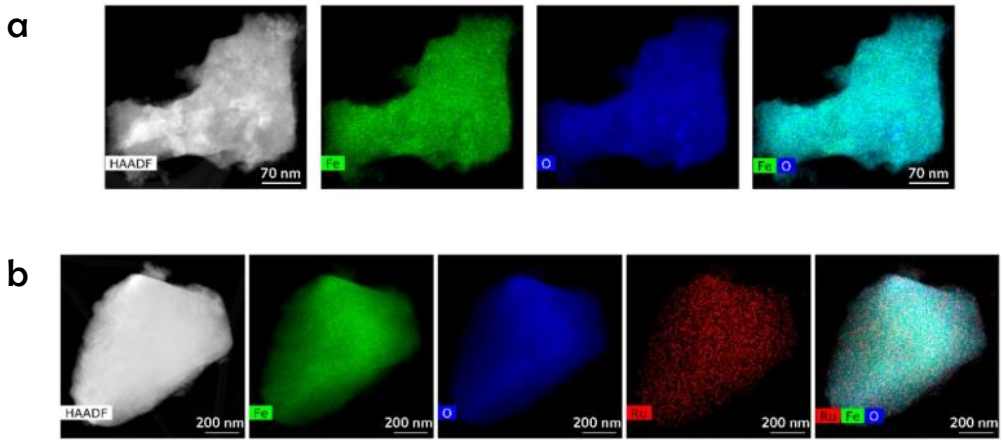

Figure 2.11: STEM-HAADF images and elemental EDS mapping of a: bare hematene; b: Ru-hematene; adapted from ref. [116].

XPS) of both materials were performed as well as an electron paramagnetic resonance (EPR) study. The deconvoluted spectrum is shown in Figure 2.12a and reveals ruthenium in two different oxidation states, Ru^{4+} peak at around 280.5 eV further proves presence of RuO_2. However, the Ru^{3+} band below 282 eV suggests co-presence of residual $RuCl_3$ on the sample (1.2 at.%) coming from the ruthenium loading source.

According to VB-XPS, shown in Figure 2.12b, the valence band edge remains at +1.1 eV after loading, while the density of states (DOS) showed an increasing tail at around +0.5 eV below the Fermi level. This change is related to higher photoactivity of of the composite compared to bare hematene, as these energy state levels provide orbital overlaps that facilitate the transportation of photogenerated hole to RuO_2 and oxidized ammonia to N_2. The photogenerated electrons on the other hand, went through the hematene and reduced ammonia to H_2. Moreover, the spatial separation of charge in the place of RuO_2 and the hematene heterojunction further improved the photoactivity of the composite compared to bare hematene. The schematic of the proposed mechanism is depicted in Figure 2.12c.

To exclude any changes in the crystal structure of hematene, that could occur during ruthenium loading and subsequent calcination on hematene at 300°C, we collected the

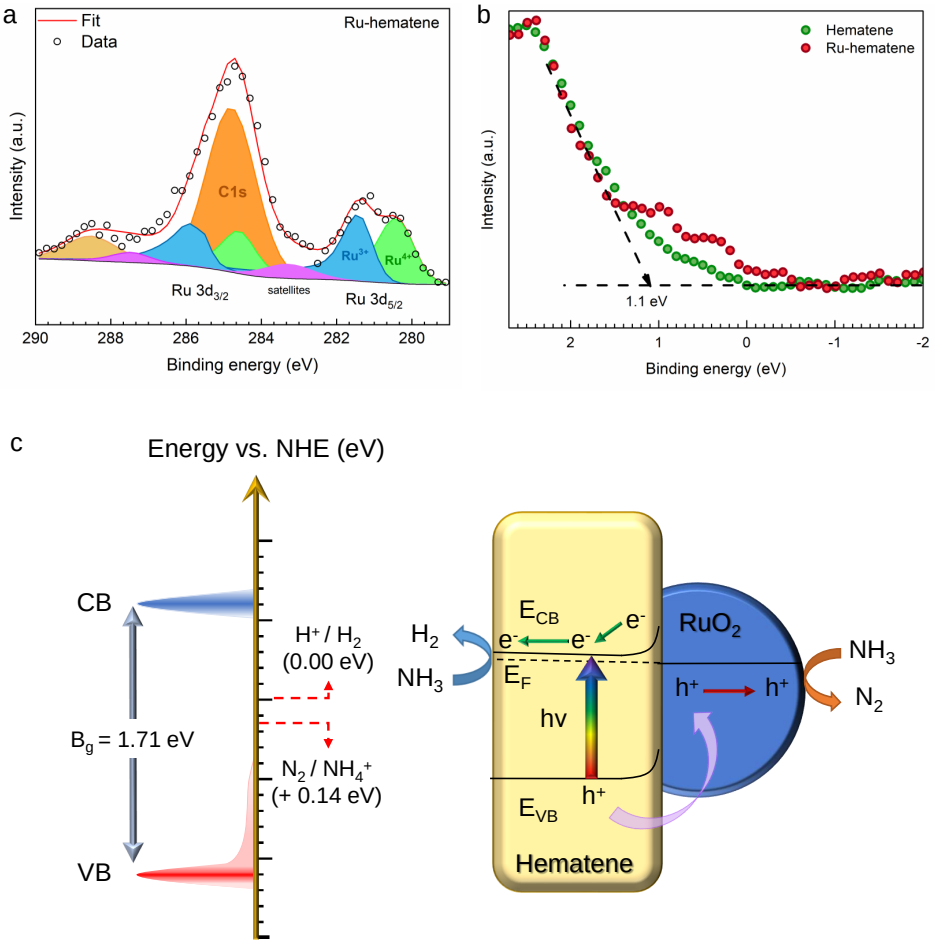

Figure 2.12: a: HR-XPS of Ru 3d region; b: VB-XPS of bare hematene (dark green dots) and Ru-hematene (dark red dots); c: schematic depiction of DOS and band edge positions of the Ru-hematene main electronic levels relative to the energy levels of the redox couples of aqueous ammonia and the proposed mechanism of ammonia photodecomposition by the Ru-hematene photocatalyst; adapted from ref. [116].

XRD patterns of both materials, as shown in Figure 2.13a. The ruthenium in a form of crystalline RuO_2 was confirmed by a negligible diffraction peak around 32.5° 2θ and no other phase changes were observed.

The EPR spectra reveal a major change in hematene behavior after ruthenium loading as visible from Figure 2.13b. The EPR silence of bare hematene is in agreement with the antiferromagnetic ordering at the experimental temperature (below T_M).

Furthermore, the absence of any EPR signal can be connected to the fast spin-lattice relaxation of the Fe^{3+} centres under an exchange coupled regime that became perturbed after Ru loading resulting in a broad, asymmetric resonant line in the Ru-hematene sample EPR spectrum with an average g-value of about $\approx 2,7$. We assume that the Ru ions partially altered the fraction of the Fe-O-Fe superexchange path by reacting with oxygen on top of hematene surface to form small RuO_2 nanoparticles. Furthermore, a weak modulation of the Fe^{3+} envelope was observed at $g \approx 2.09$ corresponding to the signal of Ru^{3+} in the resonant line of $RuCl_3$. Since the Ru loading was very low (0.5 wt.%), we could only detect the Ru^{3+} species via EPR and part of these fragments may also indicate a residual $RuCl_3$ in the composite as observed by XPS.

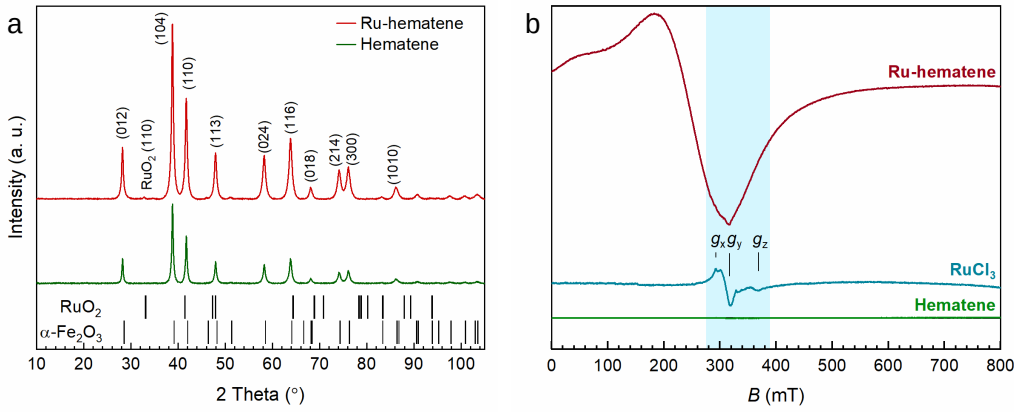

Figure 2.13: a: XRD patterns of bare hematene (dark green line) and Ru-hematene (dark red line); b: X-band CW EPR spectra of bare hematene (lower dark green line), $RuCl_3$ (middle blue line) and Ru-hematene (upper dark red line) recorded in frozen DI water dispersion ($T = 80\,\mathrm{K}$); adapted from ref. [116].

Photocatalytic activity

Both hematene and Ru-hematene suitability for ammonia photodecomposition was tested by means of UV-Vis diffuse reflectance spectroscopy (UV-Vis DRS), see Figure 2.14a, b. The band edge absorption for both samples was around 729 nm proving that these materials can absorb UV and visible part of the light spectrum. The amount of

light absorbed, especially in the visible region was highly increased in the Ru-hematene sample – one of the main conditions for an ideal photocatalyst. The optical band gap energy of hematene and Ru-hematene calculated by the Tauc plot [145] based on the Kubelka Munk [146] theory was 1.70 eV and 1.71 eV respectively – almost the same in spite of the huge difference in the absorbed light.

The control experiments under dark conditions showed almost zero catalytic activity of both materials for ammonia decomposition. Furthermore, the photodecomposition of ammonia without the presence of photocatalyst at 24°C was zero.

After confirming ruthenium as an ideal co-catalyst for hematene to decompose ammonia, several optimization were performed. The testing of different Ru loading amount is shown in Figure 2.14c, where the optimum amount of Ru proves to be 0.5 wt.% and leads to continuously increasing amount of H_2 within 24 h. In lower amounts of Ru, the charge separation was not effective enough to produce H_2. Higher amounts of Ru provided recombination centres at the hematene surface. Another optimization concerned the mass of photocatalyst against the photoactivity, as it is not necessarily proportional due to limitation of light absorption and diffusion conditions [147, 148]. The loading of 2 mg of the photocatalyst was optimal for both materials, as visible from Figure 2.14d.

Finally, the reusability of optimal photocatalyst amount was tested, see Figure 2.14e. The Ru-hematene decreased in activity by 11% after five photocatalytic runs (24 h per run) for the total of 120 h. The decrease can be associated with the loss of photocatalyst caused by attachment to the reactor or magnetic stirrer or by passivation with reactants, products or intermediate species, as the catalyst was not washed after each photoreaction run.

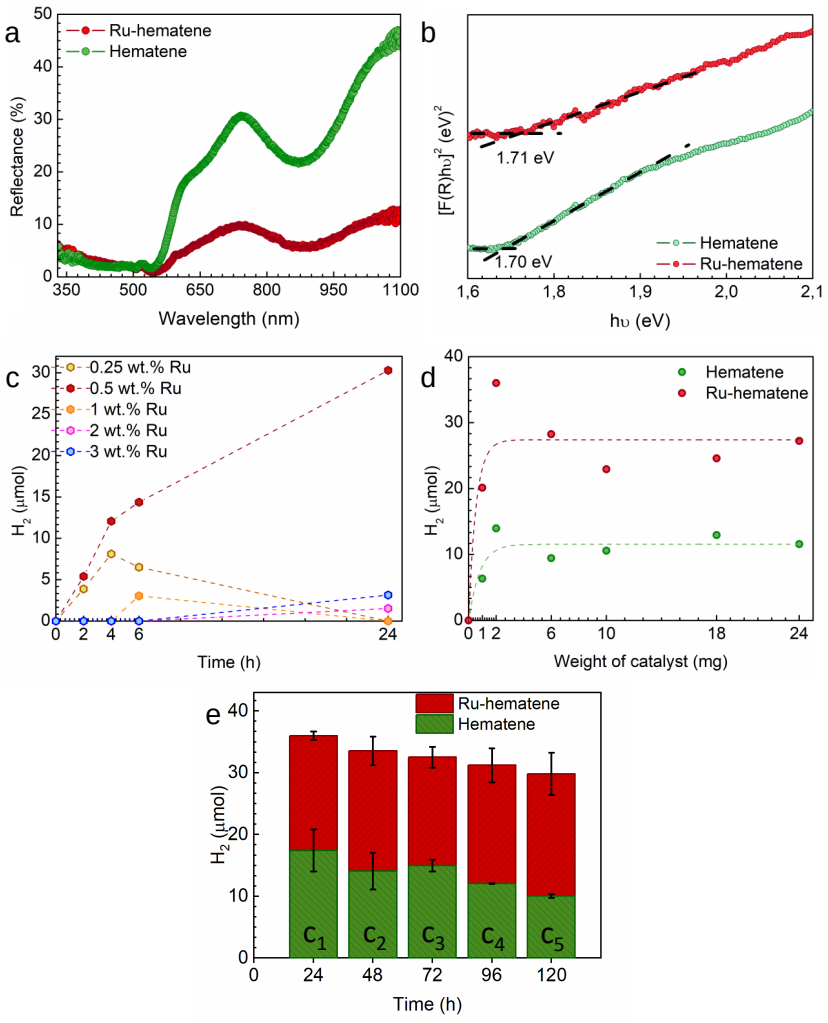

Figure 2.14: a: UV-Vis DRS of hematene and Ru-hematene and b: corresponding Tauc plot based on Kubelka-Munk model; c: optimizing of Ru co-catalyst loading amount (reactors were loaded with 8 mg of photocatalyst); d: the amount of evolved H_2 from photodecomposition of ammonia with different loading amount of pristine hematene and Ru-hematene (reactors were under illumination for 24 hours); e: reusability of 2 mg of hematene and Ru-hematene for H_2 evolution from ammonia photo decomposition demonstrated by consecutive cycles (c_1–c_5). After each cycle, the solution was sonicated and bubbled with Ar for 15 min. In all cases, the reactor was under visible LED illumination (wavelength 400 – 700 nm, power 3 W $\cdot$ m^{-2}); adapted from ref. [116].

3 Conclusion

The presented dissertation thesis focused on the investigation of three different 2D materials whose unique properties allowed them to be applied in the fields of energy storage and photocatalysis. We demonstrated the key role of TGA and XRD in the description of advanced 2D systems based on graphene derivatives and MXenes. The techniques contributed to the understanding of the internal structure, quantity and bonding interactions of the functionalities, which was essential to properly explain the performance of the materials in energy storage. The graphene polysulfide derivative based on fluorographene chemistry showed outstanding results as LSB cathode with capacity of 800 $\mathrm{mAh\,g^{-1}}$ (3 times higher than conventionally sulphurized graphene). The MXene/graphene derivative heterostructures proved to have variable adhesion between the layers that enabled better supercapacitor efficiency.

In the field of (quasi) 2D non-van der Waals (n-vdW) materials, we showed that their preparation does not rely on the use of toxic solvent such as DMF and that, when compromising with the reachable thickness (down to 3-5 layers), hematene can be prepared via exfoliation in DI water dispersion. Then, we investigated lattice strain in hematene via XRD and STEM and revealed, that the stress in the hematene lattice generally increases with decreasing layer thickness at long-range level. However, in very thin sheets the strain is non-uniform. An understanding of the intrinsic strain is crucial for tailoring hematene properties to suit the desired application.

Hematene possesses distinct properties compared to its bulk counterpart, for example a narrower band gap, which leads to easier formation of electrons and holes. By decorating the hematene sheets with RuO_2 nanoparticles, we created a synergistic system able to decompose ammonia via photocatalysis induced by visible light, that could lead to future production of hydrogen as a fuel. This way, we presented hematene

as a low cost, eco friendly (quasi) 2D material, that can be applied in numerous fields on its own or serve as a platform for single atom engineering.

Furthermore, we started to explore the iron oxide transitions for converting hematene to other iron oxides while keeping the 2D morphology. This way, we can open the doors towards other 2D iron oxide based materials that might be more difficult to prepare by exfoliation.

Bibliography

[1] K. S. Novoselov *et al.*, Science **306**, 666 (2004).

[2] A. K. Geim, Science **324**, 1530 (2009).

[3] Y. Gogotsi, editor, *Nanomaterials Handbook*, 2 ed. (CRC Press, Boca Raton, 2017).

[4] G. Yang, L. Li, W. B. Lee, and M. C. Ng, Science and Technology of Advanced Materials **19**, 613 (2018).

[5] D. Akinwande *et al.*, Extreme Mechanics Letters **13**, 42 (2017).

[6] A. H. Castro Neto, F. Guinea, N. M. R. Peres, K. S. Novoselov, and A. K. Geim, Rev. Mod. Phys. **81**, 109 (2009).

[7] A. Bianco *et al.*, Carbon **65**, 1 (2013).

[8] J. Sturala, J. Luxa, M. Pumera, and Z. Sofer, Chemistry – A European Journal **24**, 5992 (2018).

[9] M. Inagaki and F. Kang, J. Mater. Chem. A **2**, 13193 (2014).

[10] A. Bakandritsos *et al.*, ACS Nano **11**, 2982 (2017).

[11] I. Tantis *et al.*, Advanced Functional Materials **31**, 2101326 (2021).

[12] T. M. Magne *et al.*, J Nanostruct Chem **12**, 693 (2022).

[13] V. Šedajová *et al.*, Energy Environ. Sci. **15**, 740 (2022).

[14] D. D. Chronopoulos, A. Bakandritsos, M. Pykal, R. Zbořil, and M. Otyepka, Applied Materials Today **9**, 60 (2017).

[15] V. Mazánek *et al.*, Nanoscale **7**, 13646 (2015).

[16] R. Zbořil *et al.*, Small **6**, 2885 (2010).

[17] V. Hrubý *et al.*, Applied Surface Science **587**, 152839 (2022).

[18] M. Naguib *et al.*, Advanced Materials **23**, 4248 (2011).

[19] G. Deysher *et al.*, ACS Nano **14**, 204 (2020).

[20] R. E. Ustad *et al.*, Nanoscale (2023).

[21] Y. Gogotsi and B. Anasori, ACS Nano **13**, 8491 (2019).

[22] U. Amara, I. Hussain, M. Ahmad, K. Mahmood, and K. Zhang, Small **19**, 2205249 (2023).

[23] M. Shekhirev, C. E. Shuck, A. Sarycheva, and Y. Gogotsi, Progress in Materials Science **120**, 100757 (2021).

[24] Introduction to the Iron Oxides, in *The Iron Oxides*, chap. 1, pp. 1–7, John Wiley & Sons, Ltd, 2003.

[25] Crystal Structure, in *The Iron Oxides*, chap. 2, pp. 9–38, John Wiley & Sons, Ltd, 2003.

[26] T. Danno *et al.*, J. Phys.: Conf. Ser. **200**, 082003 (2010).

[27] T. Danno *et al.*, Crystal Growth & Design **13**, 770 (2013).

[28] R. Zboril, M. Mashlan, and D. Petridis, Chem. Mater. **14**, 969 (2002).

[29] J. Havlakova, J. Tucek, and R. Zboril, Stoichiometry Issue of Iron(iii) Oxide Nanomaterials by Mossbauer Spectroscopy, in *10th Anniversary International Conference on Nanomaterials - Research & Application (Nanocon 2018 (r))*, pp. 93–99, Slezska, 2019, Tanger Ltd.

[30] A. Cervellino, R. Frison, G. Cernuto, A. Guagliardi, and N. Masciocchi, J Appl Cryst **47**, 1755 (2014).

[31] D. Kubániová *et al.*, Journal of Magnetism and Magnetic Materials **472**, 96 (2019).

[32] J. A. Sans *et al.*, Nat Commun **9**, 4554 (2018).

[33] R. K. Sharma *et al.*, Green Chemistry **18**, 3184 (2016).

[34] K. Hola, Z. Markova, G. Zoppellaro, J. Tucek, and R. Zboril, Biotechnology Advances **33**, 1162 (2015).

[35] M. Kilianová *et al.*, Chemosphere **93**, 2690 (2013).

[36] J. Tuček, K. C. Kemp, K. S. Kim, and R. Zbořil, ACS Nano **8**, 7571 (2014).

[37] L. Lv *et al.*, Nanoscale Res Lett **16**, 138 (2021).

[38] Y. Lee *et al.*, Advanced Functional Materials **31**, 2006854 (2021).

[39] S. D. Roy, K. C. Das, and S. S. Dhar, Inorganic Chemistry Communications **134**, 109050 (2021).

[40] F. C. Voogt, T. Hibma, P. J. M. Smulders, L. Iesen, and T. Fujii, MRS Online Proceedings Library **474**, 211 (1997).

[41] B. K. McMillin, P. Biswas, and M. R. Zachariah, Journal of Materials Research **11**, 1552 (1996).

[42] Y. Wang *et al.*, Advanced Materials **35**, 2209465 (2023).

[43] Y. Li, X. Zhao, Y. Cui, F. Yang, and X. Bao, J. Phys. D: Appl. Phys. **54**, 204003 (2021).

[44] A. Puthirath Balan *et al.*, Nat. Nanotechnol. **13**, 602 (2018).

[45] A. Puthirath Balan *et al.*, Chem. Mater. **30**, 5923 (2018).

[46] P. Serles *et al.*, Science Advances **7**, eabk2041 (2021).

[47] R. Singla, T. A. Hackett, S. Kumar, J. Sharma, and M. K. Kashyap, Nanoscale Advances **2**, 5890 (2020).

[48] J. Shi *et al.*, Journal of Materials Chemistry A **10**, 17766 (2022).

[49] A. Bandyopadhyay, N. C. Frey, D. Jariwala, and V. B. Shenoy, Nano Lett. **19**, 7793 (2019).

[50] C. Bacaksiz, M. Yagmurcukardes, F. M. Peeters, and M. V. Milošević, 2D Mater. **7**, 025029 (2020).

[51] Y. Xu, L. Wang, and Y. Li, J. Phys. Chem. Lett. **13**, 7629 (2022).

[52] Y. Wei, M. Ghorbani-Asl, and A. V. Krasheninnikov, J. Phys. Chem. C **124**, 22784 (2020).

[53] A. Kumar, R. Zhang, M. Venkatesan, P. Stamenov, and J. M. D. Coey, Journal of Magnetism and Magnetic Materials **542**, 168507 (2022).

[54] A. Thejas Prasannakumar *et al.*, ACS Appl. Opt. Mater. (2022).

[55] A. Koutsioukis *et al.*, Journal of Materials Chemistry C **11**, 3244 (2023).

[56] B. Mohanty *et al.*, Journal of Materials Chemistry A **8**, 6709 (2020).

[57] Z. Zhang, M. Ye, E. J. Harvey, and G. Merle, J. Electrochem. Soc. **166**, H135 (2019).

[58] N. Abid *et al.*, Advances in Colloid and Interface Science **300**, 102597 (2022).

[59] S. Hao *et al.*, Frontiers in Chemistry **8** (2020).

[60] B. Cho and Y. Kim, Nanomaterials **10**, 764 (2020).

[61] H. Cui, Y. Guo, W. Ma, and Z. Zhou, ChemSusChem **13**, 1155 (2020).

[62] H. Schift, Appl. Phys. A **121**, 415 (2015).

[63] M. V. Pugachev, A. I. Duleba, A. A. Galiullin, and A. Y. Kuntsevich, Micromachines **12**, 850 (2021).

[64] W. Song *et al.*, Small **17**, 2101209 (2021).

[65] G. Wu *et al.*, Ceramics International **45**, 23841 (2019).

[66] Z. Cai, B. Liu, X. Zou, and H.-M. Cheng, Chem. Rev. **118**, 6091 (2018).

[67] F. Wang and X. Wang, Nanoscale **6**, 6398 (2014).

[68] R. Sui *et al.*, J. Phys. Chem. C **122**, 5141 (2018).

[69] R. Erni, *Aberration-Corrected Imaging In Transmission Electron Microscopy: An Introduction (2nd Edition)* (World Scientific Publishing Company, 2015).

[70] A. Howie, Journal of Microscopy **117**, 11 (1979).

[71] S. J. Pennycook and D. E. Jesson, Ultramicroscopy **37**, 14 (1991).

[72] Handbook of Thermal Analysis | Wiley, https://www.wiley.com/en-us/Handbook+of+Thermal+Analysis-p-9780471983637.

[73] P. Gabbott, A Practical Introduction to Differential Scanning Calorimetry, in *Principles and Applications of Thermal Analysis*, chap. 1, pp. 1–50, John Wiley & Sons, Ltd, 2008.

[74] M. Schirowski, F. Hauke, and A. Hirsch, Chemistry – A European Journal **25**, 12761 (2019).

[75] F. G. Brunetti *et al.*, J. Am. Chem. Soc. **130**, 8094 (2008).

[76] J. H. Williams, *Crystal Engineering: How Molecules Build Solids* (Morgan & Claypool Publishers, 2017).

[77] E. Westsson, S. Picken, and G. Koper, Chem. Commun. **55**, 1338 (2019).

[78] D. Nath, F. Singh, and R. Das, Materials Chemistry and Physics **239**, 122021 (2020).

[79] M. De and S. P. S. Gupta, Pramana - J Phys **23**, 721 (1984).

[80] J. I. Langford and A. J. C. Wilson, Journal of Applied Crystallography **11**, 102 (1978).

[81] S. Das Bakshi, D. Sinha, and S. Ghosh Chowdhury, Materials Characterization **142**, 144 (2018).

[82] M. S. Guney and Y. Tepe, Renewable and Sustainable Energy Reviews **75**, 1187 (2017).

[83] J. Xie and Y.-C. Lu, Nat Commun **11**, 2499 (2020).

[84] Q. Zhu *et al.*, Advanced Energy Materials **9**, 1901081 (2019).

[85] T. Kim, W. Song, D.-Y. Son, L. K. Ono, and Y. Qi, Journal of Materials Chemistry A **7**, 2942 (2019).

[86] I. Tantis *et al.*, Adv Funct Materials **31**, 2101326 (2021).

[87] J. Liu *et al.*, Nat Energy **4**, 180 (2019).

[88] M. Armand *et al.*, Journal of Power Sources **479**, 228708 (2020).

[89] S. Evers and L. F. Nazar, Acc. Chem. Res. **46**, 1135 (2013).

[90] Z. Wang *et al.*, Nat Commun **5**, 5002 (2014).

[91] X. Ji, K. T. Lee, and L. F. Nazar, Nature Mater **8**, 500 (2009).

[92] M. Medveď *et al.*, Nanoscale **10**, 4696 (2018).

[93] D. Matochová *et al.*, J. Phys. Chem. Lett. **9**, 3580 (2018).

[94] R. Steudel, Sulfur: Organic Polysulfanes, in *Encyclopedia of Inorganic Chemistry*, John Wiley & Sons, Ltd, 2007.

[95] Y. Yang, G. Lu, Y. Li, Z. Liu, and X. Huang, ACS Appl. Mater. Interfaces **5**, 13478 (2013).

[96] X. Wang *et al.*, ACS Appl. Mater. Interfaces **6**, 16182 (2014).

[97] Y. Ono, Y. Hayashi, S.-h. Urashima, and H. Yui, International Journal of Applied Glass Science **13**, 676 (2022).

[98] R. Fang *et al.*, Advanced Materials **29**, 1606823 (2017).

[99] J. Yan, Q. Wang, T. Wei, and Z. Fan, Advanced Energy Materials **4**, 1300816 (2014).

[100] Q. Wang, J. Yan, and Z. Fan, Energy Environ. Sci. **9**, 729 (2016).

[101] B. Hariprakash *et al.*, Electrochem. Solid-State Lett. **7**, A66 (2004).

[102] P. Albertus, S. Babinec, S. Litzelman, and A. Newman, Nat Energy **3**, 16 (2018).

[103] J. Sun, B. Luo, and H. Li, Advanced Energy and Sustainability Research **3**, 2100191 (2022).

[104] X. He and X. Zhang, Journal of Energy Storage **56**, 106023 (2022).

[105] T. Lin *et al.*, Science **350**, 1508 (2015).

[106] J. Hou, C. Cao, F. Idrees, and X. Ma, ACS Nano **9**, 2556 (2015).

[107] Y. Zhu *et al.*, Science **332**, 1537 (2011).

[108] A. Izadi-Najafabadi *et al.*, Advanced Materials **22**, E235 (2010).

[109] H. Tang *et al.*, Progress in Natural Science: Materials International **28**, 133 (2018).

[110] H. Saini *et al.*, ACS Nano **15**, 18742 (2021).

[111] V. Šedajová *et al.*, Energy Environ. Sci. **15**, 740 (2022).

[112] V. Šedajová, P. Jakubec, A. Bakandritsos, V. Ranc, and M. Otyepka, Nanomaterials **10**, 1731 (2020).

[113] B. E. Warren, Phys. Rev. **59**, 693 (1941).

[114] M. Shekhirev, C. E. Shuck, A. Sarycheva, and Y. Gogotsi, Progress in Materials Science **120**, 100757 (2021).

[115] M. Anayee *et al.*, Chemical Communications **56**, 6090 (2020).

[116] J. Dzíbelová *et al.*, Applied Materials Today **34**, 101881 (2023).

[117] D. K. Craig, R. J. Weir, W. Wagner, and D. Groth, Drug and Chemical Toxicology **7**, 551 (1984).

[118] T. H. Kim and S. G. Kim, Safety and Health at Work **2**, 97 (2011).

[119] COMMISSION REGULATION (EU) 2021/2030, 2021.

[120] Z.-y. Gao, W. Sun, and Y.-h. Hu, Transactions of Nonferrous Metals Society of China **24**, 2930 (2014).

[121] T. Fujii *et al.*, Phys. Rev. B **59**, 3195 (1999).

[122] X. Lu *et al.*, Adv. Mater. **26**, 3148 (2014).

[123] S. Chahal, S. M. Kauzlarich, and P. Kumar, ACS Mater. Lett. **3**, 631 (2021).

[124] A. M. Smith, A. M. Mohs, and S. Nie, Nature Nanotech **4**, 56 (2009).

[125] S. Maiti *et al.*, Energy & Environmental Science **14**, 3717 (2021).

[126] S. Wang *et al.*, ACS Appl. Mater. Interfaces **15**, 20200 (2023).

[127] L. Hou *et al.*, Advanced Energy Materials **13**, 2300177 (2023).

[128] B. Gilbert, F. Huang, H. Zhang, G. A. Waychunas, and J. F. Banfield, Science **305**, 651 (2004).

[129] J. Srisuriyachot *et al.*, Carbon **200**, 347 (2022).

[130] M. K. Ozturk, E. Arslan, İ. Kars, S. Ozcelik, and E. Ozbay, Materials Science in Semiconductor Processing **16**, 83 (2013).

[131] K. R. Desai *et al.*, Physica B: Condensed Matter **614**, 413054 (2021).

[132] B. Goris *et al.*, Nano Lett. **15**, 6996 (2015).

[133] G. Argentero *et al.*, Nano Lett. **17**, 1409 (2017).

[134] A. Ishizuka, M. Hytch, and K. Ishizuka, Journal of Electron Microscopy **66**, 217 (2017).

[135] L. Jones *et al.*, Ultramicroscopy **179**, 57 (2017).

[136] Y. L. Tang, Y. L. Zhu, and X. L. Ma, Ultramicroscopy **160**, 57 (2016).

[137] U. Ludacka *et al.*, npj 2D Mater Appl **2**, 1 (2018).

[138] J. C. Meyer *et al.*, Nature **446**, 60 (2007).

[139] N. S. Lewis and D. G. Nocera, Proc. Natl. Acad. Sci. **103**, 15729 (2006).

[140] H. Wang *et al.*, Adv. Mater. **33**, 2008422 (2021).

[141] W. I. F. David *et al.*, J. Am. Chem. Soc. **136**, 13082 (2014).

[142] A. Iwase, K. Ii, and A. Kudo, Chem. Commun. **54**, 6117 (2018).

[143] M. Reli *et al.*, Intl. J. Hydrog. Energy **40**, 8530 (2015).

[144] Y. Shu *et al.*, Appl. Catal. B **300**, 120688 (2022).

[145] J. Tauc, R. Grigorovici, and V. Vancu, Phys. Status Solidi **15**, 627 (1966).

[146] P. Makuła, M. Pacia, and W. Macyk, J. Phys. Chem. Lett. **9**, 6814 (2018).

[147] S. Cao and L. Piao, Angew. Chem. **132**, 18468 (2020).

[148] M. Qureshi and K. Takanabe, Chem. Mater. **29**, 158 (2017).